Universidade de Aveiro Departamento de Engenharia Cerâmica e do Vidro
2006

Aliaksandr Shaula

Novos Materiais com Ferro, com Alta Condutividade Iónica de Oxigénio

Novel Iron-Containing Materials with Fast Oxygen Ionic Transport

Universidade de Aveiro Departamento de Engenharia Cerâmica e do Vidro
2006

Aliaksandr Shaula

Novos Materiais com Ferro, com Alta Condutividade Iónica de Oxigénio

dissertação apresentada à Universidade de Aveiro para cumprimento dos requisitos necessários à obtenção do grau de Doutor em Ciência e Engenharia de Materiais, realizada sob a orientação científica do Doutor Fernando Marques, Professor Catedrático do Departamento de Engenharia Cerâmica e do Vidro, e do Doutor Vladislav Kharton, Investigador Principal do Departamento de Engenharia Cerâmica e do Vidro

Apoio financeiro da FCT e do FSE no âmbito do III Quadro Comunitário de Apoio.

o júri

presidente

Prof. Dr. António Ferreira Pereira de Melo
professor catedrático da Universidade de Aveiro

Prof. Dr. Fernando Manuel Bico Marques
professor catedrático da Universidade de Aveiro

Prof. Dr. Michael John Smith
professor associado da Escola de Ciências da Universidade do Minho

Prof. Dra. Verónica Cortés de Zea Bermudez
professora associada da Universidade de Trás-os-Montes e Alto Douro

Dr. Vladislav Vadimovich Kharton
investigador principal convidado da Universidade de Aveiro

Dr. Derek Clark Sinclair
reader do Departamento de Engenharia Materiais da Universidade do Sheffield, UK

acknowledgements

I would like to express my sincere gratitude to the following people:

My supervisors Dr. Vladislav Kharton and Prof. Fernando Marques;

Dr. Eugene Naumovich and Alexandr Viskup, for the time they have generously spent for discussions and advices, while introducing me to the solid state chemistry and the measurement techniques;

My present and former colleagues, particularly Prof. Jorge Frade, Drs. Aleksey Yaremchenko, Andrei Kovalevsky, Filipe Figueiredo, Duncan Fagg, Glenn Mather, Ekaterina Tsipis, Ivan Marozau, Nikolai Vyshatko and Dmitrii Logvinovich, for their help, discussions and encouragement;

Our collaborators from other institutions, in particular Drs. Mikhail Patrakeev, João Waerenborgh, Frans Snijkers, Jozef Cooymans, Maxim Avdeev, Ilia Leonidov and Prof. Victor Kozhevnikov, for their cooperation, important contributions and discussions;

functionaries and technicians of the Department of Ceramics and Glass Engineering, especially Sr. Luís Costa, for invaluable help;

my parents, for rearing and educating me, as well as for their patience and support through these years.

palavras-chave

Condutividade Iónica, Condutividade Electrónica, Expansão Térmica, Permeabilidade Electroquímica ao Oxigénio, Membrana, Estabilidade, Electrólito Sólido, Condutor Misto.

resumo

Pretende-se com este trabalho avaliar o potencial de novos materiais para aplicações de alta temperatura, nomeadamente membranas para separação de oxigénio e oxidação parcial de hidrocarbonetos, e pilhas de combustível de electrólito sólido para produção de energia eléctrica. O estudo incidiu na avaliação da expansão térmica e na determinação das condutividades iónica e electrónica, através de técnicas modificadas de medição da eficiência faradaica e da força electromotriz, assim como de medidas de permeabilidade electroquímica de oxigénio. As perovesquites à base de $SrFe(Al)O_{3-\delta}$ e $Sr(La)Fe(Ga)O_{3-\delta}$ apresentam o mais alto nível de permeabilidade de oxigénio e expansão térmica moderada. Nas apatites da família $La_{10}Si_6O_{27}$, a condutividade iónica é predominante em largas gamas de pressão parcial de oxigénio e temperatura, sendo os valores medidos comparáveis aos de electrólitos sólidos convencionais.

keywords

Ionic Conductivity, Electronic Transport, Thermal Expansion, Oxygen Permeation, Membrane, Stability, Solid Electrolyte, Mixed Conductor

abstract

The purpose of this work is the electrochemical characterization of the potential materials for high-temperature applications such as membrane reactors for oxygen permeation and/or partial oxidation of hydrocarbons, and solid oxide fuel cells for electric power generation. The particular emphasis was given to the determination of partial oxygen ionic and electronic conductivities using modified faradaic efficiency and electromotive force techniques, as well as specific oxygen permeability measurements. Perovskite-type $SrFe(Al)O_{3-\delta}$ and $Sr(La)Fe(Ga)O_{3-\delta}$ possess high levels of the oxygen permeation and moderate thermal expansion. Apatite-type $La_{10}Si_6O_{27}$-based materials own predominant oxygen ionic conductivity in a large oxygen pressure range and show oxygen ionic conductivity comparable to that of conventional solid electrolytes.

Table of Contents

Introduction

Oxide ceramics with high oxygen ionic conductivity are key materials for numerous high-temperature electrochemical applications, such as solid oxide fuel cells (SOFCs), gas electrolyzers, oxygen sensors, and electrocatalytic reactors for natural gas conversion. These electrochemical technologies provide important advantages with respect to conventional industrial processes. In particular, the use of SOFCs for electric power generation is characterized by a high energy-conversion efficiency, environmental safety and fuel flexibility including the prospect of direct operation with natural gas. Practical application of SOFCs is, however, still limited due to high costs of the component materials and processing. Membrane technologies based on mixed conductors may provide significant economical benefits due to the infinite theoretical oxygen permselectivity of such membranes and an ability to integrate oxygen separation, steam reforming and partial oxidation into a single step for the natural gas conversion. This might increase energy efficiency of oxygen-based combustion processes, decrease capital investments into gas-to-liquid industry and to recover or to use remote gases that would otherwise be flared or re-injected. The materials showing highest oxygen permeability exhibit, however, serious disadvantages such as unsatisfactory stability under large oxygen chemical potential gradients. The development of novel solid electrolytes and mixed conductors is thus of vital importance.

The objective of this work was to develop new materials for SOFCs and oxygen membranes, with fast oxygen ionic transport, low cost and sufficient stability under typical operation conditions. Particular goals were:

- to select most promising groups of oxygen ion-conducting ceramics and to study phase relationships, thermal expansion, ion and electron transport, stability and other properties relevant to practical applications;
- to identify compositions suitable for use in high-temperature electrochemical devices, and to study their defect chemistry;
- to optimize ceramic processing conditions and to assess the role of ceramic microstructure on the partial ionic and electronic conductivities, oxygen permeability and thermal expansion;
- to perform long-term testing under typical electrochemical cell operation conditions, to reveal dominant degradation mechanisms and stability limits of the novel materials.

1. Literature review: oxygen ion-conducting materials and their technological applications

1.1. Oxygen ionic transport in oxide materials

1.1.1. Basic relationships

The process of mass/charge transfer may be characterized [1] by the flux density (j_k), which is equal to a number of moles of k-type particles that pass through the unit area (S = 1 cm^2) during the unit time (t = 1 s). If c_k and υ_k are the concentration and drift velocity of moving species, respectively, then

$$j_k = c_k \upsilon_k \tag{1.1}$$

The driving force for a flux is the concentration (or chemical potential) gradient. According to the Fick's first law, the flux and concentration gradient are interrelated as [2]

$$j_k = -D_k \nabla c_k \tag{1.2}$$

The minus sign before the right-hand side of the equation shows that a transfer occurs from the higher concentration region to the lower concentration one. The coefficient of proportionality D_k is called the diffusion coefficient. Its physical meaning is the flux velocity for unit area and unit concentration gradient; the dimensionality corresponds to cm^2/s.

Taking into account the relationship between concentration and chemical potential (μ) for ideal solution [2], when activity and concentration of k-type component are equal,

$$\mu_k = \mu_k^0 + RT \ln c_k \tag{1.3}$$

the Fick's first law may be re-written as:

$$j_k = -c_k \frac{D_k}{RT} \nabla \mu_k \tag{1.4}$$

where R is the gas constant and T is the absolute temperature. The corresponding current density (I) is proportional to the flux of charged species [2]:

$$I_k = z_k F j_k \tag{1.5}$$

where z_k is the charge number and F is the Faraday constant. Hence, the current density due to a chemical potential gradient

$$I_k = -c_k z_k F \frac{D_k}{RT} \nabla \mu_k = -c_k u_k \nabla \mu_k \tag{1.6}$$

$$u_k = z_k F \frac{D_k}{RT} \tag{1.7}$$

Here u_k denotes the mobility, expressed in $cm^2\ s^{-1}\ V^{-1}$, that is the velocity of k-type particles under unit electrical potential (φ) gradient. The product of mobility and electrical potential gradient yields υ_k:

$$\upsilon_k = u_k \nabla \varphi \tag{1.8}$$

Substitution of Eqs. (1.8) and (1.5) into Eq. (1.1) gives the current density due to an electrical potential gradient:

$$I_k = -c_k z_k F u_k \nabla\varphi \tag{1.9}$$

From comparison with the Ohm's law [2]

$$I_k = \sigma_k \nabla\varphi \tag{1.10}$$

the conductivity can be expressed as

$$\sigma_k = c_k z_k F u_k \tag{1.11}$$

The sum of Eqs. (1.6) and (1.9) presents the overall current density under both chemical and electrical potential gradients:

$$I_k = -c_k u_k \nabla\mu_k - c_k z_k F u_k \nabla\varphi = -c_k u_k (\nabla\mu_k + z_k F \nabla\varphi) = -c_k u_k \nabla\eta_k \tag{1.12}$$

where η_k is the electrochemical potential of k-type species. Substitution of Eqs. (1.11) and (1.12) into Eq. (1.5) leads to Wagner's law for isothermal conditions [3]:

$$j_k = -\frac{\sigma_k}{z_k^2 F^2} \nabla\eta_k \tag{1.13}$$

Generally, particles of n different types participate in the charge transfer, and the corresponding transference number value defines the contribution of the k-type species to the total conductivity [2]:

$$t_k = \sigma_k / \sigma = \sigma_k \Big/ \sum_{i=1}^{n} \sigma_i \tag{1.14}$$

1.1.2. Defect formation and diffusion mechanisms

The atoms in a crystal always vibrate around their equilibrium positions. The oscillation energy of some atoms is high enough to shift them from regular sites into interstitial cavities (Frenkel-type disordering). As a result, two kinds of point defects are created: interstitial atoms and vacancies. Moreover, vacancies may form at the gas-solid phase boundary (Schottky-type disordering). The latter process can be seen as dissolution of vacuum in a crystal. The free energy change at constant volume (ΔG_d) results from the compensation between the increase of enthalpy (ΔH_d) required for the formation of a defect and increasing entropy (ΔS_d) resulting from disorder promotion [2]:

$$\Delta G_d = \Delta H_d - T\Delta S_d \tag{1.15}$$

Clearly, the defect concentration can only theoretically be zero at 0 K and should increase on heating. In solid oxides both cations and anions may generate Frenkel- and Schottky-type defects. According to

the Kröger-Vink notation [4], basic character, subscript letter and superscript symbols describe atom (or vacancy), its location and charge, correspondingly (Fig. 1.1).

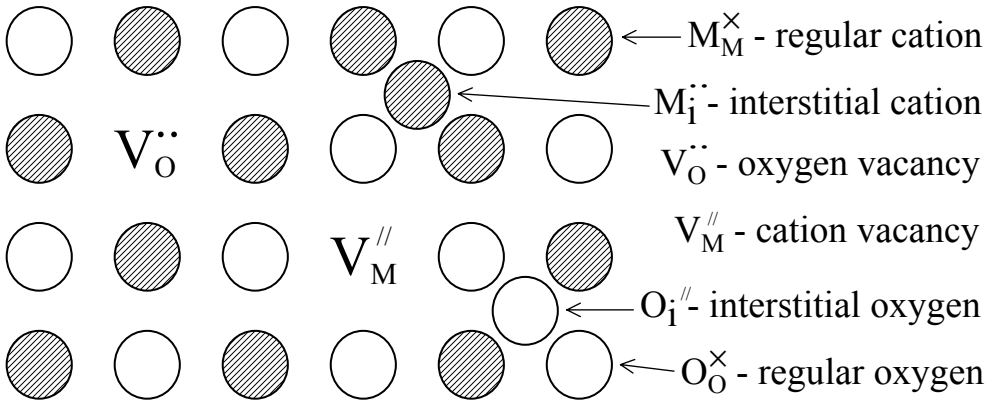

Fig. 1.1. Kröger-Vink nomenclature of structure elements.

For instance, $V_O^{\bullet\bullet}$ is an oxygen vacancy with effective double positive charge, formed by the transference of an oxygen ion from a normal site, $O_O^{\times}$, to the gaseous state or into an interstitial position $O_i^{//}$. The regular cations and anions have effective charge zero, since the ideal crystal is a reference in this case. The charge carriers in an oxide may, in principle, include cations, anions, electrons (e') and holes ($h^{\bullet}$). Using Kröger-Vink notation, formation of these intrinsic defects in a binary oxide MO may be presented as [2]:

$$M_M + O_O = V_M^{//} + V_O^{\bullet\bullet} + M_i^{\bullet\bullet} + O_i^{//} \qquad \text{(Frenkel-type disordering)} \qquad (1.16)$$

$$0 = V_M^{//} + V_O^{\bullet\bullet} \qquad \text{(Schottky-type disordering)} \qquad (1.17)$$

$$0 = e' + h^{\bullet} \qquad \text{(electronic disordering)} \qquad (1.18)$$

The symbol "0" in Eqs. (1.17) and (1.18) denotes an ideal crystal.

Incorporation of atoms different from M and O also creates structural and electronic imperfections. For example, substitutional dissolution of lower-valency cations into the oxide lattice leads to the formation of oxygen vacancies in order to maintain charge electroneutrality [2]:

$$Md_2O = 2Md_M' + O_O^{\times} + V_O^{\bullet\bullet} \qquad (1.19)$$

In the case of MO the crystal structure consists of M and O sublattices. Within a sub-lattice, any ion adjacent to a vacancy may "jump" into the unoccupied site owing to energy fluctuations.

Evidently, when an ion jumps to a vacant position, this creates a vacancy, where the jumping ion was originally situated. Consequently, the diffusion of ions can alternatively be visualized as migration of vacancies, moving in the direction opposite to that of the ions. The interstitial ions may shift into neighboring interstitial sites, thus providing an alternative diffusion mechanism to the vacancy one. It is also possible that an interstitial ion occupies the position of a regular ion displacing it into another interstitial site. Both the vacancy and interstitial migration suggest that the movement of ions in a crystal can only take place via the diffusion of lattice defects. In particular, the oxygen ionic conduction requires the presence of oxygen vacancies and/or interstitials. Typically one type of defects dominates and determines the diffusion mechanism. For migration of randomly distributed oxygen vacancies all "jumps" are supposed to occur in all directions independently of previous jumps, except for isotopic effects. The probability of a jump per time, ν, called the jump frequency, depends exponentially upon the free energy of activation, ΔG, of the jumps [2]:

$$\nu = \nu_0 \exp\left(-\frac{\Delta G_m}{RT}\right) = \nu_0 \exp\left(\frac{\Delta S_m}{R}\right)\exp\left(-\frac{\Delta H_m}{RT}\right) \tag{1.20}$$

where ν_0 is the vibration frequency (jump attempt frequency). Assuming ΔS_m to be temperature independent:

$$\nu = f \exp\left(-\frac{\Delta H_m}{RT}\right) \tag{1.21}$$

$$f = \nu_0 \exp\left(\frac{\Delta S_m}{R}\right) \tag{1.22}$$

where f is a constant, and ΔH_m corresponds to the minimal energy necessary for a jump. Such an energy barrier is determined by the potential energy of the distorted crystal lattice.

An applied electrical potential gradient decreases the energy barrier in the forward direction and increases it in the reverse direction. If $\nabla\varphi \neq 0$ and d_j is the jump distance, the activation energy is equal to $\Delta H_m - z_k F \nabla\varphi d_j/2$ in the forward direction and $\Delta H_m + z_k F \nabla\varphi d_j/2$ in the reverse direction. The drift velocity is the product of the jump frequency, the jump distance and the difference in the forward and reverse directions:

$$\upsilon_k = f\frac{d_j}{2}\left[\exp\left(-\frac{\Delta H_m - z_k F d_j \nabla\varphi/2}{RT}\right) - \exp\left(-\frac{\Delta H_m + z_k F d_j \nabla\varphi/2}{RT}\right)\right] \tag{1.23}$$

For electrical fields used in practice $z_k F \nabla\varphi d_j << 2RT$ and Eq. (1.23) simplifies to

$$\upsilon_k = f\frac{d_j^2 z_k F \nabla\varphi}{2RT}\exp\left(-\frac{\Delta H_m}{RT}\right) \tag{1.24}$$

From Eqs. (1.8) and (1.11) follows that the partial conductivity can be rewritten as

$$\sigma_k = c_k z_k F \frac{\upsilon_k}{\nabla\varphi} \tag{1.25}$$

Substitution of Eq. (1.24) into Eq. (1.25) gives:

$$\sigma_k = f \frac{c_k d_j^2 z_k^2 F^2}{2RT} \exp\left(-\frac{\Delta H_m}{RT}\right) \tag{1.26}$$

If considering the oxygen ionic conductivity (σ_O) via $V_O^{\bullet\bullet}$ migration

$$\sigma_O = \frac{A[V_O^{\bullet\bullet}]}{T} \exp\left(-\frac{\Delta H_m}{RT}\right) \tag{1.27}$$

$$A = f \frac{2 d_j^2 F^2}{R} \tag{1.28}$$

When oxygen vacancies are formed in MO via Eq. (1.17), their concentration in a solid oxide is determined by the temperature and free energy change as it was shown in [2]:

$$[V_O^{\bullet\bullet}] = \exp\left(-\frac{\Delta G_d}{2RT}\right) = \exp\left(\frac{\Delta S_d}{2R}\right) \exp\left(-\frac{\Delta H_d}{2RT}\right) \tag{1.29}$$

Substitution of Eq. (1.29) into Eq. (1.27) finally yields the standard Arrhenius equation:

$$\sigma_O = \frac{A_0}{T} \exp\left(-\frac{\Delta H_m + \Delta H_d / 2}{RT}\right) \tag{1.30}$$

$$A_0 = A \exp\left(\frac{\Delta S_d}{2R}\right) \tag{1.31}$$

If a solid oxide is a pure oxygen ionic conductor ($\sigma = \sigma_O$), the pre-exponential factor and sum of enthalpies of oxygen vacancy formation and diffusion can be evaluated from the slope of $\ln(\sigma T)$ vs. $1/T$ dependence (Arrhenius plot).

Note that the ionic conductivity due to migration of any structural defect follows the Arrhenius temperature dependence, analogous to Eq. (1.30), and therefore increases on heating.

1.1.3. Oxygen permeation

Within specific temperature and oxygen pressure ranges a number of solid oxides exhibit both oxygen ionic (σ_O) and electronic (σ_e) conductivities. The simultaneous movement of ionic and electronic charge carriers under the driving force of the chemical potential gradient enables oxygen transport through the oxide bulk. Assuming that the mobile ionic defects are oxygen vacancies, formed according to

$$1/2 O_2 + V_O^{\bullet\bullet} + 2e^{/} = O_O^{\times} \tag{1.32}$$

the flux densities of oxygen vacancies and electrons under open circuit conditions (no electrical current) are given by [5]

$$j_{V_O^{\cdot\cdot}} = -\frac{\sigma_{V_O^{\cdot\cdot}}}{4F^2}\nabla\eta_{V_O^{\cdot\cdot}} \tag{1.33}$$

$$j_{e'} = -\frac{\sigma_{e'}}{F^2}\nabla\eta_{e'} \tag{1.34}$$

$$j_{h^{\cdot}} = -\frac{\sigma_{h^{\cdot}}}{F^2}\nabla\eta_{h^{\cdot}} \tag{1.35}$$

as results from Eq. (1.13). Since no charge accumulation occurs at steady state conditions, the fluxes of ionic and electronic defects are interrelated by the charge balance:

$$j_{e'} - j_{h^{\cdot}} = 2j_{V_O^{\cdot\cdot}} \tag{1.36}$$

Substitution of Eqs. (1.33)-(1.35) into Eq. (1.36) eliminates the electrical potential gradient from $\nabla\eta$, and fluxes can be considered in terms of the chemical potential gradient only. It follows from Eqs. (1.18) and (1.32) that

$$\nabla\mu_{e'} = -\nabla\mu_{h^{\cdot}} \tag{1.37}$$

$$1/2\nabla\mu_{O_2} = -\nabla\mu_{V_O^{\cdot\cdot}} - 2\nabla\mu_{e'} \tag{1.38}$$

Combination of Eqs. (1.33)-(1.38) with the relationship $j_{O_2} = -1/2\, j_{V_O^{\cdot\cdot}}$ yields the Wagner equation [3]:

$$j_{O_2} = -\frac{1}{16F^2}\frac{\left(\sigma_{e'} + \sigma_{h^{\cdot}}\right)\sigma_{V_O^{\cdot\cdot}}}{\sigma_{e'} + \sigma_{h^{\cdot}} + \sigma_{V_O^{\cdot\cdot}}}\nabla\mu_{O_2} \tag{1.39}$$

The flux of molecular oxygen can also be expressed as [5]

$$j_{O_2} = -\frac{1}{16F^2}\frac{\sigma_e\sigma_O}{\sigma_e + \sigma_O}\nabla\mu_{O_2} \tag{1.40}$$

where $\sigma_O = \sigma_{V_O^{\cdot\cdot}}$ and $\sigma_e = \sigma_{e'} + \sigma_{h^{\cdot}}$.

The ratio of the product to the sum of the partial electronic and oxygen ionic conductivitites represents the so-called ambipolar conductivity:

$$\sigma_{amb} = \frac{\sigma_e\sigma_O}{\sigma_e + \sigma_O} \tag{1.41}$$

When a membrane is placed under one oxygen pressure gradient, this induces the simultaneous motion of oxygen ionic and electronic defects (Fig. 1.2). Integration of Eq. (1.40) across the membrane thickness (d) leads to an integral form of Wagner's equation ($p_2(O_2) > p_1(O_2)$):

$$j_{O_2} = \frac{RT}{16F^2 d} \int_{\ln p_1(O_2)}^{\ln p_2(O_2)} \frac{\sigma_e \sigma_O}{\sigma_e + \sigma_O} d \ln p(O_2) \quad (1.42)$$

For a MIEC with predominant electronic conduction ($\sigma_e >> \sigma_O$) the oxygen flux density is proportional to the oxygen ionic conductivity:

$$j_{O_2} = \frac{RT}{16F^2 d} \int_{\ln p_1(O_2)}^{\ln p_2(O_2)} \sigma_O d \ln p(O_2) \quad (1.43)$$

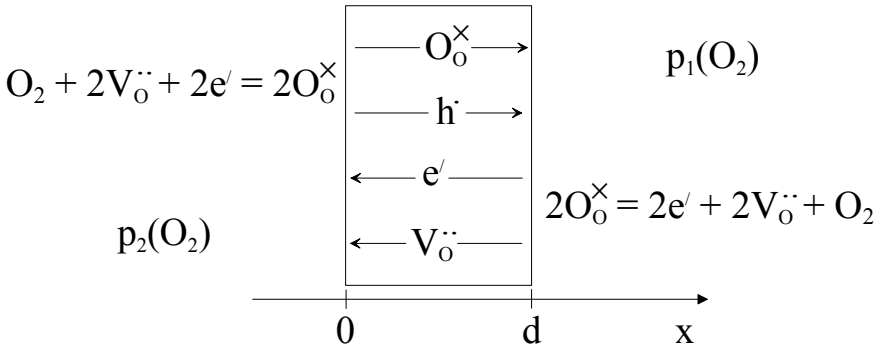

Fig. 1.2. Schematic representation of oxygen permeation through a mixed electronic-oxygen ionic conducting dense membrane.

The overall process of oxygen transport through a membrane includes, together with bulk oxygen diffusion, the exchange of oxygen between gas phase and oxide surface. Possible steps of such an exchange during oxygen reduction are the adsorption of O_2 on the surface, dissociation, charge transfer and incorporation of oxygen anions into the lattice. The oxidation is supposed to follow the same steps in reverse direction.

The Wagner's equation is valid for sufficiently thick membranes when the bulk oxide-ion conductivity determines the oxygen transport rate (Fig. 1.3), i.e., when the oxygen chemical potential drop is distributed across the membrane bulk only. If the surface exchange rate is limited, decreasing membrane thickness leads to increasing drop of $\nabla\mu_{O_2}$ by the surface reaction kinetics. For a certain membrane thickness (d_C), specific for a given oxide, bulk and surface processes consume equal parts of the total oxygen chemical gradient (so-called mixed control):

$$\Delta\mu_{O_2}^{bulk} = \Delta\mu_{O_2}^{surface} \quad (1.44)$$

If the surface reaction is rate-limiting only at one surface and linear kinetics for diffusion and interfacial exchange is postulated [6],

$$j_{O_2} = -\frac{1}{1+d_C/d}\frac{1}{16F^2}\frac{\sigma_e\sigma_O}{\sigma_e+\sigma_O}\frac{\Delta\mu_{O_2}^{total}}{d} \tag{1.45}$$

The oxide surface and gas phase exchange oxygen even in the absence of an oxygen chemical potential gradient. The equilibrium rate of the molecular oxygen transfer may be expressed as [5]:

$$j_{O_2}^S = \frac{k_S}{4}c_O \tag{1.46}$$

where k_S is the surface exchange coefficient (cm/s) and c_O is the concentration of oxygen anions.

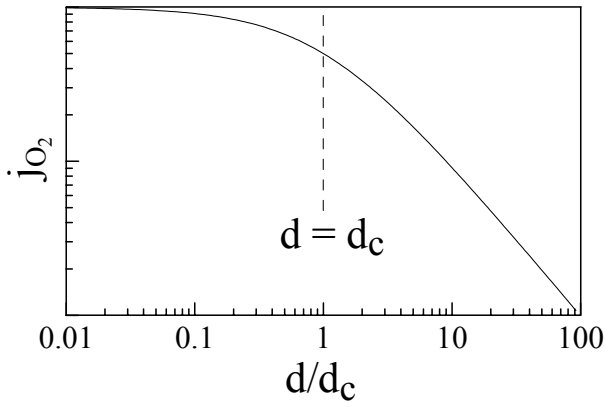

Fig. 1.3. Thickness dependence of the oxygen flux calculated using Eq. (1.45).

The characteristic thickness is inversely proportional to $j_{O_2}^S$:

$$d_C = \frac{RT}{16F^2}\frac{\sigma_e\sigma_O}{\sigma_e+\sigma_O}\frac{1}{j_{O_2}^S} \tag{1.47}$$

For prevailing electronic conductivity ($\sigma_e >> \sigma_O$), Eq. (1.47) may be simplified:

$$d_C = \frac{RT}{16F^2}\frac{\sigma_O}{j_{O_2}^S} \tag{1.48}$$

Combination of Eqs. (1.7) and (1.11) leads to the classical Nernst-Einstein equation [5]:

$$\sigma_O = \frac{16F^2}{RT}c_O D_S \tag{1.49}$$

where D_S is the self-diffusion coefficient of O^{2-}. By substitution of Eqs. (1.46) and (1.49) into Eq. (1.48):

$$d_C = \frac{D_S}{k_S} \tag{1.50}$$

The permeation processes can be analyzed either using the oxygen permeation flux density j (mol s^{-1} cm^{-2}) or the specific oxygen permeability $J(O_2)$ (mol s^{-1} cm^{-1}), interrelated as [7]:

$$J(O_2) = jd\left[\ln\frac{p_2}{p_1}\right]^{-1} \tag{1.51}$$

The latter quantity is convenient in order to identify a limiting effect of the surface exchange rate on the oxygen permeation, on the basis of the thickness dependence of the permeation flux. As $J(O_2)$ is proportional to j × d by definition, oxygen permeability should be independent of thickness if surface limitations to the oxygen permeation flux are negligible. In this case $J(O_2)$ relates to the ambipolar conductivity averaged for a given oxygen pressure range:

$$J(O_2) = \frac{RT}{16F^2}\overline{\sigma_{amb}} = \frac{RT}{16F^2}\overline{\frac{\sigma_e\sigma_O}{\sigma_e+\sigma_O}} = \frac{RT}{16F^2}\overline{\sigma t_e t_O} \tag{1.52}$$

where t_e and t_O are the electron and oxygen ion transference numbers, respectively.

1.1.4. Ionic conduction in perovskite-type oxides

As given below, significant oxygen ionic conductivity and permeability were found for many perovskite-type oxide systems.

The lattice of oxides having ideal perovskite structure ABO_3 consists of a cubic array of corner sharing BO_6 octahedra. These polyhedra create the cavities occupied by A-cations. Therefore, A- and B-cations have 12- and 6-fold coordination by oxygen, respectively, and anions are linked to 6 cations (4A and 2B). Fig. 1.4 represents the unit cell with a B-cation at the body center. In this case oxygen anions occupy the face centers and the A-cations are found at the corners.

Presuming that the ions are in contact with each other, the following relationship between their radii [8] for cubic cell geometry should be derived: $r_A + r_O = \sqrt{2}(r_B + r_O)$. However, the perovskite-like structure of ABO_3 compounds is retained even if this equation is not exactly obeyed. To estimate the deviation from the ideal case, Goldschmidt [9] has proposed a tolerance factor (t):

$$t = \frac{r_A + r_O}{\sqrt{2}(r_B + r_O)} \tag{1.53}$$

By definition, the cubic perovskite lattice exists for tolerance factor values close to unity. Since A-cations occupy the voids formed by BO_6 octahedra, the size of the A-cation is limited by B-O-B length. Beyond this limit BO_6 octahedra are obliged to share faces, like in $SrMnO_3$ [10], instead of

corners. As a result, the perovskite structure is kept for t values, only slightly higher than 1. For example, the cubic lattice of $BaTiO_3$ (t = 1.06) undergoes a transition into the hexagonal phase with face-sharing BO_6 octahedra at 1705 K in air [11]. When t is lower than 1, the ideal structure deforms in order to tailor the crystal cell for smaller A-cations (and/or larger B-cations). The deformation occurs via a distortion of the BO_6 octahedra and their cooperative tilting. This decreases the unit cell symmetry and at first gives rise to rhombohedrally- and, afterwards, orthorhombically-distorted lattices still related to the perovskite type [12]. For instance, substitution of Al^{3+} with larger Ga^{3+} or Sc^{3+} in $LaAlO_3$, rhombohedrally-distorted at room temperature, leads to orthorhombic structures characteristic of $LaGaO_3$ and $LaScO_3$. The crystal lattice may also suffer structural transitions on heating, as orthorhombic → rhombohedral in $LaGaO_3$ at 418 K and rhombohedral → cubic in $LaAlO_3$ at 723 K [13]. The perovskite-like structure remains down to tolerance factor values as low as 0.75 [14]. If the size of A-cations is comparable with that of B-cations (t < 0.75), like in $CoTiO_3$ and $MnTiO_3$, ilmenite-type phases may form [15].

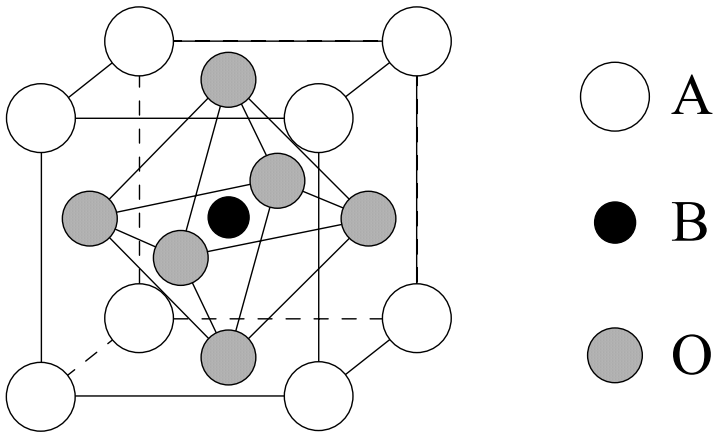

Fig. 1.4. Ideal perovskite structure.

The transport of oxygen ions in perovskites occurs via migration of oxygen vacancies, at least for oxygen-deficient phases [16]. As expected for a structure with close-packed oxygen planes, formation of interstitial O^{2-} and their diffusion are highly unfavorable [17]. Atomistic simulation studies of perovskite-like oxides confirm the migration of oxygen vacancies to provide the lowest energy path [18]. The migrating oxygen anion should jump along the edge of BO_6 octahedra, passing the so-called “saddle-point” between one B- and two A-cations (Fig. 1.5).

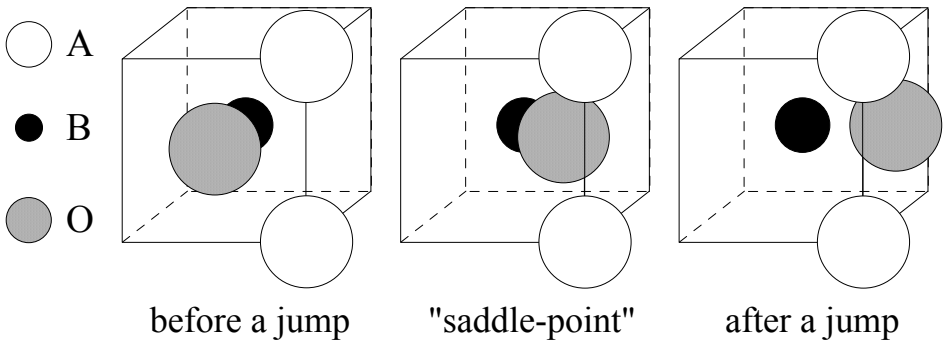

Fig. 1.5. Migration of an oxygen anion to a vacant O-site.

According to Eq. (1.11) the oxygen ionic conductivity due to the diffusion of oxygen vacancies is proportional to their concentration and mobility:

$$\sigma_O = 2F[V_O^{\bullet\bullet}]u_{V_O^{\bullet\bullet}} \qquad (1.54)$$

Apparently, the ionic transport in stoichiometric ABO_3 perovskite-type ceramics is very low, determined by minor impurities and microstructure. The oxygen ionic conductivity increases with acceptor doping [19], when the substitution of host cations with lower-valency ions leads to the formation of oxygen vacancies in order to maintain charge electroneutrality. Feng and Goodenough [20] and Ishihara with his group [21] were the first who reported high oxygen ionic transport (10^{-2}-10^{-1} S/cm) in lanthanum gallate moderately doped with Sr and Mg (Fig. 1.6), at elevated temperatures (973-1273 K) for a wide range of oxygen pressure (10^{-15}-10^{5} Pa). The ionic conduction in $Ln_{1-x}Sr_xGa_{1-y}Mg_yO_{3-\delta}$ (Ln = rare-earth element) decreases in the order La > Nd > Sm > Gd > Y > Yb, i.e., with decreasing radius of the A-cation [22]. The studies of oxygen ionic transport in $La_{0.9}Sr_{0.1}B_{0.9}Mg_{0.1}O_{3-\delta}$ (B = Al, Ga, Sc, In) showed the fastest oxygen ionic conduction for $LaGaO_3$-based ceramics [13]. The latter phases are solid electrolytes, since the electronic conductivity is insignificant under given conditions, i.e., $t_O \approx 1$.

On the contrary, electronic transport prevails ($t_e \approx 1$) in the perovskite-like oxides where B-sites are occupied by transition metals (Mn [23], Fe [24], Co [25] and others). These materials may also possess the oxygen ionic conductivity comparable or even higher than that of $La_{1-x}Sr_xGa_{1-y}Mg_yO_{3-\delta}$ (LSGM) oxides (Fig. 1.6), resulting in high oxygen permeation. For $La_{1-x}Sr_xCo_{1-y}Fe_yO_{3-\delta}$ series, extensively studied by Teraoka et al. [26-28], the maximum oxygen permeation was found in $SrCo_{0.8}Fe_{0.2}O_{3-\delta}$, where the ionic transport is limited by both bulk oxide-ion conductivity and surface exchange rate [27]. The oxygen permeation of $La_{0.6}Sr_{0.4}Co_{0.8}B_{0.2}O_{3-\delta}$ (B = Cr, Mn, Fe, Co, Ni, Cu)

increases according to the trend in the periodical system: Cr ≈ Mn < Fe < Co < Ni < Cu [29]. This phenomenon may basically result from higher oxygen mobility due to weaker B-O bonds, as indicates the stability of $La_{1-x}Sr_xBO_3$ phases in reducing atmospheres [5,30]. The influence of A-site dopant depends on B-site composition, for instance, the flux density in $La_{0.6}A_{0.4}Co_{0.8}Fe_{0.2}O_{3-\delta}$ [28] and $La_{0.4}A_{0.6}Co_{0.2}Fe_{0.8}O_{3-\delta}$ [31] (A = Ca, Sr, Ba) systems increases in the sequences Sr < Ca < Ba and Ca < Ba < Sr, correspondingly.

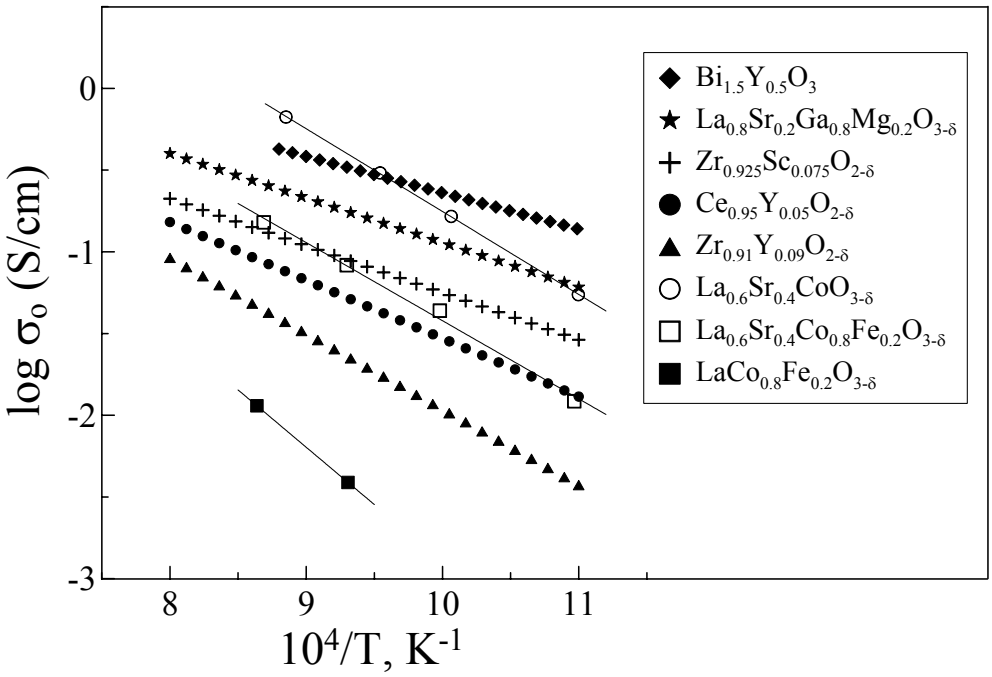

Fig. 1.6. Ionic conductivity of various solid electrolytes [22] and $LaCoO_3$-based phases [29].

Various perovskite-like MIECs with substantial oxygen ionic transport have been studied so far. Representative examples include alkaline-earth titanates $ATi_{1-x}B_xO_{3-\delta}$ (A = Ca, Sr; B = Fe, Ga, Sc) [32-34], chromites $La_{1-x}Ca_xCrO_{3-\delta}$ [35], ferrites $Sr_{1-x}Bi_xFeO_{3-\delta}$ [36], $BaFe_{0.8-x}Bi_xCo_{0.2}O_{3-\delta}$ [37] and $La_{1-x}A_xFe_{1-y}M_yO_{3-\delta}$ (A = Sr, Ba; M = Ti, Cr, Mn, Co, Ni) [38-41], cobaltites $Ba_{1-x}Y_xCoO_{3-\delta}$ [42], transition metal and Mg-doped lanthanum gallates $La_{1-x}Sr_xGa_{1-y-z}M_yMg_zO_{3-\delta}$ (M = V, Cr, Mn, Fe, Co, Ni) [43-48]. Also, new solid electrolytes were developed: aluminates $Nd_{1-x}A_xAl_{1-y}Ga_yO_{3-\delta}$ (A = Ca, Sr, Ba) [49,50], gallates $La_{1-x}Ba_xGa_{1-y}Mg_yO_{3-\delta}$ [51], scandates $La_{1-x}Sr_xSc_{1-y}Al_yO_{3-\delta}$ [52], indates $BaIn_{1-y}Zr_yO_{3-\delta}$ [53] and $La_{1-x}A_xInO_{3-\delta}$ (A = Mg, Ca, Sr, Ba) [54].

1.1.5. Oxygen ionic transport in fluorite-type solid solutions

The crystal structure of cubic fluorite oxides having general formula AO_2 (space group Fm3m, no. 225) consists of a simple cubic oxygen lattice with alternate body centers occupied by cations [2]. Hence, anions are linked to 4 cations, whereas cations are 8-coordinated by oxygen. Among binary oxides, important for electrochemical applications, the fluorite-type structure was found for ZrO_2 [55], HfO_2, CeO_2, ThO_2 [56] and δ-modification of Bi_2O_3 [57]. Ceria and thoria exhibit no phase transitions up to the melting point. The smaller Zr^{4+} and Hf^{4+} cations maintain the cubic fluorite structure at higher temperatures only. For instance, pure zirconia crystallizes in three polymorphs under atmospheric pressure. The monoclinic phase ($P2_1/c$, no. 14), stable at room temperature, transforms at 1440 K into tetragonally-distorted fluorite ($P4_2/nmc$, no. 137), which rearranges at 2640 K into the cubic one [58]. Note, however, that the temperatures of these reversible phase transitions depend on the impurities content. The cubic phase may be stabilized down to the low temperatures by doping [56]. The cubic and tetragonally-distorted fluorite-type lattices are compared in Fig. 1.7.

The oxygen ionic transport in fluorites occurs via the migration of oxygen vacancies. Maximum conduction is characteristic of cubic fluorite phase, as illustrates the sudden increase of the oxygen ionic conductivity in Bi_2O_3 about 1000 K, reflecting a transition from the monoclinic polymorph into the cubic δ-phase [57,59]. The cubic structure of bismuth oxide remains until melting near 1100 K [2]. Within this narrow temperature range, Bi_2O_3 has the highest oxygen ionic conductivity (2-3 S/cm) among all solid electrolytes known so far. The superior ionic transport of δ-Bi_2O_3 might result from high concentration of oxygen vacancies (two vacant O-sites per unit cell) and weak oxygen bonding to the cation sublattice.

Doping with yttrium or rare-earth elements (REE) stabilizes the cubic fluorite-type phase with high ionic conductivity towards lower temperatures [57,59]. The larger the difference between the ionic radii of Bi^{3+} and the dopant cation, the smaller amount of dopant is necessary to stabilize the δ-phase. Therefore, the minimum stabilizing concentration increases with cation radius from 15-20 mol% Er_2O_3 to 30-35 mol% Gd_2O_3 [60]. These materials are also solid electrolytes; electron transference numbers are typically lower than 0.1 [57]. The oxygen ionic conduction in $(Bi_2O_3)_{1-x}(Ln_2O_3)_x$ (Ln = Y and REE) was found to decrease with increasing concentration of the stabilizing cation. Such an influence is due to decreasing unit cell volume and increasing average strength of M^{3+}-O^{2-} bond [60]. Clearly, the solid oxides containing minimum amount of dopant exhibit the highest ionic transport. Both ionic transport and minimum stabilizing concentration of dopant increase with increasing Ln^{3+} radius, but the influence of the latter tendency prevails. As a result, the highest oxygen ionic conductivity (0.37 S/cm at 973 K) was reported for $(Bi_2O_3)_{0.8}(Er_2O_3)_{0.2}$ with small dopant content [57].

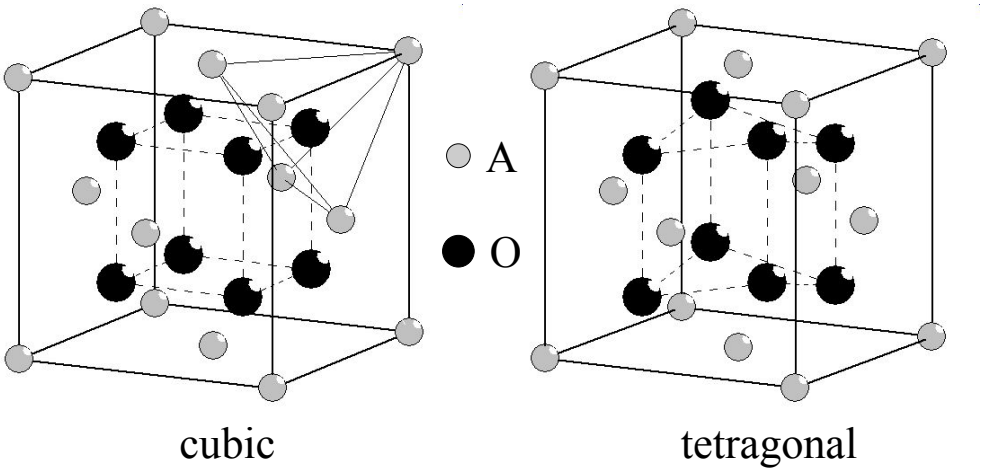

Fig. 1.7. Comparison of the cubic (left) and tetragonal (right) fluorite-type structures.

The cubic polymorph of zirconia and hafnia can be stabilized towards lower temperatures by substitution with alkaline-earth elements (AEE), Sc, Y and REE [55,56,58]. The typical minimum concentration of dopants, necessary for such a stabilization, is about 8-12 mol% for zirconia [58] and somewhat higher for the corresponding HfO_2-based fluorites [56]. As for any acceptor-type doping, oxygen vacancies are generated in order to maintain electroneutrality. The highest ionic transport is observed at 8-10 mol% of stabilizing cation and decreases with further doping [55]. The maximum of the conductivity versus composition curves is essentially temperature-independent at T < 1300 K and close to a minimum stabilizing concentration. Contrary to $(Bi_2O_3)_{1-x}(Ln_2O_3)_x$, the oxygen ionic conductivity of ZrO_2- and HfO_2-based fluorites decreases, when the dopant radius increases. The highest ionic transport is known for scandium-doped zirconia (8 mol% Sc_2O_3): 0.32 S/cm at 1273 K [58]. The conductivity of zirconates is higher than that of corresponding hafnates [56,61]. Since Sc-, Lu- and Yb-stabilized ZrO_2 are more expensive than Y-doped one, zirconia with 8 mol% Y_2O_3 (8YSZ) has been considered as solid electrolyte of choice. This material shows satisfactory level of oxygen ionic conduction (0.14 S/cm at 1273 K) and stability from oxidizing conditions till extremely reducing atmospheres with oxygen pressure as low as 10^{-25} Pa [5].

The ionic conduction of pure ceria and thoria in air is relatively low due to insignificant oxygen nonstoichiometry. Substitution with AEE, Sc, Y and REE (above 40 mol% in some cases) introduces oxygen vacancies and thus increases the oxygen ionic transport of CeO_2- and ThO_2-based fluorites [56,62]. The ionic conductivity reaches maximal values at 10-20 mol% of dopants and declines at higher content, tendency essentially independent of temperature. The activation energy

follows an opposite trend. These tendencies are typically explained by the association of oxygen vacancies and substituting ions [62]. Ionic transport in doped cerias is faster if compared with corresponding thoria-based fluorites. Typically, trivalent cations enhance more effectively the ionic conduction with respect to divalent ones [63]. Maximum oxide-ion conductivity is found in $(CeO_2)_{1-x}(MO_{1.5})_x$ and $(CeO_2)_{1-x}(MO)_x$ where substitution causes minimal expansion or contraction of the fluorite lattice relative to pure CeO_2 [62]. Namely, the highest oxygen ionic conduction was found in $Ce_{0.8}Sm_{0.2}O_{2-\delta}$ and $Ce_{0.8}Gd_{0.2}O_{2-\delta}$ (CGO), 0.25 and 0.20 S/cm at 1273 K in air, respectively [64]. Ionic transport prevails in ceria-based fluorites under oxidizing atmospheres. The t_O decreases with increasing temperature and reducing oxygen pressure. For CeO_2-based fluorites, the low $p(O_2)$ limit of the electrolytic domain corresponds to 10^{-15}-10^{-10} Pa within 973-1273 K [63]. As solid electrolytes, doped cerias are used in intermediate-temperature (873-1073 K) electrochemical applications [56]. The Bi_2O_3-based fluorites decompose at 873-973 K when the oxygen pressure is lower than 10^{-10}-10^{-7} Pa [57], which makes the possible use of these ceramics as problematic.

1.1.6. Mixed oxygen ionic and electronic conductivity of composite materials

Under an oxygen pressure gradient, the oxygen flux through a gas-tight membrane is only possible if oxygen ions (or oxygen vacancies) move together with electron holes (or electrons), as it was shown in 1.1.3. Hence, the membrane material should exhibit both oxygen ionic and electronic conductivities as high as possible to provide faster oxygen permeation. Such a mixed conduction is observed, e.g., for numerous perovskite- and fluorite-like solid solutions [2,5,26-29,55-57]. In these oxides, ionic and electronic transport occurs within the same phase. In the 90s, the concept of a dual-phase membrane for oxygen permeation, reported first by Mazanec et al. [65], has been extensively assessed [66-81]. The composite consists of two percolated (3-dimensionally continuous) phases, one having predominant electronic conductivity and another being a solid electrolyte (Fig. 1.8). The oxygen ions (or oxygen vacancies) diffuse mainly through the ionic conducting phase ($t_O \approx 1$), whereas the counter flux of electrons (or electron holes) is preferential in the electronic conducting phase ($t_e \approx 1$).

Commonly, metals (Ni, Pd, Pt, Ag, Au), perovskite-type cobaltites and manganites are exploited as electronically-conductive component, whilst fluorite- and perovskite-like solid electrolytes represent the ion-conductive one [65-67,70-81]. The oxygen permeability of a resulting composite depends on the transport properties of constituent phases and on their volume ratio. According to a parallel layer model [66],

$$\sigma_C^{total} = \sigma_{ion}\omega_{ion} + \sigma_{el}\omega_{el} \qquad (1.55)$$

where the subscripts *c*, *ion* and *el* stand for composite, oxygen ionic and electronic conducting component and ω is the corresponding volume fraction. The continuity of the electrolyte component is partially blocked by the other phase, and the ionic partial blocking factor F_b can be introduced in Eq. (1.55):

$$\sigma_C^{total} = F_b \sigma_{ion} \omega_{ion} + \sigma_{el} \omega_{el} \quad (1.56)$$

To define the ambipolar conduction of a composite, the effect of microstructure was also taken into account - as dimensionless factors τ_{ion} and τ_{el} [67]:

$$\frac{1}{\sigma_C^{amb}} = \frac{\tau_{ion}}{\sigma_{ion} \omega_{ion}} + \frac{\tau_{el}}{\sigma_{el} \omega_{el}} \quad (1.57)$$

McLachlan et al. [68] proposed the effective medium approximation to describe the compositional dependence of a transport property using the term of critical (percolation) volume fraction ω_C:

$$\frac{(\sigma_{ion}^{1/t_g} - \sigma_C^{1/t_g})}{\sigma_{ion}^{1/t_g} + A\sigma_C^{1/t_g}} \omega_{ion} + \frac{(\sigma_{el}^{1/t_g} - \sigma_C^{1/t_g})}{\sigma_{el}^{1/t_g} + A\sigma_C^{1/t_g}} \omega_{el} = 0 \quad (1.58)$$

where t_g is an exponent related to a grain shape (typically 1.65-2.00 for three-dimensional morphology) and $A = (1 - \omega_C) / \omega_C$. Similar equation was deduced in terms of a percolation model [69]:

$$\frac{\sigma_C - \sigma_{ion}}{2\sigma_C + \sigma_{ion}} \omega_{ion} + \frac{\sigma_C - \sigma_{el}}{2\sigma_C + \sigma_{el}} \omega_{el} = 0 \quad (1.59)$$

Solving (1.59) for σ_C yields:

$$\sigma_C = \frac{E_1 + \sqrt{E_1^2 + E_2}}{4} \quad (1.60)$$

where $E_1 = 3 (\sigma_{ion} \omega_{ion} + \sigma_{el} \omega_{el}) - (\sigma_{ion} + \sigma_{el})$ and $E_2 = 8 \sigma_{ion} \sigma_{el}$. Using (1.58) and (1.59), the total and partial conductivities of $La_2(Zr,Y)_2O_{7-\delta}$-$LaCoO_{3-\delta}$ [70], $(Ce,Gd)O_{2-\delta}$-$(Gd,Ca)CoO_{3-\delta}$ [71] and $(Ce,Gd)O_{2-\delta}$-$(La,Sr)MnO_{3-\delta}$ [72] systems were described.

Theoretically, both phases of a composite percolate when their volume fractions are larger than 1/3. Indeed, the mainly reported percolation threshold corresponds to 30-40 vol%, e.g., in $(Zr,Y)O_{2-\delta}$-Pd [73] and $(Zr,Y)O_{2-\delta}$-NiO [74], $(Bi,Er)_2O_{3-\delta}$-Ag [67] and $(Bi,Y,Sm)_2O_{3-\delta}$-Ag [75]. Within such a compositional range the ambipolar conduction and, consequently, oxygen permeation may achieve maximum level, higher than that of initial materials, as confirmed by the studies of Bi_2O_3- and $(Ce,Gd)O_{2-\delta}$-based composites [67,75-77]. At the same time, composites possess lower oxygen ionic conductivity with respect to the ion-conducting component [71,76-78], particularly due to a significant tortuosity of the latter constituent and the presence of "dead ends" (Fig. 1.8). For membrane thickness above 1.0 mm, the permeation fluxes are typically limited by relatively slow oxygen diffusion in

composite bulk [75,77-80]. Consequently, the volume fraction of the ionic conducting component should be the largest possible.

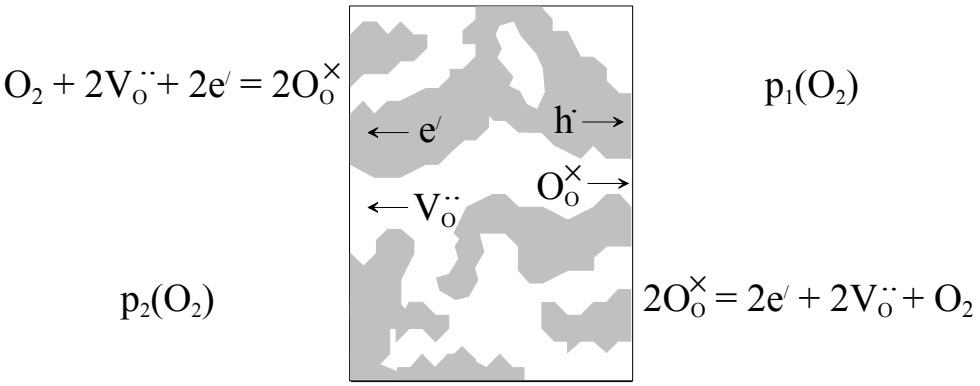

Fig. 1.8. Dual-phase composite membrane.

The surface exchange reaction may occur mainly within the three-phase boundary (tpb) between the gas, electronic and ionic conducting phases [5]. Hence, large tpb length or area results in higher oxygen flux. This emphasizes a considerable influence of composite microstructure on the permeability. Also, the activity of both constituents towards oxygen exchange reaction plays an important role in the electrode processes. Replacing catalytically active silver, one of the best oxygen electrode materials, for inert gold in $(Bi,Er)_2O_{3-\delta}$-based composite leads to a substantial decline (about one order of magnitude) of the flux density and to a switch of permeation-limiting factor from the bulk ionic conduction to the surface kinetics [81].

In spite of high oxygen permeability values, excellent mechanical strength and thermal-shock resistance of composites with Pd, Pt and Ag as the electronic conducting phase [65,73,75], cheaper materials are needed to replace the noble metals. Recently, relatively high oxygen permeability was revealed for $(Ce,Gd)O_{2-\delta}$-$(Gd,Ca)CoO_{3-\delta}$ [71], $(Ce,Gd)O_{2-\delta}$-$(La,Sr)MnO_{3-\delta}$ and $(Ce,Gd)O_{2-\delta}$-$(La,Sr)(Fe,Co)O_{3-\delta}$ [77] systems. However, the interdiffusion of cations between the phases (during sintering and long-term exposure at working temperatures) was found to affect the initial composition of the components and deteriorate the ionic transport [70,71,77]. Further development of composites with high and time-independent oxygen permeability is clearly necessary.

1.1.7. Oxygen ionic transport in apatite-type phases

In the 90s, several research groups reported significant oxygen ionic conductivity for the apatite-like oxides with general formula $A_{10-x}(MO_4)_6O_{2\pm\delta}$, where A corresponds to rare- and alkaline-earth metals; M refers typically to V, Si and Ge [82-84], but some other elements, e.g. Mn, Fe, Co, Al and Ga, may also occupy M-sites [85-87].

The apatite lattice can be viewed as a "hybrid" structure consisting of covalent MO_4 tetrahedra and ionic-like A/O channels. Three possible space groups correspond to the apatite unit cell, and the lattice symmetry increases in the order: trigonal $P\bar{3}$ (no. 147) < hexagonal $P6_3$ (no. 173) < hexagonal $P6_3/m$ (no. 176). The latter one, as most symmetrical, is generally employed in structural refinement and was therefore used to build an illustration of the apatite-type crystal structure (Fig. 1.9). Isolated MO_4 tetrahedra create the cavities where are located A-atoms, 7- and 9-coordinated by oxygen. The additional oxygen anions are surrounded each by three A-site cations and form channels running through the structure along c-axis.

The studies of single crystals with an apatite structure clearly indicated an anisotropy of the conductivity: ionic transport parallel to the c-axis is about 10 times higher than perpendicular to the c-axis [88]. The structural analysis revealed high values of the anisotropic thermal parameter of channel oxide-ions along the c-axis [87,89-92]. Moreover, this parameter is higher for apatites having faster ionic conductivity [87,89]. Therefore oxygen channels in the apatite lattice seem to be responsible for the high oxide-ion conduction, which should be one-dimensional in this case, unlike isotropic oxygen transport in perovskites and fluorites. The electromotive force (EMF) tests suggested that ionic conduction is predominant in rare-earth silicates and germanates [82,84]. The total conductivity of these apatites is essentially independent of oxygen pressure, confirming a minor contribution of the electronic transport [86,90].

The oxygen-ion conduction in $Ln_{10}Si_6O_{27}$ (Ln = La, Pr, Nd, Sm, Gd, Dy) increases with increasing radius of Ln^{3+} cations whilst the activation energy of ionic transport decreases; maximum conductivity was obtained for the La-containing phase [82]. The same correlation was mentioned for perovskite-type and Bi_2O_3-based solid electrolytes. Such a tendency might reflect the decreasing energy of electrostatic interaction between channel O^{2-} and Ln^{3+}, when Ln^{3+} radius increases. Also, increasing ionic size of Ln^{3+} leads to unit cell expansion and may thus facilitate ion diffusion. Likewise, the radius of Ge^{4+} is larger compared with Si^{4+} [8], and apatite-like germanates exhibit faster oxygen transport than their silicium analogues [84,93]. However, the activation energy within a given temperature range is typically higher in germanates, including the cases of $La_{10}M_6O_{27}$, $La_9SrM_6O_{26.5}$

[84] and $La_{9.33}M_6O_{26}$ [93]. For instance, above 1023 K $La_{10}Ge_6O_{27}$ possesses an oxygen ionic conduction comparable with that of LSGM and CGO, whereas $La_{10}Si_6O_{27}$ shows oxygen transport higher than 8YSZ only below 823-873 K [84]. Nonetheless, silicates are considered as promising materials for practical applications rather than germanates, since the latter family shows a crucial structural instability due to Ge volatilization [90,91,93]. The loss of germanium leads to the segregation of La_2GeO_5 as an impurity phase, having electrical conductivity (3×10^{-5} S/cm at 1073 K) 10^3-10^4 times lower than, for example, the conductivity of $La_{9.33}Si_2Ge_4O_{26}$ (0.06 S/cm at 1073 K). The formation of insulating La_2GeO_5 layers drastically deteriorates the bulk transport properties of apatite [93].

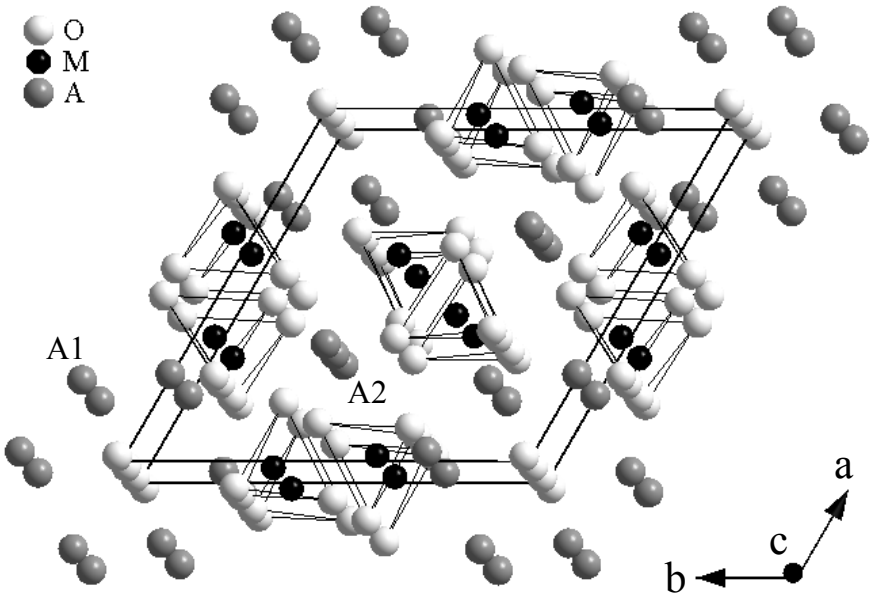

Fig. 1.9. A view of apatite-type crystal structure along c-axis.

The mechanism of oxygen ionic conduction in the apatite-type oxides is still under open discussion, partially due to scarce experimental data. Nevertheless, most of the results obtained so far indicated an importance of interstitial oxygen sites [83,84,86,87,91-93]. Generally, the ionic transport rises on increasing oxygen concentration, whilst the activation energy decreases. Typical examples are the $Ca_{10-x}La_xV_6O_{25+x/2}$ [83] and $La_{10-x}Sr_xSi_6O_{27-x/2}$ [84]. The highest ionic conductivity is characteristic of the oxygen-hyperstoichiometric (more than 26 atoms per formula unit) apatites. For instance, values as high as 0.05 S/cm for $La_9SrGe_6O_{26.5}$, 0.04 S/cm for $La_{9.75}Sr_{0.25}Si_6O_{26.875}$ [84] and 0.03 S/cm for

$La_9BaGe_6O_{26.5}$ [91] were measured at 1073 K. The level of the oxygen-ion conduction in $Ln_{10}Si_6O_{27}$ ceramics with maximum oxygen content is slightly lower (e.g. 2.1×10^{-3} S/cm at 1073 K for $La_{10}Si_6O_{27}$) due to segregated secondary phases [82].

Powder neutron diffraction studies of $La_{9.33}Si_6O_{26}$ showed that about 14% of the channel oxygen atoms are displaced to the interstitial positions located midway between regular channel sites [89]. Such a Frenkel-type disorder in $La_{9.33}Si_6O_{26}$ was also demonstrated by atomistic simulation of the defect formation [94]. Moreover, modelling results indicated another interstitial position, which lies at the periphery of the oxygen channel, and a non-linear "sinusoidal-like" mechanism was proposed as the lowest energy migration path for oxide-ion. The structural analysis of $La_{9.55}Si_6O_{27-\delta}$ and $La_{9.60}Ge_6O_{27-\delta}$ verified that oxygen anions may indeed occupy these predicted interstitial O-sites located close to SiO_4 tetrahedra [92]. The diffusion of oxygen anions via these positions requires a considerable local displacement of SiO_4 units towards A2-cations (Fig. 1.9), therefore A-site deficiency facilitates such cooperative structural relaxation. As expected, stoichiometric apatites exhibit low ionic transport: $La_{10}Si_4Ga_2O_{26}$ – 4.1×10^{-6} S/cm at 773 K [87], $La_8Sr_2Si_6O_{26}$ – 2.9×10^{-7} S/cm at 973 K [89] and $La_8Ba_2Ge_6O_{26}$ – 5.5×10^{-5} S/cm at 1073 K [91].

1.2. High-temperature electrochemical devices

1.2.1. Solid oxide fuel cells

1.2.1.1. Operation principles

Fuel cells are electrochemical devices that transform the chemical energy of a reaction directly into electrical energy [96,97]. Theoretically, any substance capable of chemical oxidation can be burned galvanically as fuel, and any substance capable of chemical reduction can be the oxidant. The solid oxide fuel cells (SOFCs) operate typically at 873-1273 K and are made primarily of solid ceramic and metallic materials. The fundamental components of a SOFC are (i) cathode (positive electrode) where oxygen is reduced to yield O^{2-} ions that diffuse through the (ii) electrolyte to the (iii) anode (negative electrode) and react with the fuel (hydrogen, hydrocarbons, carbon monoxide). A schematic representation of a SOFC with atmospheric O_2 as the oxidant and H_2 as the fuel is shown in Fig. 1.10.

The open-circuit voltage E_o of the cell is related with the free energy change of the electrochemical reaction and with the oxygen pressure values at the cathode and at the anode:

$$E_O = \frac{RT}{nF}\ln\frac{p_c(O_2)}{p_a(O_2)} = -\frac{\Delta G}{nF} = E^0 + \frac{RT}{4F}\ln\frac{p^2(H_2)p(O_2)}{p^2(H_2O)} \qquad (1.61)$$

where n is the electron equivalent of oxygen (n = 4).

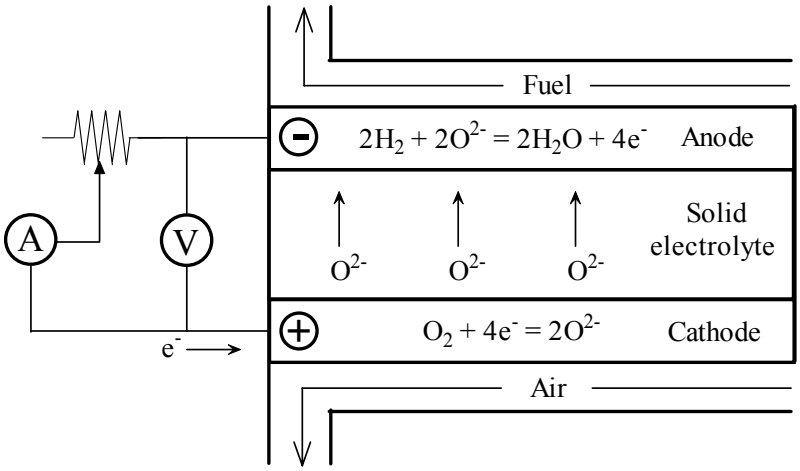

Fig. 1.10. Operation concept of a SOFC.

The open-circuit voltage for the SOFC working with hydrogen and air is about 1 V at 1273 K [96]. Therefore, individual fuel cells should be linked in series by interconnectors to provide considerable voltage levels. So far, SOFC-based electric power generators of tubular, planar and monolithic design were constructed, with a power capacity up to 100 kW [96,97]. Electrical energy can be obtained from a fuel cell under closed-circuit condition only, when an electrical current (I) is not zero. However, the increasing current decreases the cell voltage owing to activation, ohmic and concentration polarization. Activation polarization (η_{act}) is due to the electrochemical nature of the reaction at the electrodes. Ohmic polarization (η_{ohm}) originates from the resistance (R_{Ohm}) of electrodes and electrolyte to the flow of charge carriers. The current density may reach a critical level when a reagent is consumed at the electrode so fast, that the actual flow rate of a reagent is unable to maintain its bulk concentration close to the electrode surface. Thus, concentration polarization (η_{conc}) appears and is significant at practical current densities. The cell voltage can now be expressed as:

$$E_{cell} = E_O - |\eta_{cathode}| - |\eta_{anode}| - IR_{Ohm} \qquad (1.62)$$

Fig. 1.11 illustrates the cell voltage and power density (product of the cell voltage and current density) versus current density for a fuel cell operating with humidified hydrogen and air [98].

As working temperatures increase, the polarization decreases. This leads to higher cell voltage and power density at a given current density (Fig. 1.11). An improved performance can also be gained raising the pressure of the oxidant and the fuel [97]. In theory, the SOFC produces electrical energy as long as the fuel and oxidant are supplied to the electrodes.

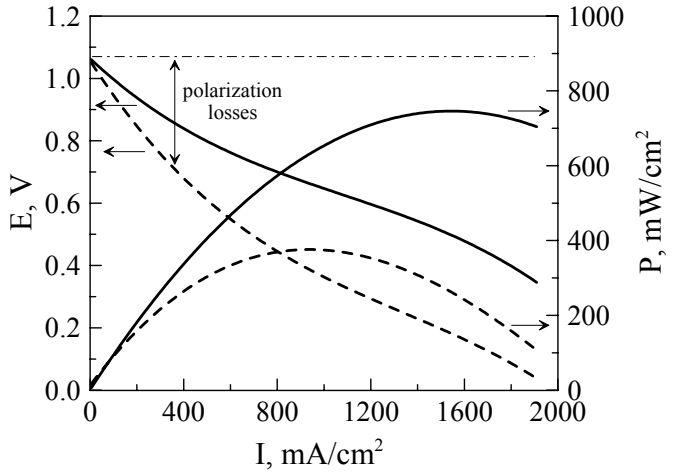

Fig. 1.11. Performance of a fuel cell [98] at 973 K (– –) and 1073 K (—). Electrolyte: scandia-stabilized zirconia (SSZ), cathode: Pt-SSZ, anode: Ni-SSZ.

1.2.1.2. Conventional solid electrolytes

The solid electrolyte should possess ionic conductivity as high as possible, and minimum or no electronic conduction. This material should be dense and gas-tight (free of open porosity), otherwise gaseous reagents would permeate from one side of the electrolyte to the other. The ohmic polarization over the electrolyte causes a significant voltage loss in SOFCs. Thin layers have lower resistance, increasing the cell performance. Hence, good mechanical properties (high strength and toughness) of the solid electrolyte are required to obtain durable films. The electrolyte should be chemically stable in both oxidizing and reducing atmospheres, as well as exhibit phase stability during thermal cycling and operation over 40000-50000 hours. Such ceramics must have a wide electrolytic $p(O_2)$ domain ($t_O >$ 0.99) at working temperatures, at least from 10^{-15} to 10^5 Pa [99,100].

From the first SOFCs until the contemporary ones, cubic yttria-stabilized zirconia (YSZ) has been used as the electrolyte [96-101]. ZrO_2 doped with 8-10 mol% yttria is the electrolyte of choice at present. This system was selected over the years because of its substantial oxygen ionic conduction (around 0.15 S/cm at 1273 K), satisfactory electrolytic domain and stability in oxidizing and reducing environments [55,58]. Cubic yttria-stabilized zirconia shows tolerable decrease of conductivity as a function of time at operating temperatures [100]. Thin layers of YSZ (100-150 or even 10-15 μm for self- or electrode-supported SOFCs, respectively) can be produced due to fine mechanical characteristics. For example, 8YSZ has bending strength as high as 240-280 MPa at 298 K [96,102].

The fuel cells with YSZ-based electrolyte operate typically at 1173-1273 K. Such high temperatures narrow the choice of other SOFC materials, limit considerably the lifetime of a SOFC and promote the performance degradation due to interaction between components. Lowering the operating temperature would diminish these factors and decrease substantially the overall cost, but this requires a solid electrolyte with ionic conductivity superior to that of YSZ [97]. A lot of work is devoted to the zirconia materials in order to improve their transport and mechanical properties. The oxygen-ion conduction of scandia-doped (8-10 mol%) ZrO_2 [103] is the highest among zirconia-based solid electrolytes, being about twice that of 8YSZ (Fig. 1.12). However, the $Zr(Sc)O_{2-\delta}$ oxides are more expensive owing to high cost of scandia, and their conductivity is known to degrade rapidly with time at the SOFC operation temperatures [96,104]. Minor additions of Al_2O_3 were found to strengthen the electrolyte matrix without serious increase of resistivity [97,105].

The maximum oxygen ionic transport is characteristic of Bi_2O_3 stabilized with Er and Y (Fig. 1.12). At the same time, Bi_2O_3-based ceramics reveal several disadvantages, crucial for SOFC applications, namely, thermodynamic instability and significant electronic conduction in reducing conditions, volatilization of bismuth oxide at elevated temperatures, high chemical reactivity and low mechanical strength [57]. Hence, in spite of the high ionic conductivity, practical use of Bi_2O_3-based solid electrolytes in the electrochemical cells is very complicated.

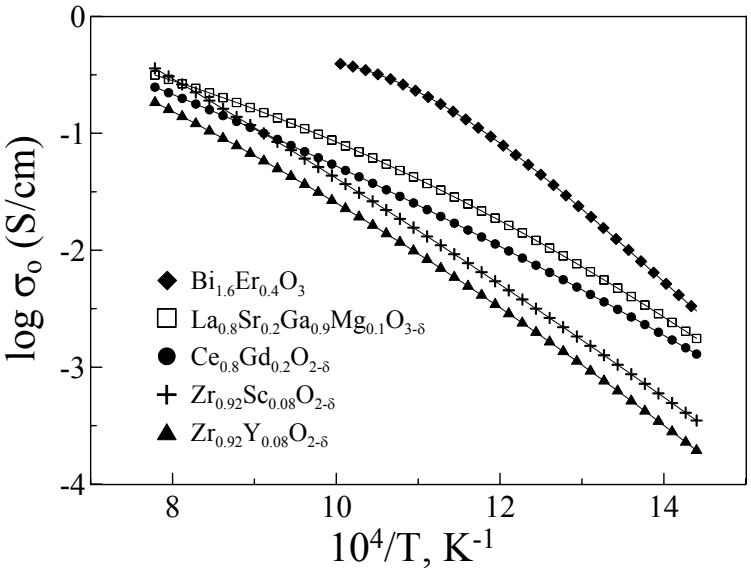

Fig. 1.12. Oxygen ionic conductivity of various solid electrolytes [58,59,103,106].

Doped ceria with the fluorite-type structure is another well-known candidate for intermediate-temperature fuel cells. The main advantages of ceria-based ionic conductors include a higher ionic conductivity and a lower cost with respect to stabilized ZrO_2 [61-64]. Highest level of ionic transport is characteristic of the solid solutions $Ce_{1-x}M_xO_{2-\delta}$, where M = Gd (CGO) or Sm, x = 0.10-0.20 (Fig. 1.12). The main disadvantages of doped $CeO_{2-\delta}$ ceramics are related to the lower mechanical strength with respect to YSZ and a high electronic transport at low oxygen pressures [56,100,107]. Therefore, a decrease of operating temperatures down to 773-873 K and use of a thin protective YSZ layer between the ceria-based electrolyte and the anode may be desirable [96,99].

Alternative electrolytes, perovskite-like oxides based on lanthanum gallate, were extensively studied by Feng and Goodenough [20] and Ishihara [21]. The optimized $La_{1-x}Sr_xGa_{1-y}Mg_yO_{3-\delta}$ (LSGM) series, where x and y are within 0.10-0.20, show ionic conduction comparable or slightly higher than that of doped ceria (Figs. 1.6 and 1.12) and a wider electrolytic domain [96,99]. The major problems in this case are associated with lower bending strength and toughness compared with YSZ, relatively high cost of gallium and volatilization of gallium oxide in reducing atmospheres [99,100]. Clearly, development of new solid electrolytes with adequate properties and further modifications of ceria-based and LSGM electrolytes, particularly to improve their stability, are necessary for the commercialization of SOFCs.

1.2.1.3. Electrodes and cell interconnection materials

The functions of electrodes in SOFCs are (i) to provide a surface site where oxygen reduction (cathode) and fuel oxidation (anode) occur, (ii) to catalyze these processes, (iii) to conduct electrons into or away from the reaction sites. The electrode materials must be stable under the SOFC fabrication and operation conditions, including negligible reactivity with other components, and should exhibit thermal expansion similar to that of the solid electrolyte. A three phase boundary (TPB) is established between two solid phases (electrode and electrolyte) and gas phase (oxidant or fuel). The performance of an electrode rises when the TPB length increases thus demanding porous electrode morphology rather than dense [97].

Numerous types of cathode materials were studied. In the 1930s, Fe_3O_4 was used by Baur and Preis [101] due to its high electrical conductivity (300 S/cm at 293 K). However, magnetite showed no catalytic activity and caused performance degradation at 1173-1273 K in air, upon oxidizing into poorly conducting Fe_2O_3. After subsequent experiments with Fe-Al_2O_3 composite and $MgFe_2O_4$, cathodes were produced as thin porous layers of catalytically active platinum, though the Pt usage in

large-scale plants is inappropriate [96]. Platinum and silver have been mixed with YSZ or CGO [98]; these cathodes showed a high activity in contact with ceria-based electrolytes. Sn-doped In_2O_3 was proposed [108] and frequently used in the 1970s, sometimes mixed with praseodymium oxide [97]. The studies of $La_{1-x}B_xMO_{3-\delta}$ (B = Ca, Sr; M = Cr, Mn, Fe, Co), $PrCoO_{3-\delta}$ and $GdCoO_{3-\delta}$ cathodes with perovskite structure were of remarkable importance [109]. The oxides with mixed electronic and oxygen ionic conduction enabled to suppress considerably the polarization losses, lowering operating temperatures. High electrical transport and attractive catalytic activity were reported for $La_{1-x}Sr_xCoO_{3-\delta}$ [110], but in combination with insufficient compatibility with YSZ. The TEC of $LaCoO_{3-\delta}$ is (22-24)$\times10^{-6}$ K^{-1} at 373-1273 K, whereas that of 8YSZ is (10-11)$\times10^{-6}$ K^{-1} [96]. Moreover, the interaction of $La_{1-x}Sr_xCoO_{3-\delta}$ with zirconia leads to the formation of low-conductivity phases, $SrZrO_3$ and $La_2Zr_2O_7$ [55], contrary to ceria where no reaction product was detected. The TEC of $Ce_{0.8}Gd_{0.2}O_{2-\delta}$ is (12-13)$\times10^{-6}$ K^{-1} [111] so the thermal expansion of $La_{1-x}Sr_xCoO_{3-\delta}$ needs to be reduced.

At present, Ca- or Sr- doped lanthanum manganites (LSM) are most commonly used in SOFSc with zirconia electrolytes [97]. These materials are reasonably stable in contact with YSZ and show no mismatch in thermal expansion (TEC of $La_{0.9}Sr_{0.1}MnO_{3-\delta}$ is 10.4$\times10^{-6}$ K^{-1}) [112]. In order to enlarge TPB length, the cathode often includes a layer of the percolating LSM-YSZ composite; this also improves cathode adhesion to the electrolyte [99]. However, the intermediate-temperature (IT) SOFCs require cathodes with higher electrochemical activity compared with LSM [100]. The $La_{1-x}Sr_xFe_{1-y}Co_yO_{3-\delta}$ (LSFC) system has been extensively studied as a potential family of cathode materials due to excellent transport properties and electrode kinetics [31,39,41]. These oxides do not react with ceria-based electrolytes and have relatively low thermal expansion (for example, the TEC of $La_{0.8}Sr_{0.2}Fe_{0.8}Co_{0.2}O_{3-\delta}$ is 15.4$\times10^{-6}$ K^{-1} at 373-1073 K [113]).

Extensive work is carried out on alternative cathode materials, including perovskite-like ferrites $Y_{1-x}Ca_xFeO_{3-\delta}$ [24,114], $Ce_{1-x}Sr_xFe_{1-y}M_yO_{3-\delta}$ (M = Co and Ni [115]) and $La_{1-x}Sr_xFe_{1-y}M_yO_{3-\delta}$ (M = Cr [39], Mn [40], Ni [41,116], Cu [117] and Al [118]), manganites $Ln_{1-x}Sr_xMn_{1-y}Co_yO_{3-\delta}$ (Ln = La [119], Ce and Pr [115]) and cuprates $La_{1-x}Sr_xCuO_{3-\delta}$ [120]. Oxides with other crystal structures like Ru-based pyrochlores [121], nickelates $La_{2-x}Sr_xNi_{1-y}M_yO_{4\pm\delta}$ (M = Mn, Fe, Co and Cu) [122,123] and $YBa_2Cu_3O_x$ [124] were also studied in terms of their electrode behavior. One of research objectives is to lower the cathode cost. For this purpose, mixed lanthanides were tested instead of pure lanthanum, without deterioration of the cell performance. Also, the use of less expensive raw chemicals instead of rare-earth compounds is favorable [97].

The first anode materials, e.g. carbon, platinum and iron, were substituted during the 1960s for nickel due to its excellent catalytic properties and rather low cost [101]. The fuel oxidation is a

certainly more complex process with respect to the cathode reaction, emphasizing a particular importance of the electrochemical activity, well-developed microstructure and porosity. The Ni-YSZ cermets are used [125] in order to adjust the thermal expansion of the fuel electrode, to enlarge the surface area of the reaction, to prevent sintering of the nickel particles and to improve the adhesion. The state-of-the-art fuel electrode has a porosity of 20-40% and consists of metallic Ni (30-40 vol%) and a YSZ skeleton [97,100]. SOFCs with thin YSZ electrolyte layer on Ni-YSZ anode supports exhibit high power densities up to 1 W/cm^2 at 1073 K [126]. Nevertheless, the long-term stability is limited by agglomeration of Ni particles and Ni dewetting of zirconia [100]. The Ni-YSZ cermet can work down to 873-973 K [96]. At low temperatures, the coke deposition promoted by nickel leads to blocking of gas channels and disintegration of the anode structure. The use of YSZ doped with TiO_2 (5-10 mol%) in combination with nickel resulted in lower degradation rate due to better adherence of Ni on the TiO_2-YSZ ceramic compared to that on YSZ [127].

As possible alternative, Ni- and Cu-ceria fuel electrodes were studied [96,128]. Minor coke precipitation was only detected for Gd- and Sm-doped ceria anodes after operation in methane and steam; the cell performance was stable. This might enable reforming light hydrocarbons without anode inactivation in SOFCs. The Cu-Ni alloy is frequently prepared, combining negligible coke formation for copper with high melting point and electrocatalytic activity of nickel. Doped CeO_2 was successfully used itself, due to significant electronic conductivity under reducing conditions [129]. However, ceria exhibits a high chemical expansion when Ce^{4+} is reduced to Ce^{3+}; its resistance to oxidation-reduction cycles is hence questionable [56].

The metallic component was almost all replaced by the electronically-conductive $La_{0.8}Sr_{0.2}Cr_{0.8}Mn_{0.2}O_{3-\delta}$ in composite anodes; the amount of nickel was kept minimum (4 wt%) to avoid coking [130]. Again, many perovskite-like oxides were found to catalyze hydrocarbon oxidation reactions or even substitute conventional Ni-YSZ anodes and offer higher microstructural stability and tolerance to sulfur compounds. Relevant examples include titanates $Ca_{1-x}Sr_xTiO_{3-\delta}$ [131], chromites $La_{1-x}Ca_xCr_{1-y}M_yO_{3-\delta}$ (M = Ti, V, Fe) [132] and $LaCr_{1-x}Ni_xO_{3-\delta}$ [133], manganites $La_{1-x}Ba_xMnO_{3-\delta}$ [134], ferrites $La_{1-x}Sr_xFe_{1-y}Co_yO_{3-\delta}$ [135] and cerates $SrCe_{1-x}Y_xO_{3-\delta}$ [136]. Oxides with non-perovskite crystal lattices also received significant attention, in particular, tetragonal tungsten bronze type niobates $A_{0.6}Nb_{1-x}M_xO_{3-\delta}$ (A = Ca, Sr, Ba, La; M = Mg, Cr, Mn, Fe, Ni, In, Sn) [137], pyrochlores $Gd_2Ti_{2-x}Mo_xO_{7\pm\delta}$ and $Pr_2Zr_{2-x}Ce_xO_{7\pm\delta}$ [138], and layered perovskites $La_2Sr_{n-2}Ti_nO_{3n+1}$ [139] were assessed.

The cell interconnection materials should exhibit electronic conductivity as high as possible and, contrary to the electrodes, must be impervious to fuel and oxidant gases. These should be chemically stable in both the cathode and anode atmospheres, and show zero reactivity and similar

thermal expansion with respect to other cell components. High thermal conductivity and mechanical strength are also favorable for uniform heat distribution and SOFC durability, respectively. Lanthanum chromite doped with Ca, Sr or Mg satisfies most of these requirements and has thus been used as most common interconnection material since the 1970s [96,97]. However, chromites experience stresses due to different thermal expansion in oxidizing and reducing conditions, possess extremely low thermal conductivity (< 5 W m^{-1} K^{-1}) and may react with CO_2 generated at the anode. Their fabrication cost is relatively high [100,140]. In recent years Cr-based alloys and Cr-rich ferritic steels are tested as they are cheaper, less brittle, easier to machine and show high thermal and electrical conductivities [141]. The thermal expansion is, in principle, suitable (12-13×10^{-6} K^{-1}) and can still be adjusted varying the composition. Main problems appear at high temperatures (above 973-1073 K) and are associated with the formation of low-conductive oxide layers and carburization in the cathode and anode environment, correspondingly, and also with the vaporization of Cr gaseous species that may poison the electrodes and thus decrease their performance [141]. Trying to suppress these processes, the effect of small additives of various elements e.g. Al, Si, Ti, Mn, Ni, Y, Mo, La, Ce is now studied [141,142]. Also, protective coatings based on $La_{1-x}Sr_xMO_{3-\delta}$ (M = Cr, Mn) perovskites or $MnCr_{2-x}Co_xO_4$ spinels have been suggested [96,100,142-144].

Apparently, reducing the operation temperature down to 773-873 K will decrease substantially requirements, imposed to the SOFC components, will inhibit the performance degradation and extend the range of applicable compounds, in particular the use of inexpensive alloys or steels as the interconnection materials. The SOFC-based power plants could be commercially viable if their cost becomes lower than 1 US$ per 1 W, whereas at present this value is several times higher [145]. Therefore the development of suitable cheap materials and fabrication technologies are the key challenges facing SOFCs.

1.2.2. Mixed-conductive ceramic membranes

1.2.2.1. Oxygen separation

The permeation of the oxygen ions through dense MIEC membrane under an oxygen pressure gradient was described in Chapter 1.1.3. This process can be used to yield high-purity oxygen separating it from air. Several membrane concepts are possible: employing (i) single-phase material (Fig. 1.3), (ii) dual-phase ceramics (Fig. 1.8) and (iii) thin supported membrane (Fig. 1.13). Though oxygen is more expensive oxidant than air, the industrial processes operating on oxygen show often a higher efficiency [146]. Oxygen or oxygen-enriched atmospheres are needed for many processes, for example metallurgical, petrochemical, food, glass and paper industries, water aeration and purification. In

smaller quantities, oxygen is also consumed for medical, aerospace and military purposes. The upgrading of abundant resources of natural gas, often found in remote regions, to an easily transported liquid fuel is another potential market [146].

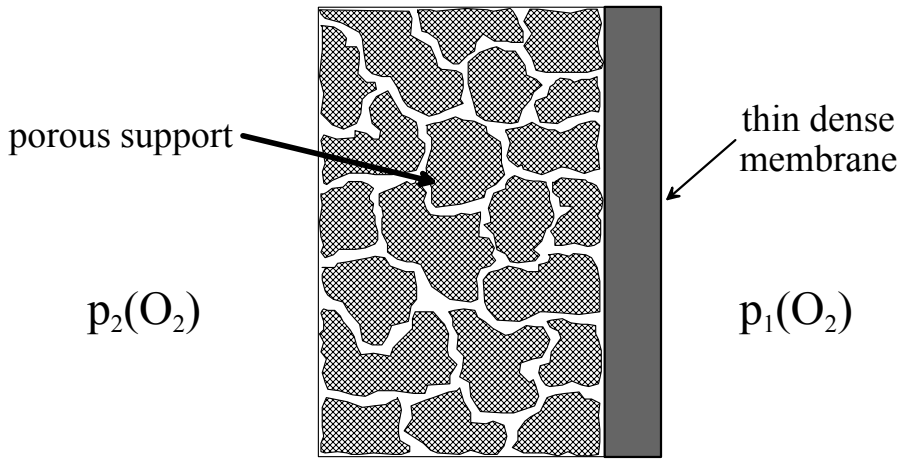

Fig. 1.13. Membrane concept based on thin supported MIEC oxide.

At present, oxygen is mainly produced by cryogenic distillation of air. This technology needs high capital investments and becomes only remunerative at large-scale plants (100-2000 ton/day) [147]. The smaller factories have to deal with even more expensive liquid oxygen or to extract oxygen from air via pressure swing adsorption. The discontinuity of this process is a crucial disadvantage. Recent approaches deal with organic polymer or porous inorganic, for instance, silica membranes. However, their efficiency is still not optimal, so that oxygen separation requires multiple cycles thus increasing the overall cost [147]. The use of mixed conductors for oxygen separation at elevated temperatures is a cost-effective alternative for smaller-scale facilities and becomes substantially cheaper, if integrated into a high-temperature process that consumes pure oxygen or into a power generation cycle [148]. It is worth noting that oxygen production using dense MIEC membrane enables theoretically to achieve infinite selectivity, due to the specific nature of the separation process [5].

1.2.2.2. Oxidation of light hydrocarbons

A mixture of hydrogen and carbon monoxide, i.e. synthesis gas (syngas) is the most important feedstock for commercial Fischer-Tropsch synthesis of value-added products including paraffins, olefins and alcohols. At present, syngas is produced via steam reforming of methane, the main

component of natural gas: $CH_4 + H_2O = CO + 3H_2$. This process is, however, energy consuming due to the highly endothermic nature of the latter reaction (ΔH^0_{1073} = 225 kJ/mol), gives a H_2/CO ratio higher than necessary for subsequent conversion, and represents the most expensive step (50-60% of the total cost) in the Fischer-Tropsch gas-to-liquid route. As an alternative, the catalytic partial oxidation of methane is used: $CH_4 + O_2 = CO + 2H_2$. This reaction is mildly exothermic (ΔH^0_{1073} = -23 kJ/mol) and yields an optimum H_2/CO ratio of 2. To achieve a thermally self-sustained technology, these two processes are combined into the so-called auto-thermal reforming, where oxygen separation in cryogenic plants constitutes a major cost factor (40-45%) of the syngas production [148,149].

When oxidant gas (e.g. air) and fuel (e.g. natural gas) are supplied to a MIEC membrane, the oxygen pressure gradient and the heat (due to exothermic oxidation reactions) necessary for the oxygen separation process both appear; oxygen separation, partial oxidation and reforming are combined in a single cell. Such a technological scheme (Fig. 1.14), eliminating the need for separate oxygen production and fuel oxidation, has potential to substantially decrease the actual cost of gas-to-liquid plants and distributed hydrogen. Additional advantages are that (i) the ceramic membrane is a physical barrier for air impurities, (ii) lattice oxygen may couple methane more selectively than gaseous oxygen, and (iii) the membrane material may also serve as oxygen reduction and/or methane coupling catalyst. Compared with SOFC-type reactors, the MIEC membranes are simpler since they operate without external circuitry; the electronic conductivity in the solid acts as an internal short circuit for electrons or holes in order to counteract the oxygen flux.

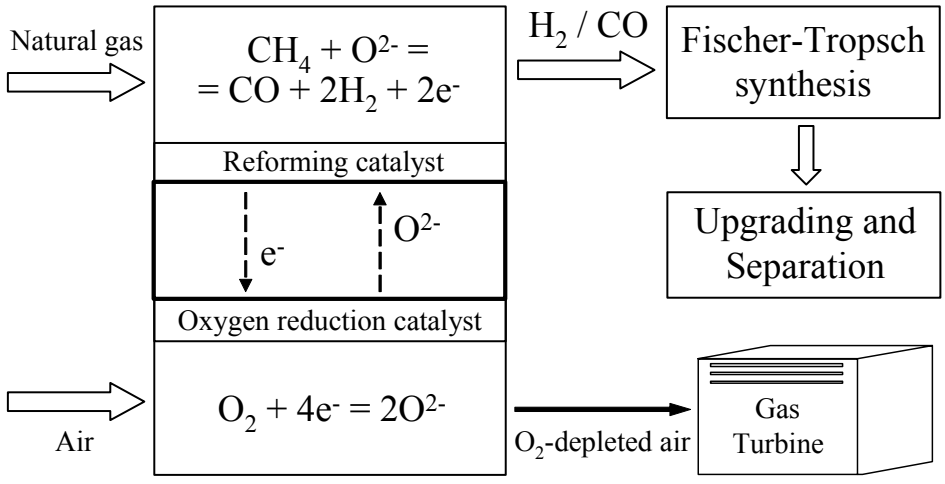

Fig. 1.14. Natural gas conversion based on MIEC membrane.

A standard configuration consists of a tubular membrane, over which air flows outside the membrane whilst methane is passing inside [149]. To improve the methane conversion and selectivity towards desired products, the tube can be filled with a reforming catalyst. These reactors can be easily adopted for large-scale plants and, owing to their compactness and energy self-sufficiency, allow access to remote sources of natural gas [148].

1.2.2.3. Membrane materials

For successful operation the membrane material must (i) sustain a certain oxygen flux, (ii) exhibit moderate thermally- and chemically-induced expansion, and be (iii) stable under large oxygen pressure gradients (like syngas/air) at working temperature, (iv) compatible with the reduction and reforming catalysts, (v) and sufficiently dense to prevent leakage.

Since the reports on high oxygen permeation in $La_{1-x}Sr_xCo_{1-y}Fe_yO_{3-\delta}$ system by Teraoka et al. [27], extensive research has been conducted on acceptor-doped oxygen-deficient perovskites with general formula $Ln_{1-x}A_xM_{1-y}B_yO_{3-\delta}$ (A = Ca, Sr, Ba; M = Fe, Co; B = Ti, Cr, Mn, Fe, Ni, Cu) [28,29,31-41,153]. Their transport properties are discussed briefly in Chapter 1.1.4. The highest permeation fluxes were measured for Co-rich oxides like $Ba_{0.5}Sr_{0.5}Co_{0.8}Fe_{0.2}O_{3-\delta}$ [150], $SrCo_{0.8}Fe_{0.2}O_{3-\delta}$ [27], $La_{0.6}A_{0.4}Co_{0.8}Fe_{0.2}O_{3-\delta}$ [28], $La_{0.6}Sr_{0.4}Co_{0.8}B_{0.2}O_{3-\delta}$ (B = Ni, Cu) [29] and are given in Table 1.1.

Many membranes show a decrease in performance with time, due to a number of reasons. The membrane material may react with support, catalyst, gaseous species like CO_2, SO_2, H_2O, H_2S etc. or decompose due to reduction at the permeate side exposed to the syngas atmosphere [153]. The reduction processes are associated with volume changes and may thus lead to crack formation [149]. Moreover, the oxygen chemical potential gradient across the MIEC may cause differential expansion (resulting in high mechanical stresses and subsequent structural failure), and gradients of elemental concentration if the mobilities of the cations are non-negligible. The membrane feed-side exposed to air becomes enriched with the faster moving cations. Obviously, the MIEC ceramics may disintegrate even if considered thermodynamically stable [154].

In particular, the use of Co-containing oxides as membranes for syngas production is hampered due to excessive chemical expansion. For example, the low $p(O_2)$ side of the $La_{0.2}Sr_{0.8}Co_{0.4}Fe_{0.6}O_{3-\delta}$ membrane (air/methane gradient, 1123 K) expanded an additional 2% over the feed side, provoking tube break [155]. Most cobaltites show a high and non-linear thermal expansion; the TEC values vary in the range of $(15\text{-}30)\times10^{-6}$ K^{-1} [153]. The membrane failure owing to decomposition in syngas environment was reported for $SrCo_{0.8}Fe_{0.2}O_{3-\delta}$, where strontium carbonate, metallic iron and cobalt

formed at the reaction side [156]. Increasing iron content decreases both the thermal and chemical expansion of LSFC, but lowers the permeation fluxes as well [27,113].

Table 1.1. Oxygen fluxes through selected perovskite-type cobaltites.

Membrane material		T, K	d, mm	j, mol/(cm^2×s)	Gradient	Ref.
$La_{1-x}Sr_xCoO_{3-\delta}$	x = 0.2	1173	2.0	2.2×10^{-8}	air/He	[5]
	x = 0.4	1173	2.0	7.4×10^{-8}	air/He	[5]
	x = 0.6	1173	2.0	2.0×10^{-7}	air/He	[5]
	x = 0.6	1173	2.0	4.9×10^{-7}	air/He	[5]
$La_{0.6}Sr_{0.4}Co_{0.8}B_{0.2}O_{3-\delta}$	B = Fe	1138	1.5	0.4×10^{-6}	air/He	[28]
	B = Co	1138	1.5	0.7×10^{-6}	air/He	[28]
	B = Ni	1138	1.5	1.0×10^{-6}	air/He	[28]
	B = Cu	1138	1.5	1.3×10^{-6}	air/He	[28]
$Ba_{0.5}Sr_{0.5}Co_{0.8}Fe_{0.2}O_{3-\delta}$		1148	1.5	8.5×10^{-6}	air/syngas	[150]
$La_{0.35}Sr_xCoO_{3-\delta}$	x = 0.65	1153	1.4	2.8×10^{-7}	air/8.4 kPa	[152]
	x = 0.60	1153	1.4	2.0×10^{-7}	air/8.4 kPa	[152]
	x = 0.55	1153	1.4	1.7×10^{-7}	air/8.4 kPa	[152]
$Ln_{0.3}Sr_{0.7}CoO_{3-\delta}$	Ln = La	1153	1.4	2.6×10^{-7}	air/8.4 kPa	[152]
	Ln = Nd	1153	1.4	1.6×10^{-7}	air/8.4 kPa	[152]
	Ln = Sm	1153	1.4	1.0×10^{-7}	air/8.4 kPa	[152]
	Ln = Gd	1153	1.4	4.1×10^{-8}	air/8.4 kPa	[152]
$SrCo_{1-x}Fe_xO_{3-\delta}$	x = 0.2	1123	1.0	2.1×10^{-6}	air/He	[27]
	x = 0.6	1123	1.0	1.5×10^{-6}	air/He	[27]
$SrCo_{0.85}Fe_{0.1}Cr_{0.05}O_{3-\delta}$		1153	1.4	5.2×10^{-7}	air /8.5 kPa	[152]
$SrCo_{0.8}Ti_{0.2}O_{3-\delta}$		1153	1.4	4.8×10^{-7}	air /8.5 kPa	[152]

At 1273 K, the stability increases in the order $LaCoO_{3-\delta}$ (10^{-2} Pa) < $LaMnO_{3-\delta}$ (10^{-10} Pa) < $LaFeO_{3-\delta}$ (10^{-12} Pa) < $LaCrO_{3-\delta}$ (10^{-15} Pa), and the decomposition boundary shifts towards higher oxygen pressure upon increasing the content of acceptor-type dopants like strontium or barium [30,153]. The membrane surface exposed to the syngas experiences a low oxygen pressure, 10^{-20}-10^{-14} Pa [150,157]; this is clearly lower than the stability limit of $La_{1-x}A_xFe_{1-y}Co_yO_{3-\delta}$ (A = Sr and Ba) ceramics. However, numerous LSFC and LBFC membranes are kinetically stable under syngas/air gradient [149,150,155,158]. This phenomenon is a consequence of slow surface exchange at the membrane permeate side. As shown in Chapter 1.1.3, the oxygen chemical potential gradient across the membrane bulk is always lower than the total one, if the surface electrochemical processes influence

the overall oxygen transport. The surface slow kinetics increases the local oxygen potential and, although in syngas atmosphere, a material faces higher oxygen chemical potential than in the case of zero surface limitations. For a certain membrane thickness, specific for each composition, the oxygen potential may become higher than the stability boundary. If the decomposed layer still limits oxygen permeation and is not porous, it will protect the membrane bulk from reduction [149,158].

A promising approach to improve the stability of perovskite-type oxides under methane conversion conditions refers to B-site doping with stable oxidation-state cations like Mg^{2+}, Al^{3+}, Ga^{3+}, Gd^{3+} and Zr^{4+} [13,48,118,152,159-162]. This makes it possible to obtain compositions with a moderate thermal and chemical expansion [152,162], while oxygen permeability is still significant (Table 1.2). For example, high values of permeation flux were measured for $La_{0.3}Sr_{0.7}Co_{0.8}Ga_{0.2}O_{3-\delta}$ [163], $BaCo_{0.4}Fe_{0.4}Zr_{0.2}O_{3-\delta}$ [164] and $BaCe_{0.8}Gd_{0.2}O_{3-\delta}$ [160] membranes. Typically, a reforming catalyst is needed to provide high (>90%) methane conversion and CO [164] or C_2 hydrocarbon [160] selectivity, as most of membrane materials promote CO_2 formation [158,165].

Table 1.2. Oxygen fluxes through mixed-conductive membranes.

Membrane material	T, K	d, mm	j, mol/(cm^2×s)	Gradient	Ref.
$La_{0.8}Sr_{0.2}Ga_{0.6}Co_{0.2}Mg_{0.2}O_{3-\delta}$	1223	1.0	1.0×10^{-7}	air /2.1 kPa	[162]
$La_{0.8}Sr_{0.2}Ga_{0.6}Fe_{0.2}Mg_{0.2}O_{3-\delta}$	1223	1.0	1.0×10^{-7}	air /2.1 kPa	[162]
$La_{0.9}Sr_{0.1}Ga_{0.65}Ni_{0.2}Mg_{0.15}O_{3-\delta}$	1223	1.0	1.9×10^{-7}	air /2.1 kPa	[162]
$La_{0.5}Pr_{0.5}Ga_{0.65}Ni_{0.2}Mg_{0.15}O_{3-\delta}$	1223	1.0	1.1×10^{-7}	air /2.1 kPa	[162]
$LaGa_{0.65}Ni_{0.2}Mg_{0.15}O_{3-\delta}$	1223	1.0	1.0×10^{-7}	air /2.1 kPa	[162]
$La_{0.3}Sr_{0.7}Co_{0.8}Ga_{0.2}O_{3-\delta}$	1223	1.0	4.8×10^{-7}	air /2.1 kPa	[163]
$BaCo_{0.4}Fe_{0.4}Zr_{0.2}O_{3-\delta}$	1173	1.0	5.6×10^{-7}	air/He	[164]
$SrFeCo_{0.5}O_{3\pm\delta}$	1173	0.25-1.2	$(2\text{-}3)\times10^{-6}$	air/syngas	[166]
$Sr_{1.7}La_{0.3}Fe_{1.4}Ga_{0.6}O_{5+\delta}$	1173	1.7	$(4\text{-}5)\times10^{-6}$	air/syngas	[168]
$La_2Ni_{0.98}Fe_{0.02}O_{4+\delta}$	1123	1.0	0.8×10^{-7}	air /2.1 kPa	[162]
$La_2Ni_{0.9}Co_{0.1}O_{4+\delta}$	1223	1.0	1.2×10^{-7}	air /2.1 kPa	[169]
$La_2Ni_{0.9}Cu_{0.2}O_{4+\delta}$	1223	1.0	0.8×10^{-7}	air /2.1 kPa	[169]
Pd (50 vol%) - YSZ	1373	0.8	1.4×10^{-6}	air / H_2	[65]
$In_{1.8}Pr_{0.2}O_{3-\delta}$ (50 vol%) - YSZ	1373	0.8	1.6×10^{-6}	air / H_2	[65]
$In_{1.9}Pr_{0.05}Zr_{0.05}O_{3-\delta}$ (50 vol%) - YSZ	1373	0.3	5.4×10^{-6}	air / H_2	[65]
Ag (40 vol%) - $Bi_{1.5}Er_{0.5}O_{3-\delta}$	1073	1.6	1.2×10^{-7}	air /2.1 kPa	[81]
Ag (40 vol%) - $Bi_{1.5}Y_{0.3}Sm_{0.2}O_{3-\delta}$	1123	1.3	5.8×10^{-7}	air /0.9 kPa	[75]
Ag (35 vol%) - $Bi_{1.5}Y_{0.5}O_{3-\delta}$	1023	1.0	3.1×10^{-7}	air / N_2	[5]

Balachandran and co-workers [166] reported for $SrFeCo_{0.5}O_{3\pm\delta}$ high permeability and an orthorhombic intergrowth structure, where perovskite layers alter with $(Fe,Co)O_4$ and $(Fe,Co)O_5$ polyhedra. However, this phase decomposes at low oxygen pressure values [167]. The brownmillerite-like $La_{2-x}Sr_xGa_{2-y}Fe_yO_{5+\delta}$ membranes were proposed for syngas production [168]. Here, increasing temperature induces disordering of the oxygen vacancies necessary for ionic conduction. Doped lanthanum nickelates with K_2NiF_4-type structure are quite promising membrane materials for methane conversion, owing to considerable permeation fluxes, relatively low thermal expansion, presence of catalytically-active Ni at the surface and kinetic stabilization under syngas/air gradient [153,165,169]. Dual-phase membranes for partial oxidation of hydrocarbons were employed by Mazanec et al. [65].

An economical analysis [149] showed that membrane reactors for syngas production (membrane material cost of 1600 US$/m^2) may compete with conventional auto-thermal reforming if the membrane supports an oxygen flux higher than 7×10^{-6} mol/(cm$^2\times$s). The highest reported fluxes (Tables 1.1 and 1.2) seem to satisfy such condition, especially if a supported thin film membrane is used. For most MIECs of interest, oxygen flux increases on decreasing membrane thickness down to ≈ 100 μm and finally becomes thickness-independent [146]. However, oxides with fastest ionic transport are typically unstable under operating conditions or contain costly elements, such as Ga, Zr or noble metals. Further progress can be achieved by improving surface kinetics (deposition of surface-active species and/or increasing the effective surface area using a graded porous layer of the same material) and by developing of new low temperature MIECs.

1.2.3. Oxygen pumps and sensors

The oxygen separation and delivery can be electrically driven, using a solid electrolyte (Fig. 1.15). The driving force for oxygen-ion transport through the electrolyte is an externally applied electrical potential between the electrodes. Typically, such devices are able to pump oxygen from the low to the high $p(O_2)$ side. The direction and magnitude of this DC voltage are imposed to overcome the rising and counteracting oxygen chemical potential gradient and to provide at the anode side an oxygen pressure and purity necessary for an application in question. The oxygen pump may supply oxygen at elevated pressures thus eliminating the need for an auxiliary compressor [146,148,170].

As for SOFCs, two most convenient designs of an oxygen pump are planar [148] and tubular [171]. The tubular arrangement offers better thermal cycling stability and requires no high-temperature sealing, whereas the planar concept yields higher oxygen transfer per unit volume but needs seals. As an alternative, honeycomb-type structures for oxygen generation have been reported [172]. The yttria-stabilized zirconia (YSZ) is the common solid electrolyte used in an oxygen pump [171,173]. Its

working temperature can be reduced from 1273 to 1073 K if thin-film membranes are used. Ceria- and Bi_2O_3-based materials also operate successfully at 873-1073 K in oxidizing environments and at low overvoltages [148,172]. Of increasing interest is a recently developed $La_{1-x}Sr_xGa_{1-y}Mg_yO_{3-\delta}$ solid solution with larger electrolytic $p(O_2)$ domain compared to ceria [146,174].

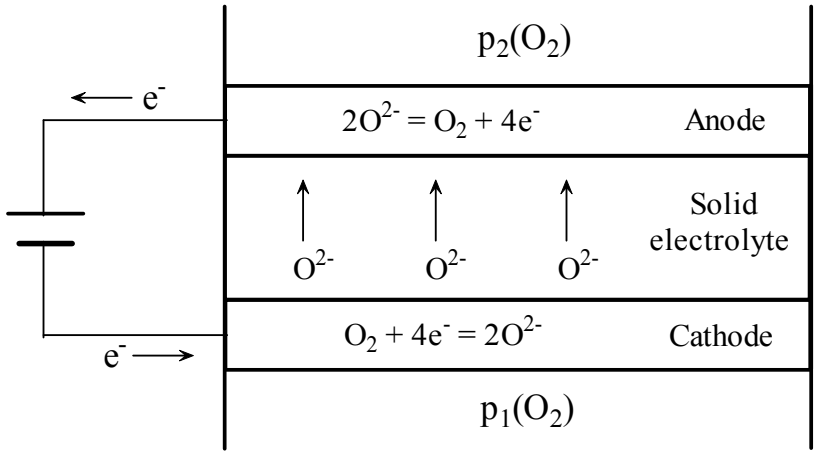

Fig. 1.15. Electrochemical oxygen pump.

The flux of oxygen produced/removed is directly proportional to the current through-passing the electrolyte membrane: 1A = 3.5 ml/min. Decreasing membrane resistance (using thinner or more conductive ceramics) and/or increasing the current density would enhance the productivity of an oxygen generator. However, high potentials induce partial reduction of a solid electrolyte [171,175]. This leads to an increase in the electronic conductivity, thus losing efficiency, and even membrane cracking due to the chemical expansion. Therefore commonly applied current densities are about 0.5-1 A/cm^2 [171,173,175]. As electrode materials, porous $La_{1-x}Sr_xMnO_{3-\delta}$ (LSM), $La_{1-x}Sr_xCo_{1-y}Fe_yO_{3-\delta}$ [146] and composites LSM/YSZ or Pt/YSZ [173] are used.

The oxygen pump technology is more developed than for SOFC and mixed-conducting membrane and close to commercialization. A stand-alone oxygen pump for oxygen separation from air consisting of multi-plate stack, heat exchanger, control unit and blower was built and tested [148]. Devices providing oxygen fluxes of 11 and 16 $l/(m^2 \times min)$ were constructed [146]. Such high productivity already opens these small-scale oxygen generators for numerous medical, military, aerospace and food applications as well as cutting and welding of metals. An oxygen pump producing over 1000 ton/day could be cost competitive with a cryogenic distillation unit [146]. The oxygen

electrolyzers are also widely employed; one of perspective applications is oxygen generation from the CO_2-rich Martian atmosphere [173]. Since oxygen transfer is directly proportional to the current, an oxygen pump provides much better control than MIEC membranes. Precise control of oxygen concentration in gas streams or enclosures is possible integrating an oxygen sensor and using it in the feed back loop mode with a DC current source. For instance, inert gas mixtures with a definite oxygen content can be produced in this way [171,174].

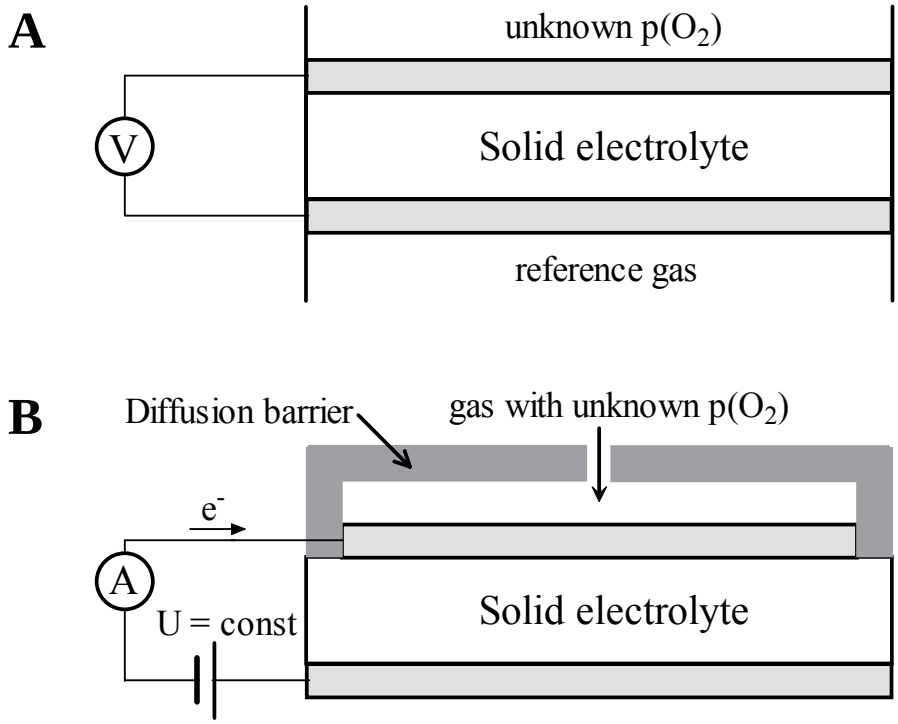

Fig. 1.16. Main oxygen sensor concepts: A – potentiometric; B – amperometric.

Solid electrolytes (typically zirconia-based) are also used for the measurement of the oxygen partial pressure [176,177]. When temperature is high enough to enable equilibrium at the electrolyte-electrode interfaces, an electrical potential difference between the electrodes is observed. Its value, monitored by a voltage meter (Fig. 1.16A), is determined by the ratio of the oxygen pressures on either side of the electrolyte, according to the Nernst law:

$$E = \frac{RT}{4F} \ln \frac{p^{high}(O_2)}{p^{low}(O_2)} \qquad (1.62)$$

The oxygen partial pressure of a gas stream or closed compartment can be evaluated using this open-circuit voltage and known $p(O_2)$ value for a gas (e.g. air) at another side of the membrane.

The diffusion barrier enables to determine the oxygen partial pressure in an amperometric mode (Fig. 1.16B). Each molecule passing through this barrier reacts immediately at the electrode. The measured limiting current under externally applied voltage is a unique function of the geometric parameters and the oxygen pressure. Recently, amperometric sensors have been studied with respect to the determination of H_2, CO, light hydrocarbons and NO_x [176,178]. Major application areas are monitoring of the furnace installations and measurement of exhaust gas emissions in the automotive industry. Sensors are also necessary for optimization of combustion systems [179,180].

1.3. Ionic and electronic transport in ferrite-based phases

1.3.1. Electronic conductivity

A number of oxides, especially transition metal-containing, exhibit metallic-type electronic conductivity, when transport decreases with increasing temperature [2]. The electronic conduction of semiconductors typically increases on heating [25]. For an intrinsic semiconductor, charge carriers (electrons and holes) originate from electronic disordering: $0 = e^{/} + h^{\cdot}$, whilst their concentration in an extrinsic semiconductor is mainly determined by the content of impurities or dopants [181].

In many oxides the electronic transport is associated with a polarization of the neighboring lattice (local deformation of the structure) when electrons and/or holes move through the solid [2]. Such an electron (hole) together with associated deformation (polarization field) is called a polaron. The interaction between an electron (hole) and its closest surrounding is relatively weak for large polarons, which thus behave like free carriers. If this interaction is relatively strong, the polaron is referred to as a small polaron. In the latter case, an electron (hole) is trapped at a certain lattice site and can move to an adjacent site via hopping, quite similar to ion migration (see Chapter 1.1.2).

The type of the major charge carriers can be estimated from the Seebeck coefficient, α. This quantity represents the ratio between potential and temperature gradients across a homogeneous conductor (typically a bar of studied material with one end being heated or cooled more than the other):

$$\alpha = -\frac{E_{hot} - E_{cold}}{T_{hot} - T_{cold}} \qquad (1.63)$$

Since the energy of charge carriers increases with temperature, their drift from hot to cold occurs, giving rise to a potential difference whose sign depends on the type of the major charge carrier. The cold tip (as well as Seebeck coefficient) of metals and n-type semiconductors becomes negative, whereas for positive holes in p-type semiconductors it is positively charged [2,181].

The Seebeck coefficient measurements have frequently been performed to evaluate the concentration of the charge carriers [24,113,117,163,169]. For a p-type semiconductor with electronic transport by hopping:

$$\alpha = \frac{R}{F}\left[\ln\left(\frac{1}{\beta}\frac{N-p}{p} + \frac{s}{R}\right) + \frac{q}{RT}\right] \qquad (1.64)$$

where β is the spin degeneracy factor, p and N are the concentrations of holes and sites available for hole jumps, s and q are the transported entropy and heat of a polaron [2]. The two latter contributions to thermoelectric power may be neglected if compared with that of configurational entropy [24]. The spin degeneracy factor is defined as:

$$\beta = \frac{2S_n + 1}{2S_{n+1} + 1} \tag{1.65}$$

with S_n and S_{n+1} being the spin values for the reduced and oxidized state of a cation, respectively. At high temperatures iron ions Fe^{3+} and Fe^{4+} are in the high-spin state ($S_3 = 5/2$ and $S_4 = 2$). The value of $\beta = 6/5$ is therefore used for p-type conduction in ferrites [182]. Inspection of Eq. (1.64) shows that at high concentration of holes ($p > 5N/11$ in this case) the sign of the Seebeck coefficient becomes negative, in spite of prevailing p-type electronic transport.

If the concentration of holes and the conductivity are both known, the mobility of holes can be directly calculated from Eq. (1.11). The magnitude of μ_p and its temperature dependence are essential to distinguish between a large and a small polaron mechanism. The mobility of large polarons, generally in the range of 1-100 $cm^2\ V^{-1}\ s^{-1}$, decreases with increasing temperature; the small-polaron mobility, typically reported to be of the order of 10^{-4}-10^{-2} $cm^2\ V^{-1}\ s^{-1}$, increases. The value of 0.1 $cm^2\ V^{-1}\ s^{-1}$ is a rough criterion separating large and small polaron mechanisms [2].

Analogously to the ionic conduction via vacancy diffusion, the small-polaron electronic transport is a hopping process, with a temperature dependence similar to Eq. (1.27):

$$\sigma_p = \frac{A_0}{T} \exp\left(-\frac{E_a}{RT}\right) \tag{1.66}$$

where σ_p is the p-type electronic conductivity, E_a is the activation energy, A_0 can be expressed as

$$A_0 = f \frac{d_j^2 F^2}{R V_m} p(N - p) \tag{1.67}$$

where f is a constant, corresponding to the vibrational frequency of a polaron (jump probability) and the jump entropy change (see Eq. (1.22)), d_j is the jump distance (about 3.8 Å in cubic perovskite-type ferrites), V_m is the molar volume of an oxide [24].

1.3.2. Iron-based perovskites

Ferrites $AFeO_3$ (A = Y, La, Pr, Nd, Sm, Gd, Dy, Er and Yb) are orthorhombically-distorted perovskites (space group Pnma, no. 62) in a wide temperature range [24,183-185]. Their unit cell contracts when the radius of a rare-earth ion decreases [183]. Under oxidizing conditions at low temperatures, the electronic charge carriers, holes and electrons, form owing to the intrinsic electronic disordering in the B-sublattice ($2Fe_{Fe}^{\times} = Fe_{Fe}^{\bullet} + Fe_{Fe}^{/}$), whilst the concentration of ionic charge carriers is negligible [24,185,186]. If $[Fe_{Fe}^{\bullet}] \ll [Fe_{Fe}^{\times}]$ and $[Fe_{Fe}^{/}] \ll [Fe_{Fe}^{\times}]$, the equilibrium constant for electronic disproportionation can be expressed as:

$$K_D = [Fe_{Fe}^{\bullet}][Fe_{Fe}^{/}] = np \qquad (1.68)$$

Since the mobility of holes is higher than that of electrons [186], $AFeO_3$ are p-type semiconductors in air with high positive values of Seebeck coefficient, 200-800 μV/K [24,186]. Their total conductivity is relatively low: 0.05 S/cm at 1273 K in $YFeO_3$ [24], 0.03 S/cm at 1093 K in $NdFeO_3$ [187]; the activation energy is as high as 100-120 kJ/mol (Fig. 1.17). The calculated mobility of holes and electrons in $LaFeO_3$ is 0.107 and 0.056 $cm^2\ V^{-1}\ s^{-1}$, respectively [186]. The analysis of these data clearly indicates that the electronic conduction in ferrites occurs by a hopping small-polaron mechanism. Note that the electrical properties of $AFeO_3$, as intrinsic semiconductors, are strongly dependent on A/Fe ratio [186]. Small deviations from stoichiometry cause different electronic conductivity reported for the same nominal composition, as for $YFeO_3$ [24,188] and $NdFeO_3$ [185,187].

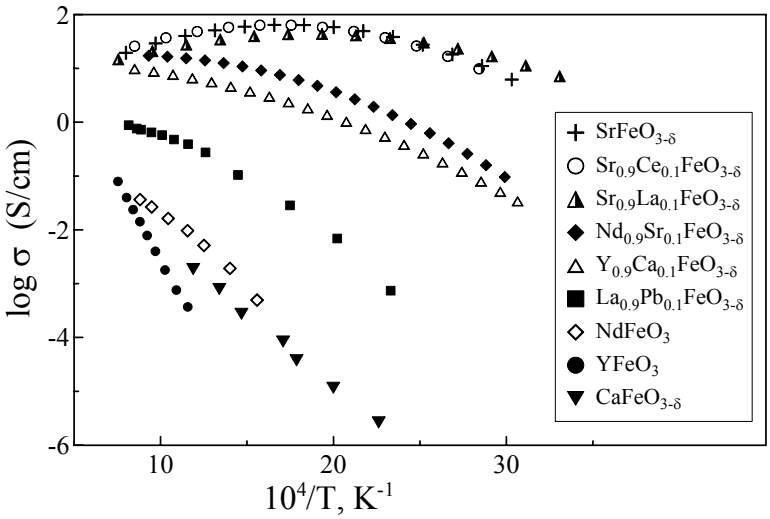

Fig. 1.17. The total conductivity of ferrites in air [24,45,185,187,190,191].

When $p(O_2)$ decreases, oxygen vacancies are formed; this leads to increasing concentration of n-type charge carriers in order to maintain electroneutrality:

$$O_O^{\times} + 2Fe_{Fe}^{\times} \rightleftarrows 1/2O_2 + V_O^{\bullet\bullet} + 2Fe_{Fe}^{/} \qquad (1.69)$$

In turn, the concentration of holes decreases, according to Eq. (1.68). In fact, the electronic conductivity remains essentially $p(O_2)$-independent down to 0.01-0.1 Pa for $LaFeO_3$ [186] and 10^{-5}-10^{-3} Pa for $YFeO_3$ [24] where it starts to decrease, reaches minimal values and increases with further

reducing oxygen pressure due to a major contribution of n-type electronic transport. Seebeck coefficient values pass zero and become negative (Fig. 1.18A). Finally, the oxygen deficiency of ferrites may reach a certain critical value resulting in the loss of stability and structural collapse.

The substitution of A^{3+} with divalent cations such as Ca [24,187], Sr [185,189] and Pb [190] leads to formation of holes and/or oxygen vacancies, and the electroneutrality condition is given by

$$[Sr'_{La}] + [Fe'_{Fe}] = 2[V_O^{\bullet\bullet}] + [Fe^{\bullet}_{Fe}] \quad (1.68)$$

As shown by structural studies of $La_{1-x}Sr_xFeO_{3-\delta}$ [191], $Nd_{1-x}Ca_xFeO_{3-\delta}$ [187] and $Nd_{1-x}Sr_xFeO_{3-\delta}$ [185], the unit cell volume decreases within each system upon increasing x, at least for moderate doping ($0 \le x \le 0.5$), though Ca^{2+} and Sr^{2+} are larger than La^{3+} and Nd^{3+} [8]. This means that at low concentration of an acceptor dopant, the charge compensation occurs preferentially via oxidation of Fe^{3+} into smaller Fe^{4+}.

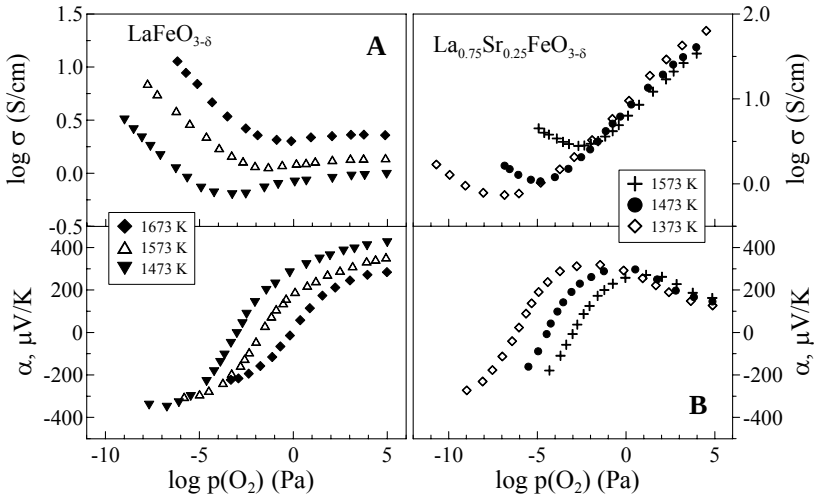

Fig. 1.18. Oxygen pressure dependencies of the total conductivity and thermopower for $LaFeO_{3-\delta}$ [186] and $La_{0.75}Sr_{0.25}FeO_{3-\delta}$ [189].

Additionally, the tetravalent iron cations strengthen and hence shorten the Fe-O bonds. At intermediate content of Ca and Sr, the charge compensation mechanism switches progressively from formation of holes to departure of lattice oxygen, as confirmed by Mőssbauer spectroscopy and chemical analysis [187].

In air, the electrical transport of acceptor-doped ferrites is several orders of magnitude higher than that of orthoferrites $AFeO_3$ (Fig. 1.17), whilst the activation energy is remarkably lower: 10-50

kJ/mol [24,185,190,191]. The Ca-rich compositions adopt brownmillerite-type crystal structure, where oxygen vacancies are immobilized and all iron is trivalent [187], so that the total conductivity of $CaFeO_{3-\delta}$ is low and comparable with that of $NdFeO_3$; the oxygen ionic conduction in $CaFeO_{3-\delta}$ is lower than 0.001 S/cm at 1223 K [192]. The Sr-rich ferrites also undergo cubic perovskite ↔ brownmillerite transition on cooling and/or reducing oxygen pressure, which results in deterioration of the transport properties [193]. The conductivity of $La_{0.75}Sr_{0.25}FeO_{3-\delta}$ decreases with reducing oxygen pressure even in oxidizing conditions, contrary to $LaFeO_{3-\delta}$ (Fig. 1.18B). Nonetheless, the conduction behavior of acceptor-doped and acceptor-free oxides at $p(O_2)$ < 0.1-1 Pa are similar: the total conductivity reaches minimal values and increases on subsequent decreasing oxygen pressure due to increasing contribution of n-type electronic transport. The estimated mobility of holes and electrons in $La_{0.75}Sr_{0.25}FeO_{3-\delta}$ is 0.09 and 0.07 $cm^2\ V^{-1}\ s^{-1}$, respectively [189]. As for $AFeO_3$, the data on electrical transport and Seebeck coefficient suggests small polaron hopping in the Fe-sublattice as the electronic conduction mechanism in Ca- and Sr-doped ferrites.

Acceptor-type substitution provokes more intensive losses of lattice oxygen, decreasing the concentration of holes and the p-type electronic transport. This factor is significant above 500-600 K and overcomes the temperature impact. Therefore, the apparent activation energy decreases on increasing temperature, the total conductivity reaches the maximum and even starts to decrease on further heating (Fig. 1.17), like in the case of metals. This phenomenon is called pseudo-metallic conduction, since the electronic transport still occurs by small polarons hopping.

In oxidizing environments, the oxygen ionic transference numbers for ferrites are relatively low ($10^{-4} < t_O < 10^{-2}$), though ionic conductivity may achieve values of 0.1-0.5 S/cm at 1023-1223 K, which is comparable with conventional solid electrolytes (Fig. 1.19). The activation energy varies from 60 to 180 kJ/mol. The p-type electronic conduction decreases on reducing $p(O_2)$ thus increasing the contribution of ionic transport to the total conductivity up to 40-60% within the oxygen pressure range 10^{-10}-10^{-5} Pa. Lower $p(O_2)$ leads to lower t_O values due to a higher role of the n-type electronic transport [16,45,192,193]. The combination of significant electronic and significant oxygen ionic conductivities gives rise to considerable oxygen-permeation fluxes through ferrite-based membranes if under an oxygen pressure gradient, Table 1.3 [194,195].

As for A-site substitution, the transport properties are influenced by doping in the Fe-sublattice. A number of perovskite-type oxides, where iron is partially substituted for transition metals (Ti [32,33,38], Cr [39], Mn [40], Co [26-29], Ni [41,116,153], Cu [117]) and stable-valence elements (Al^{3+} [118], Ga^{3+} [43,48], Zr^{4+} [164], Sn^{4+} [196]), have been studied.

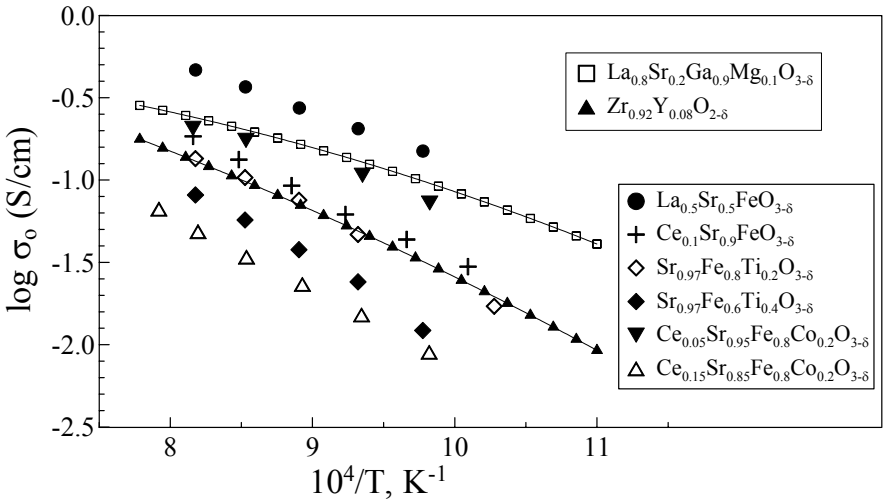

Fig. 1.19. The oxygen ionic conductivity of ferrite-based perovskite-type oxides [45,115,193,198] compared with that of LSGM [106] and 8YSZ [58].

The substitution of iron with the tetravalent titanium can be used in order to enhance the stability in reducing atmospheres and decrease the "chemical" expansion [38,197]. In $Sr_{1-y}Fe_{1-x}Ti_xO_{3-\delta}$, the incorporation of Ti stabilizes the disordered cubic lattice, whilst A-site deficiency improves sinterability and suppresses reactivity with CO_2 [198]. All $SrFe_{1-x}Ti_xO_{3-\delta}$ ($0 \le x \le 1$) materials are cubic perovskites [199], except $SrFeO_{3-\delta}$ at certain nonstoichiometry values when this oxide adopts oxygen vacancy-ordered structures [192]. $La_{1-y}Sr_yFe_{1-x}Ti_xO_{3-\delta}$ compositions can be usually indexed as orthorhombically-distorted perovskites [197]. Increasing titanium concentration decreases both the total iron content and the Fe^{4+} fraction [199], resulting in the unit cell expansion since Ti^{4+} is larger than Fe^{4+} [8]. At the same time, the thermal expansion and electronic conductivity (Fig. 1.20) decrease, whereas the electronic transport activation energy increases from 20 to 50 kJ/mol.

The A-site deficiency was found to deteriorate the electrical transport below 723-823 K, enlarge the unit cell and increase thermal expansion. In $Sr_{0.97}Fe_{1-x}Ti_xO_{3-\delta}$ ($0.1 \le x \le 0.8$) system, the contribution of the oxygen ionic conduction is about 0.1-1% in air, increasing with temperature and Ti doping [197]. The behavior of total conductivity as a function of the oxygen pressure [32] is similar to that of $La_{0.75}Sr_{0.25}FeO_{3-\delta}$ (Fig. 1.18B).

The oxygen ionic conductivity of some Ti-containing ferrites, e.g. $Sr_{0.97}Fe_{0.8}Ti_{0.2}O_{3-\delta}$, is comparable to that of 8YSZ (Fig. 1.19) and decreases when titanium content increases [32,198], thus decreasing the number of oxygen vacancies and strengthening B-O bonds. A slight A-site deficiency

(3-6%) improves considerably the ionic transport [197,198]. This phenomenon is attributed mainly to increasing structural disorder when A-site deficiency increases. The σ_O activation energy is 165 kJ/mol in the case of $Sr_{0.97}Fe_{0.9}Ti_{0.1}O_{3-\delta}$ and decreases down to 100 kJ/mol for $Sr_{0.97}Fe_{1-x}Ti_xO_{3-\delta}$ ($0.2 \leq x \leq 0.6$) oxides. Maximum oxygen permeation fluxes were measured for $Sr_{0.97}Fe_{0.8}Ti_{0.2}O_{3-\delta}$ (Table 1.3). The relatively high oxygen permeability of Ti-doped ferrites is limited by both the bulk ambipolar conduction and the surface kinetics [198].

Table 1.3. Oxygen fluxes through ferrite-based ceramic membranes.

Membrane material	T, K	d, mm	j, mol/(cm^2×s)	gradient	Ref.
$La_{0.9}Sr_{0.1}FeO_{3-\delta}$	1223	1.0	1.0×10^{-8}	air/He	[194]
$La_{0.8}Sr_{0.2}FeO_{3-\delta}$	1223	1.0	4.6×10^{-8}	air/He	[194]
$La_{0.7}Sr_{0.3}FeO_{3-\delta}$	1223	1.0	7.2×10^{-8}	air/He	[194]
$La_{0.7}Sr_{0.3}FeO_{3-\delta}$	1223	1.0	1.3×10^{-6}	air/ CO,CO_2	[195]
$La_{0.6}Sr_{0.4}FeO_{3-\delta}$	1223	1.0	1.3×10^{-7}	air/He	[194]
$Sr_{0.97}Fe_{0.9}Ti_{0.1}O_{3-\delta}$	1223	1.0	6.3×10^{-8}	21 kPa/2.1 kPa	[198]
$Sr_{0.97}Fe_{0.8}Ti_{0.2}O_{3-\delta}$	1223	1.0	2.9×10^{-7}	21 kPa/2.1 kPa	[198]
$Sr_{0.97}Fe_{0.6}Ti_{0.4}O_{3-\delta}$	1223	1.0	2.0×10^{-7}	21 kPa/2.1 kPa	[198]
$Sr_{0.97}Fe_{0.4}Ti_{0.6}O_{3-\delta}$	1223	1.0	8.8×10^{-8}	21 kPa/2.1 kPa	[198]
$La_{0.2}Sr_{0.8}Fe_{0.7}Cr_{0.2}Co_{0.1}O_{3-\delta}$	1273	1.0	4.5×10^{-6}	air/ CO,CO_2	[201]
$BaFe_{0.6}Bi_{0.2}Co_{0.2}O_{3-\delta}$	1223	1.5	7.4×10^{-7}	air/He	[37]
$SrFeO_{3-\delta}$	1123	1.0	1.4×10^{-6}	air/He	[27]
$SrFe_{0.67}Co_{0.33}O_{3-\delta}$	1273	2.0	1.5×10^{-6}	air/He	[211]
$SrFe_{0.6}Co_{0.4}O_{3-\delta}$	1123	1.0	1.5×10^{-6}	air/He	[27]
$La_{0.2}Sr_{0.8}FeO_{3-\delta}$	1123	1.0	4.6×10^{-7}	air/He	[27]
$La_{0.2}Sr_{0.8}Fe_{0.6}Co_{0.4}O_{3-\delta}$	1123	1.0	4.3×10^{-7}	air/He	[27]
$La_{0.6}Sr_{0.4}Fe_{0.6}Co_{0.4}O_{3-\delta}$	1123	1.0	1.3×10^{-7}	air/He	[27]
$La_{0.4}Ca_{0.6}Fe_{0.75}Co_{0.25}O_{3-\delta}$	1173	0.7	8.3×10^{-7}	air/He	[209]
$LaFe_{0.5}Ni_{0.5}O_{3-\delta}$	1223	1.0	1.0×10^{-8}	21 kPa/2.1 kPa	[219]
$BaFe_{0.4}Co_{0.4}Zr_{0.2}O_{3-\delta}$	1173	1.0	5.6×10^{-7}	air/He	[221]
$BaFe_{0.4}Co_{0.4}Zr_{0.2}O_{3-\delta}$	1123	1.0	4.2×10^{-6}	air/CH_4	[164]
$La_{0.3}Sr_{0.7}Fe_{0.8}Al_{0.2}O_{3-\delta}$	1223	1.0	1.5×10^{-7}	21 kPa/2.1 kPa	[227]
$La_{0.3}Sr_{0.7}Fe_{0.6}Al_{0.4}O_{3-\delta}$	1223	1.0	8.8×10^{-8}	21 kPa/2.1 kPa	[227]
$La_{0.5}Sr_{0.5}Fe_{0.8}Ga_{0.2}O_{3-\delta}$	1123	2.0	1.0×10^{-7}	air/He	[232]
$La_{0.3}Sr_{0.7}Fe_{0.4}Ga_{0.6}O_{3-\delta}$	1223	1.7	6.0×10^{-8}	21 kPa/0.1 kPa	[48]
$La_{0.3}Sr_{0.7}Fe_{0.4}Ga_{0.6}O_{3-\delta}$	1273	0.5	1.0×10^{-6}	air/He	[231]
$La_{0.8}Sr_{0.2}Fe_{0.3}Ga_{0.7}O_{3-\delta}$	1273	0.5	1.0×10^{-6}	air/ N_2	[226]

Partial substitution of iron with chromium and manganese, analogously to Ti-doping, increases the stability of perovskite-type ferrites in reducing atmospheres, also decreasing the reactivity with YSZ [39,200]. Ferrites $LaFe_{1-x}Cr_xO_{3-\delta}$ ($0 \le x \le 1$) [202] and $NdFe_{1-x}Cr_xO_{3-\delta}$ ($0 \le x \le 1$) [203] are orthorhombically-distorted perovskites. Their cell volume decreases monotonously with increasing x since Cr^{3+} is smaller than Fe^{3+} in the high-spin state [8]. The electrical transport of $NdFe_{1-x}Cr_xO_{3-\delta}$ oxides, predominantly p-type electronic in air, is relatively low and increases on Cr-doping (Fig. 1.20), according to Seebeck coefficient measurements, owing to increasing mobility of holes. The latter tendency could be associated with shorter B-O distances and higher B-O-B angles when chromium content increases. The activation energy decreases with x from 85 to 15 kJ/mol [203]. The conductivity of acceptor-doped $La_{0.2}Sr_{0.8}Fe_{0.8}Cr_{0.2}O_{3-\delta}$ is several orders of magnitude higher with respect to $NdFe_{1-x}Cr_xO_{3-\delta}$ and $LaFeO_{3-\delta}$ [204]. Reducing oxygen pressure down to 10^{-10}-10^{-15} Pa leads to prevailing n-type electronic conduction [205].

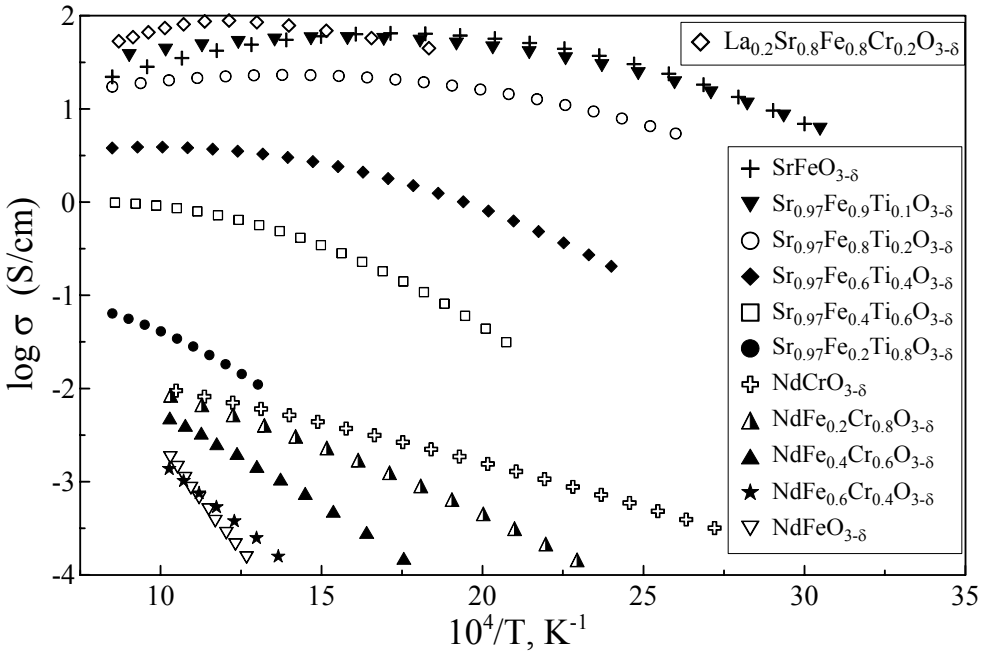

Fig. 1.20. The total conductivity of $Sr_{0.97}Fe_{1-x}Ti_xO_{3-\delta}$ ($0.1 \le x \le 0.8$) [198], $NdFe_{1-x}Cr_xO_{3-\delta}$ ($0 \le x \le 1$) [203], $La_{0.2}Sr_{0.8}Fe_{0.8}Cr_{0.2}O_{3-\delta}$ [204] and $SrFeO_{3-\delta}$ [191] in air.

The manganoferrites $SrFe_{1-x}Mn_xO_{3-\delta}$ ($1/3 \le x \le 2/3$) and Sr-rich compositions of the $La_{0.3}Sr_{0.7}Fe_{1-y}Mn_yO_{3-\delta}$ series ($0.2 \le y \le 0.8$) adopt cubic perovskite structure, whilst $La_{0.5}Sr_{0.5}Fe_{1-}$

$_yMn_yO_{3-\delta}$ perovskites ($0.2 \leq y \leq 0.8$) are rhombohedrally-distorted. In La-rich $La_{0.8}Sr_{0.2}Fe_{1-y}Mn_yO_{3-\delta}$ ($0.2 \leq y \leq 0.5$), the orthorhombic and rhombohedral lattices coexist [206,207]. The substitution of iron with manganese contracts the unit cell since Mn^{4+} is smaller than Fe^{4+} and Fe^{3+} [8]. The total conductivity of $SmFe_{1-y}Mn_yO_{3-\delta}$ ($0.1 \leq y \leq 0.3$), measured at 240-440 K, was found to increase with y [208], whereas Mn-doping in $SrFe_{1-x}Mn_xO_{3-\delta}$ ($1/3 \leq x \leq 2/3$) suppresses the electrical transport at 120-300 K [206]. The mechanism is, again, small-polaron based [203,208]. The mobile oxygen vacancies and fast surface exchange in Cr- and Mn-doped $La_{1-x}Sr_xFeO_{3-\delta}$ ($0.2 \leq x \leq 0.6$) [39,40] provide significant oxygen permeation fluxes for phases with optimized composition (Table 1.3).

After the discovery of high oxygen permeability in $La_{1-x}Sr_xFe_{1-y}Co_yO_{3-\delta}$ system by Teraoka et al [27], a huge number of studies have been devoted to perovskite-type cobaltoferrites [26-29,31,113,115,135,151-153]. The Ca- [209], Sr- [210,211] and Ba-rich [158] phases hold cubic symmetry. Increasing concentration of rare-earth cations with lower radii [8] at first induces rhombohedral and then orthorhombic perovskite lattice distortions. Nonetheless, the unit cell does expand revealing simultaneous oxidation of Fe^{3+} into smaller Fe^{4+} [212,213]. At fixed A-site composition, doping with cobalt decreases the cell volume [113,210,214] as Fe^{n+} are larger than Co^{n+} [8]. This increases the symmetry of crystal structure, so that orthorhombic → rhombohedral transition occurs in $La_{0.8}Sr_{0.2}Fe_{1-y}Co_yO_{3-\delta}$ system when y increases up to 0.3 [113].

The crystal lattice changes, caused by increasing Co content (decreasing cell volume and increasing symmetry), are advantageous for electronic conduction. For a constant A-site array, the electrical transport of $La_{1-x}Ca_xFe_{1-y}Co_yO_{3-\delta}$ [31], $La_{1-x}Sr_xFe_{1-y}Co_yO_{3-\delta}$ [113], $La_{1-x}Ba_xFe_{1-y}Co_yO_{3-\delta}$ [31], $SrFe_{1-y}Co_yO_{3-\delta}$ [211] and $Ce_{1-x}Sr_xFe_{1-y}Co_yO_{3-\delta}$ [214], predominantly p-type electronic in air, increases upon Co incorporation (Fig. 1.21). At the same time, the activation energy values decrease, for example, from 15 to 5 kJ/mol when the composition gradually changes from $La_{0.8}Sr_{0.2}FeO_{3-\delta}$ to $La_{0.8}Sr_{0.2}CoO_{3-\delta}$ [113]. For invariable Fe/Co ratio, the total conductivity increases with alkaline-earth concentration, reaches a maximum and then decreases [31]. In $La_{1-x}Sr_xFe_{0.8}Co_{0.2}O_{3-\delta}$ series, the highest electrical transport was measured for x = 0.4 [215]. This reflects preferential mechanism of acceptor-doping charge compensation: formation of holes and oxygen vacancies at lower and higher x, correspondingly [187]. In oxidizing conditions the total conductivity of $La_{1-x}Sr_xFe_{1-y}Co_yO_{3-\delta}$ [216] and $Ce_{1-x}Sr_xFe_{1-y}Co_yO_{3-\delta}$ [214] decreases on reducing oxygen pressure, passes a minimum at $p(O_2) = 10^{-12}$-10^{-7} Pa and increases on subsequent reduction. The electronic conductivity of perovskite-type cobaltoferrites is, again, treated in terms of a hopping mechanism [31,212,216].

The oxygen ionic conduction in $Ln_{1-x}A_xFe_{1-y}Co_yO_{3-\delta}$ (Ln = rare-earth, A = alkaline-earth) increases both with acceptor- and Co-doping, owing to the same reason – growing population of

oxygen vacancies [26,31,214]. The ionic transport attains values comparable or even higher (0.2-0.9 S/cm at 1123-1223 K) than those of yttria-stabilized zirconia (Fig. 1.19). Note also, that Co-O bonds are weaker if compared with Fe-O. The activation energy of ionic transport varies within 80-150 kJ/mol; the higher oxygen conductivity level, the lower E_a value. In air, the electronic conductivity is much higher with respect to the ionic conductivity, giving t_O values as low as 10^{-2}-10^{-4} [26,31,115,158]. The influence of the composition on the oxygen permeation fluxes is essentially the same as for the bulk ionic conductivity, since the latter process is a limiting factor for thick membranes. Also, their E_a values are comparable. For instance, the activation energy for permeation through $La_{0.4}Ca_{0.6}Fe_{1-y}Co_yO_{3-\delta}$ ($0 \le y \le 0.5$) membranes is in the range of 75-120 kJ/mol [209]. The level of permeability of $SrFe_{1-y}Co_yO_{3-\delta}$ [27] and $Ln_{1-x}A_xFe_{1-y}Co_yO_{3-\delta}$ [28,158,214] is one of the highest reported so far (Table 1.3).

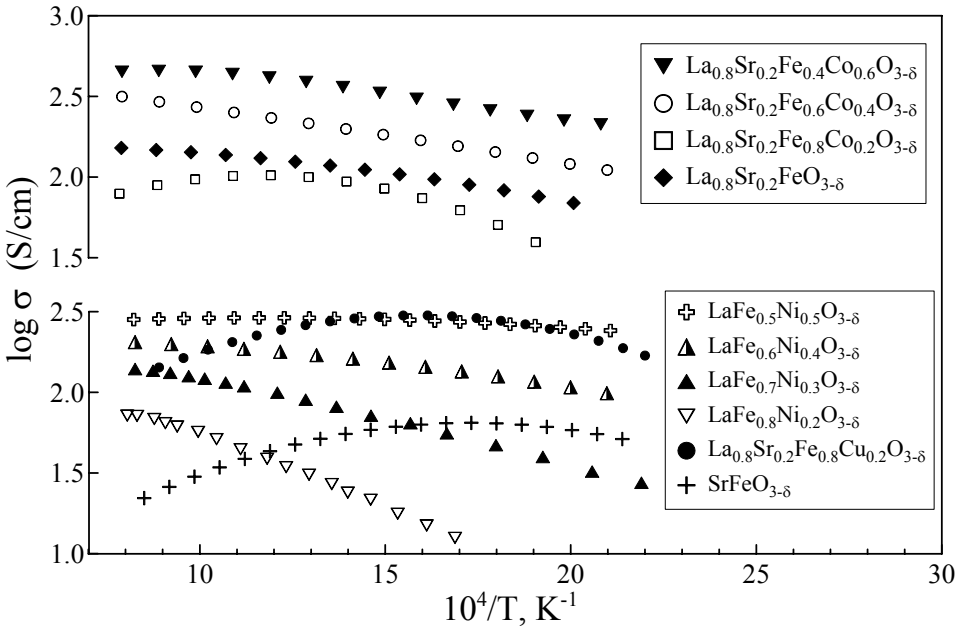

Fig. 1.21. The total conductivity of $La_{0.8}Sr_{0.2}Fe_{1-x}Co_xO_{3-\delta}$ ($0 \le x \le 0.6$) [113], $LaFe_{1-x}Ni_xO_{3-\delta}$ ($0.2 \le x \le 0.5$) [219], $La_{0.8}Sr_{0.2}Fe_{0.8}Cu_{0.2}O_{3-\delta}$ [117] and $SrFeO_{3-\delta}$ [191] in air.

Ni- and Cu-doped ferrites with perovskite-type structure were characterized [41,116,117,217-220]. Ferrites $LaFe_{1-x}Ni_xO_{3-\delta}$ ($0 \le x \le 0.5$) have orthorhombically-distorted lattices, whilst heavier Ni-doping leads to rhombohedral distortions [217,218], analogously to $La_{1-x}Sr_xFe_{1-y}Co_yO_{3-\delta}$ system [113]. The substitution of lanthanum with strontium increases the symmetry so that consecutive transitions orthorhombic → rhombohedral and rhombohedral → cubic do occur [116]; Sr-rich

$La_{0.2}Sr_{0.8}Fe_{0.7}Ni_{0.3}O_{3-\delta}$, $La_{0.2}Sr_{0.8}Fe_{1-y}Cu_yO_{3-\delta}$ ($0.1 \le y \le 0.4$) are cubic [117,220]. As for Co-containing ferrites [113,210,214], the improvement in the crystal cell symmetry of $La_{1-x}Sr_xFe_{1-y}M_yO_{3-\delta}$ (M = Ni [41,116,217,218] and Cu [117]) is accompanied by lattice contraction, since M^{n+} are smaller than Fe^{3+} and incorporation of Sr^{2+} is compensated by higher average oxidation state, hence, smaller radius, of the B-cations [8].

The electrical transport, however, is not a monotonic function of Ni or Sr concentration. The maximum values of σ were found for rhombohedrally-distorted $La_{1-x}Sr_xFe_{1-y}Ni_yO_{3-\delta}$ oxides (x + y = 0.5-0.7); the conductivity of orthorhombic and cubic phases is lower [116,218]. For instance, the highest electrical conduction in $La_{0.9}Sr_{0.1}Fe_{1-y}Ni_yO_{3-\delta}$ system was observed at y = 0.45, in $La_{0.5}Sr_{0.5}Fe_{1-y}Ni_yO_{3-\delta}$ – at y = 0.2. The total conductivity of the materials with low strontium content ($0 \le x \le 0.2$) increases on nickel doping (Fig. 1.21) until $0.4 \le y \le 0.6$ [116]. At the same time, the activation energy decreases, varying within 5-25 kJ/mol [41,219].

In oxidizing atmospheres, the total conductivity of Ni- and Cu-doped ferrites decreases with reducing oxygen pressure, and Seebeck coefficient values are positive [41,117]. This suggests prevailing p-type electronic transport. In ferrites, trivalent nickel is easily reduced [41]:

$$Fe_{Fe}^{\times} + Ni_{Fe}^{\times} = Fe_{Fe}^{\bullet} + Ni_{Fe}^{/} \qquad (1.69)$$

As a result, the electronic conductivity increases. On the other hand, increasing Ni amount might lead to a progressive delocalization of electrical charge and increases the metallicity of B-O bonds, which also should increase the electrical transport and decrease its activation energy [219].

Decreasing bond energy and increasing concentration of oxygen vacancies in the order Fe - Co - Ni - Cu results in a high oxygen permeation through $Ln_{1-x}A_xFe_{1-y}M_yO_{3-\delta}$ (M = Co, Ni, Cu) membranes, but also decreases stability of these oxides in reducing environments. These start to decompose at higher $p(O_2)$ values than those in, for example, $CH_4 + H_2O$ stream [29,30]. In order to suppress large oxygen losses at lower oxygen pressure leading to a structural failure, cations with stable oxidation state (Al^{3+} [118], Ga^{3+} [48], Zr^{4+} [164], Sn^{4+} [196]) can be introduced in the Fe-sublattice.

Iron was successfully substituted by tetravalent zirconium [164,221,222] and tin [196,223] when divalent alkaline-earth metals (Sr or Ba) occupy A-sites. In $SrFe_{1-x}Sn_xO_{3-\delta}$, the crystal symmetry is cubic up to x = 0.6, whereas the phases with $x \ge 0.7$ are orthorhombically-distorted [223]. The cubic structure was also found in ferrites moderately doped with zirconium: $SrFe_{1-x}Zr_xO_{3-\delta}$ ($0.04 \le x \le 0.24$) [222] and $BaFe_{1-x}Zr_xCo_{0.4}O_{3-\delta}$ ($0 \le x \le 0.2$) [221]. Zr^{4+} and Sn^{4+} are larger than Fe^{3+} or Fe^{4+} [8]; the unit cell expands upon incorporation of former ions [196,222,223].

Zr-doping reduces oxygen losses on heating and on decreasing oxygen pressure, suppresses formation of brownmillerite-type phases and increases the stability against reduction in hydrogen atmospheres. The Zr^{4+} and O^{2-} build very stable, randomly distributed octahedra making removal of oxygen in an ordered way quite unlikely [222]. The $BaFe_{0.4}Zr_{0.2}Co_{0.4}O_{3-\delta}$ membrane was stable under CH_4/air gradient at 1023-1223 K over more than 2000 hours. Both feed and permeate sides kept cubic perovskite structure after such treatment [164]. However, Ba-containing phases react partially with carbon dioxide, so the oxygen permeability decreases considerably [221].

Incorporation of cations with stable oxidation state deteriorates the electronic conductivity of ferrites (Fig. 1.22), as expected, since it decreases the total concentration of B-sites participating in the hopping process, and even Fe^{4+} fraction, like in case of $SrFe_{1-x}Sn_xO_{3-\delta}$. The activation energy increases from 10 to 40 kJ/mol at $0 \leq x \leq 0.75$ [196]. $SrFe_{1-x}Sn_xO_{3-\delta}$ perovskites are predominantly electronic conductors over a large $p(O_2)$ range (10^{-18}-10^5 Pa), though the contribution of the oxygen ionic transport varies within 10-50% for $0.1 \leq x \leq 0.2$ [223]. In the $BaFe_{1-x}Zr_xCo_{0.4}O_{3-\delta}$, deterioration of the permeation flux due to Zr-doping was found for $x > 0.2$ only, and $BaFe_{0.4}Zr_{0.2}Co_{0.4}O_{3-\delta}$ showed stable membrane performance, whilst the permeability of $BaFe_{0.6}Co_{0.4}O_{3-\delta}$ dropped by 30-35% during the first 200 hours [221].

The substitution of iron with isovalent aluminum and gallium is possible for both divalent and trivalent A-site cations [48,118]. At room temperature, orthoferrites $LaFe_{1-x}Al_xO_{3-\delta}$ have orthorhombic ($0 \leq x \leq 0.3$) and rhombohedral ($0.3 < x \leq 1$) structures [224], whilst $LaFe_{1-x}Ga_xO_{3-\delta}$ oxides are orthorhombically-distorted for the entire compositional range [183,225]. Ionic radii increase in the order $Al^{3+} < Ga^{3+} < Fe^{3+}$ [8], and decreasing average B-cation radius in case of Al-doping leads to a more pronounced improvement of the crystal symmetry. However, Ga-containing ferrites undergo orthorhombic → rhombohedral transition on heating (873 K for $LaFe_{0.5}Ga_{0.5}O_{3-\delta}$); the transition temperature is lower when gallium concentration is higher [225]. Sr-doped oxides are orthorhombically- or rhombohedrally-distorted perovskites [224,226], unless the strontium amount is high as in $La_{0.3}Sr_{0.7}Fe_{1-y}Al_yO_{3-\delta}$ ($0 \leq y \leq 0.4$) and $La_{0.5}Sr_{0.5}Fe_{0.8}Ga_{0.2}O_{3-\delta}$ phases, which are cubic [227,228]. All iron ions in $LaFe_{1-x}Al_xO_{3-\delta}$ are trivalent [118], whereas Fe^{4+} was found in $La_{1-x}Sr_xFe_{1-y}Al_yO_{3-\delta}$, and the ratio $[Fe^{4+}] / [Fe^{3+}]$ decreases with increasing aluminum content [224]. Analogous defect chemistry is expected for $La_{1-x}Sr_xFe_{1-y}Ga_yO_{3-\delta}$ oxides. Since the ionic radius increases in the order $Al^{3+} < Fe^{4+} < Ga^{3+}$, higher aluminum concentration leads to lower unit cell volume in $La_{0.3}Sr_{0.7}Fe_{1-y}Al_yO_{3-\delta}$ [227] and $La_{0.8}Sr_{0.2}Fe_{1-y}Al_yO_{3-\delta}$ [229], whilst gallium incorporation has no essential influence on $La_{0.8}Sr_{0.2}Fe_{1-y}Ga_yO_{3-\delta}$ lattices [226].

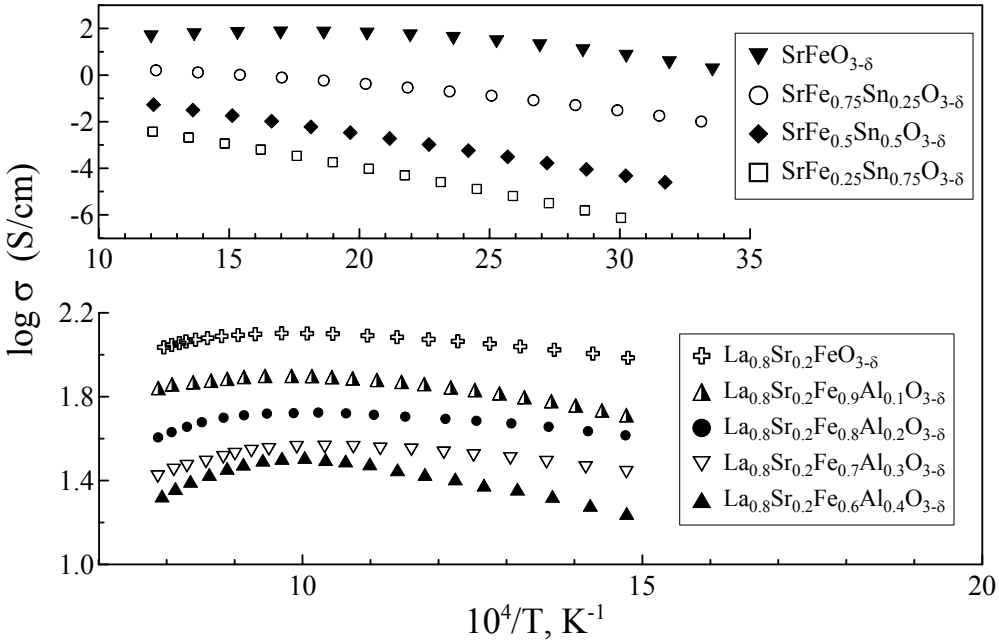

Fig. 1.22. The total conductivity of $SrFe_{1-x}Sn_xO_{3-\delta}$ ($0.25 \leq x \leq 0.75$) [196], $SrFeO_{3-\delta}$ [191] and $La_{0.8}Sr_{0.2}Fe_{1-x}Al_xO_{3-\delta}$ ($0 \leq x \leq 0.4$) [230] in air.

As for Zr- and Sn-containing ferrites, doping with aluminum [230] or gallium [161,231] decreases the electronic conductivity (Fig. 1.22). The activation energy varies within 10-20 kJ/mol in $La_{0.8}Sr_{0.2}Fe_{1-x}Al_xO_{3-\delta}$ ($0 \leq x \leq 0.4$) [230] and increases from 11 to 37 kJ/mol for x = 0 and 0.4, respectively, in $La_{0.3}Sr_{0.7}Fe_{1-x}Al_xO_{3-\delta}$ [227]. Under oxidizing conditions, the total conductivity of Al- and Ga-doped lanthanum strontium ferrites decreases with decreasing oxygen pressure, whilst thermopower values are positive [226-228]. This indicates prevailing p-type electronic transport. The mobility of holes in $La_{0.3}Sr_{0.7}Fe_{0.8}Al_{0.2}O_{3-\delta}$ and $La_{0.3}Sr_{0.7}Fe_{0.6}Al_{0.4}O_{3-\delta}$ increases on heating and is in range of 0.01-0.1 $cm^2/(V \cdot s)$ [227]. Therefore, the electronic conduction in aluminum- or gallium-substituted ferrites is believed to occur via small-polaron hopping mechanism.

The incorporation of aluminum decreases the ionic conductivity, possibly due to greater Al-O bond energy compared to Fe-O bonds. Nonetheless, moderately doped phases like $La_{0.3}Sr_{0.7}Fe_{0.8}Al_{0.2}O_{3-\delta}$ show oxygen ionic transport comparable with that of 8YSZ. The t_O values increase with temperature and aluminum content and vary within 0.001-0.01 in $La_{0.3}Sr_{0.7}Fe_{0.8}Al_{0.2}O_{3-\delta}$ and $La_{0.3}Sr_{0.7}Fe_{0.6}Al_{0.4}O_{3-\delta}$ at 1023-1223 K; the activation energy of the ionic conductivity is about 100 kJ/mol [227].

The oxygen ionic transference numbers measured for Ga-rich $La_{1-x}Sr_xFe_{0.4}Ga_{0.6}O_{3-\delta}$ ($0.2 \leq x \leq 0.4$) materials are about 0.5, thus indicating comparable contributions of electronic and ionic transport [231]. According to Eq. (1.42), such a ratio between ionic and total conductivities is advantageous for fast oxygen permeation. Indeed, the oxygen permeation rates through $La_{0.8}Sr_{0.2}Fe_{1-x}Ga_xO_{3-\delta}$, with maximum at x = 0.6-0.7 [226], are relatively high (Table 1.3). The Ga-doped ferrites possess considerably higher ionic conductivity with respect to aluminum-containing analogues, in agreement with literature data showing that the ionic conductivity in $La_{1-x}Sr_xGa_{1-y}Mg_yO_{3-\delta}$ is much higher compared to $La_{1-x}Sr_xAl_{1-y}Mg_yO_{3-\delta}$ [13]. The studies on CH_4 conversion showed sufficient stability and quite stable oxygen permeability of $La_{0.8}Sr_{0.2}Fe_{0.4}Ga_{0.6}O_{3-\delta}$ [161] and $La_{0.5}Sr_{0.5}Fe_{0.8}Ga_{0.2}O_{3-\delta}$ [232] membranes.

1.3.3. Iron-rich phases with perovskite-related structures

The perovskite-type $AFeO_{3-\delta}$ (A = Ca, Sr) oxides are able to accommodate large content of oxygen vacancies so that δ varies within 0 and 0.5. A series of vacancy-ordered phases ($Sr_nFe_nO_{3n-1}$; n = 2, 4, 8, ∞) was described where end members n = ∞ and 2 correspond to cubic $SrFeO_3$ and brownmillerite-type $SrFeO_{2.5}$, respectively [233]. The latter structure contains alternating layers of iron octahedra (FeO_6) and tetrahedra (FeO_4) perpendicular to the b-axis (Fig. 1.23). This creates rows of oxygen vacancies along the c-axis in every other perovskite layer. Such an ordering happens at lower temperatures and/or oxygen pressure values; it is favored by the possibility to adopt trivalent iron in both octahedral and tetrahedral sites. Heating leads to disordering oxygen sublattice [187,192]. In the case of $SrFeO_{3-\delta}$, only perovskite crystal structure is detected above 1123 K, even in reducing atmospheres [234]. The substitution of strontium with calcium promotes this transition, and $CaFeO_{3-\delta}$ has a brownmillerite-type lattice in air [187], as for Al-doped calcium ferrite [235]. When δ = 0.5, all iron is trivalent and the electronic conductivity determined by temperature-activated disproportionation is very low (Figs. 1.17 and 1.24). The ordered oxygen vacancies are immobilized, and the oxygen ionic conduction of $CaFeO_{2.5}$ [192] and $CaFe_{0.5}Al_{0.5}O_{2.5}$ (Fig. 1.25) does not exceed 0.001 S/cm at 1223 K. The oxygen permeation through $CaFe_{0.5}Al_{0.5}O_{2.5}$ membranes, limited by the bulk ambipolar conductivity, is relatively low (Table 1.4). The oxygen-ion transport in brownmillerite-type oxides is possible mainly due to one-dimensional migration of the hyperstoichiometric oxygen anions in tetrahedral layers along the c-axis [235], whereas perovskite-type $SrFeO_{3-\delta}$ having a three-dimensional network for diffusion pathways shows 10^2-10^3 times faster ionic conduction. However, perovskite ↔ brownmillerite transition, starting below 1123 K, deteriorates the oxygen ionic transport of strontium ferrite at low-temperature (Fig. 1.25).

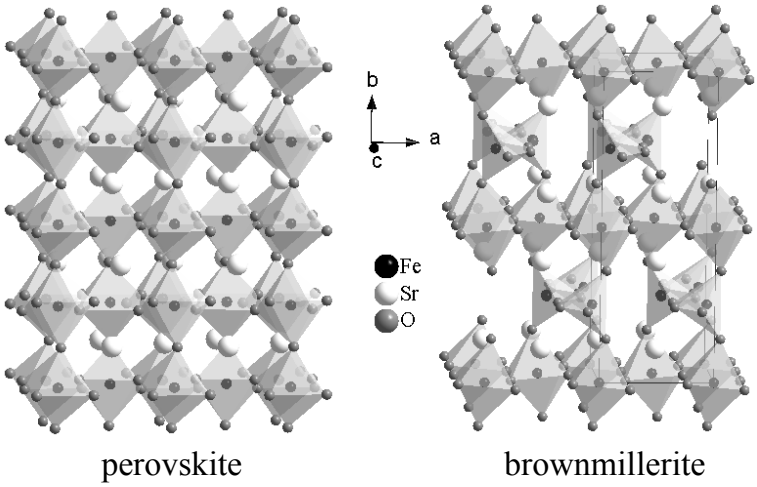

Fig. 1.23. Comparison of the orthorhombically-distorted perovskite (left) and brownmillerite (right) structures.

Another family of perovskite-related phases is the Ruddlesden-Popper series $A_{n+1}Fe_nO_{3n+1}$ (A = rare- and alkaline-earth elements; n = 1, 2, 3 and ∞) where the end member n = ∞ corresponds again to the perovskite-type $AFeO_3$ [236]. The crystal structure of this series can be viewed as perovskite stacks consisting of n $AFeO_3$ layers, sandwiched with SrO rock-salt sheets. As an example, the unit cell of Sr_2FeO_4 (n = 1) is presented in Fig. 1.26. Among strontium ferrites of the Ruddlesden-Popper series, only $Sr_3Fe_2O_{7-\delta}$ is stable up to the melting point. $Sr_2FeO_{4-\delta}$ and $Sr_4Fe_3O_{10-\delta}$ decompose at 1123-1223 K in air yielding $Sr_3Fe_2O_{7-\delta}$. At room temperature, all three oxides react with H_2O and CO_2 of ambient air [237]. This becomes even more pronounced when iron is partially substituted by cobalt [238]. Stabilization of strontium ferrites can be achieved replacing Sr^{2+} by La^{3+} [239]. Incorporation of lanthanum expands the unit cell due to diminishing Fe^{4+} fraction [238,240]. The substitution of Fe^{4+}/Fe^{3+} with larger Ti^{4+} or smaller Co^{4+}/Co^{3+} [8] leads to increasing [241] or decreasing [238,239] cell volume, correspondingly.

In air, the Ruddlesden-Popper type ferrites contain both tri- and tetravalent iron even above 1273 K. To obtain Fe^{2+}, these oxides should be treated in N_2 or H_2/He at 773-973 K [238,239,241]. The electronic conductivity is therefore p- and n-type in oxidizing and reducing conditions, respectively, passing through a minimum at intermediate oxygen pressure, 10^{-10}-10^{-5} Pa [241]. In $Sr_{2-x}La_xFeO_{4\pm\delta}$, the total conductivity in air is maximum for x = 0.7 [242]. As for perovskite-type ferrites [113,198], the electrical transport decreases on Ti-doping, like in $Sr_3Fe_{2-x}Ti_xO_{7-\delta}$ [241], and increases with cobalt

content (Fig. 1.24) e.g. in $Sr_{2.7}La_{0.3}Fe_{2-x}Co_xO_{7-\delta}$ [238] and $Sr_3LaFe_{3-x}Co_xO_{10-\delta}$ [239]. The activation energy decreases slightly on Co-doping and varies from 7-13 kJ/mol [238,239].

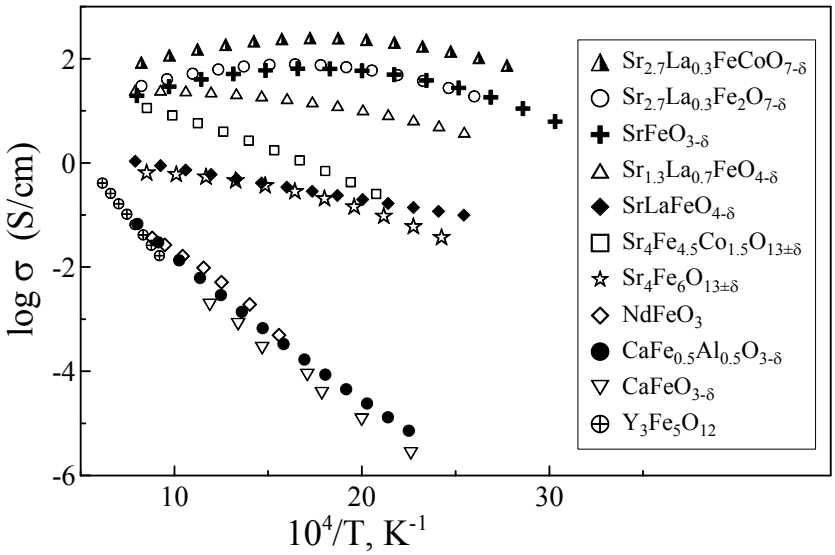

Fig. 1.24. The total conductivity of ferrites in air [187,191,235,238,242,244,251].

Structural considerations of Ruddlesden-Popper ferrites suggest two-dimensional oxygen ionic transport via vacancy migration in perovskite blocks and/or interstitial diffusion in rock salt layers. This deteriorates the oxygen-ion conduction of such phases if compared with perovskite-type oxides. However, it is still higher than the one-dimensional ionic conductivity of brownmillerite-type ferrites (Fig. 1.25). The ion transference numbers vary within 0.01-1% in air [238,241], increase up to 40-60% at intermediate (10^{-10}-10^{-5} Pa) oxygen pressure and decrease on further reduction [241]. As expected, ionic transport lowers on Ti-doping [241] and increases (Fig. 1.25) with cobalt content [238]. The oxygen permeability of $Sr_{1-x}La_xFeO_{4-\delta}$ is low [243] and close to that of brownmillerite-type $CaFe_{0.5}Al_{0.5}O_{3-\delta}$ (Table 1.4). The permeation fluxes through $Sr_{2.7}La_{0.3}Fe_{2-x}Co_xO_{7-\delta}$ [238] and $Sr_3LaFe_{3-x}Co_xO_{10-\delta}$ [239] are significantly higher and close to those of perovskite-type ferrites (Table 1.3). The oxygen permeability for a fixed n increases when concentrations of strontium [238] and cobalt [239,243] increase. The apparent activation energy of permeation flux in $Sr_{2.7}La_{0.3}Fe_{2-x}Co_xO_{7-\delta}$ and $Sr_3LaFe_{3-x}Co_xO_{10-\delta}$ systems varies from 60-110 kJ/mol [238,239].

After Balachandran et al. [166] report on high oxygen permeation through $SrFeCo_{0.5}O_{3+\delta}$-based membranes (Table 1.4), $Sr_{4-x}Ca_xFe_{6-y}Co_yO_{13\pm\delta}$ has been extensively studied [167,244]. The crystal

structure of the parent phase, $Sr_4Fe_6O_{13\pm\delta}$, is orthorhombic (space group Iba2, no. 45). It consists of alternating perovskite layers $[Sr_4Fe_2O_8]^{2-}$, where iron cations are in octahedral oxygen coordination, and $[Fe_4O_5]^{2+}$ layers containing two types of FeO_5 polyhedra – tetragonal pyramids and trigonal bipyramids. Every kind of pyramids shares edges among themselves only. Polyhedra of different kinds are connected to each other by sharing corners (Fig. 1.26).

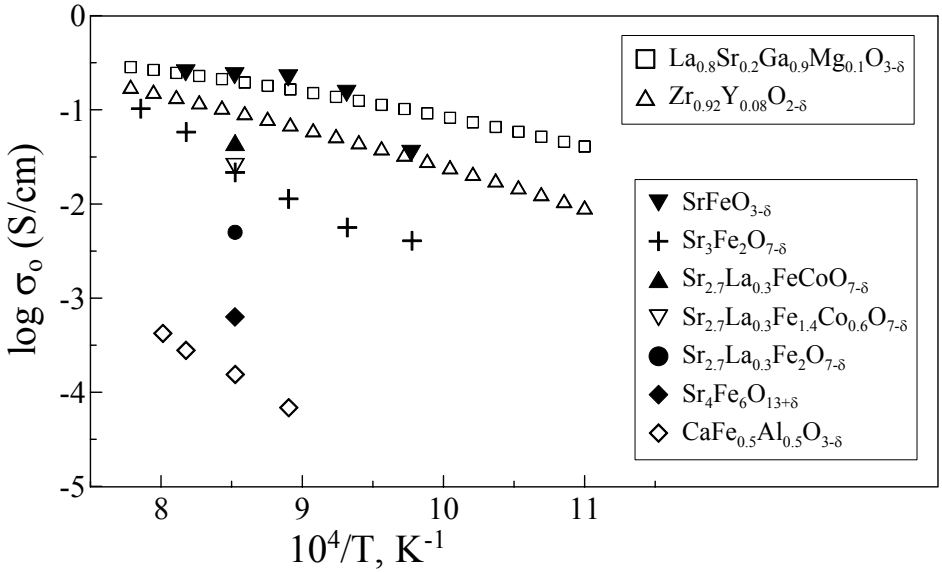

Fig. 1.25. The oxygen ionic conductivity of iron-based oxides [234,235,238,241] compared with that of LSGM [106] and 8YSZ [58].

The substitution of strontium with smaller calcium decreases the unit cell volume, as well as incorporation of cobalt into the Fe-sublattice. The $Sr_4Fe_6O_{13}$-type structure is stable for $0 \le x \le 3.2$, and $CaFe_2O_4$ is formed if the calcium content is higher. Moreover, the solubility of Ca^{2+} decreases on Co-doping [244]. $Sr_4Fe_{6-y}Co_yO_{13\pm\delta}$ materials are single-phase at low cobalt concentration, but are multiphase for y > 1.5-1.8 when they consist of $Sr_4Fe_6O_{13}$-type intergrowth, $SrFe_{1-z}Co_zO_{3-\delta}$ perovskite and a trace amount of the spinel phase $Co_{3-w}Fe_wO_4$ [243,245]. The perovskite fraction increases with growing cobalt content, so that y = 2.4 composition yields only $SrFe_{1-z}Co_zO_{3-\delta}$ and $Co_{1-w}Fe_wO$ [246]. Note that phase relationships in $Sr_4Fe_{6-y}Co_yO_{13\pm\delta}$ system are quite complex and very sensitive to temperature changes [237,247]. Attempts to substitute Sr^{2+} with Ba^{2+} or La^{3+} give the impurity phases $SrBaFe_4O_8$ or $Sr_{1-x}La_xFeO_{3-\delta}$, correspondingly. Though a considerable amount of iron can be replaced

by Co, incorporation of Ti, Cr, Mn, Ni, Cu, Al and Ga all results in the formation of the perovskite-type phase with $SrFe_{12}O_{19}$ and binary oxides [244,248].

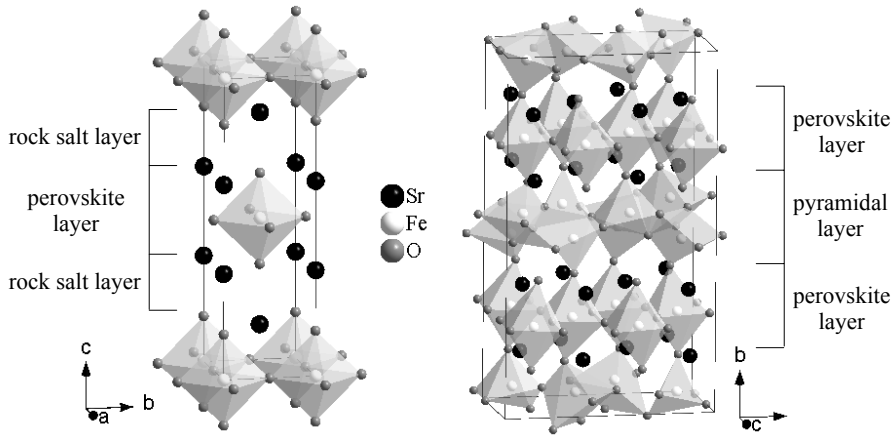

Fig. 1.26. Crystal structures of the K_2NiF_4- (left) and $Sr_4Fe_6O_{13}$-type (right) phases.

The $Sr_4Fe_6O_{13}$-based oxides are hyperstoichiometric in air, and B-site cations are tri- and tetravalent, though oxygen excess decreases with Ca- and Co-doping [244,246]. Most Fe^{4+} is situated in pyramidal layers [249]. The concentration of holes and therefore the electronic conductivity in $Sr_4Fe_6O_{13\pm\delta}$ is considerably lower with respect to $SrFeO_{3-\delta}$ and $Sr_3Fe_2O_{7-\delta}$ [234]. Substitution of iron with cobalt increases the electrical transport (Fig. 1.24). Contrary to perovskite-type $Sr_{1-x}Ca_xFeO_{3-\delta}$, calcium incorporation has also a positive effect on the conductivity [244]. The mobility of holes in $Sr_4Fe_6O_{13\pm\delta}$ and $Sr_3Fe_2O_{7-\delta}$ (0.005-0.02 $cm^2\ V^{-1}\ s^{-1}$ at 923-1223 K) is consistent with the small-polaron hopping mechanism [234]. As expected for p-type conduction, the electrical transport of $Sr_4Fe_6O_{13\pm\delta}$ in oxidizing conditions decreases on decreasing $p(O_2)$. The values of the Seebeck coefficient of $Sr_{4-x}Ca_xFe_6O_{13\pm\delta}$ are positive in air [244]. In reducing atmospheres, n-type electronic conductivity dominates [248].

Relatively high values of the oxygen ionic transport were reported for Co-doped $Sr_4Fe_6O_{13\pm\delta}$ (e.g., 8 S/cm at 1173 K for $Sr_4Fe_{4.8}Co_{1.2}O_{13\pm\delta}$ in air). Ionic conduction increases with cobalt concentration [167]. In the presence of hyperstoichiometric oxygen, the diffusion of interstitial oxide ions is expected to dominate and occur mainly in the pyramidal layers, where 5-coordinated Fe^{3+} may easily oxidize towards 6-coordinated Fe^{4+} [246]. In the oxygen-deficient state, vacancy migration (also within non-perovskite slab) governs the level of ionic conductivity [234]. Apparently, oxygen transport

is two-dimensional, confined to the *ac* plane. The mobility of vacancies seems to be lower than that of interstitials, since $Sr_4Fe_6O_{13\pm\delta}$ shows poor ionic conduction in reducing conditions (Fig. 1.25). Note that oxygen transport in $Sr_4Fe_{6-y}Co_yO_{13\pm\delta}$ materials is very sensitive to the presence of perovskite-type $SrFe_{1-z}Co_zO_{3-\delta}$ impurity phase and increases with its amount [243]. Hence, oxygen permeation through $Sr_4Fe_{6-y}Co_yO_{13\pm\delta}$ membranes increases upon cobalt incorporation (Table 1.4) and perovskite segregation [243-245]. In particular, high values of oxygen flux for $SrFeCo_{0.5}O_{3+\delta}$ ceramics [166] might be due to the phase co-existence.

Table 1.4. Oxygen fluxes through iron-based ceramic membranes.

Membrane material	T, K	d, mm	j, mol/(cm^2×s)	Gradient	Ref.
$CaFe_{0.5}Al_{0.5}O_{3-\delta}$	1223	0.6	5.8×10^{-10}	21 kPa/2.1 kPa	[235]
$CaFe_{0.5}Al_{0.5}O_{3-\delta}$	1223	1.0	3.7×10^{-10}	21 kPa/2.1 kPa	[235]
$Sr_{1.2}La_{0.8}FeO_{4-\delta}$	1173	1.5	3.7×10^{-10}	21 kPa/10 Pa	[243]
$Sr_3Fe_2O_{7-\delta}$	1173	1.5	3.5×10^{-8}	air/He	[238]
$Sr_{2.7}La_{0.3}Fe_2O_{7-\delta}$	1173	1.5	2.0×10^{-8}	air/He	[238]
$Sr_{2.7}La_{0.3}Fe_{1.4}Co_{0.6}O_{7-\delta}$	1173	1.5	5.0×10^{-8}	air/He	[238]
$Sr_{2.7}La_{0.3}FeCoO_{7-\delta}$	1173	1.5	7.5×10^{-8}	air/He	[238]
$Sr_3LaFe_3O_{10-\delta}$	1173	1.5	3.0×10^{-8}	air/He	[239]
$Sr_3LaFe_{2.5}Co_{0.5}O_{10-\delta}$	1173	1.5	4.0×10^{-8}	air/He	[239]
$Sr_3LaFe_2CoO_{10-\delta}$	1173	1.5	1.0×10^{-7}	air/He	[239]
$Sr_3LaFe_{1.5}Co_{1.5}O_{10-\delta}$	1173	1.5	1.5×10^{-7}	air/He	[239]
$Sr_4Fe_6O_{13\pm\delta}$	1173	1.85	4.0×10^{-10}	21 kPa/60 Pa	[243]
$Sr_4Fe_{4.8}Co_{1.2}O_{13\pm\delta}$	1173	1.85	1.0×10^{-9}	21 kPa/60 Pa	[243]
$Sr_4Fe_{4.5}Co_{1.5}O_{13\pm\delta}$	1173	1.85	1.4×10^{-9}	21 kPa/60 Pa	[243]
$Sr_4Fe_{4.2}Co_{1.8}O_{13\pm\delta}$	1173	1.85	6.0×10^{-9}	21 kPa/60 Pa	[243]
$Sr_4Fe_4Co_2O_{13\pm\delta}$	1173	1.5	1.0×10^{-8}	21 kPa/60 Pa	[243]
$Sr_4Fe_4Co_2O_{13\pm\delta}$	1123	0.25-1.2	2.2×10^{-7}	air/(CH_4 + Ar)	[166]

1.3.4. Iron-based phases with garnet- and spinel-type structures

The crystal structure of garnet-type ferrites $A_3Fe_5O_{12}$ (A = alkaline-, rare-earth metals and Y) is quite complex (Fig. 1.27). It can be viewed as a framework of iron atoms, octahedrally- and tetrahedrally-coordinated by oxygens. The relative content of octahedral to tetrahedral sites is 2:3. Polyhedra are corner-shared, so that each tetrahedron is linked to four octahedral and each octahedron is connected to six tetrahedra. Their network creates cavities occupied by the A-site cations dodecahedrally-

coordinated by oxygen atoms (Fig. 1.27). When the A-sublattice is formed by trivalent rare-earth metals and yttrium, most iron is also trivalent as in, for instance, $Y_3Fe_5O_{12}$ [250]. The relatively low electronic conduction in such phases is therefore determined by intrinsic electronic disorder and is comparable to that of perovskite-type $NdFeO_3$ and brownmillerite-type $CaFeO_{2.5}$ (Fig. 1.24). As indicated by positive values of the Seebeck coefficient, $Y_3Fe_5O_{12}$ is a p-type semiconductor in air. However, reducing $p(O_2)$ down to 0.1-10 Pa at 1270-1570 K leads to prevailing n-type electronic transport [251]. In the system $Y_{3-2x}Ca_{2x}Fe_{5-x}V_xO_{12}$, simultaneous incorporation of calcium and vanadium increases the total concentration of charge carriers and the fraction of electrons. As a result, the conductivity increases, switching gradually from dominating p- ($0 \le x \le 0.6$) to n-type ($x > 0.6$), via a small-polaron mechanism [252]. The oxygen ionic conduction in garnets like $Y_3Fe_5O_{12}$ occurs by vacancy migration [251] and might be even lower than that of brownmillerite-type $CaFe_{0.5}Al_{0.5}O_{2.5}$ [235], considering peculiarities of garnet-type structure, where oxygen ions should diffuse over crooked pathways including alternating octahedra and tetrahedra.

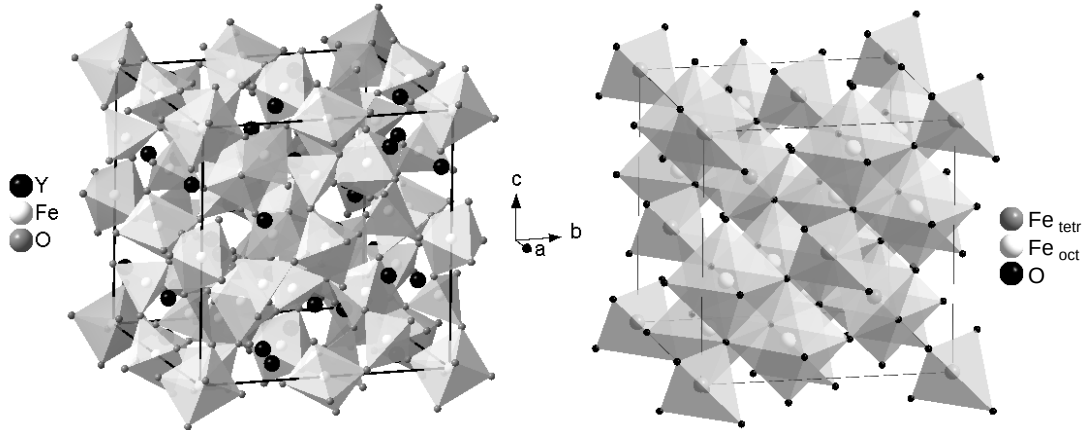

Fig. 1.27. Crystal structures of the garnet- (left) and spinel-type (right) phases.

The spinel-type crystal structure represents a cubic close-packed oxygen lattice where metals occupy 1/8 tetrahedral and 1/2 octahedral hollows. In the so-called normal spinels, like $MgAl_2O_4$, divalent cations populate tetrahedral voids, whilst trivalent ones are octahedrally-coordinated by oxygen anions. Magnetite $Fe_{3-\delta}O_4$ at room temperature is an example of the inverse spinels, since trivalent iron is equally distributed between tetrahedral and octahedral sites, and divalent cations hold

octahedral coordination (Fig. 1.27). Its formula can thus be written as $(Fe^{3+})_{tetr}[Fe^{2+}Fe^{3+}]_{oct}O_4$ [2]. Increasing temperature promotes charge disordering and leads to a random distribution above 1173-1273 K [253]. In oxidizing conditions, cationic vacancies are the only atomic defects. Iron deficiency decreases on heating and reducing oxygen pressure. As a result, interstitial cations become the major atomic defects when $\delta < 0$ [2]. Fe_3O_4 shows high n-type electronic conductivity (near 125 S/cm at room temperature in air) that increases on heating; the activation energy is about 10-20 kJ/mol. Such a fast electronic transport (via small-polaron hopping mechanism) is associated with the rapid electron exchange between Fe^{2+} and Fe^{3+} in the octahedral sublattice [2,253]. Spinel-type iron oxide can tolerate significant concentrations of various dopants, for example, Al, Cr, Mn, Co, Ni, Zn, Cd, Sn. However, any substitution deteriorates the electronic conduction of the magnetite [254-256]. In iron-based spinels, no mobile anionic defects are presumed, and existent ionic conductivity (10^{-5}-10^{-3} S/cm at 1373-1573 K in $Mn_{0.54}Zn_{0.35}Fe_{2.11}O_4$) is attributed to the cationic diffusion [256].

1.4. Final remarks

Literature data discussed above show that materials with perovskite-type structures possess an attractively high level of mixed electronic and oxygen ionic conductivity. Among these oxides, ferrites offer a promising combination of transport and thermo-mechanical characteristics, on the one hand, and relatively large $p(O_2)$ stability domain, on the other [24,153,195]. The systems $SrFe_{1-x}Al_xO_{3-\delta}$ ($0 \le x \le 0.5$) and $La_{1-x}Sr_xFe_{1-y}Ga_yO_{3-\delta}$ ($0.1 \le x \le 0.8$, $0 \le y \le 0.95$) were selected in order to evaluate an effect of incorporation of the cations with stable oxidation states on transport properties, thermal expansion and stability of the ferrite-based perovskites.

Another interesting approach discussed in Chapter 1.1.6 deals with dual-phase composites where a solid electrolyte is mixed with an electronic conductor. The resultant materials may benefit from each component to attain a desirable combination of properties, which can be still optimized by the choice of appropriate components and adjustment of their volume ratio. $(La_{0.9}Sr_{0.1})_{0.98}Ga_{0.8}Mg_{0.2}O_{3-\delta}$, from the lanthanum gallate (LSGM) family, well-known for having high oxygen ionic conductivity and stability in a wide range of oxygen pressure [20,21,106,111], was mixed with $La_{0.8}Sr_{0.2}Fe_{0.8}Co_{0.2}O_{3-\delta}$, a MIEC showing significant ionic contribution to the electrical conduction and moderate thermal expansion close to that of $(La_{0.9}Sr_{0.1})_{0.98}Ga_{0.8}Mg_{0.2}O_{3-\delta}$ [26,77,153,212], to compare the performance of these composite with that of single-phase ferrites.

Information on the ionic conduction in Fe-containing garnet-type oxides, though scarce, indicates their oxygen transport to be lower than that of analogous perovskites [251]. Hence, garnets

might be used as thin-film membranes with a porous support. $Ln_{3-x}A_xFe_{5-y}B_yO_{12-\delta}$ (Ln = Y, Gd; A = Ca, Pr, Nd; $0 \leq x \leq 0.8$, B = Co, Ni; $0 \leq y \leq 1$) system, including both acceptor- and donor-type doping, was prepared aiming to enhance the low oxygen ionic transport of $Ln_3Fe_5O_{12}$ ceramics. Particular emphasis was given to the influence of structural factors on the ionic conduction.

Another crystal structure providing mobile atomic defects with significant oxygen ionic conductivity is the fluorite-type one (Chapter 1.1.5). Yttria-stabilized zirconia (YSZ) and gadolinia-doped ceria (CGO) are conventional solid electrolytes for high- and intermediate-temperature SOFCs, respectively [96-105]. The level of the electrical transport of CGO is similar to that of LSGM [56,111], whilst YSZ exhibits lower ionic conduction [55,58]. Doped $CeO_{2-\delta}$ ceramics possess lower mechanical strength with respect to YSZ and undesirably high electronic transport at low oxygen pressures [56,100,107]. This factor constitutes a crucial disadvantage of Bi_2O_3-based solid electrolytes also, and can be accompanied with decomposition at higher $p(O_2)$ values than operating ones [57]. Development of novel phases with dominant oxygen ionic conductivity is clearly necessary. Recently, considerable ionic conduction was reported for apatite-type oxides [82-95]. Though Ge-based apatites typically exhibit faster oxygen transport than their silicium analogues, the latter materials seem to be more convenient since they are cheaper and more stable. Ceramics with general formula $La_{10-z}Si_{6-y}Al_yO_{26\pm\delta}$ ($0 \leq x \leq 0.33$, $0.5 \leq y \leq 1.5$) were prepared for the measurement of transport properties, aiming at a better understanding of the potential of such materials.

The perovskite- and fluorite-type solid electrolytes are known to incorporate some additions of iron (to enhance ceramics sinterability) without secondary phase segregation. YSZ lattice may tolerate up to 10-15 mol% of iron. At first, Fe-doping decreases slightly the electrical transport maintaining its ionic nature. When iron concentration is above 5-6 mol%, electronic conductivity increases [55]. Minor amounts (2 mol%) of iron in CGO have no considerable influence on the ionic conduction, whereas electronic transport is 8-30 times higher than in pure CGO [257]. Fe-doped LSGM (about 10 mol%) shows essentially the same total and oxygen ionic conductivity as the undoped one. Higher iron concentration results in sharp increase of the electronic transport so that the solid oxide becomes a mixed conductor [258]. $La_{9.83-x}Pr_xSi_{4.5}Fe_{1.5-y}Al_yO_{26\pm\delta}$ ($0 \leq x \leq 6$, $0 \leq y \leq 1$) and $La_{10}Si_{6-y}Fe_yO_{26\pm\delta}$ ($0 \leq x \leq 6$, $0 \leq y \leq 1$) systems were thus prepared to study the influence of iron incorporation in apatite-type electrolytes.

2. Experimental

2.1. Synthesis and ceramic processing

The chemicals used for the synthesis as starting materials were produced by Aldrich, Fluka, Merck or Riedel-de Haën companies. Two different methods were applied for ceramics synthesis: a standard solid-state route (SSR) and the glycine-nitrate processing route (GNP). The former technique is probably the most widely used tool for the preparation of polycrystalline solids by direct reaction of a mixture of chemicals, typically solid oxides [181]. Substances like carbonates, nitrates and oxalates, which can be easily transformed into oxides by moderate heating, are also used. Sometimes, oxides are dissolved in HNO_3 solution, in order to achieve higher activity and homogeneity of a reacting medium, with subsequent drying and nitrate decomposition. Stoichiometric amounts of precursors were ball-milled (zirconia balls) together and solid-state reactions were conducted in alumina crucibles, in air at 1273-1693 K, with multiple intermediate grinding steps, until constant phase composition of the resulting material. Before weighing, oxides were calcined in air: SiO_2 – at 873 K, Ga_2O_3, La_2O_3 and Gd_2O_3 – at 1273-1473 K.

Perovskite-type $La_{1-x}Sr_xFe_{1-y}Ga_yO_{3-\delta}$ ($0.1 \leq x \leq 0.8$, $0 \leq y \leq 0.95$) oxides were synthesized using La_2O_3, Ga_2O_3, $SrCO_3$ and $FeC_2O_4 \cdot 2H_2O$. The starting chemicals were firstly dissolved in an aqueous solution of nitric acid, dried and annealed to form fine powders. A similar procedure was carried out to prepare garnet-like $Ln_{3-x}A_xFe_{5-y}B_yO_{12-\delta}$ (Ln = Y, Gd; A = Ca, Pr; B = Co, Ni; $0 \leq x, y \leq 1$) phases, starting from Gd_2O_3, Pr_6O_{11}, $Y(NO_3)_3 \cdot 6H_2O$, $Nd(NO_3)_3 \cdot 6H_2O$, $Ca(NO_3)_2 \cdot 4H_2O$, $Fe(NO_3)_3 \cdot 9H_2O$, $Co(NO_3)_2 \cdot 6H_2O$ and $Ni(NO_3)_2 \cdot 6H_2O$. To obtain the $La_{10-x}Si_{6-y}Al_yO_{26\pm\delta}$ ($0 \leq x \leq 0.33$, $0.5 \leq y \leq 1.5$), $La_{9.83}Si_{4.5}Fe_{1.5-y}Al_yO_{26\pm\delta}$ ($0 \leq y \leq 1$), $La_{10-x}Si_{6-y}Fe_yO_{26\pm\delta}$ ($0 \leq x \leq 0.67$, $1 \leq y \leq 2$), $La_7Sr_3Si_6O_{25.5\pm\delta}$ and $La_6Sr_3Si_6O_{24\pm\delta}$ apatites, La_2O_3 and SiO_2 were mixed with nitrates $Sr(NO_3)_2$, $Al(NO_3)_3 \cdot 9H_2O$ and $Fe(NO_3)_3 \cdot 9H_2O$ in one agate mortar before reaction (temperatures of synthesis are listed in Table 2.1).

GNP is a self-combustion method using glycine (NH_2CH_2COOH) as fuel and nitrates of metal components as oxidant. This technique is known as especially appropriate for the synthesis of multicomponent oxide compounds when the solid-state reaction is stagnated due to kinetic reasons [259]. A precursor is made by combining glycine with metal nitrates in specific ratios for different materials, in an aqueous solution. In our work, the glycine/nitrate molar ratio was twice the stoichiometric one, calculated assuming that the only gaseous products of reaction are N_2, CO_2 and H_2O. Aqueous solutions were heated on a hot-plate to evaporate excess water yielding a viscous liquid, that finally auto-ignites. The combustion is rapid and results in a fine powder having foam-like structure. To remove residual organic substances, powders were annealed at 1273 K for 2 hours in air.

In such a way, perovskite-like $SrFe_{1-x}Al_xO_{3-\delta}$ ($0.1 \leq x \leq 0.5$) were obtained from $Sr(NO_3)_2$, $Fe(NO_3)_3 \cdot 9H_2O$, $Al(NO_3)_3 \cdot 9H_2O$. Garnet-type $Y_{2.5}Nd_{0.25}Ca_{0.25}Fe_5O_{12-\delta}$ and $Y_{2.5}Ca_{0.5}Fe_4NiO_{12-\delta}$ were also synthesized by GNP from $Y(NO_3)_3 \cdot 6H_2O$, $Nd(NO_3)_3 \cdot 6H_2O$, $Ca(NO_3)_2 \cdot 4H_2O$, $Fe(NO_3)_3 \cdot 9H_2O$ and $Ni(NO_3)_2 \cdot 6H_2O$, since attempts to attain single-phase powders via SSR failed. To prepare $La_{3.83}Pr_6Si_{4.5}Fe_{1.5}O_{26\pm\delta}$ and $La_{6.83}Pr_3Si_{4.5}Fe_{1.5}O_{26\pm\delta}$ apatites, Pr_6O_{11} was dissolved in an aqueous solution of nitric acid with $La(NO_3)_3 \cdot 6H_2O$, $Fe(NO_3)_3 \cdot 9H_2O$, glycine and highly dispersed SiO_2 additions. Then the mixtures were dried and fired.

Table 2.1. Temperature ranges of synthesis and sintering.

Composition	Method	Temperature range, K	
		Synthesis	Sintering
$La_{1-x}Sr_xFe_{1-y}Ga_yO_{3-\delta}$	SSR	1473-1643	1523 - 1873
$SrFe_{1-x}Al_xO_{3-\delta}$	GNP	–	1523 - 1623
$Ln_{3-x}A_xFe_{5-y}B_yO_{12-\delta}$	SSR	1273 - 1693	1493 - 1743
$Y_{2.5}Nd_{0.25}Ca_{0.25}Fe_5O_{12-\delta}$	GNP	–	1543
$Y_{2.5}Ca_{0.5}Fe_4NiO_{12-\delta}$	GNP	–	1543
$La_{10-x}Si_{6-y}Al_yO_{26\pm\delta}$	SSR	1273 - 1473	1923 - 1973
$La_{9.83}Si_{4.5}Fe_{1.5-y}Al_yO_{26\pm\delta}$	SSR	1273 - 1473	1873
$La_{10-x}Si_{6-y}Fe_yO_{26\pm\delta}$	SSR	1273 - 1473	1773 - 1873
$La_{7-x}Sr_3Si_6O_{25.5\pm\delta}$	SSR	1273 - 1473	1873
$La_{9.83-x}Pr_xSi_{4.5}Fe_{1.5}O_{26\pm\delta}$	GNP	–	1873

$(La_{0.9}Sr_{0.1})_{0.98}Ga_{0.8}Mg_{0.2}O_{3-\delta}$ – $La_{0.8}Sr_{0.2}Fe_{0.8}Co_{0.2}O_{3-\delta}$ (LSGM-LSFC) composites were produced using commercial powders of LSGM and LSFC (Praxair Speciality Chemicals, Seattle). Taking into account that the fraction of ion-conducting phase is critical for the oxygen transport [77], the selected LSGM/LSFC ratio was 60:40 wt%. To study the influence of the interaction between initial phases on the composite properties, the LSGM-LSFC mixtures were prepared by different procedures. One series of composite ceramics, marked as LL, was fabricated via ball-milling of the commercial powders for 6 hours in ethanol (Method 1). For another series (LLc), the LSGM powder was coarsened by annealing at 1423 K during 4 hours and then mixed with LSFC powder in an agate mortar (Method 2). Fig. 2.1 compares SEM micrographs of LSGM-LSFC powders obtained by these two techniques.

All prepared powders were uniaxially pressed (stainless steel moulds, 120-400 MPa) into disks and rods, and sintered in air during 1-50 hours. The sintering temperatures are given in Tables 2.1 and

2.2. After sintering, the samples were annealed at 1173-1273 K in air and then furnace-cooled in order to achieve oxygen nonstoichiometry at low temperatures as close to the equilibrium as possible. Gas-tightness of ceramic pellets (thickness of 0.6-1.4 mm) was validated by the absence of argon leakage through them under positive pressure (0.1-0.2 MPa) of argon applied to one side. Electrode layers were applied, if needed, by a brush using platinum paste (Engelhard, Platinum Ink 6926), further annealed at 1273 K in air for 1 hour. The experimental density was measured by the picnometric procedure in n-butanol at 293 K, using the usual formula:

$$d^{293} = \frac{d_b^{293} m}{m + m_1 - m_2} \qquad (2.1)$$

where d_b^{293} - n-butanol density at 293 K (0.8098 g/cm^3), m – weight of sample, m_1 – weight of the picnometer with n-butanol, m_2 – weight of the picnometer with n-butanol and sample.

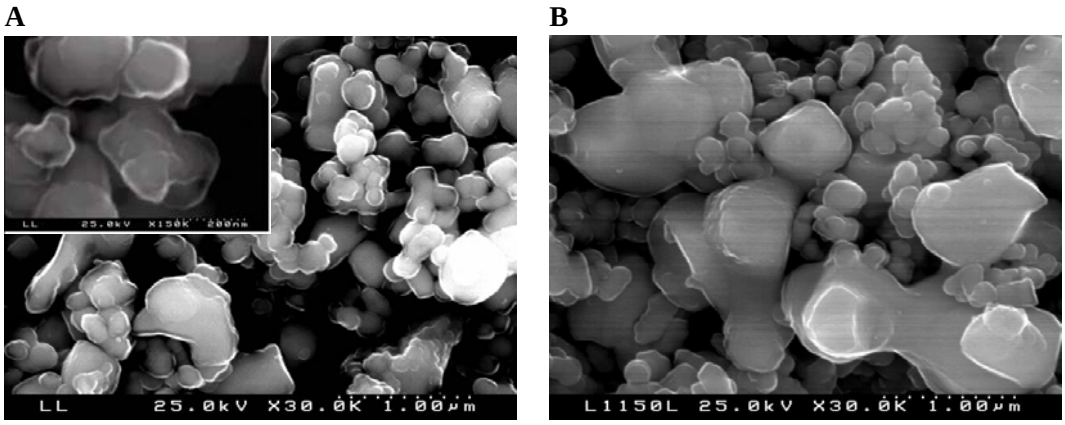

Fig. 2.1. SEM micrographs of LSGM-LSFC powders obtained by Method 1 (A) and 2 (B).

Table 2.2. Abbreviations and sintering conditions of LSGM-LSFC composites.

Abbreviation	Pre-annealing of LSGM		Sintering		Gas-tightness
	T, K	Time, h	T, K	Time, h	
LL1240	–	–	1513	1	–
LL1320	–	–	1593	1	+
LLc1320	1423	4	1593	1	+
LL1410	–	–	1683	4	+
LLc1410	1423	4	1683	4	+

2.2. X-ray diffraction, Mössbauer spectroscopy and chemical analysis

The phase composition was studied by X-ray powder diffraction (XRD). Data were collected at room temperature (Rigaku D/Max-B diffractometer, CuK_α radiation) within 2Θ-range of 10-100°, 2Θ-step of 0.02° and counting time of 1-5 s/step. For structural identification, the JCPDS (International Centre for Diffraction Data) database was used. The crystal lattice parameters were refined employing the least-square Rietveld powder profile Fullprof program [260] and used, in particular, to calculate the theoretical density:

$$d_{theor} = \frac{N_U M}{N_A V} \qquad (2.2)$$

where N_U – number of formula units per elementary cell, M – molar weight, N_A – Avogadro constant, V – elementary cell volume.

A pseudo-Voigt profile shape function, $K_{\alpha1}/K_{\alpha2}$ intensities ratio of 0.5, and a factor of 0.7998 for the monochromator polarization correction were used. The background was refined with a polynomial function.

The local structure of iron-containing oxides was also examined by ^{57}Fe Mössbauer spectroscopy (MS), in framework of collaborative work with Dr. J.C. Waerenborgh and Dr. D.P. Rojas, Chemistry Department of the Technological and Nuclear Institute, Sacavem. Data were acquired at room temperature in the transmission mode using a conventional constant-acceleration spectrometer from Wissenchaftliche Elektronik (Wissel) composed of a MA-260 velocity transducer and MRG-500 drive. A Reuther Stokes P3-1605-261 proportional counter and Canberra electronic modules for γ-radiation and data collection were used. The γ-radiation source was a Wissel 25 mCi ^{57}Co source in a Rh matrix; the velocity scale was calibrated using α-Fe foil. The absorbers were obtained by pressing the powdered samples (about 5 mg of natural Fe/cm^2) into Perspex holders. The spectra were fitted to Lorentzian lines using a non-linear least-square method. The width and areas of both peaks in each quadrupole doublet were kept equal during refinement. The distributions of quadrupole splittings (QS) were fitted according to the histogram method [261].

The chemical composition of synthesized phases was confirmed by inductively coupled plasma (ICP) spectroscopic analysis with a Jobin Yvon (model JY 70 Plus) spectrometer. The deviation of the determined cationic composition from the expected one was lower than 1 at%.

2.3. Microstructural studies

The samples for microstructural studies were usually polished using silicon carbide sand papers #400-#2400 (Struers) and diamond pastes of 0.25-15 μm grade (Cafro). The polishing was manual or

employing a Buehler Metaserv 2000 grinder/polisher (50-500 rpm). The samples were glued to a holder with conductive carbon cement (Neubauer Chemikalien). Then a uniform carbon powder layer was sputtered over the samples (Emitech K950 evaporator). The microstructure of polished or cracked ceramics was studied by scanning electron microscopy (SEM) using a Hitachi S-4100 microscope equipped with (i) a Rontec UHV Detection system for the energy dispersive x-ray spectroscopy (EDS) analysis and (ii) Robinson detector controle module to acquire micrographs in a back-scattering mode. The electron beam voltage is 25 kV; the microscope magnifies items by 40-300000 times; the resolution varied from 100 nm to 1000 μm, allowing the observation of objects in the 10^{-2}-10^{2} μm range. EDS provides elemental identification with 0.1-1 wt% precision depending on element and matrix. Targets as small as about 1×1 μm can be analyzed.

2.4. Dilatometry and thermal analysis

Thermal expansion and shrinkage were measured in alumina Linseis L75 (vertical) and DIL 801L (horizontal) dilatometers with a constant heating rate of 5-10 K/min in air, from 300-1300 K. The temperature was controlled using one B-type thermocouple (PtRh6%-PtRh30%) with accuracy of ± 0.1 K, whilst the resolution of the elongation sensor was 50 nm. The instrument error was lower than 0.05×10^{-6} K^{-1}. The thermal expansion coefficients (TECs) were calculated from dilatometric curves via a least-square method.

The thermogravimetric and differential thermal analysis (TGA-DTA) were conducted in the Setaram Labsys TGA-DTA/DSC analyzer, from 300-1300 K in flowing air with a constant heating and cooling rate of 5-10 K/min. One of two symmetrical alumina crucibles was filled with the sample powder (~50 mg); the other crucible contained alumina powder, used as a reference. The temperature was controlled using one B-type thermocouple with accuracy of ± 0.1 K.

2.5. Measurements of the total electrical conductivity and Seebeck coefficient

The total conductivity (TC) of ceramic bars (~ 4×4×15 mm) was measured by a 4-probe DC technique in air (Agilent E3640A DC power supply and Agilent 34401A voltmeter). The electrical transport of pellet-shaped solid oxides (~ 1 mm of thickness and ~10 mm of diameter) was determined by AC impedance spectroscopy in flowing 10% H_2 – 90% N_2 mixture, argon or air, employing one HP4284A precision LCR meter (20 Hz – 1 MHz). The studies were carried out in alumina sample holders with platinum wires and samples with deposited platinum electrodes. The temperature varied from RT to 1300 K and was measured using B- or K-type (chromel NiCr10% – alumel NiAl5%) thermocouples

with accuracy of ± 0.5 K. The oxygen partial pressure in the measuring chamber (for flowing 10% H_2 – 90% N_2 mixture or argon) was monitored by an YSZ oxygen sensor.

The isothermal measurements of total conductivity and Seebeck coefficient (SC) as a function of the oxygen partial pressure (10^{-16}-10^{5} Pa) were performed at 973-1223 K in an YSZ cell comprising one electrochemical oxygen pump and sensor, with Yokogawa 7651 DC sources and Philips PM 2534 multimeter (Fig. 2.2). The ceramic bar (~ 2×3×15 mm) for thermopower studies was located along the cell natural temperature gradient (~ 15 K/cm). For the total by 4-probe DC conductivity measurements by 4-probe DC, the second sample (~ 3×4×15 mm) was placed perpendicular to this orientation near the middle of the Seebeck coefficient sample. Platinum wires were used as connectors; the temperature was determined using B-type thermocouples with accuracy of ± 0.5 K.

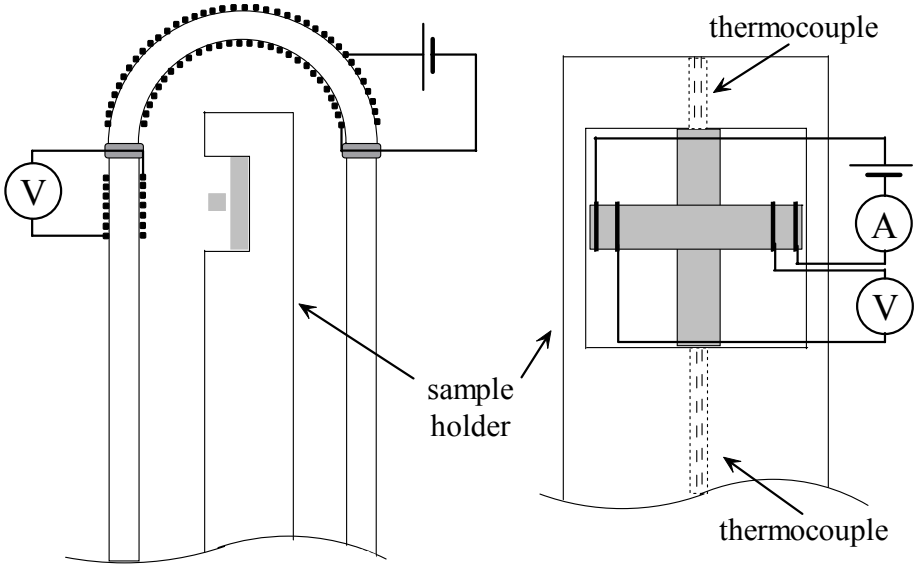

Fig. 2.2. Set-up for the measurements of total conductivity and Seebeck coefficient as a function of the oxygen pressure.

Before heating, the cell was filled with a 50% O_2 – 50% CO_2 mixture. This gas composition ensures improved oxygen sensor performance within an extended oxygen pressure range, based on the combined role of the couple CO/CO_2 in gas phase transport and surface equilibrium with the surrounding atmosphere during redox cycles. The measurements were conducted in the decreasing $p(O_2)$ mode. Data points were obtained upon achievement of equilibrium between the sample and

ambient: the conductivity change should be less than 0.1% and the Seebeck coefficient variation should be inferior to 0.005 μV/K per minute. The conductivity relaxation time varied up to dozens of hours, depending on oxygen pressure, temperature and sample composition. After a desired low $p(O_2)$ limit was achieved, data readings were interrupted until the starting high $p(O_2)$ limit was reached, where the measurements were repeated in order to verify reversibility of the results, before the cell was brought to the next temperature. The experimental error for both the electrical conductivity and thermopower is lower than 1-2%.

The conductivity values were calculated from:

$$\sigma = \frac{L}{R_{AC} S_A} \tag{2.3}$$

$$\sigma = \frac{I_1 + I_2}{V_1 - V_2} \frac{L}{S_A} \tag{2.4}$$

where L – sample length; R_{AC} – sample resistance; S_A – sample cross area; V_1, V_2, I_1 and I_2 – voltage drop over the sample and current, for each of two opposite current directions. The activation energy was calculated using the standard Arrhenius equation (1.66).

2.6. Measurements of oxygen permeability

The oxygen permeability (OP) of gas-tight ceramic membranes (0.6-1.4 mm of thickness and ~10 mm of diameter) was studied using YSZ cells comprising one electrochemical oxygen pump and one sensor, with platinum wires as contacts. The YSZ disk, sintered from commercially available powder (Tosoh) at 1873 K, with platinum electrodes was used as pump with both surfaces connected to Agilent E3640A or Yokogawa 7651 DC sources. The YSZ tube with platinum electrodes, both internally and externally, was used as potentiometric sensor, being connected to a Fluke 45 voltmeter. The electromotive force (EMF) was determined using air as a reference atmosphere outside the cell.

In order to minimize the possible influence of the pump current on sensor readings, one additional YSZ ring was inserted between pump and sensor. During fabrication of these cells, pieces were furthermore insulated from each other by a layer of the high-temperature sealant. The samples were hermetically glued on the sensor top by another high-temperature sealant with lower melting point (Fig. 2.3A). The measurements were carried out at 973-1273 K, and temperature was controlled using K- or B-type thermocouples with accuracy of ± 0.5 K. At these temperatures, the resistance between cell units was higher than 1 MOhm. The oxygen permeation of the cell with one YSZ disk sealed instead of the sample membrane was determined; the electrochemical equivalent of such a

leakage was lower than 1 μA. Before sealing a sample, oxygen was pumped in the measuring cells in order to avoid possible gas diffusion stagnation due to the presence of nitrogen in their small volume. The samples were finally sealed upon reaching sensor readings corresponding to the oxygen pressure inside the cell (~ 100 kPa). Then the set-up was cooled down to the desired temperature, and current was applied to the pump resulting in decreasing oxygen pressure in the cell.

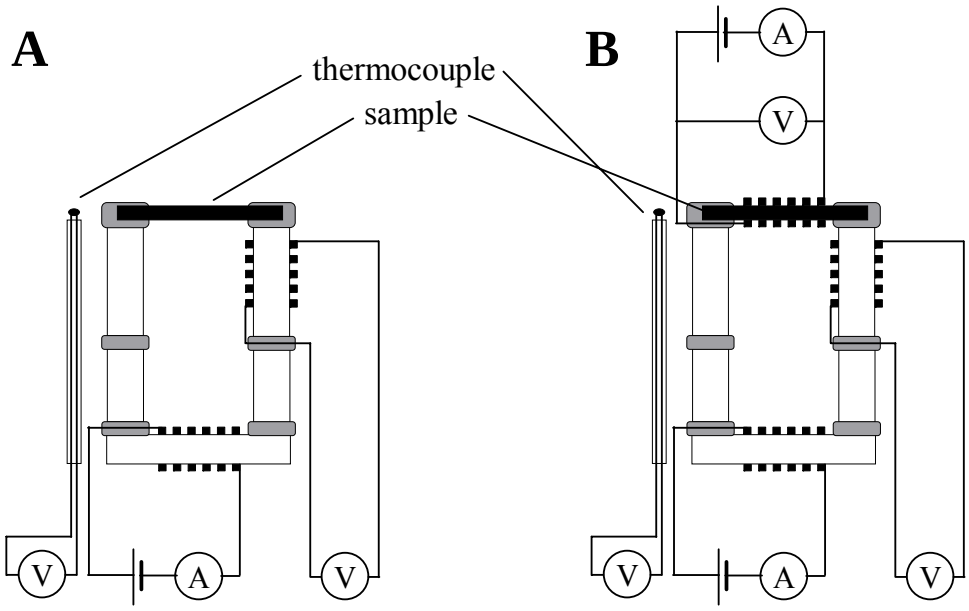

Fig. 2.3. Electrochemical YSZ cells with platinum electrodes for measurements of (A) oxygen permeability and (B) faradaic efficiency (see text).

Upon reaching steady state conditions, the current through the pump corresponds to the oxygen ionic flux across the sample:

$$j = \frac{I_{pump}}{4FS} \qquad (2.5)$$

where j is the permeation flux density (mol cm^{-2} s^{-1}), F is the Faraday constant (96484.56 C mol^{-1}), S is the effective area of the membrane surface exposed for oxygen permeation (cm^2) and I is the electrical current applied to the pump for a given EMF, related to the oxygen pressure inside the cell by the Nernst law:

$$E_{sensor} = \frac{RT}{4F} \ln \frac{p_2}{p_1} \qquad (2.6)$$

where R is the molar gas constant, F is the Faraday constant, T is the sample temperature (K), p_2 is the oxygen pressure at the membrane feed side (21 kPa) and p_1 is the oxygen pressure at the membrane permeate side ($p_2 > p_1$).

The specific oxygen permeability $J(O_2)$ (mol s^{-1} cm^{-1}) and j are interrelated [7]:

$$J(O_2) = jd\left[\ln\frac{p_2}{p_1}\right]^{-1} \tag{2.7}$$

where d is the membrane thickness. $J(O_2)$ can also be determined as [151]:

$$J(O_2) = \frac{RT}{16F^2}\frac{d}{S}\frac{I_{pump}}{E_{sensor}} \tag{2.8}$$

Permeation measurements were performed at $E_{sensor} < 100$ mV (0.1 kPa < p_1 < 21 kPa) to avoid excessively reducing conditions and gas diffusion limitations inside the cell. About five data points, corresponding to different values of oxygen pressure gradient, were taken for every temperature. The time necessary to attain the steady state conditions for each data point varied up to ten hours, depending on oxygen pressure gradient, temperature and sample composition. The experimental error for the permeation flux density and specific oxygen permeability was lower than 15%.

When the permeation flux is limited by the bulk ambipolar conductivity (Chapter 1.1.3), the oxygen ionic transference numbers can be calculated from the Wagner equation (1.42) and permeability data (for a relatively small oxygen pressure gradient):

$$\sigma_{amb} = t_O(1-t_O)\sigma = \frac{16F^2d}{RT}\left(\frac{\partial j}{\partial \ln(p_2/p_1)}\right)_{p_1\to p_2} = 4Fd\left(\frac{\partial j}{\partial E_{sensor}}\right)_{E_{sensor}\to 0} \tag{2.9}$$

$$t_O = \frac{1}{2} - \frac{1}{2}\sqrt{1-4\frac{\sigma_{amb}}{\sigma}} \tag{2.10}$$

2.7. Faradaic efficiency studies

The faradaic efficiency (FE) technique was used as a principal method to determine partial oxygen ionic and electronic conductivities. The measuring cell is identical to that of oxygen permeation studies, except for the platinum electrodes on both surfaces of a sample (Fig. 2.3B). The sealing procedure is the same, and the Yokogawa 7651 DC sources and Fluke 45 voltmeter were also used. In the course of the measurements, the oxygen permeation fluxes through the membrane were first defined at the required permeate-side oxygen pressures. The oxygen was removed from the cell by the pump, while the current through the sample was zero. After E_{sensor} became time-independent, the

permeation flux J (mol s^{-1}) for the given T and p_1 is proportional to the current through the oxygen pump:

$$J = \frac{I'_{pump}}{4F} \tag{2.11}$$

Then a current was applied to the sample in order to deliver oxygen into the cell, and the pump current was changed to maintain the same E_{sensor}. After reaching steady state conditions, the oxygen ionic flux through the pump is equal to the sum of the oxygen fluxes driven through membrane by the chemical and electrical potential gradients:

$$\frac{I_{pump}}{4F} = \frac{I'_{pump}}{4F} + \frac{t_O I_{sample}}{4F} \tag{2.12}$$

Oxygen ionic transference numbers at the given E_{sensor} can be therefore calculated as:

$$t_O = \frac{I_{pump} - I'_{pump}}{I_{sample}} \tag{2.13}$$

In air, t_O was measured under the condition $E_{sensor} = 0$. Since $I'_{pump} = 0$ in this case then:

$$t_O^{air} = \frac{I_{pump}}{I_{sample}} \tag{2.14}$$

Determined transference numbers are valid only if the effect of the electrode process on the electrical transport is negligible. When the electrode polarization is significant, the corresponding overpotential deviates the measured t_O from the true value. The apparent transference number is thus [262]

$$t_O^{obs} = \frac{I_o}{I_{total}} = \frac{R_e}{R_e + R_o + R_\eta} \tag{2.15}$$

whereas the true oxygen ionic transference number is defined as:

$$t_O = \frac{R_e}{R_e + R_o} \tag{2.16}$$

Substituting (2.15) into (2.16) and considering:

$$R_{AC} = \frac{R_e R_o}{R_e + R_o} \tag{2.18}$$

$$R_{DC} = R_e + R_o + R_\eta \tag{2.19}$$

the following equation was obtained:

$$t_O = 1 - \frac{R_{AC}}{R_{DC}}(1 - t_O^{obs}) = 1 - \frac{R_{AC} I_{sample}}{U_{sample}}(1 - t_O^{obs}) \tag{2.20}$$

where R_{AC} values were determined by AC impedance spectroscopy using one HP4284A precision LCR meter (20 Hz – 1 MHz). The studies of the oxygen ionic transference numbers via this modified FE technique were carried out at 973-1273 K and $E_{sensor} < 100$ mV (0.1 kPa < p_1 < 21 kPa). The relaxation time periods were similar to those of oxygen permeation studies. The values of voltage applied to a sample varied from 0 to 200 mV; the pump and sample currents were in the range 0-20 mA. Several data points were measured for each t_O value. In the studied voltage range, the transference numbers were current-independent within the limits of experimental error (< 1%).

2.8. Modified electromotive force (e.m.f.) technique

Whilst FE allows measurements of oxygen ionic transference numbers under zero or small oxygen pressure gradients, the e.m.f. method enables t_O determination under large $p(O_2)$ gradients, for example, air/H_2. The measuring cell consists of a sample membrane (with platinum electrodes on both surfaces), hermetically sealed onto the YSZ oxygen sensor (which in turn is sealed onto the long YSZ tube), thus separating two gas atmospheres (Fig. 2.4).

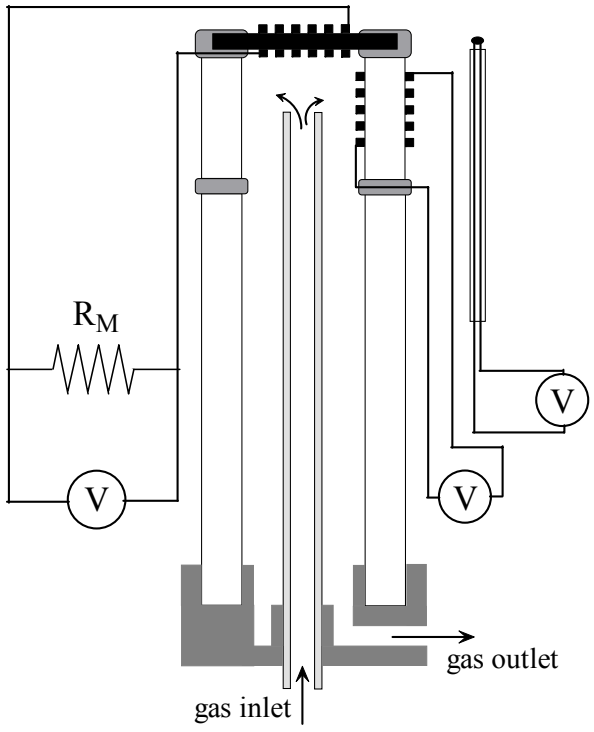

Fig. 2.4. E.m.f. set-up (see text).

One side of the membrane was always exposed to the atmospheric air, whereas different gases (10% H_2 – 90% N_2 mixture, argon or oxygen) were continuously supplied (200-250 ml/min) to the other side via a thin alumina tube. The gas fluxes were measured by Bronkhorst mass flow controllers. The studies were carried out at 973-1273 K, and temperature was controlled using K- or B-type thermocouples with accuracy of ± 0.5 K. Platinum wires were used as connectors, and voltages were measured by the Fluke 45 multimeter.

The potential of an electrochemical cell O_2 (p_2), Pt | sample | Pt, O_2 (p_1) can be calculated using Wagner and Nernst equations:

$$E_{sample} = \frac{RT}{4F}\int_{\ln p_1(O_2)}^{\ln p_2(O_2)} t_O \, d\ln p(O_2) = \overline{t_O}\frac{RT}{4F}\ln\frac{p_2}{p_1} = \overline{t_O}E_{sensor} \qquad (2.21)$$

where $\overline{t_O}$ is the oxygen transference number averaged for a given $p(O_2)$ gradient. Again, non-negligible electrode polarization leads to underestimated t_O values. Considering the equivalent circuit showed in Fig. 2.5A, $E_{theor} = E_{sensor}$, $E_{obs} = E_{sample}$ and equations (2.15) and (2.21):

$$\frac{E_{sensor}}{E_{sample}} - 1 = \left(R_o + R_\eta\right)\frac{1}{R_e} \qquad (2.22)$$

When an external variable resistance (R_M) is added to the circuit (Fig. 2.5B) E_{sample} can be measured as a function of such a simulated and enhanced electronic conductivity. In this case [262],

$$\frac{E_{sensor}}{E_{sample}} - 1 = \left(R_o + R_\eta\right)\left[\frac{1}{R_e} + \frac{1}{R_M}\right] \qquad (2.23)$$

At low overpotentials, when the overpotential-current trend is linear, the dependence ($E_{sensor}/E_{sample} - 1$) versus $1/R_M$ is also linear with a slope of ($R_o + R_\eta$). The intercept of this line over the ($1/R_M$) axis is equal to ($-1/R_e$), and R_e values can be calculated by fitting data to the linear model:

$$\frac{E_{sensor}}{E_{sample}} - 1 = A\left(\frac{1}{R_M}\right) + B \qquad (2.24)$$

where A and B are regression parameters and R_e = A/B. Taking into account equations (2.16) and (2.18) the oxygen transference numbers are found as

$$t_O = 1 - \frac{R_{AC}}{R_e} \qquad (2.25)$$

where R_{AC} values were determined by AC impedance spectroscopy. The R_M resistances varied from (2-5)R_{AC} to 100 kOhm. Every t_O value was determined using 5-7 data points each requiring up to several hours for equilibrium. The experimental error of t_O measurements was lower than 1%.

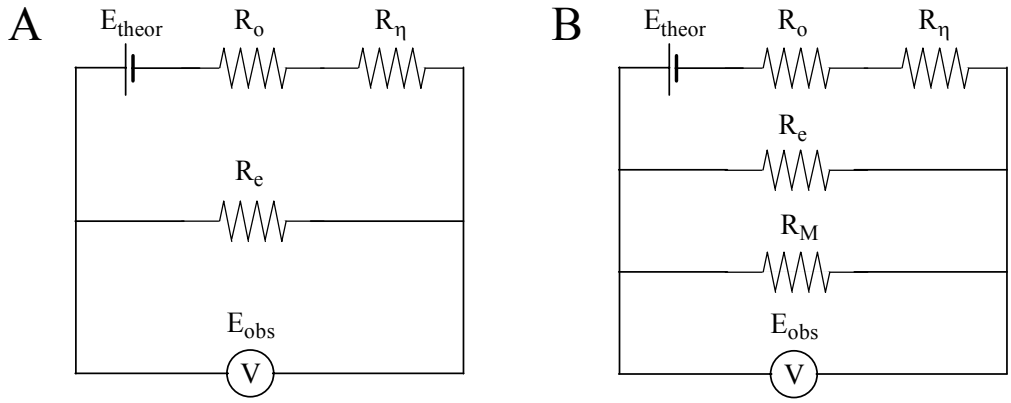

Fig. 2.5. Equivalent circuits for the classical (A) and modified (B) e.m.f. techniques.

Summarizing Chapter 2, Table 2.3 lists methods and techniques used for the materials characterization. Abbreviation DIL means dilatometry; TC/SC corresponds to isothermal measurements of total conductivity and Seebeck coefficient as functions of the oxygen pressure.

Table 2.3. Brief outline of employed methods and techniques.

Composition	XRD	SEM	MS	DIL	TC	OP	FE/e.m.f.	TC/SC
$La_{1-x}Sr_xFe_{1-y}Ga_yO_{3-\delta}$	+	+	–	+	–	+	–	–
$SrFe_{1-x}Al_xO_{3-\delta}$	+	+	+	+	+	+	–	+
$Ln_{3-x}A_xFe_{5-y}B_yO_{12-\delta}$	+	+	+	+	+	+	–	–
$Y_{2.5}Nd_{0.25}Ca_{0.25}Fe_5O_{12-\delta}$	+	+	–	+	+	+	–	–
$Y_{2.5}Ca_{0.5}Fe_4NiO_{12-\delta}$	+	+	–	+	+	+	–	–
LSGM-LSFC	+	+	–	+	+	+	–	–
$La_{10-z}Si_{6-y}Al_yO_{26\pm\delta}$	+	+	–	+	+	–	+	+
$La_{9.83}Si_{4.5}Fe_{1.5-y}Al_yO_{26\pm\delta}$	+	+	+	+	+	–	+	+
$La_{10-x}Si_{6-y}Fe_yO_{26\pm\delta}$	+	+	+	+	+	–	+	+
$La_{7-x}Sr_3Si_6O_{25.5\pm\delta}$	+	+	–	+	+	–	+	–
$La_{9.83-x}Pr_xSi_{4.5}Fe_{1.5}O_{26\pm\delta}$	+	+	+	+	+	–	+	+

3. Ionic and electronic transport in $SrFe_{1-x}Al_xO_{3-\delta}$ perovskites

3.1. Phase relationships and ceramic microstructure

XRD studies of $SrFe_{1-x}Al_xO_{3-\delta}$ ($0.1 \le x \le 0.5$) ceramics, equilibrated in air, showed formation of a cubic perovskite phase (space group $Pm\bar{3}m$, see Appendix 1A). The absence of supercell reflections indicates a random B-site distribution for the Fe and Al cations. The materials with $x \le 0.3$ are single-phase, whilst minor impurity peaks were detected in the XRD patterns at $0.4 \le x \le 0.5$. In the case of $SrFe_{0.6}Al_{0.4}O_{3-\delta}$ the secondary phase was identified as $Sr_3Al_2O_6$; about 1 wt%, as estimated from the results of Rietveld refinement of the XRD patterns. In the case of $SrFe_{0.6}Al_{0.4}O_{3-\delta}$ the secondary phase was identified as $Sr_3Al_2O_6$; about 1 wt%, estimated as before. For $SrFe_{0.5}Al_{0.5}O_{3-\delta}$, the phase impurities include $SrAl_2O_4$, Al_2O_3 and another cubic perovskite phase; the total amount of the secondary phases is less than 2 wt%. Therefore, the maximum solubility of Al^{3+} cations in the iron sublattice of $SrFeO_{3-\delta}$ is close to 35%. Such a conclusion is confirmed by the variations of the perovskite unit cell parameter (Table 3.1): the lattice volume increases up to $x = 0.4$ and then becomes essentially independent of aluminum content. This estimate is in agreement with the solid solution formation range in the system $La_{0.8}Sr_{0.2}Fe_{1-x}Al_xO_{3-\delta}$, where the perovskite phase exists at $0 \le x \le 0.5$ [229].

Table 3.1. Properties of $SrFe_{1-x}Al_xO_{3-\delta}$ ceramics.

Composition	Unit cell parameter, Å	ρ_{exp}, g/cm^3	Thermal expansion		Total conductivity	
			T, K	$\alpha \times 10^6$ K^{-1}	T, K	E_a, kJ/mol
$SrFe_{0.9}Al_{0.1}O_{3-\delta}$	3.882(6)	4.89	373 – 823 823 – 1273	16.4 ± 0.3 31.9 ± 0.3	298 – 593	28.5 ± 0.4
$SrFe_{0.8}Al_{0.2}O_{3-\delta}$	3.889(3)	4.87	–	–	298 – 738	29.8 ± 0.2
$SrFe_{0.7}Al_{0.3}O_{3-\delta}$	3.900(4)	4.88	373 – 923 923 – 1273	15.4 ± 0.1 23.0 ± 0.1	298 – 748	29.7 ± 0.4
$SrFe_{0.6}Al_{0.4}O_{3-\delta}$	3.905(3)	4.57	–	–	298 – 778	32.5 ± 0.4
$SrFe_{0.5}Al_{0.5}O_{3-\delta}$	3.906(9)	4.65	373 – 923 923 – 1273	13.5 ± 0.1 18.6 ± 0.2	298 – 788	31.9 ± 0.6

The perovskite lattice parameters of $SrFe_{1-x}Al_xO_{3-\delta}$ are larger than for cubic $SrFeO_{3-\delta}$, 3.86 Å (PDF card 34-0638). Moreover, despite the smaller ionic radius of Al^{3+} compared to Fe^{3+} and Fe^{4+} [8], the unit cell volume of $SrFe_{1-x}Al_xO_{3-\delta}$ increases on Al doping within the solid solubility domain. This is expected, since Al additions increase the portion of trivalent iron in $SrFe_{1-x}Al_xO_{3-\delta}$, as showed Mössbauer spectroscopy (Appendix 2, Table 1). The same trend was observed for Ti- and Sn-doped

$SrFeO_{3-\delta}$ also [196,199]. Such a phenomenon may partially result from increasing oxygen deficiency and decreasing overlap of the electronic orbitals of iron and oxygen ions, caused by the incorporation of insulating Al^{3+} into the iron sub-lattice.

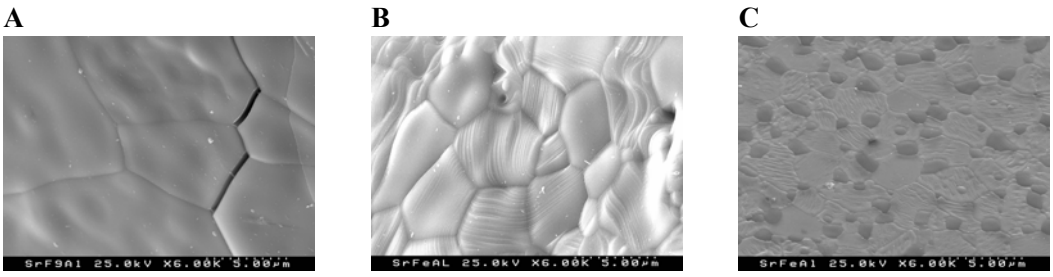

Fig. 3.1. SEM micrographs of $SrFe_{0.9}Al_{0.1}O_{3-\delta}$ (A), $SrFe_{0.7}Al_{0.3}O_{3-\delta}$ (B) and $SrFe_{0.5}Al_{0.5}O_{3-\delta}$ (C).

The segregation of secondary phases in $SrFe_{1-x}Al_xO_{3-\delta}$ ($0.4 \leq x \leq 0.5$) was confirmed by SEM/EDS analysis; typical SEM micrographs are presented in Fig. 3.1. Increasing aluminum content leads to a significant decrease in the grain size, from 5-10 μm at x = 0.1 down to 1-2 μm at x = 0.5. Suppressing grain growth by alumina additions is well known for zirconia-based materials and enables 30-50% increase in the mechanical strength of $Zr(Y)O_{2-\delta}$ [102]. Furthermore, $SrFe_{1-x}Al_xO_{3-\delta}$ ceramics with small Al concentration exhibit a tendency to microcrack formation at the grain boundaries, as illustrated in Fig. 3.1A. These microcracks form in the course of sintering and subsequent cooling, presumably due to high thermal expansion associated with extensive changes of oxygen nonstoichiometry [263]. As a result, sintering of gas-tight $SrFe_{1-x}Al_xO_{3-\delta}$ ($0.1 \leq x \leq 0.3$) membranes was only possible using relatively low heating/cooling rates, 0.5-1.5 K/min. The substitution of 30-40% Al^{3+}, with constant oxidation state, for iron, decreases oxygen content variations, as for $La_{1-x}Sr_xFe_{1-y}Ga_yO_{3-\delta}$ [263].

3.2. Thermal expansion

The average thermal expansion coefficients (TECs) of $SrFe_{1-x}Al_xO_{3-\delta}$ ceramics, calculated from dilatometric data in air (Fig. 3.2), decrease with Al additions (Table 3.1). At temperatures below 823-923 K, the TECs vary from 13.5×10^{-6} to 16.4×10^{-6} K^{-1}. Further heating leads to increasing TECs up to $(18.6\text{-}31.9)\times10^{-6}$ K^{-1}. This behavior is typical for perovskite-type ferrites and results partly from the oxygen losses on heating [198,263]. The average oxidation state of iron cations decreases due to

increasing oxygen nonstoichiometry, while their size increases; this causes the so-called "chemical" contribution to the thermal expansion. The incorporation of cations with a stable oxidation state, Al^{3+}, suppresses oxygen content variations and, thus, decreases apparent thermal expansion coefficients.

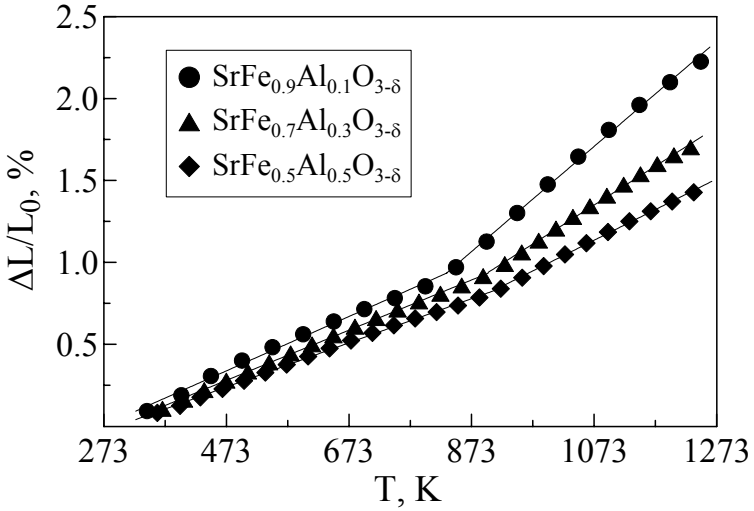

Fig. 3.2. Dilatometric curves of $SrFe_{1-x}Al_xO_{3-\delta}$ ceramics in air.

3.3. Total conductivity and Seebeck coefficient

As for thermal expansion, the electrical transport (σ) of $SrFe_{1-x}Al_xO_{3-\delta}$ ceramics, predominantly p-type electronic in air, decreases monotonically with increasing content of insulating Al^{3+} cations incorporated into iron sites (Fig. 3.3). At x = 0.4-0.5, however, the conductivity values are quite close, indicating similar [Fe]/[Al] ratio in the major perovskite phase. This confirms the solid solution formation limit estimated from the XRD data.

The $SrFe_{1-x}Al_xO_{3-\delta}$ perovskites exhibit a transition to pseudometallic behavior at temperatures above 873 K in air, similar to $SrFeO_{3-\delta}$ [192]. This reflects decreasing concentration of the p-type electronic charge carriers, caused by oxygen losses on heating. Aluminum doping decreases the total concentration of B-sites participating in the electronic transport processes and, according to the Mössbauer spectroscopy data (Appendix 2, Table 1), the concentration of electron holes localized on iron cations. The values of activation energy, E_a, calculated by the standard Arrhenius model, are similar for all compositions and vary from 28.5 to 32.5 kJ/mol (Table 3.1). This indicates no alteration of the conduction mechanism with doping and, most likely, that neither charge carrier nor transition in the electronic sublattice occur on heating.

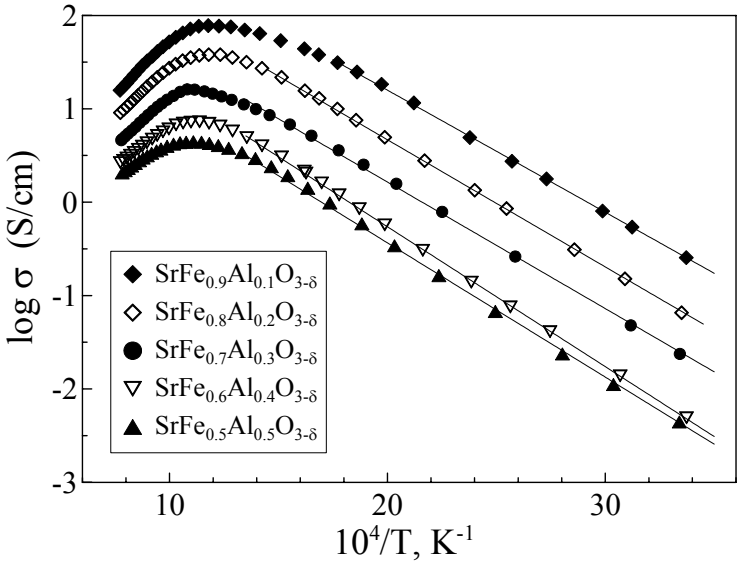

Fig. 3.3. Temperature dependencies of the total conductivity of $SrFe_{1-x}Al_xO_{3-\delta}$ ceramics in air.

The dependencies of total conductivity and Seebeck coefficient (α) on the oxygen partial pressure (Fig. 3.4) indicate predominant *p*-type electronic conduction under oxidising conditions. When the oxygen pressure is higher than 1-10 Pa, the values of σ decrease with reducing $p(O_2)$, whereas α increases and has positive sign. On further reduction, the conductivity reaches a minimum and starts to increase due to increasing *n*-type electronic transport. The Seebeck coefficient values become negative, pass through a minimum and then increase. The range of moderately reducing $p(O_2)$ was excluded from consideration due to errors associated with stagnated diffusion processes in the gas phase [268].

The formation of electron holes and electrons can be described as [189]

$$\tfrac{1}{2}O_2 + V_O + 2Fe^{3+} = O^{2-} + 2Fe^{4+} \quad (3.1)$$

$$O^{2-} + 2Fe^{3+} = \tfrac{1}{2}O_2 + V_O + 2Fe^{2+} \quad (3.2)$$

with the corresponding equilibrium constants

$$K_{ox} = \frac{[O^{2-}][Fe^{4+}]^2}{[V_O][Fe^{3+}]^2 p(O_2)^{1/2}} \quad (3.3)$$

$$K_{red} = \frac{[V_O][Fe^{2+}]^2 p(O_2)^{1/2}}{[O^{2-}][Fe^{3+}]^2} \quad (3.4)$$

The latter equations can be re-written as:

$$[Fe^{4+}] = [Fe^{3+}]\sqrt{\frac{K_{ox}[V_O]}{[O^{2-}]}}p(O_2)^{1/4} \quad (3.5)$$

$$[Fe^{2+}] = [Fe^{3+}]\sqrt{\frac{K_{red}[O^{2-}]}{[V_O]}}p(O_2)^{-1/4} \quad (3.6)$$

The charge carrier concentrations are interrelated via the iron disproportionation reaction and the crystal electroneutrality condition:

$$2Fe^{3+} = Fe^{2+} + Fe^{4+} \qquad K_i = \frac{[Fe^{2+}][Fe^{4+}]}{[Fe^{3+}]^2} = \frac{pn}{(N-p-n)^2} \quad (3.7)$$

$$1 + n = p + 2[V_O] = p + 2\delta \quad (3.8)$$

where $1 = [Sr^{2+}]$, $N = [Fe^{2+}] + [Fe^{3+}] + [Fe^{4+}]$, p and n are the concentrations of p-type (Fe^{4+}) and n-type (Fe^{2+}) electronic charge carriers, respectively.

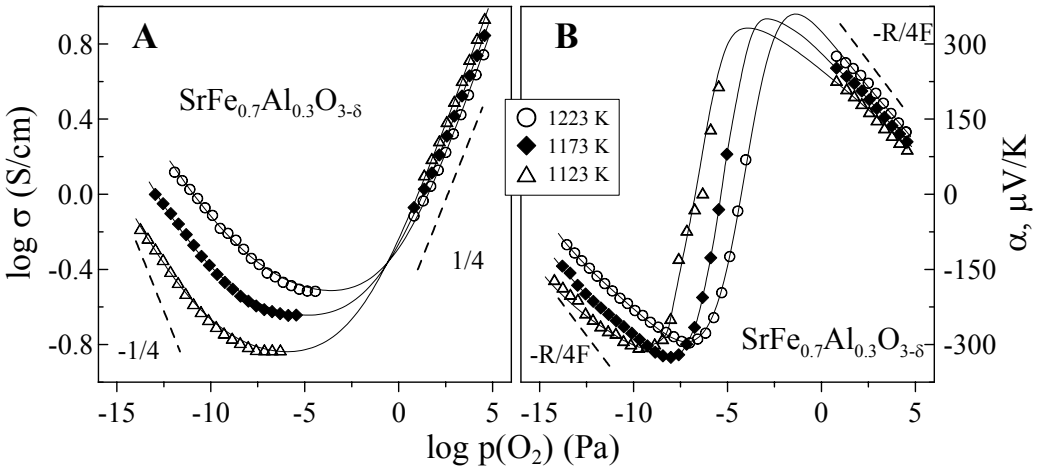

Fig. 3.4. Oxygen pressure dependencies of the total conductivity (A) and Seebeck coefficient (B) of $SrFe_{0.7}Al_{0.3}O_{3-\delta}$ ceramics. Dashed lines correspond to the theoretical slopes.

When the oxygen partial pressure is far from the $p(O_2)$ range corresponding to the conductivity minimum, one type of electronic charge carriers is expected to dominate, namely $[Fe^{4+}] \gg [Fe^{2+}]$ in oxidizing atmospheres and $[Fe^{4+}] \ll [Fe^{2+}]$ under strongly reducing conditions. As the conductivity is proportional to the concentration of charge carriers, their charge and mobility, one can obtain the classical power dependencies for partial p- and n-type conductivities

$$\sigma_p = \sigma_p^0 p(O_2)^{1/4} \qquad \sigma_n = \sigma_n^0 p(O_2)^{-1/4} \tag{3.7}$$

where σ_p^0 and σ_n^0 are temperature-dependent, corresponding to the relevant conductivity values at unit oxygen pressure. The exponent, ±1/4, corresponds to the situation where the variations of the oxygen vacancy concentration are small with respect to the total δ value, i.e. the chemical potential of oxygen ions remains essentially constant under a given $p(O_2)$ range. This situation takes place in the vicinity of the conductivity minimum. Assuming that the ionic conductivity (σ_o) at these $p(O_2)$ values is independent of oxygen pressure, a known model can be used:

$$\sigma = \sigma_o + \sigma_p^0 p(O_2)^{1/4} + \sigma_n^0 p(O_2)^{-1/4} \tag{3.8}$$

Isothermal plots of the sum of the partial electronic conductivity ($\sigma_p + \sigma_n$) obtained fitting data to Eq. (3.8) are shown in Fig. 3.5. The slopes of *log* ($\sigma_p + \sigma_n$) – *log* $p(O_2)$ dependencies are in excellent agreement with expected values: +1/4 and -1/4 under oxidizing and reducing conditions, respectively. A slight deviation from -1/4 for the n-type electronic transport relates to a significant decrease in the oxygen content; in these case Eq. (3.8) is no more valid. The same is true at high $p(O_2)$ when the p-type conductivity exhibits dependencies even higher than +1/4 at $p(O_2) = 10^3$-10^5 Pa. Here, the mobility of holes increases with increasing oxygen pressure due to growing number of Fe-O-Fe links responsible for electronic transport.

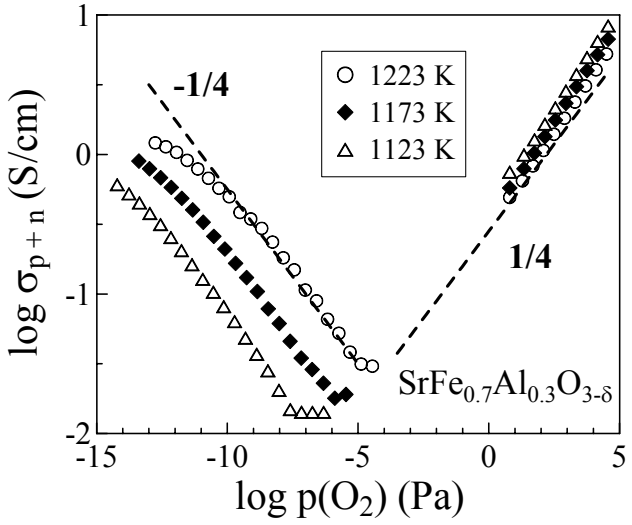

Fig. 3.5. Oxygen pressure dependencies of the sum of the partial p- and n-type electronic conductivities of $SrFe_{0.7}Al_{0.3}O_{3-\delta}$. Dashed lines correspond to the theoretical slopes.

If the transported entropy and enthalpy of a polaron in Eq. (1.64) is neglected, the Seebeck coefficient for a predominant electronic conductor is related to the concentration of holes as follows [169]:

$$\alpha = \frac{R}{F}\ln\left(\frac{1}{\beta}\frac{N-p}{p}\right) \tag{3.9}$$

For $SrFe_{0.7}Al_{0.3}O_{3-\delta}$ the value of N is equal to the total concentration of Fe cations and β is equal to 6/5. Taking the electroneutrality condition into account, one can calculate the concentration of holes and oxygen nonstoichiometry from the Seebeck coefficient data. Then, assuming $\sigma_p \approx \sigma$ under oxidising atmospheres, the mobility of holes may be estimated from Eq. (1.11):

$$u_p = \frac{\sigma_p}{ep} \tag{3.10}$$

The results of such calculations are shown in Fig 3.6. When the p/N ratio is fixed, the mobility of holes follows an Arrhenius-type dependence on temperature, indicative of a small-polaron conductivity mechanism. Also, the absolute u_p values, 0.009-0.016 $cm^2V^{-1}s^{-1}$ at 1073-1223 K, are essentially lower than 0.1 $cm^2\ V^{-1}\ s^{-1}$, a characteristic boundary between polaron and broad-band conductor mobilities.

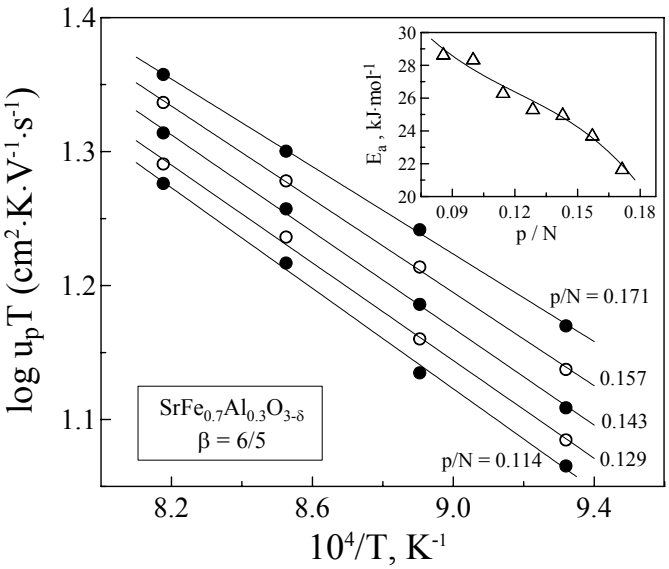

Fig. 3.6. Temperature dependencies of hole mobility in $SrFe_{0.7}Al_{0.3}O_{3-\delta}$ at fixed hole concentration. The inset shows mobility activation energy vs. p/N ratio.

The mobility activation energy was found to progressively decrease with increasing $p(O_2)$ when the oxygen-ion and hole concentrations increase (inset in Fig. 3.6). This tendency is associated with lattice contraction and higher average oxidation state of Fe cations, leading to a greater overlap of iron and oxygen electron orbitals and, thus, to a stronger covalence of the Fe-O-Fe bonds and higher delocalisation of the electron charge carriers.

3.4. Oxygen permeability and ionic conductivity

Typical relationships between oxygen permeation fluxes through dense $SrFe_{0.7}Al_{0.3}O_{3-\delta}$ ceramics and membrane thickness (d) under oxidizing conditions are illustrated in Fig. 3.7A. The specific permeability is thickness-independent, within the limits of experimental uncertainty, at 1223 K (Fig. 3.7B). At lower temperatures, however, increasing membrane thickness results in decreasing permeation fluxes, while the $J(O_2)$ values increase due to a decreasing role of the surface exchange kinetics. These tendencies are common for Fe-containing perovskites with a high oxygen permeability [198] and indicate non-negligible surface limitations to the oxygen transport, which become more pronounced on decreasing $p(O_2)$.

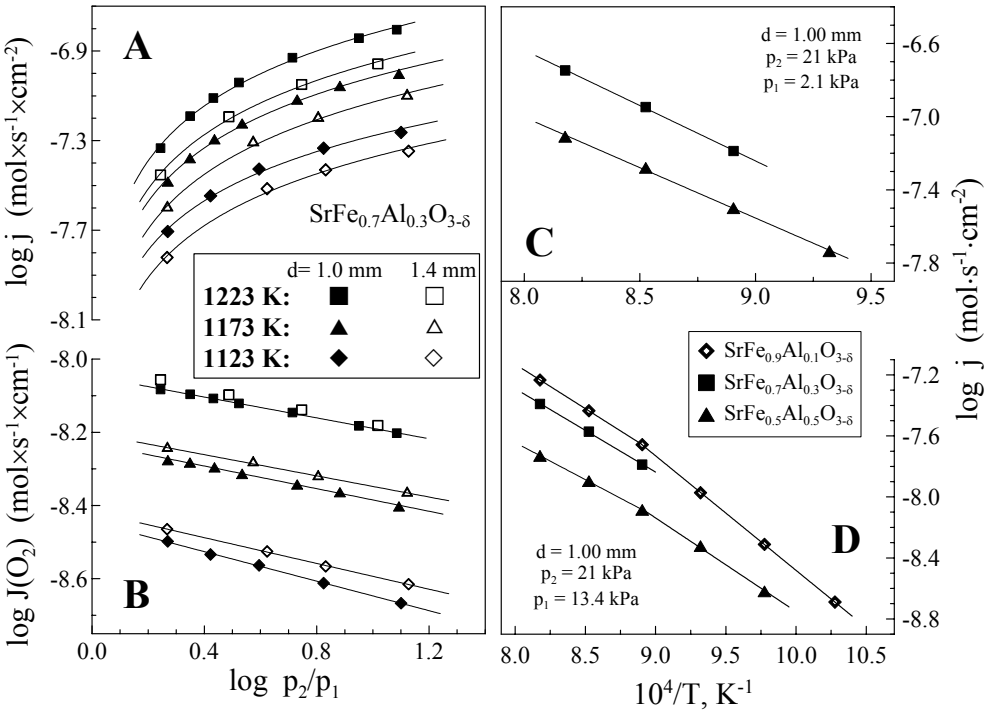

Fig. 3.7. Oxygen permeation flux and specific oxygen permeability of $SrFe_{1-x}Al_xO_{3-\delta}$.

Single-phase $SrFe_{1-x}Al_xO_{3-\delta}$ ($0.1 \leq x \leq 0.3$) show quite similar levels of oxygen permeation fluxes (j) under a fixed oxygen chemical potential gradient (Fig. 3.7D). Further doping leads to 2-3 times lower oxygen permeability. $SrFe_{0.5}Al_{0.5}O_{3-\delta}$ has lower activation energy for oxygen transport at temperatures below 1050 K, when the tendency to formation of vacancy-ordered microdomains in the oxygen sublattice of $SrFeO_3$-based compounds becomes critical [198]. The relatively low activation energy may originate from the doping-induced disordering due to statistical distribution of Al^{3+} cations, locally distorting the lattice. If compared to other ferrite phases (Tables 1.3 and 1.4), the oxygen permeability of $SrFe_{1-x}Al_xO_{3-\delta}$ ($0.1 \leq x \leq 0.3$) ceramics is slightly lower than the maximum observed for Co-free perovskites with a high oxygen deficiency and a low degree of vacancy ordering. This level of oxygen transport is, however, 10^2-10^3 times higher with respect to Fe-containing phases with the intergrowth and garnet-type structures. Notice also that the effect of Al^{3+} content on the permeation fluxes through $SrFe_{1-x}Al_xO_{3-\delta}$ ceramics is substantially smaller than the influence of Ti^{4+} concentration in the $SrFe_{1-x}Ti_xO_{3-\delta}$ system [198].

Fig. 3.8 compares the ionic conductivity of $SrFe_{0.7}Al_{0.3}O_{3-\delta}$ in oxidising and reducing conditions, evaluated from the oxygen permeation (OP) data and calculated from the $p(O_2)$ dependencies of total conductivity (TC) using Eq. (3.8) as regression model, respectively. As for $La_{0.3}Sr_{0.7}FeO_{3-\delta}$ [193], $SrFe_{0.7}Al_{0.3}O_{3-\delta}$ exhibits a higher ionic conduction in reducing atmospheres, whilst the activation energy is essentially independent of the oxygen pressure.

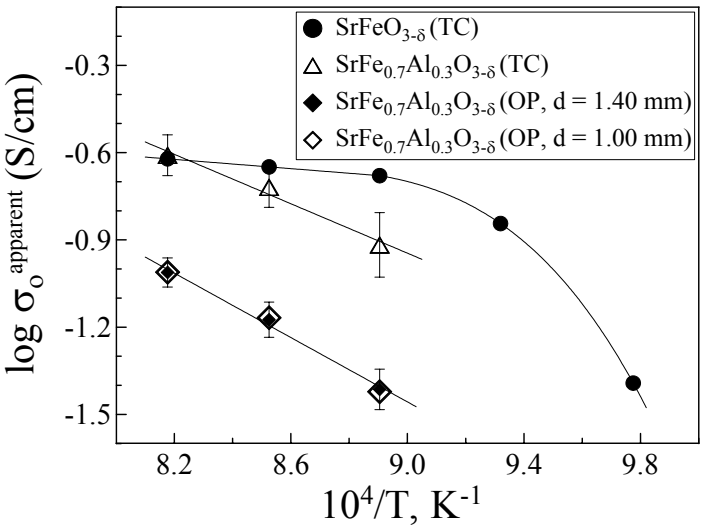

Fig. 3.8. Comparison of the oxygen ionic conductivity of $SrFeO_{3-\delta}$ [192] and $SrFe_{0.7}Al_{0.3}O_{3-\delta}$, determined from the data on oxygen permeation (OP) and total conductivity (TC).

In agreement with the random walk theory for ionic transport [106], this behaviour results from increasing oxygen vacancy concentration in the perovskite lattice, with the ion migration enthalpy independent of the oxygen chemical potential. One should mention that such trend does not contradict Eq. (3.8) since at oxygen pressures lower than 1-10 Pa, when the ionic contribution to the total conductivity becomes significant, the oxygen deficiency tends to a plateau close to the p-n transition in mixed conductors. At the same time, the variations of oxygen nonstoichiometry (5-10%) are considerably lower than the changes in ionic conductivity on reducing $p(O_2)$, 40-50% (Fig. 3.8). This suggests that part of the oxygen vacancies in $SrFe_{0.7}Al_{0.3}O_{3-\delta}$ is blocked, presumably in ordered microdomains [198]. In the case of undoped $SrFeO_{3-\delta}$, the temperature dependence of ionic conductivity in reducing atmospheres on heating is non-linear due to a transition from vacancy-ordered brownmillerite into perovskite. No such transition is observed for $SrFe_{0.7}Al_{0.3}O_{3-\delta}$ at temperatures above 1173 K, and the ionic conductivity of the latter follows an Arrhenius trend.

3.5. Phase stability limits

At oxygen partial pressure lower than 10^{-12}-10^{-14} Pa, the conductivity of $SrFe_{0.7}Al_{0.3}O_{3-\delta}$ starts to deviate from Eq. (3.8), shown in Fig. 3.9A as solid lines; further reduction leads to irreversible degradation of the electrical properties. The oxygen pressure, at which the slope of *log σ – log p(O₂)* curves starts to change, was considered as the stability limit at a given temperature.

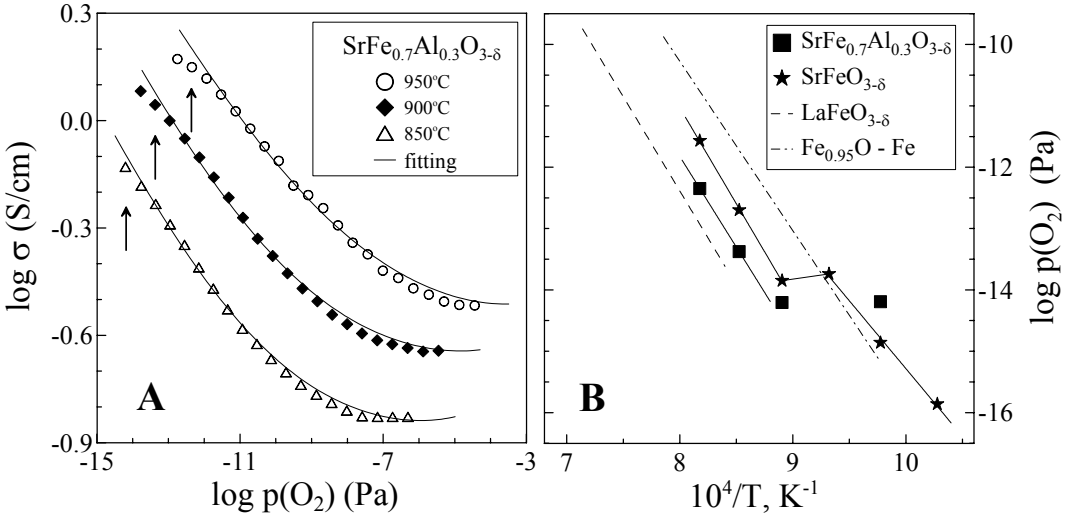

Fig. 3.9. Estimation of low-$p(O_2)$ stability boundary of $SrFe_{0.7}Al_{0.3}O_{3-\delta}$ (A) and its comparison with data on $SrFeO_{3-\delta}$ [234], $LaFeO_{3-\delta}$ [30,269] and $Fe_{0.95}O$ – Fe [270] (B).

Fig. 3.9B presents the stability boundary of $SrFe_{0.7}Al_{0.3}O_{3-\delta}$ at reduced oxygen partial pressures as estimated from these data on the total conductivity. The anomalous behavior of $SrFe_{0.7}Al_{0.3}O_{3-\delta}$ at temperatures below 1100 K is associated with progressive ordering of the oxygen sublattice on cooling and the formation of brownmillerite-like domains. This trend is similar to that observed on reduction of the parent compound, $SrFeO_{3-\delta}$ [234]. Such variations of the stability boundary can be explained in terms of a lower bonding energy of oxygen ions in the brownmillerite lattice when compared to the $FeO_{2.5}$ pyramids of the disordered cubic $SrFeO_{2.5\pm\delta}$ [234]. In general, the phase stability is quite similar for all perovskite-related ferrites as their decomposition boundaries are all determined by the Fe–O bond strength; the substitution of iron with aluminum in the lattice of $SrFeO_{3-\delta}$ leads to a moderate increase of stability in reducing atmospheres.

It should be mentioned, however, that no essential phase changes were observed by XRD in the ceramic samples annealed at 1023-1073 K in atmospheres with various $p(O_2)$ close to the decomposition limit (Fig. 3.10); apparently the ceramics remain single perovskite phase without traces of other phases. The absence of metallic iron was also verified by the Mössbauer spectroscopy. In spite of the low sensitivity of XRD to the oxygen sublattice, such patterns are indicative of co-existence of perovskite and brownmillerite-like domains at reduced $p(O_2)$, in agreement with the Mössbauer spectroscopy data.

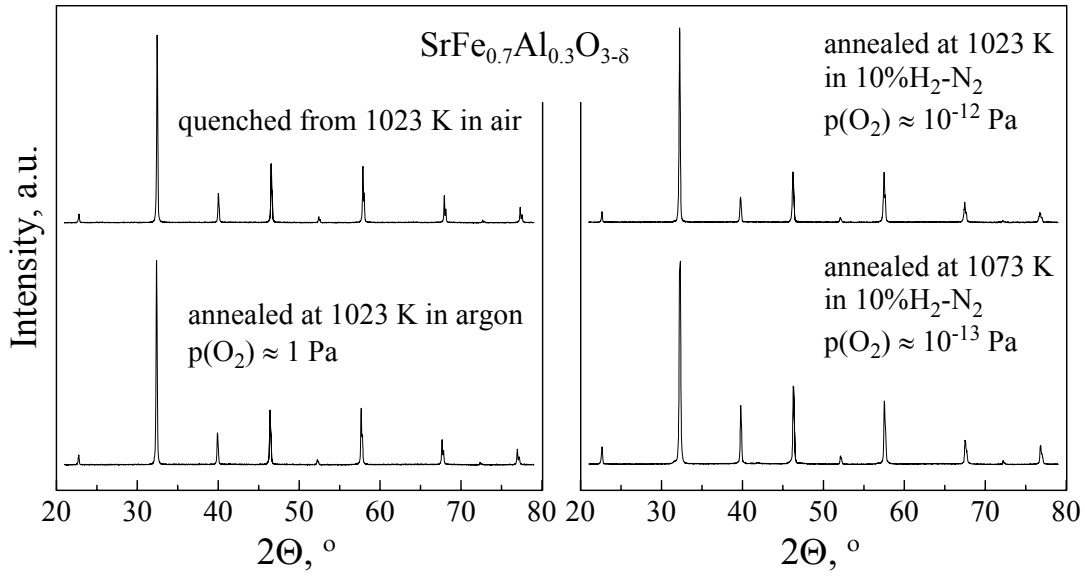

Fig. 3.10. XRD patterns of $SrFe_{0.7}Al_{0.3}O_{3-\delta}$ after annealing in various atmospheres.

3.6. Processing of $Sr(Fe,Al)O_{3-\delta}$–based ceramic membranes

Taking into account data on thermal expansion, oxygen permeability and stability, perovskite-type $SrFe_{0.7}Al_{0.3}O_{3-\delta}$ was selected as a model membrane material to optimize the ceramic processing techniques. Fig. 3.11 illustrates the effects of pressure on the density of green compacts (A) and sintered disk-shaped samples (B), all made via the uniaxial pressing of GNP-synthesized $SrFe_{0.7}Al_{0.3}O_{3-\delta}$ powder. Although the green density increases with pressure, the density of ceramics after thermal treatment is essentially pressure-independent and is determined by the sintering conditions, including maximum temperature, time, heating/cooling rates and other features of the sintering profiles.

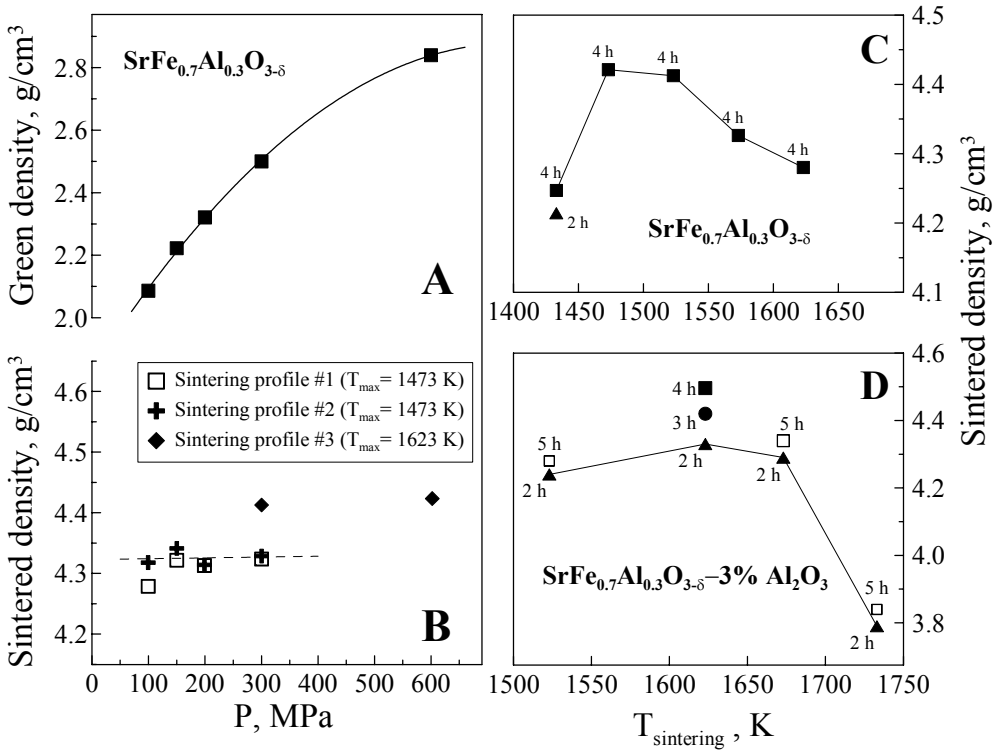

Fig. 3.11. Pressure dependencies of the density of $SrFe_{0.7}Al_{0.3}O_{3-\delta}$ green compacts (A) and sintered ceramics (B), and density of $SrFe_{0.7}Al_{0.3}O_{3-\delta}$ ceramics without (C) and with 3 wt.% Al_2O_3 addition (B) as a function of the sintering temperature and time.

Sintering profile #1 corresponds to heating up at 300-973, 973-1273 K, and then up to the maximum temperature with rates of 1, 0.5 and 1 K/min, respectively; the sintering time was 2 hours.

For sintering profile #2, the corresponding heating rates were 1, 0.5 and 4 K/min; the sintering time was 4 hours. For profile #3, the heating rates were 2, 0.5 and 4 K/min; the sintering time was 3 hours.

The highest density could be obtained at 1473-1523 K (Fig. 3.11C). However, isostatically-pressed tubular membranes, sintered at these temperatures, demonstrated poor mechanical properties with a density of 90.5% of the theoretical value calculated from XRD data (Table 3.1). Increasing the sintering temperature leads to enhanced mechanical strength, with easy handling of the $SrFe_{0.7}Al_{0.3}O_{3-\delta}$ tubes, but increases porosity. A significant improvement in the sinterability was achieved by minor additions of alumina to $SrFe_{0.7}Al_{0.3}O_{3-\delta}$ (Fig. 3.11D), with an optimum at approximately 3 wt% (Fig. 3.12).

Adding 3 wt% Al_2O_3 enables sintering at 1623 K for 3-4 h of gas-tight ceramics with good mechanical strength. The XRD analysis showed the presence of a secondary phase, $SrAl_2O_4$; exact calculations of the theoretical density are impossible in this case due to unknown distribution of cations between these two phases and also to probable segregation of components, such as alumina, at the grain boundaries. Nonetheless, the density of 3% Al_2O_3-enriched ceramics was 92% of the theoretical value for pure $SrFe_{0.7}Al_{0.3}O_{3-\delta}$ and about 95% with respect to one hypothetical two-phase mixture, where the perovskite phase and $SrAl_2O_4$ are assumed to be Sr-deficient and to have nominal composition, respectively. SEM inspections confirmed closed low porosity (Fig. 3.12).

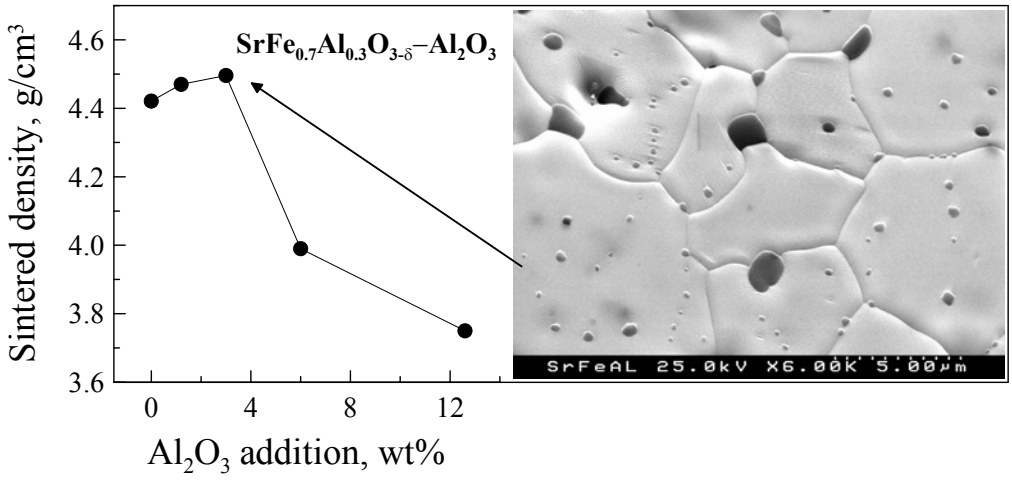

Fig. 3.12. Sintered density of $SrFe_{0.7}Al_{0.3}O_{3-\delta}$ – Al_2O_3 composites, obtained after uniaxial pressing at 200-300 MPa and sintering at 1473-1673 K, vs. Al_2O_3 content (left-hand side) and SEM micrograph of $SrFe_{0.7}Al_{0.3}O_{3-\delta}$ with 3 wt.% Al_2O_3 addition (right-hand side).

Minor alumina additions influenced also the thermal expansion and oxygen permeability. The average TECs of 3 wt% Al_2O_3-doped $SrFe_{0.7}Al_{0.3}O_{3-\delta}$ ceramics decreased to the level characteristic of $SrFe_{0.5}Al_{0.5}O_{3-\delta}$. On the contrary, the oxygen permeation fluxes were found to increase by approximately 10% if compared to the cation-stoichiometric $SrFe_{0.7}Al_{0.3}O_{3-\delta}$. The latter effect is similar to that observed for strontium-deficient $Sr_{1-x}(Fe,Ti)O_{3-\delta}$ perovskites, where creation of the A-site vacancies promotes disorder in the oxygen sublattice and thus increases ionic conductivity [198].

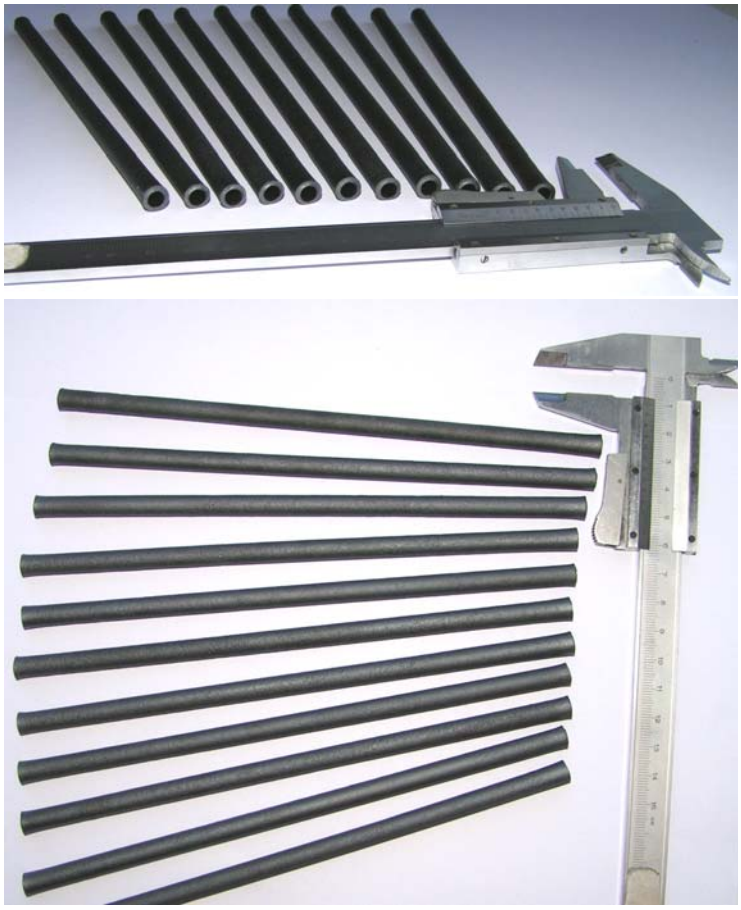

Fig. 3.13. Dense tubular membranes of $SrFe_{0.7}Al_{0.3}O_{3-\delta}$ with 3 wt.% Al_2O_3 addition.

On the basis of these results, high-quality tubular membranes of $SrFe_{0.7}Al_{0.3}O_{3-\delta}$ with 3 wt% Al_2O_3 addition (Fig. 3.13) were produced in framework of collaborative research with the Drs. F.M.M. Snijkers, J.F.C. Cooymans and J.J. Luyten, Materials Department of the Flemish Institute for Technological Research (VITO, Belgium). The tubes were prepared by cold isostatic pressing at 175

MPa, using a Burton Corblin instrument with one pressure vessel of 90 mm in diameter and 500 mm in length. In the course of processing, the ball-milled powder was filled around a steel mandrel with 6.35 mm diameter in a flexible latex rubber hose; special care was taken to distribute the powder symmetrically around the mandrel in order to avoid as much as possible eccentricity, i.e. variation of circular wall thickness. Gas-tight tubes with the inner diameter of 5 mm, wall thickness of 1.0-1.2 mm and length of 170-200 mm were sintered at 1623 K for 3-4 h.

4. Oxygen permeability of perovskite-like $La_{1-x}Sr_xFe_{1-y}Ga_yO_{3-\delta}$

4.1. Phase relationships

Phase composition of $La_{1-x}Sr_xFe_{1-y}Ga_yO_{3-\delta}$ (x = 0.1-0.8; y = 0-0.95) materials and an approximate boundary for single perovskite-type phases are schematically shown in Fig. 4.1A. For the compositions with $x \geq 0.2$, increasing gallium content leads to segregation of a secondary phase, $SrLaGa_3O_7$. Formation of $SrLaGa_3O_7$ is quite typical for $LaGaO_3$-based ceramics when strontium additions are larger than 10% of the A-site concentration [271-273]. Detailed analysis of the XRD patterns at $x \geq 0.2$ showed no traces of other impurity phases, including $SrLaGaO_4$, which also is often segregated in ceramic materials based on doped lanthanum gallate [271-273]. Data on minor phase impurities in $La_{0.9}Sr_{0.1}Fe_{1-y}Ga_yO_{3-\delta}$ ceramics can be found elsewhere ([43] and references cited).

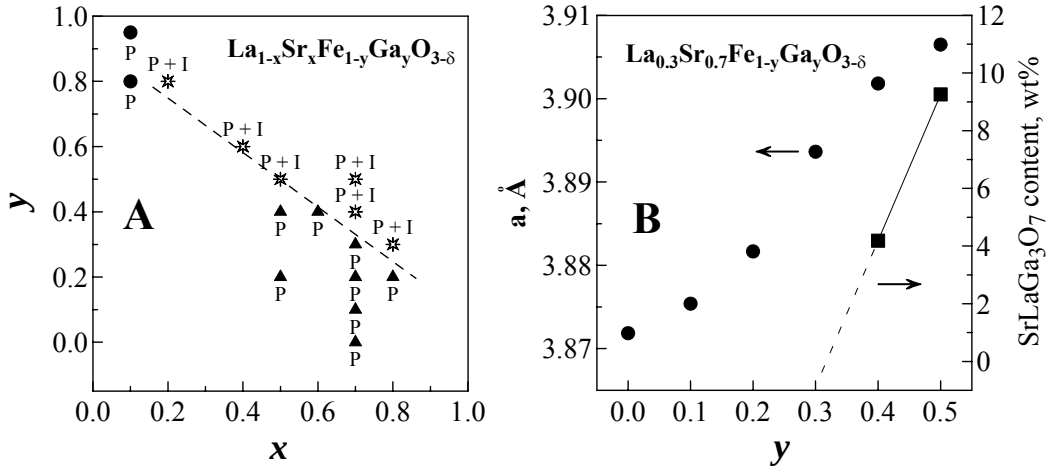

Fig. 4.1. A: phase diagram of $La_{1-x}Sr_xFe_{1-y}Ga_yO_{3-\delta}$ (P – single perovskite-type phase, P+I – perovskite with $SrLaGa_3O_7$ secondary phase); B: variation of the cubic perovskite unit cell parameter and $SrLaGa_3O_7$ phase content.

For $La_{0.3}Sr_{0.7}Fe_{1-y}Ga_yO_{3-\delta}$, the estimated weight fractions of $SrLaGa_3O_7$ were 4.2% and 9.3% for the compositions with y = 0.4 and 0.5, respectively. Extrapolation of these values to zero content of $SrLaGa_3O_7$ gives the single-phase region boundary of about 0.3. This is in agreement with the dependence of the cubic cell parameter on gallium concentration, which exhibits discontinuity at y values close to 0.3 (Fig. 4.1B). Note that further increase in Ga content leads to increasing perovskite

unit cell parameter due to reducing La/Sr ratio in the perovskite lattice, caused by $SrLaGa_3O_7$ segregation.

In general, the results summarized in Fig. 4.1 clearly show a limited solid solubility of gallium cations in the lattice of $(La,Sr)FeO_{3-\delta}$ perovskite, probably associated with the absence of perovskite-like phases in the Sr-Ga-O system. In the pseudobinary system $LaFeO_{3-\delta}$-$SrFeO_{3-\delta}$ where both end members exist as perovskite-type phases, a series of solid solutions or distinct phases with perovskite-related structures is formed, depending on oxygen nonstoichiometry and the type of oxygen vacancy ordering [274]. The literature contains no phase diagram for $LaFeO_{3-\delta}$-$LaGaO_3$, but a continuous homogeneity range was found in the system $LaCoO_{3-\delta}$-$LaGaO_3$ where both end compounds are perovskites [275]; the structural and chemical similarity of lanthanum cobaltite and ferrite makes possible to expect, at least, a high mutual solid solubility of $LaFeO_{3-\delta}$ and $LaGaO_3$ phases. In contrast, no perovskite-related phases are formed in the system Sr-Ga-O, resulting in limited solubility of Ga in $SrFeO_{3-\delta}$ and Sr in $LaGaO_3$ lattice. The literature data on Sr-doped $LaGaO_3$ [271,272] and our results on the $La_{1-x}Sr_xFe_{1-y}Ga_yO_{3-\delta}$ system (Fig.1) confirm such a statement. It should also be mentioned that Ga solubility in $La_{1-x}Sr_x(Fe,Ga)O_{3-\delta}$ decreases with increasing x. This trend, common for numerous other perovskite systems [153], is due to a decrease in the thermodynamic stability and, in particular, a lower stability of $(La,Sr)FeO_{3-\delta}$ lattice with respect to the B-site cation substitution when strontium concentration in the perovskite phase increases.

Creation of cation vacancies in the A sublattice leads to further decrease of thermodynamic stability of the perovskites, which results in phase decomposition of materials having compositions close to the phase stability boundary. For example, the A-site-stoichiometric compound $La_{0.4}Sr_{0.6}Fe_{0.6}Ga_{0.4}O_{3-\delta}$ was single phase, whilst $SrLaGa_3O_7$ segregation was observed for the composition $La_{0.35}Sr_{0.60}Fe_{0.6}Ga_{0.4}O_{3-\delta}$, studied in order to estimate the influence of the A-site cation deficiency on the oxygen ionic transport properties of $(La,Sr)(Fe,Ga)O_{3-\delta}$. This instability with respect to A-site deficiency is considerably higher than that in other perovskites such as Sr-doped $LaCrO_{3-\delta}$ and $LaCoO_{3-\delta}$; the latter compounds remain single-phase for A-site vacancy concentrations as high as 10% [153].

4.2. Crystal structure and microstructure

According to the literature data on the crystal lattice of lanthanum-strontium ferrites [274], the starting structural model for refinement of data on $La_{1-x}Sr_xFe_{1-y}Ga_yO_{3-\delta}$ ($x \geq 0.2$) was rhombohedral, space

group $R\bar{3}c$ (No. 167). However, since all XRD patterns, except that of $La_{0.8}Sr_{0.2}Fe_{0.2}Ga_{0.8}O_{3-\delta}$, show no peak splitting or broadening beyond the instrumental resolution, the rhombohedral angle α was found to vary in the range from 59.99° to 60.01°; the oxygen atomic coordinates were very close to the ideal position. Therefore, the structure of all synthesized compositions with $x \geq 0.4$, in air, was refined as cubic (see Appendix 1B) without deterioration of the refinement quality. Structural data for selected $La_{1-x}Sr_xFe_{1-y}Ga_yO_{3-\delta}$ compounds, including the unit cell volume (V) and isotropic temperature factors (B), are summarized in Table 4.1. Notice that cubic perovskite phases of $(La,Sr)(Fe,Ga)O_{3-\delta}$ are stable in air within the studied temperature range – the high-temperature XRD data revealed no changes in the phase composition or lattice symmetry at temperatures up to 1373 K.

Table 4.1. Structure refinement results for $La_{1-x}Sr_xFe_{1-y}Ga_yO_{3-\delta}$ perovskites.

y	a, Å	V, Å^3	B (La/Sr), Å^2	B (Fe/Ga), Å^2	B (O), Å^2
$La_{0.3}Sr_{0.7}Fe_{1-y}Ga_yO_{3-\delta}$ series					
0	3.8719	58.04	0.60(2)	0.37(3)	1.33(6)
0.1	3.8754	58.20	0.81(5)	0.38(4)	1.36(5)
0.2	3.8817	58.49	0.71(2)	0.44(3)	2.04(8)
0.3	3.8936	59.03	1.08(2)	0.86(3)	3.23(9)
0.4	3.9018	59.40	1.12(2)	0.86(3)	2.56(7)
0.5	3.9065	59.62	1.07(2)	1.12(3)	3.47(9)
$La_{1-x}Sr_xFe_{1-y}Ga_yO_{3-\delta}$ series (x = 1-y)					
0.2	3.8877	58.76	0.86(3)	0.56(5)	0.98(1)
0.3	3.8936	59.03	1.08(2)	0.86(3)	3.23(9)
0.4	3.9026	59.44	1.53(2)	1.24(3)	5.20(1)
0.6	3.8999	59.31	0.47(2)	0.16(4)	3.56(1)
0.8	3.8997 [a]	59.30	0.54(3)	0.46(5)	2.97(2)

[a] Pseudocubic cell parameter of the rhombohedral perovskite phase (a = 5.4978 Å, c = 13.5298 Å)

The structure of the $La_{0.8}Sr_{0.2}Fe_{0.2}Ga_{0.8}O_{3-\delta}$ perovskite-type phase at room temperature was found rhombohedrally distorted. As the lattice of $LaGaO_3$ at room temperature is orthorhombic (S.G. Pbnm) [13], a similar structure model was also considered for $La_{0.8}Sr_{0.2}Fe_{0.2}Ga_{0.8}O_{3-\delta}$, but the refinement quality was better in the case of the rhombohedral model.

The single-phase cubic perovskite unit cell parameter of $La_{1-x}Sr_xFe_{1-y}Ga_yO_{3-\delta}$ decreases with increasing iron content (Fig. 4.1B), in agreement with the literature data on $La(Sr)Ga(Mg,Fe)O_{3-\delta}$ [258], $(Sr,La)(Fe,Ga)O_{3-\delta}$ [168], and the lattice parameters of the parent compounds, $LaGaO_3$ and $SrFeO_{3-\delta}$ [276,277]. The ionic radii of high-spin 4- and 5-coordinated Fe^{3+} as well as the radius of octahedrally-coordinated Fe^{4+} are smaller than that of Ga^{3+} in the octahedral coordination, while the ionic radius of 6-coordinated Fe^{3+} is larger than that of gallium [8]. Therefore, the contraction of the perovskite unit cell with iron additions may be related to replacement of octahedrally-coordinated gallium cations with 4- and 5-coordinated Fe^{3+} and 6-coordinated Fe^{4+}. For instance, ordered brownmillerite-like microdomains with tetrahedral coordination of Fe^{3+} are found in strontium ferrite when the oxygen nonstoichiometry is intermediate between values typical of the perovskite and brownmillerite phases [278]. For the two-phase domain in the series (x = 1-y), the unit cell parameters are essentially independent of composition (Table 4.1). Further decrease of Sr and Fe concentration results in a transition from rhombohedral to typical $LaGaO_3$ orthorhombic symmetry and in a decrease of the cell volume due to further tilting of gallium-oxygen octahedra in the perovskite lattice [272].

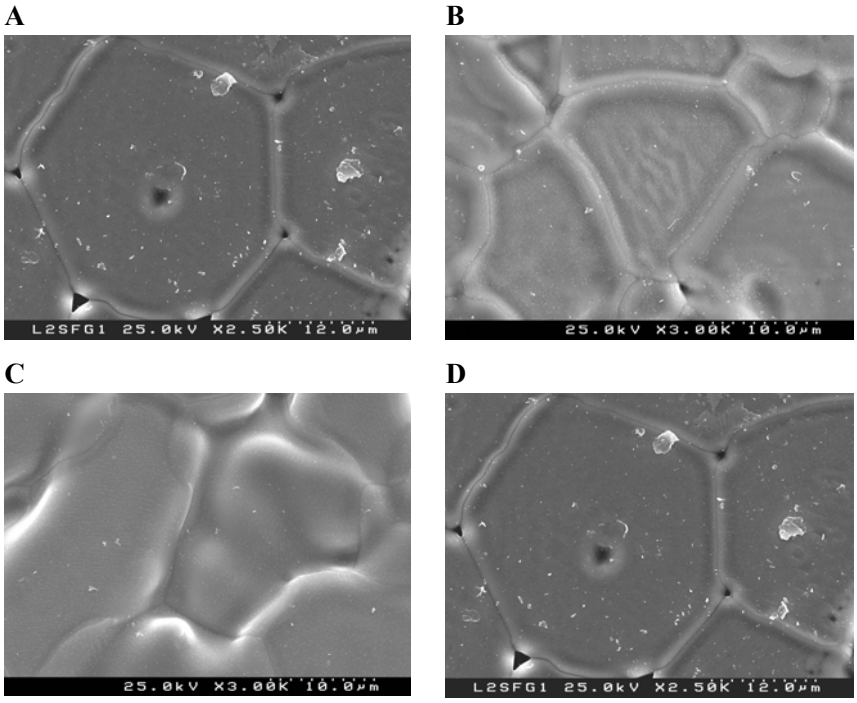

Fig. 4.2. SEM micrographs of $La_{0.3}Sr_{0.7}FeO_{3-\delta}$ (A), $La_{0.3}Sr_{0.7}Fe_{0.8}Ga_{0.2}O_{3-\delta}$ (B), $La_{0.3}Sr_{0.7}Fe_{0.6}Ga_{0.4}O_{3-\delta}$ (C) and $La_{0.2}Sr_{0.8}Fe_{0.8}Ga_{0.2}O_{3-\delta}$ (D).

SEM micrographs showing typical $La_{1-x}Sr_xFe_{1-y}Ga_yO_{3-\delta}$ ceramic microstructures are presented in Fig. 4.2. The average grain size was found to increase with increasing strontium and gallium content, varying from approximately 5 to 20 μm. The partial cation substitution with either Sr or Ga results also in traces of a liquid phase formation at the grain boundaries of ceramic materials (Fig. 4.2C). In the case of doping with gallium, these tendencies are associated with higher sintering temperatures required to obtain gas-tight membranes (for example, from 1560 K for $La_{0.3}Sr_{0.7}FeO_{3-\delta}$ to 1690 K for $La_{0.3}Sr_{0.7}Fe_{0.6}Ga_{0.4}O_{3-\delta}$). Doping with strontium decreases melting points of the materials and thus leads to a liquid phase-assisted sintering and an enhanced grain growth. Notice, however, that no deviations from the formula cation composition were detected by EDS, within the experimental error limits.

4.3. Thermal and chemically induced expansion

Thermal expansion coefficients (TECs) in air, calculated from the dilatometric and high-temperature XRD data, are listed in Table 4.2. Within experimental error, thermal expansion of $La_{0.3}Sr_{0.7}Fe_{1-x}Ga_xO_{3-\delta}$ ceramics, measured by dilatometry, and crystal lattice expansion are similar. The TEC values (α) vary in a relatively narrow range $(11.9\text{-}16.0)\times10^{-6}$ K^{-1} at temperatures below 800-900 K and increase up to $(19.3\text{-}26.7)\times10^{-6}$ K^{-1} on further heating. As for numerous $SrFeO_{3-\delta}$-based phases [198,263], this is associated with oxygen losses on increasing temperature.

Table 4.2. Average TECs of $La_{1-x}Sr_xFe_{1-y}Ga_yO_{3-\delta}$ ceramics.

Composition	Dilatometry		High-T XRD	
	T, K	$\alpha \times 10^6$, K^{-1}	T, K	$\alpha \times 10^6$, K^{-1}
$La_{0.2}Sr_{0.8}Fe_{0.8}Ga_{0.2}O_{3-\delta}$	370-800 800-1080	16.0 ± 0.7 26.7 ± 0.8	–	–
$La_{0.3}Sr_{0.7}FeO_{3-\delta}$	300-780 780-1140	13.5 ± 0.2 24.8 ± 0.8	300-770 770-1170	14.9 ± 0.3 26.4 ± 0.3
$La_{0.3}Sr_{0.7}Fe_{0.8}Ga_{0.2}O_{3-\delta}$	300-920 920-1110	12.9 ± 0.3 25 ± 1	300-770 770-1170	14.9 ± 0.3 23.7 ± 0.8
$La_{0.3}Sr_{0.7}Fe_{0.6}Ga_{0.4}O_{3-\delta}$	300-930 930-1100	12.8 ± 0.2 20 ± 2	300-770 770-1170	11.7 ± 0.3 19.5 ± 0.9
$La_{0.4}Sr_{0.6}Fe_{0.6}Ga_{0.4}O_{3-\delta}$	300-870 930-1100	12.3 ± 0.2 23 ± 1	–	–
$La_{0.35}Sr_{0.6}Fe_{0.6}Ga_{0.4}O_{3-\delta}$	340-810 810-1100	12.4 ± 0.2 21.4 ± 0.6	–	–
$La_{0.5}Sr_{0.5}Fe_{0.6}Ga_{0.4}O_{3-\delta}$	330-850 850-1070	11.9 ± 0.2 19.3 ± 0.4	–	–

Thermal expansion increases with increasing strontium content due to a greater oxygen nonstoichiometry and a higher concentration of Fe^{4+}, decreasing on heating. Doping with gallium leads to decreasing thermal expansion of $La_{0.3}Sr_{0.7}Fe(Ga)O_{3-\delta}$, which may be explained either by reduced oxygen losses from gallium-containing specimens or by smaller total concentration of iron cations. For instance, high $(La,Sr)CoO_{3-\delta}$ thermal expansion coefficients are partially associated with numerous transitions in the electronic state of cobalt [41]. Decreasing concentration of transition metal cations in the B sites should suppress the lattice expansion when temperature increases.

The average TECs, listed in Table 4.2, should be understood as apparent, resulting from a combined effect of the true thermal expansion and chemical strain of the lattice. Another necessary comment is that in the low temperature range the oxygen content and, therefore, apparent TEC values may be affected by a slow oxygen equilibration with the gas phase. For this reason, main emphasis was given to studies of thermal and chemical expansion at temperatures above 770 K, where equilibrium with the surrounding atmosphere is more likely. Dilatometric curves of $La_{0.3}Sr_{0.7}FeO_{3-\delta}$ and $La_{0.3}Sr_{0.7}Fe_{0.6}Ga_{0.4}O_{3-\delta}$ samples in atmospheres with different $p(O_2)$ are shown in Fig. 4.3, as well as the corresponding values of the oxygen nonstoichiometry calculated from coulometric titration data [264].

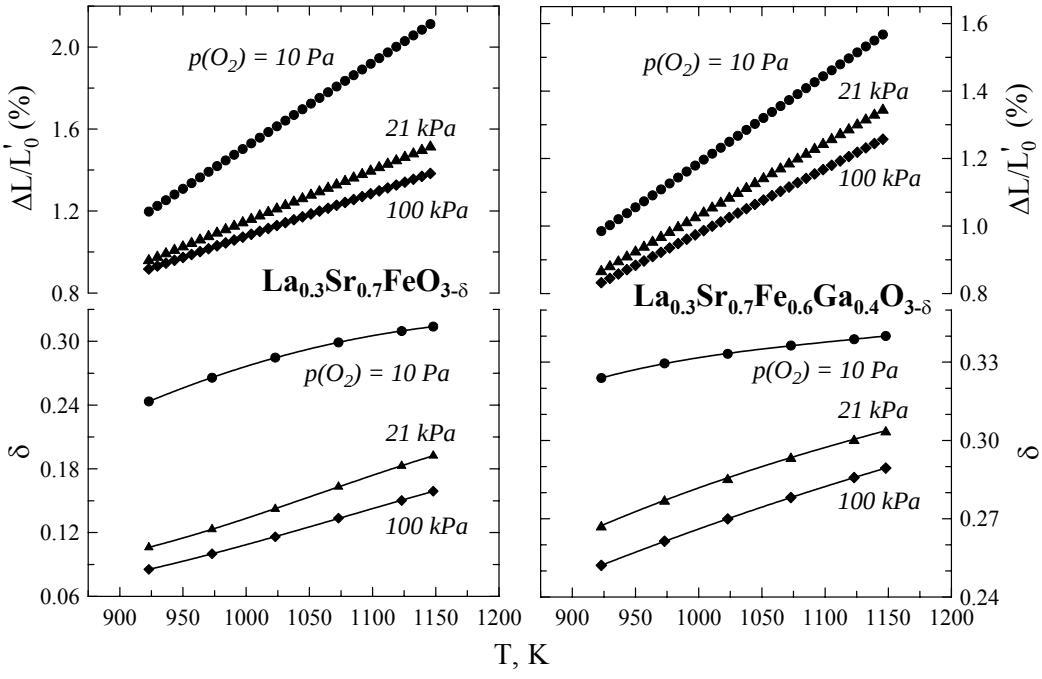

Fig. 4.3. Temperature dependencies of the relative elongation and oxygen nonstoichiometry of $La_{0.3}Sr_{0.7}FeO_{3-\delta}$ (left) and $La_{0.3}Sr_{0.7}Fe_{0.6}Ga_{0.4}O_{3-\delta}$ (right). Solid lines are for visual guidance only.

Within the studied range of oxygen pressure, the apparent thermal expansion of undoped lanthanum-strontium ferrite is higher than that of the Ga-containing composition. However, the oxygen nonstoichiometry variations with temperature or oxygen pressure are also considerably larger in the case of $La_{0.3}Sr_{0.7}FeO_{3-\delta}$ ceramics. For example, when the temperature increases from 923 to 1123 K, the changes in δ values of $La_{0.3}Sr_{0.7}Fe_{1-x}Ga_xO_{3-\delta}$ in air are approximately 0.078 and 0.033 for x = 0 and 0.4, correspondingly. When $p(O_2)$ increases from 10 Pa to 21 kPa at 1123 K, the oxygen content variations in these two materials are 0.127 and 0.039, respectively. This suggests that the great difference in TEC values for the undoped and Ga-containing ferrite ceramics, especially at low oxygen pressures (Table 4.3), is partly due to larger variations in oxygen deficiency and, hence, greater contribution of the chemical expansion to the apparent thermal expansion of $La_{0.3}Sr_{0.7}FeO_{3-\delta}$.

Table 4.3. TECs of $La_{0.3}Sr_{0.7}Fe_{1-y}Ga_yO_{3-\delta}$ ceramics in various atmospheres: average (α) and corrected for the chemical expansion due to oxygen loss in the course of heating (α_T).

Composition	$p(O_2)$, Pa	T, K	$\alpha \times 10^6$, K^{-1}	$p(O_2)$, Pa	T, K	$\alpha_T \times 10^6$, K^{-1}
$La_{0.3}Sr_{0.7}FeO_{3-\delta}$	21 kPa	298-773	12.98			
	100 kPa	773-1148	20.92	100 kPa	920-1150	9.8
	21 kPa	773-1148	24.89	21 kPa	920-1150	11.7
	10 Pa	773-1148	41.07	10 Pa	920-1150	26.3
$La_{0.3}Sr_{0.7}Fe_{0.6}Ga_{0.4}O_{3-\delta}$	21 kPa	298-773	11.65			
	100 kPa	773-1148	19.08	100 kPa	920-1150	11.5
	21 kPa	773-1148	21.47	21 kPa	920-1150	13.8
	10 Pa	773-1148	26.14	10 Pa	920-1150	22.5

The common approach, used in the literature [279,280] to describe the chemical expansion of a crystal lattice, is based on the assumption that the strain (ε_C) is a linear function of the oxygen nonstoichiometry variations. This means that, if the lattice expansion mechanism is the same within a given oxygen pressure range, the ratio ($\varepsilon_C/\Delta\delta$) should be constant. Here, the chemical strain is defined as [279]

$$\varepsilon_C = \Delta L / L_0 \qquad (4.1)$$

and a suitable reference state (L_0) can be chosen, in particular, unit oxygen pressure at a given temperature. Although this approach can be considered as a first approximation only [280], this simplification enables quantitative comparison of chemically-induced expansion in materials with

different nonstoichiometry and defect chemistry [279]. In this work the state at room temperature is denoted as L_0' (Fig. 4.3).

The parameter $\varepsilon_C/\Delta\delta$, which is used as a measure of the chemical strain, is plotted in Fig. 4.4 vs. the reciprocal temperature. For materials with x = 0 and 0.4, the temperature dependencies of ($\varepsilon_C/\Delta\delta$) are quite similar due to the similar crystal structure and composition. The absolute values of ($\varepsilon_C/\Delta\delta$) are, however, higher for Ga-containing materials. One possible explanation may refer to increasing level of structural disorder in $La_{0.3}Sr_{0.7}Fe(Ga)O_{3-\delta}$ when iron is substituted with gallium [264]. Data on Seebeck coefficient and partial thermodynamic functions of oxygen in the lattice of $La_{0.3}Sr_{0.7}Fe(Ga)O_{3-\delta}$ showed that Ga doping leads to local inhomogeneities in the lattice, such as local distortions or defect clusters near gallium cations [264]. Due to cation disorder in the B sublattice, this phenomenon suppresses long-range ordering and formation of vacancy-ordered microdomains, which is consistent with data on ionic conduction in $La_{0.3}Sr_{0.7}Fe_{1-x}Ga_xO_{3-\delta}$ in oxidizing atmospheres. Greater level of structural disorder may also explain the larger lattice chemical expansion of the Ga-containing material, with respect to the oxygen vacancy concentration.

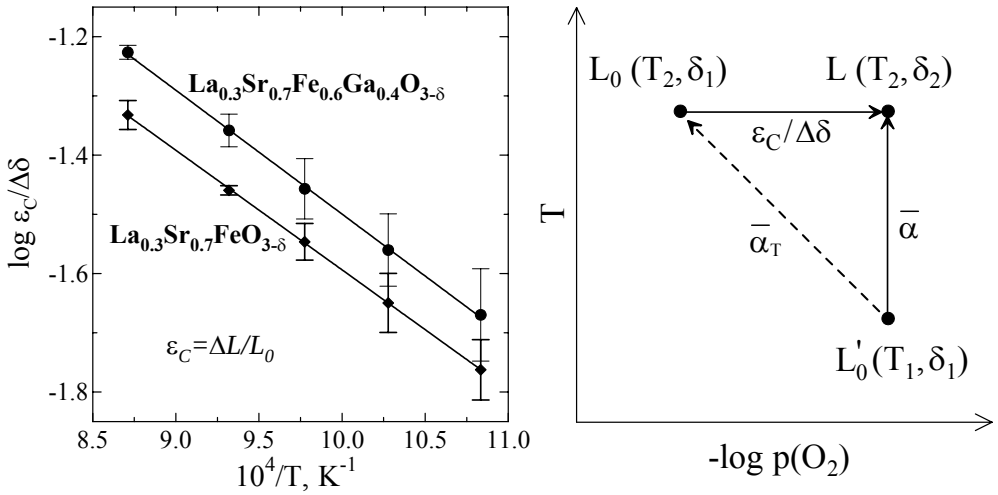

Fig. 4.4. Temperature dependence of the ($\varepsilon_C/\Delta\delta$) coefficient of $La_{0.3}Sr_{0.7}FeO_{3-\delta}$ and $La_{0.3}Sr_{0.7}Fe_{0.6}Ga_{0.4}O_{3-\delta}$ (left) and schematic illustration of the length variation on heating (right).

Another hypothesis refers to a decrease in the binding energy of oxides when the oxygen nonstoichiometry increases [281]. Such an assumption was introduced to explain the experimentally-observed correlation between the oxygen vacancy concentration and thermal expansion of

La(Sr)Ga(Mg)$O_{3-\delta}$ perovskites, and confirmed by molecular dynamics simulations [281]. In general, the δ - $\overline{\alpha}$ correlations are known in the literature [57,115] and may be explained by various factors (for example, an increase in the atomic vibration unharmonicity when the vacancy concentration increases). As the thermal and chemically-induced expansion have similar nature, both being determined by the lattice chemical bonding, the higher values of ($\varepsilon_C/\Delta\delta$) coefficient for $La_{0.3}Sr_{0.7}Fe_{0.6}Ga_{0.4}O_{3-\delta}$ with respect to $La_{0.3}Sr_{0.7}FeO_{3-\delta}$ (Fig. 4.4) may thus be considered to result from a lower binding energy due to the higher oxygen nonstoichiometry of the former composition (Fig. 4.3). The decrease in the binding energy is reflected by decreasing absolute values of the partial molar enthalpy of oxygen when gallium concentration in $La_{0.3}Sr_{0.7}Fe(Ga)O_{3-\delta}$ increases [264].

Comparison of the ($\varepsilon_C/\Delta\delta$) parameter of $La_{0.3}Sr_{0.7}Fe(Ga)O_{3-\delta}$ with literature data [279] shows that lanthanum-strontium ferrite – based ceramics exhibit significantly higher chemical expansion with respect to $LaCrO_3$-based materials. In particular, for B-site doped $La_{1-x}A_xCrO_{3-\delta}$ (A = Ca, Sr), the ratio ($\varepsilon_C/\Delta\delta$) at 1273 K varies in the range $(1.2\text{-}3.6)\times10^{-2}$. In the case of gadolinium-doped ceria, $Ce_{1-x}Gd_xO_{2-\delta}$, the relative chemical strain has values comparable to those of $La_{0.3}Sr_{0.7}Fe(Ga)O_{3-\delta}$ at temperatures above 1120 K, but is up to 7-8 times higher than that of the ferrite-based ceramics at lower temperatures [279]. The ($\varepsilon_C/\Delta\delta$) parameter in doped ceria increases with increasing Gd concentration [279]. These trends are likely to agree with the above hypothesis on the correlation between ($\varepsilon_C/\Delta\delta$) and δ values.

Summarizing the above discussion, Fig. 4.5 compares oxygen nonstoichiometry dependencies of the TECs, corrected for the chemical strain on heating, the ($\varepsilon_C/\Delta\delta$) coefficient, and the oxygen ionic conductivity of $La_{0.3}Sr_{0.7}Fe_{1-x}Ga_xO_{3-\delta}$ ceramics in air [264]. Notice that due to surface exchange-affected oxygen permeability and faradaic efficiency of $La_{0.3}Sr_{0.7}FeO_{3-\delta}$ membranes, the apparent ionic conductivity of the undoped ferrite is slightly lower than the true values; on the contrary, no surface effect was found for the two Ga-containing compositions [264]. The coefficients $\overline{\alpha}_T$ and ($\varepsilon_C/\Delta\delta$) both increase with increasing oxygen deficiency, when x increases. Similar tendencies are found for the ionic conductivity (σ_o) and the ratio σ_o/δ. As oxygen transport in perovskites occurs via the vacancy mechanism, the latter quantity is proportional to the oxygen vacancy mobility and, in theory, should be independent or slightly decrease with increasing δ due to lower concentration of sites available for the vacancy jumps. Increasing σ_o/δ ratio with δ indicates, hence, lower energetic requirement for ionic conduction when gallium is incorporated into the B sites.

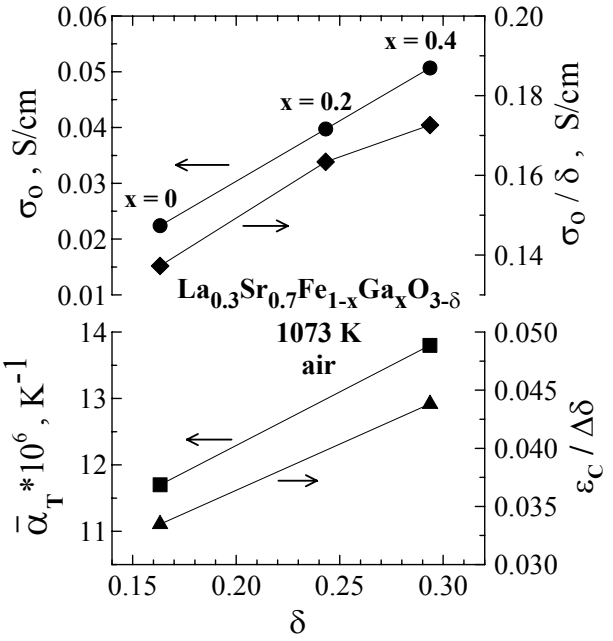

Fig. 4.5. Oxygen nonstoichiometry dependence of the ionic conductivity, σ_O/δ ratio, corrected TECs and ($\varepsilon_C/\Delta\delta$) coefficient in $La_{0.3}Sr_{0.7}Fe_{1-x}Ga_xO_{3-\delta}$ system.

The correlations between ion diffusivity and thermal expansion are well known [57,115,153] and explained by decreasing interaction of ions in the lattice as the crystal expands. One analogous explanation is applicable to the correlation between chemical strain and ionic conductivity (Fig. 4.5). The observed increase in the vacancy mobility, thermal expansion and $\varepsilon_C/\Delta\delta$ coefficient with increasing δ might also be attributed to a decrease in the binding energy of perovskite phases, resulting from greater vacancy concentration [281]. At the same time, one should briefly mention that all these correlations, including the increase in δ with x, reflect changes in thermodynamic properties of lanthanum-strontium ferrite with Ga doping. Substitution of gallium for iron was shown to affect the equilibrium of the perovskites with the gas phase, making oxygen incorporation energetically less favorable [264].

4.4. Oxygen permeability

The dependencies of oxygen permeation through $La_{0.3}Sr_{0.7}FeO_{3-\delta}$ membranes of various thickness on the oxygen partial pressure gradient are given in Fig. 4.6A; the corresponding values of the specific oxygen permeability are presented in Fig. 4.6B. While the permeation fluxes decrease with increasing

membrane thickness, the oxygen permeability clearly increases. The same dependencies were found for $La_{0.4}Sr_{0.6}Fe_{0.6}Ga_{0.4}O_{3-\delta}$. Hence, oxygen transport through $La_{0.3}Sr_{0.7}FeO_{3-\delta}$ and $La_{0.4}Sr_{0.6}Fe_{0.6}Ga_{0.4}O_{3-\delta}$ ceramics is limited by both surface exchange and bulk ambipolar conduction. Similar behavior was observed for all $La_{1-x}Sr_xFe_{1-y}Ga_yO_{3-\delta}$ membranes with $x < 0.7$ and $y \leq 0.6$, in agreement with Kim et al. [282] who reported surface-limited permeation for $La_{0.5}Sr_{0.5}Fe_{0.8}Ga_{0.2}O_{3-\delta}$ ceramics. One can assume, therefore, that the surface exchange rates of $(La,Sr)(Fe,Ga)O_{3-\delta}$ increase on doping with Ga and Sr.

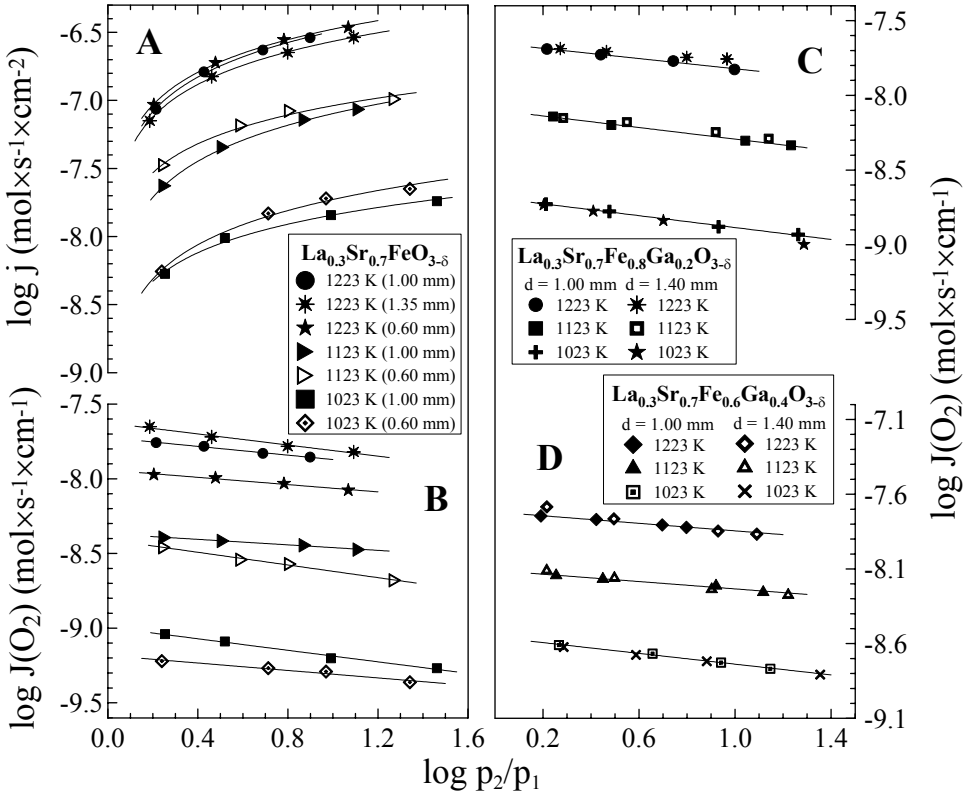

Fig. 4.6. Dependencies on the $p(O_2)$ gradient of the oxygen permeation flux (A) and specific oxygen permeability (B) of $La_{0.3}Sr_{0.7}FeO_{3-\delta}$, $La_{0.3}Sr_{0.7}Fe_{0.8}Ga_{0.2}O_{3-\delta}$ (C) and $La_{0.3}Sr_{0.7}Fe_{0.6}Ga_{0.4}O_{3-\delta}$ (D). Solid lines are for visual guidance only.

In contrast, similar results for $La_{0.3}Sr_{0.7}Fe_{1-x}Ga_xO_{3-\delta}$ ($x = 0.2$-0.4) showed negligible effect of the oxygen surface exchange on oxygen permeability of Ga-containing materials (Figs. 4.6C,D). The $J(O_2)$ values of the $La_{0.3}Sr_{0.7}Fe(Ga)O_{3-\delta}$ ceramics are independent of membrane thickness within experimental error, i.e. the integral form of the Wagner law is observed. Notice that the scale in Figs.

4.6C,D is the same as that in Fig. 4.6B. The same dependencies were found for $La_{0.2}Sr_{0.8}Fe_{0.8}Ga_{0.2}O_{3-\delta}$. Thus, the permeability of $La_{0.3}Sr_{0.7}Fe_{1-x}Ga_xO_{3-\delta}$ (x = 0.2-0.4) and $La_{0.2}Sr_{0.8}Fe_{0.8}Ga_{0.2}O_{3-\delta}$ is predominantly limited by the bulk ambipolar conductivity, which makes possible to calculate the ionic conductivity of $La_{0.3}Sr_{0.7}Fe(Ga)O_{3-\delta}$ from data on oxygen permeation and total conductivity.

The difference in the behavior of undoped and Ga-doped $La_{0.3}Sr_{0.7}FeO_{3-\delta}$ can be attributed to either increasing surface exchange rates or decreasing ionic conductivity when gallium substitutes iron in the B sublattice. The obtained results do not allow a conclusive judgement on this matter and both reasons may apply. One should also note that the observed behavior of $La_{0.3}Sr_{0.7}(Fe,Ga)O_{3-\delta}$ and $La_{0.2}Sr_{0.8}Fe_{0.8}Ga_{0.2}O_{3-\delta}$ membranes seems to be in controversy with the $La_{0.4}Sr_{0.6}Fe_{0.6}Ga_{0.4}O_{3-\delta}$ ceramics. Such a contradiction may result from the lower strontium content in the latter material. It is well known that both oxygen diffusivity and surface exchange rates in $(La,Sr)FeO_{3-\delta}$ solid solutions are functions of the La/Sr ratio [16].

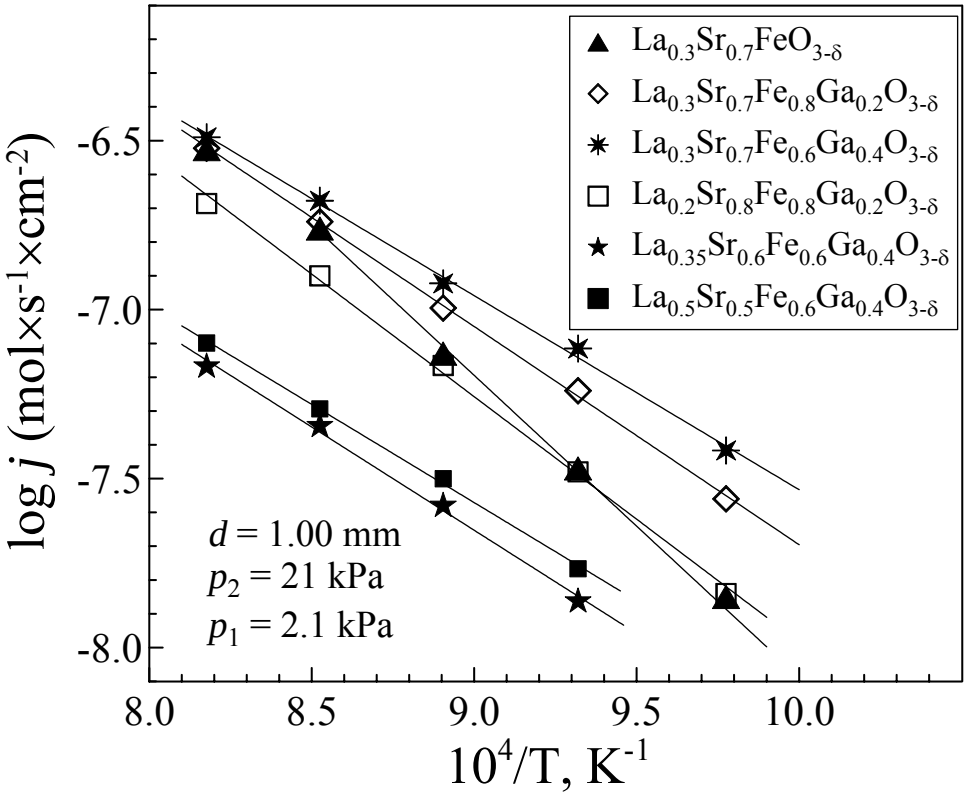

Fig. 4.7. Temperature dependencies of the oxygen permeation flux density through $La_{1-x}Sr_xFe_{1-y}Ga_yO_{3-\delta}$ membranes under fixed $p(O_2)$ gradient.

The oxygen fluxes through $La_{0.3}Sr_{0.7}Fe_{1-x}Ga_xO_{3-\delta}$ (x = 0-0.4) membranes are found to increase with x, whereas the apparent activation energy for oxygen permeability decreases with gallium additions (Fig. 4.7). For Ga-containing compositions (x = 0.2-0.4), the temperature dependence of the permeation is determined by the activation energy for the bulk ambipolar conductivity. In the case of undoped $La_{0.3}Sr_{0.7}FeO_{3-\delta}$, however, both bulk ion transport and surface exchange rate affect the temperature dependence of the permeability. This can be confirmed comparing the obtained apparent activation energy for oxygen permeability of $La_{0.3}Sr_{0.7}FeO_{3-\delta}$ (161±4 kJ/mol) with literature data on surface exchange for $(La,Sr)FeO_{3-\delta}$ phases. For instance, the activation energy for the surface exchange coefficient of $La_{0.75}Sr_{0.25}FeO_{3-\delta}$ calculated from isotopic exchange data was 185±27 kJ/mol, while the E_a value for the vacancy diffusivity is as low as 114±23 kJ/mol [16]. Hence, the high activation energy for oxygen permeability of $La_{0.3}Sr_{0.7}FeO_{3-\delta}$ (Fig. 4.7) may partially result from the oxygen exchange limitations.

4.5. Behavior in reducing atmospheres

Testing of $La_{0.3}Sr_{0.7}Fe(Ga)O_{3-\delta}$ phases in CO_2-containing atmospheres demonstrated their satisfactory stability with respect to interaction with carbon dioxide. As an example, Fig. 4.8A presents TGA data on $La_{0.3}Sr_{0.7}Fe_{0.8}Ga_{0.2}O_{3-\delta}$ powder in purified air and in a gas mixture containing CO_2. For comparison, results of a similar test with SrO are given. Before testing, the samples were annealed in air at 1070-1250 K in the TGA cell, and then slowly cooled to 823 K. The ratio between CO_2, O_2 and N_2 concentrations was 18:15:67 in the case of $La_{0.3}Sr_{0.7}Fe_{0.8}Ga_{0.2}O_{3-\delta}$ and 19:17:64 for SrO. While formation of $SrCO_3$ from strontium oxide occurs extensively, no interaction between $La_{0.3}Sr_{0.7}Fe_{0.8}Ga_{0.2}O_{3-\delta}$ and carbon dioxide was detected by gravimetric analysis within the experimental detection limits. DTA tests with $La_{0.3}Sr_{0.7}Fe_{0.8}Ga_{0.2}O_{3-\delta}$ powders, pre-kept in the CO_2 atmosphere during different periods of time, did not reveal also any thermal effects on heating. This suggests that adsorption of CO_2 on the grain surface of the solid solutions does not result in considerable formation of carbonates and in gross decomposition of the perovskite phase.

On the other hand, infrared (IR) absorption studies of the $La_{0.3}Sr_{0.7}Fe_{0.8}Ga_{0.2}O_{3-\delta}$ powders indicate trace amounts of $SrCO_3$ after keeping samples in carbon dioxide at room temperature. The example is shown in Fig. 4.8B where a comparison is given of the Fourier Transformed IR spectra for the $La_{0.3}Sr_{0.7}Fe_{0.8}Ga_{0.2}O_{3-\delta}$ powder before and after treatment in CO_2. The IR absorption band at $\bar{\nu}$ ~860 cm^{-1} appearing in the spectrum of the CO_2-treated sample undoubtedly indicates a formation of minor amounts of strontium carbonate [283].

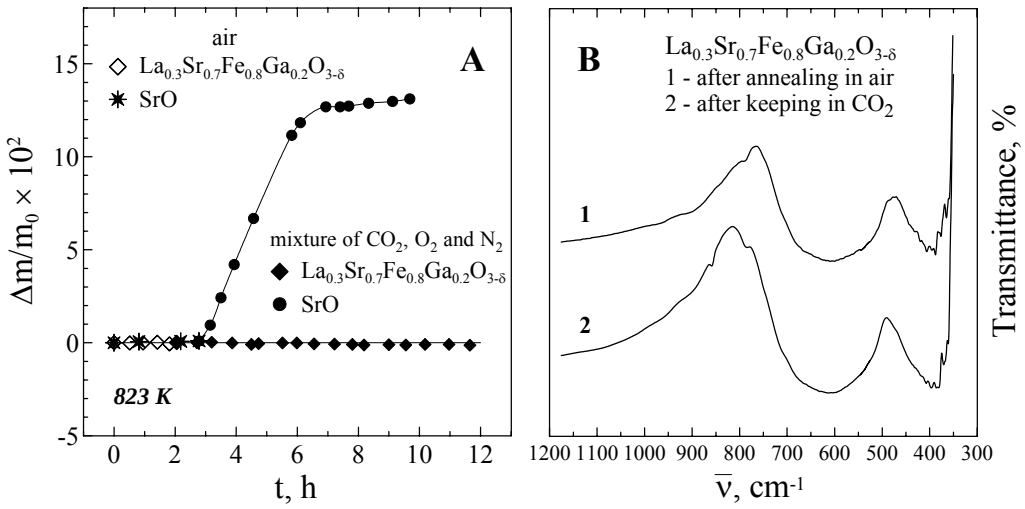

Fig. 4.8. A: relative weight changes of $La_{0.3}Sr_{0.7}Fe_{0.8}Ga_{0.2}O_{3-\delta}$ and SrO in air purified from CO_2 and in a mixture of CO_2, O_2 and N_2. B: Fourier Transformed IR absorption spectra of $La_{0.3}Sr_{0.7}Fe_{0.8}Ga_{0.2}O_{3-\delta}$.

Therefore, one must conclude that surface decomposition of the perovskite phase because of the interaction with carbon dioxide, though slow, nonetheless takes place at low temperatures. Similar behavior is found for $Sr(Fe,Ti)O_{3-\delta}$ solid solutions [284]. It is important, however, that compact sintered ceramic samples of $La_{0.3}Sr_{0.7}Fe_{1-x}Ga_xO_{3-\delta}$ did not show any evidence of the degradation even after several months of storage in CO_2 atmosphere at room temperature.

5. Ionic transport in ferrite garnets

5.1. Phase relationships and crystal structure

XRD analysis showed that all ceramic materials listed in Table 5.1 were single-phase. Their structure was identified as garnet-type (S.G. $Ia\bar{3}d$, Appendix 1C). The amount of dopants introduced in these phases was considered close to the solubility limits. For $Gd_{3-x}Ca_xFe_5O_{12-\delta}$, the solid solution formation limit corresponds to values of x lower than 0.7; further calcium additions lead to a segregation of $Ca_4Fe_{14}O_{25}$-based phase. The solid solubility of Co and Ni in the iron sublattice of $Gd_{3-x}Ca_xFe_{5-z}B_zO_{12-\delta}$ (x = 0-0.5) was found to be lower than 4 mol.%. Substitution of 4-20% of iron with transition metal cations promotes formation of a perovskite phase coexisting with a spinel; no traces of the garnet phase were observed in the XRD patterns of $Gd_{3-x}Ca_xFe_{5-z}B_zO_{12-\delta}$ at z = 0.2 - 1.0. As the thermodynamic stability of garnet ferrites increases with decreasing A-site cation radii, the attempt to substitute 20% iron in $Y_3Fe_5O_{12}$ with nickel was, on the contrary, successful, in agreement with literature data [285]. Finally, the amount of rare-earth dopants incorporated in the A-sublattice of the garnets is also close to their maximum solubility [285]. In particular, attempts to synthesize $Gd_2PrFe_5O_{12\pm\delta}$ and $Gd_2PrFe_{5-z}Co_zO_{12\pm\delta}$ garnets resulted in a segregation of $PrFeO_3$-based perovskite phases.

Table 5.1. Properties of $Gd_3Fe_5O_{12}$- and $Y_3Fe_5O_{12}$-based ceramics.

Composition	$T_{sintering}$, K	a, Å	ρ_{exp} / ρ_{theor}, %	$\alpha \times 10^6$ K^{-1} (370-1150 K)
$Gd_3Fe_5O_{12}$	1740	12.474(1)	99.3	10.86 ± 0.01
$Gd_{2.2}Pr_{0.8}Fe_5O_{12}$	1690	12.503(6)	98.0	10.76 ± 0.01
$Gd_{2.5}Ca_{0.5}Fe_5O_{12}$	1490	12.459(3)	97.4	10.36 ± 0.01
$Y_{2.5}Ca_{0.5}Fe_5O_{12}$	1510	12.377(2)	97.7	10.78 ± 0.01
$Y_{2.5}Ca_{0.5}Fe_4NiO_{12}$	1540	12.397(5)	91.2	10.0 ± 0.1
$Y_{2.5}Ca_{0.25}Nd_{0.25}Fe_5O_{12}$	1540	12.399(5)	91.8	9.4 ± 0.2

The unit cell parameter variations (Table 5.1) agree, in general, with the radii of dopant cations [8]. For instance, the lattice expands when Gd is substituted with larger Pr. The increase in the unit cell parameter on Ni doping suggests a presence of divalent nickel ions, the radius of which is larger than that of Fe^{3+}; as shown below, this leads to oxygen vacancy formation and thus to an increase in the ionic conductivity. Incorporation of calcium in the A-sublattice may be compensated, according to the electroneutrality condition, by formation of either oxygen vacancies or electron holes. The former mechanism is expected to increase the partial ionic conductivity; the latter should increase the p-type

electronic conduction due to a greater concentration of charge carriers localized on iron sites, forming Fe^{4+} cations [251,285]. Data presented below shows that both ionic and electronic conductivities of garnet phases increase when Ca^{2+} is introduced in the A site, indicating a combination of both charge compensation mechanisms. Such a situation is quite typical for perovskite-type oxides [153,190,219]. One particular result is that Ca doping leads to a lattice contraction due to formation of Fe^{4+} cations (Appendix 3, Table 2) having a smaller size than trivalent iron [8].

On the other hand, it should be mentioned that any attempt to describe the unit cell parameter variations in garnets as a direct consequence of changes in the cation size is oversimplified. The structure of garnet (Fig. 1.27) is complex and consists of 160 ions, forming Fe-O octahedra and tetrahedra and A-O dodecahedra. In contrast to the ideal perovskite structure, packing of ions in garnet lattice is loose; the unit cell parameter variations result not only from changing of the metal-oxygen bond lengths, but also from tilting of the polyhedra in the lattice.

5.2. Ceramic microstructure

When discussing microstructural features of garnet materials (Fig. 5.1), one can note that the grain size is primarily determined by the sintering temperature (Table 5.1). For $Gd_3Fe_5O_{12}$ and $Gd_{2.2}Pr_{0.8}Fe_5O_{12}$ ceramics sintered at 1690-1740 K, the grains are as large as 7-15 μm. The decreasing sintering temperature down to 1490-1540 K leads to decreasing average grain size to 2-5 μm, as observed for all Ca-containing compositions. Increasing sintering time results in grain growth; the average grain size of garnet ceramics sintered for 50 h increased up to 3-8 μm. In the case of $(Y,Ca)_3Fe_5O_{12}$-based garnets, traces of liquid-phase assisted sintering can be seen at the grain boundaries (Fig. 5.1D). At the same time, SEM studies suggest a presence of local inhomogeneities in the $Y_{2.5}Ca_{0.5}Fe_4NiO_{12-\delta}$ ceramics (Fig. 5.1D), which may be associated to a slight segregation of perovskite phase at grain boundaries, not detected in the XRD patterns.

A **B**

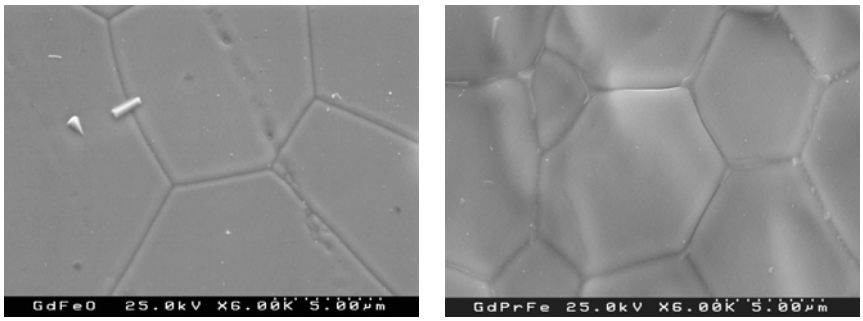

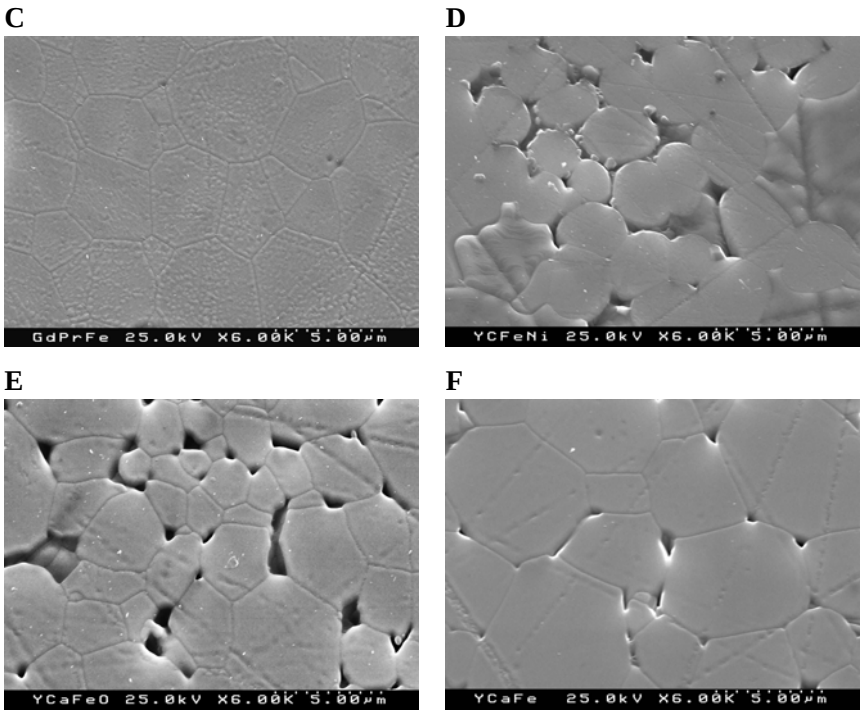

Fig. 5.1. SEM micrographs of ferrite garnet ceramics: $Gd_3Fe_5O_{12}$ (A), $Gd_{2.2}Pr_{0.8}Fe_5O_{12}$ (B), $Gd_{2.5}Ca_{0.5}Fe_5O_{12}$ (C), $Y_{2.5}Ca_{0.5}Fe_4NiO_{12}$ (D), $Y_{2.5}Ca_{0.5}Fe_5O_{12}$ sintered for 5 (E) and 50 (F) hours.

5.3. Thermal expansion and total conductivity

Contrary to Fe-containing perovskites [198,263], thermal expansion of ferrite-based garnets is linear within the studied temperature range, 373-1273 K (Fig. 5.2A), indicating an absence of phase transition. The TECs vary in the narrow range $(9.4 - 10.9)\times10^{-6}$ K^{-1} (Table 5.1). The low TEC values are compatible with those of widely-used solid electrolytes based on zirconia and ceria [111], thus enabling the use of garnet-based materials in high-temperature electrochemical cells such as sensors or SOFCs. As expected for stable oxide materials [288], sintering for a long time and grain size of $Gd_{2.5}Ca_{0.5}Fe_5O_{12}$ has no effect on the thermal expansion (inset in Fig. 5.2A).

The results on the total conductivity of garnet-based solid solutions (Fig. 5.2B) are in excellent agreement with the literature [285,251] and confirm the conclusion that electronic conduction in ferrite garnets occurs by hopping [251]. The total conductivity, predominantly electronic, increases when lower-valence cations are incorporated in the lattice due to increasing p-type charge carrier concentration. The values of the activation energy (E_a) calculated by the standard Arrhenius equation are listed in Table 5.2. Doping with calcium and nickel results in decreasing E_a from about 80 kJ/mol,

which is a typical hopping activation energy for holes in Fe-containing garnets [290], down to 20-30 kJ/mol. Such a behavior is common for perovskite-type phases with a small-polaron mechanism of p-type conduction [153].

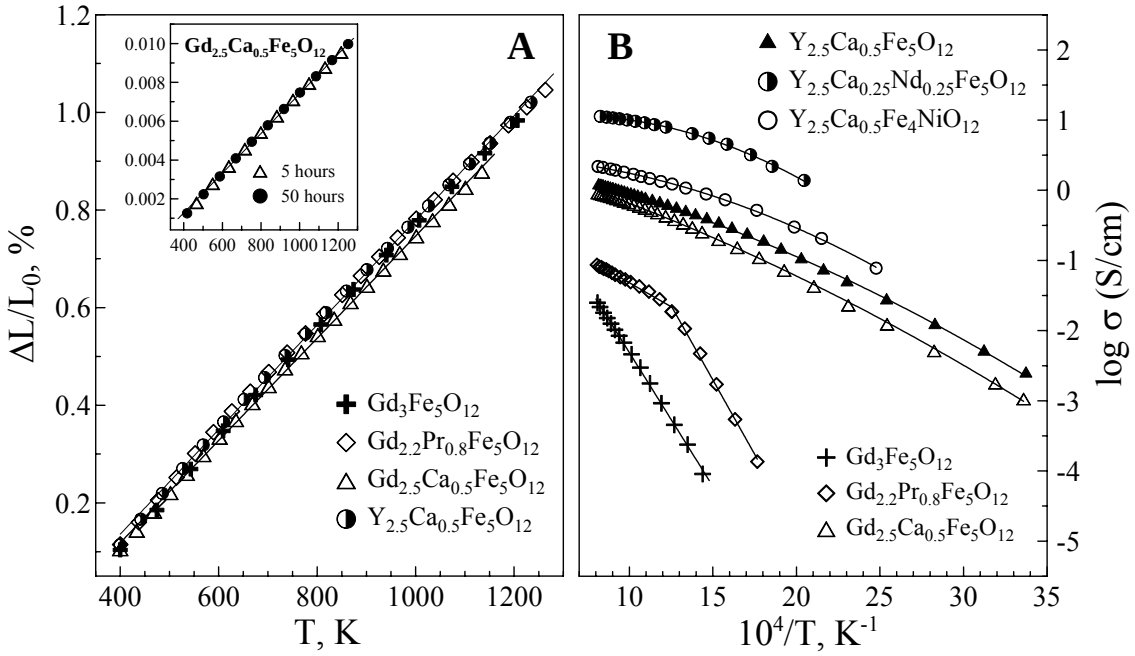

Fig. 5.2. Dilatometric curves (A) and the total conductivity (B) of garnet ceramics in air.

Substitution of A-site cations with Pr and Nd also leads to an increase in the total conductivity (Fig. 5.2B). In the case of $Gd_{2.2}Pr_{0.8}Fe_5O_{12}$, higher conductivity with respect to undoped $Gd_3Fe_5O_{12}$ is probably due to a significant contribution of variable-valence praseodymium cations (Pr^{3+}/Pr^{4+}) to the electronic transport processes; the change in the activation energy at approximately 800-850 K (Table 5.2) may be associated with oxygen losses from the lattice. The higher total conductivity of $Y_{2.5}Ca_{0.25}Nd_{0.25}Fe_5O_{12-\delta}$, than that of $Y_{2.5}Ca_{0.5}Fe_5O_{12-\delta}$, might suggest segregation of a highly-conductive perovskite-like phase at grain boundaries of Nd-containing ceramics. Although this cannot be distinguished by SEM/EDS, such an assumption is in agreement with data on oxygen permeability, presented below. Nevertheless, the difference in the conductivity values of $Y_{2.5}Ca_{0.5}Fe_5O_{12-\delta}$ and $Y_{2.5}Ca_{0.25}Nd_{0.25}Fe_5O_{12-\delta}$ is rather small.

Table 5.2. Arrhenius model parameters for the total conductivity of $Gd_3Fe_5O_{12}$- and $Y_3Fe_5O_{12}$-based ceramics in air.

Composition	T, K	E_A, kJ/mol	$\ln(A_0)$, (S K)/cm
$Gd_3Fe_5O_{12}$	700-1270	81 ± 1	11.3 ± 0.1
$Gd_{2.2}Pr_{0.8}Fe_5O_{12}$	520-800	80 ± 4	14.9 ± 0.7
	800-1270	32.6 ± 0.6	7.8 ± 0.1
$Gd_{2.5}Ca_{0.5}Fe_5O_{12}$	300-800	27.3 ± 0.1	9.91 ± 0.03
	800-1270	23.7 ± 0.1	9.34 ± 0.01
$Y_{2.5}Ca_{0.5}Fe_5O_{12}$	300-800	25.4 ± 0.4	10.1 ± 0.1
	800-1270	21.8 ± 0.1	9.40 ± 0.01
$Y_{2.5}Ca_{0.5}Fe_4NiO_{12}$	500-1250	20 ± 1	11.6 ± 0.1
$Y_{2.5}Ca_{0.25}Nd_{0.25}Fe_5O_{12}$	400-1250	21 ± 1	10.1 ± 0.1

5.4. Oxygen permeability

Fig. 5.3A presents the dependence of the oxygen permeation fluxes through $Gd_{2.5}Ca_{0.5}Fe_5O_{12-\delta}$ ceramics of various thickness on the oxygen pressure gradient. The corresponding values of the specific oxygen permeability are shown in Fig. 5.3B. Whilst the permeation fluxes decrease with increasing membrane thickness, the oxygen permeability is thickness-independent. This means that the integral form of the Wagner law is observed, indicating a negligible effect of the surface exchange kinetics on the overall transport of oxygen. A similar behavior was also found for other studied garnets. Notice that negligible surface exchange limitations to the oxygen transport in oxidizing atmospheres are characteristic of many ferrite phases with a relatively low ionic conductivity, including $La(A)FeO_{3-\delta}$ (A = Pb, Sr) [190,194], $LaFe(Ni)O_{3-\delta}$ [219] and $Sr_4Fe_6O_{13\pm\delta}$ [249].

The fact that the permeation fluxes through garnet-type ceramics are predominantly limited by the bulk ambipolar conduction, allowed the calculation of the ion transference numbers and ionic conductivity from data on oxygen permeability and total conductivity, using Eqs. (2.9) and (2.10). The values of the ambipolar conductivity were estimated from the slope of j *vs.* $\log(p_2/p_1)$ dependencies (see Eqs.(1) and (2)) at minimum oxygen pressure gradient (p_1 = 4-21 kPa).

The oxygen ion transference numbers, calculated from the oxygen permeability results, vary in the range 1×10^{-5} to 5×10^{-3} (Table 5.3). As the activation energy for ionic transport (Table 5.4) is higher than that for electronic (Table 5.2), increasing temperature leads to a greater ionic contribution to the total conductivity. It should also be mentioned that, due to low t_o values, the ambipolar

conductivity of ferrite garnets is almost independent of the electronic conduction and determined primarily by the ionic transport.

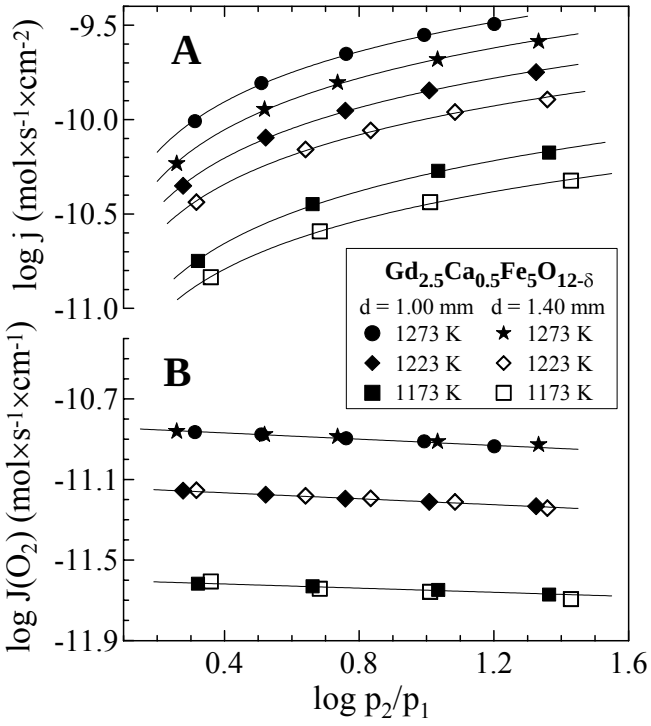

Fig. 5.3. Oxygen pressure gradient dependencies of (A) oxygen permeation flux and (B) oxygen permeability of $Gd_{2.5}Ca_{0.5}Fe_5O_{12-\delta}$ membranes.

Table 5.3. Oxygen ion transference numbers (t_O) of $Gd_3Fe_5O_{12}$- and $Y_3Fe_5O_{12}$-based phases in air.

Composition	1173 K	1223 K	1248 K	1273 K
$Gd_3Fe_5O_{12}$	1.7×10^{-3}	3.1×10^{-3}	4.1×10^{-3}	4.7×10^{-3}
$Gd_{2.2}Pr_{0.8}Fe_5O_{12}$	3.6×10^{-4}	8.9×10^{-4}	1.3×10^{-3}	1.6×10^{-3}
$Gd_{2.5}Ca_{0.5}Fe_5O_{12}$	3.9×10^{-5}	9.4×10^{-5}	1.3×10^{-4}	1.7×10^{-4}
$Y_{2.5}Ca_{0.5}Fe_5O_{12}$	4.6×10^{-5}	9.7×10^{-5}	1.4×10^{-4}	1.8×10^{-4}
$Y_{2.5}Ca_{0.5}Fe_4NiO_{12}$	1.4×10^{-5}	2.8×10^{-5}	3.6×10^{-5}	-
$Y_{2.5}Ca_{0.25}Nd_{0.25}Fe_5O_{12}$	4.1×10^{-5}	9.3×10^{-5}	1.1×10^{-4}	-

Table 5.4. Arrhenius model parameters for oxygen ionic conductivity of $Gd_3Fe_5O_{12}$- and $Y_3Fe_5O_{12}$-based phases in air.

Composition	T, K	E_A, kJ/mol	$\ln(A_0)$, (S K)/cm
$Gd_3Fe_5O_{12}$	1173-1273	214 ± 11	19 ± 1
$Gd_{2.2}Pr_{0.8}Fe_5O_{12}$	1173-1273	224 ± 14	20 ± 1
$Gd_{2.5}Ca_{0.5}Fe_5O_{12}$	1173-1273	211 ± 12	18 ± 1
$Y_{2.5}Ca_{0.5}Fe_5O_{12}$	1173-1273	191 ± 4	16.7 ± 0.4
$Y_{2.5}Ca_{0.5}Fe_4NiO_{12}$	1173-1248	176 ± 8	16.3 ± 0.8
$Y_{2.5}Ca_{0.25}Nd_{0.25}Fe_5O_{12}$	1173-1248	188 ± 25	17 ± 2

5.5. Oxygen ionic conductivity: influence of microstructure

Fig. 5.4 shows the temperature dependence of the ionic conductivity and oxygen permeation flux for two $Y_{2.5}Ca_{0.5}Fe_5O_{12-\delta}$ membranes sintered for various periods of time; the difference in their microstructures is illustrated by Fig. 5.1. In general, the tendency exhibited by the garnet ceramics is typical for ion-conducting ceramic materials, including $Ce(Gd)O_{2-\delta}$ [288] and $La(Sr)CoO_{3-\delta}$ [289]. Namely, grain growth resulting from a long sintering time leads to a higher ionic conduction due to smaller grain-boundary area per unit volume and, hence, lower boundary resistivity. For garnet ceramics, however, this effect is rather small, comparable to the level of experimental uncertainty. Such a behavior is observed, most probably, because the temperatures chosen for the permeation experiments (1173-1273 K) are quite high. As a rule, the activation energy for grain-boundary ionic conduction is higher than that for the grain bulk; therefore the contribution of boundaries to the total ionic resistivity increases when temperature decreases [288,289]. However, as the oxygen permeability of garnet ferrites is relatively low, decreasing temperature below 1173 K was undesirable due to enhanced experimental errors. Taking into account the results shown in Fig. 5.4, the presented data on ionic conductivity are considered essentially unaffected by the grain-boundary processes.

5.6. Oxygen ionic conductivity as function of cation composition

The oxygen permeation fluxes through garnet ceramics are presented in Fig. 5.5 as a function of the oxygen partial pressure gradient and temperature; Fig. 5.6A shows Arrhenius plots of the ionic conductivity. As for numerous perovskite-type oxides [153,190,194,219], incorporation of lower-valence cations, such as Ca and Ni, into the garnet lattice, leads to increasing oxygen permeability and ionic conductivity. This phenomenon, confirming a vacancy mechanism for oxygen diffusion, is in

excellent agreement with the literature [290]. The maximum oxygen permeability was found for $Y_{2.5}Ca_{0.5}Fe_4NiO_{12-\delta}$ ceramics, where the concentration of acceptor dopants is maximum. As the content of lower-valence cations in the studied garnets is close to the solid solubility limits, it is unlikely that the ionic conductivity of $Gd_3Fe_5O_{12}$- and $Y_3Fe_5O_{12}$-based phases could be further enhanced to a considerable extent.

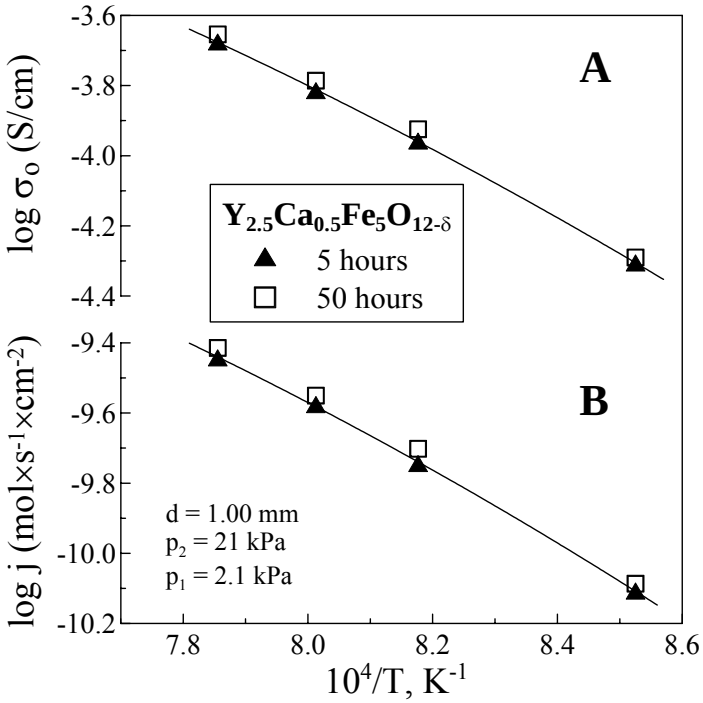

Fig. 5.4. Temperature dependence of (A) oxygen ionic conductivity and (B) oxygen permeation flux through $Y_{2.5}Ca_{0.5}Fe_5O_{12-\delta}$ ceramics sintered for 5 and 50 hours.

With respect to other garnet-type aluminates and gallates, even the ionic conductivity of undoped $Gd_3Fe_5O_{12}$ is significantly higher (Fig. 5.6B). Most probably, such a behavior is associated with a lower energy for oxygen vacancy formation in the ferrite lattice, which is reflected by the lower effective activation energy for ionic transport, varying in the range 175-225 kJ/mol (Table 5.4). For comparison, the corresponding values in $Y_3Al_5O_{12}$ and $Gd_3Ga_5O_{12}$ are 260-280 kJ/mol [290,291]. Note also that E_a values for yttrium-containing ferrites are lower compared to the phases where the A-sublattice is occupied with gadolinium.

When analyzing the ionic conduction as a function of A-site composition, one should mention that the oxygen permeability of $Gd_{2.2}Pr_{0.8}Fe_5O_{12\pm\delta}$ is slightly higher than that of undoped gadolinium ferrite, especially at temperatures above 1223 K (Fig. 5.5A). This might suggest a contribution of oxygen interstitial migration to the ionic conductivity of garnet phases with low oxygen vacancy content. The activation energy for the interstitial diffusion mechanism is typically higher than for the vacancy migration [292]; a presence of hyperstoichiometric oxygen in the lattice of $Gd_{2.2}Pr_{0.8}Fe_5O_{12\pm\delta}$ seems quite likely due to possible formation of Pr^{4+} cations, similar to Pr-containing perovskites [153]. For a combined transport mechanism, the contribution of interstitial diffusion to the total ionic conductivity is often small compared to the oxygen vacancy contribution [292].

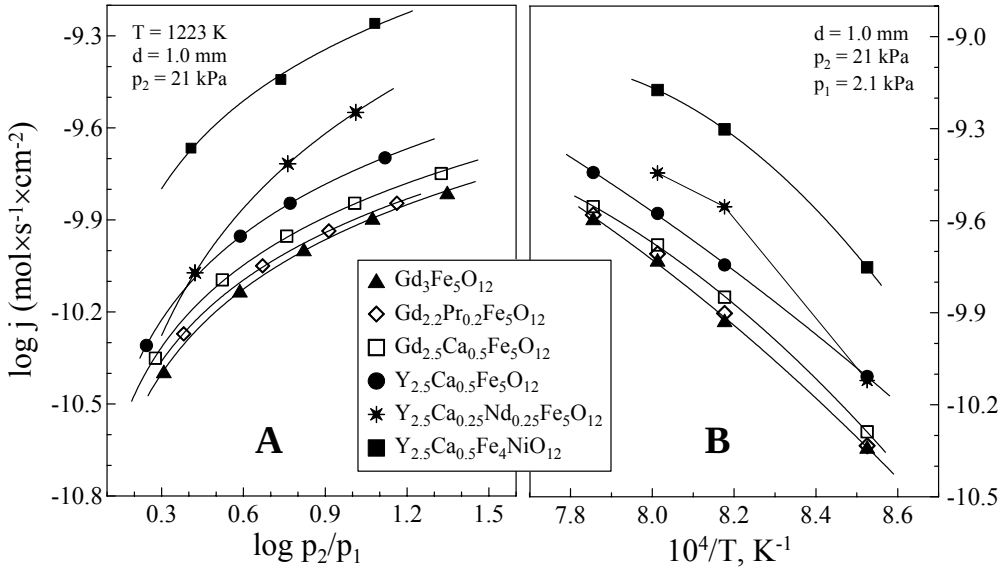

Fig. 5.5. Oxygen pressure gradient (A) and temperature (B) dependencies of the oxygen permeation flux through garnet membranes.

At the same time, the oxygen permeability of $Y_{2.5}Ca_{0.5}Fe_5O_{12-\delta}$ was found lower than that of $Y_{2.5}Ca_{0.25}Nd_{0.25}Fe_5O_{12-\delta}$, though the latter composition contains a smaller amount of calcium. Taking into account the rather unusual temperature dependence of the permeation flux and rather high total conductivity of $Y_{2.5}Ca_{0.25}Nd_{0.25}Fe_5O_{12-\delta}$ ceramics (Figs. 5.2B and 5.5B), one can assume the formation of a highly-conducting perovskite phase at grain boundaries. Phase segregation may result from the large radius of neodymium ions [8] and their high concentration close to the solid solubility limit in

garnet ferrites [285]. Since Nd^{3+} and Pr^{3+} cations have similar size, the higher oxygen permeability of $Gd_{2.2}Pr_{0.8}Fe_5O_{12\pm\delta}$ with respect to undoped $Gd_3Fe_5O_{12\pm\delta}$ may also be due to segregation of secondary phases.

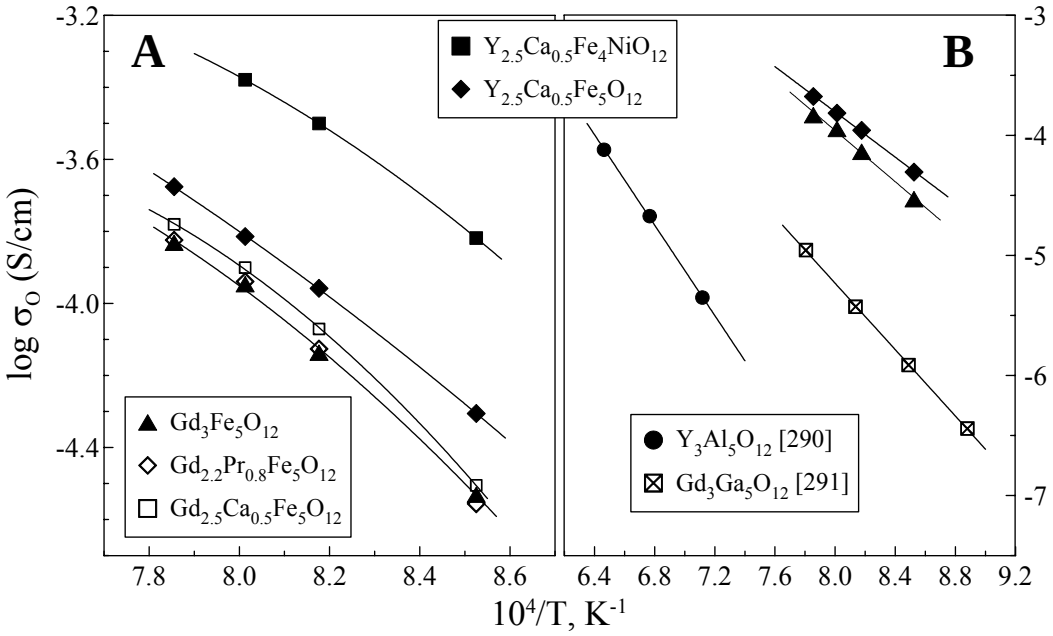

Fig. 5.6. Temperature dependencies the oxygen ionic conductivity of ferrite garnets in air.

Finally, the ionic conductivity of $Y_{2.5}Ca_{0.5}Fe_5O_{12-\delta}$ is clearly higher than that of its Gd-containing analogue, $Gd_{2.5}Ca_{0.5}Fe_5O_{12-\delta}$ (Fig. 5.6A). As the difference in behavior of these compounds having similar lattice and composition results from the different radii of Y^{3+} and Gd^{3+} cations, the structure of $Y_{2.5}Ca_{0.5}Fe_5O_{12-\delta}$ and $Gd_{2.5}Ca_{0.5}Fe_5O_{12-\delta}$ is analyzed in order to reveal factors influencing ionic transport in garnets.

5.7. Structural aspects of ionic conduction

In theory, the ionic conductivity may be affected by a number of structural parameters, such as the total and specific free unit cell volumes, tolerance factor, ion displacement from ideal positions, and the size and curvature of channels available for mobile oxygen anions [5,293-295]. The relevance of such parameters for garnet-type phases was evaluated by comparing results of Rietvield refinement with data on ionic conduction (Fig. 5.6). Selected structure refinement results of four garnet compounds,

including oxygen anion coordinates and specific free volume (V_{sf}), are listed in Table 5.5. The specific free volume was calculated as [293]

$$V_{sf} = \frac{V\text{-}V_{ion}}{V} \qquad (5.1)$$

where V is the unit cell volume, and V_{ion} is the total volume of ions constituting one unit cell. The structure refinement showed that in all studied garnets, the cations are located in their crystallographic positions, which can be described by (x, y, z) coordinates equal to (1/8, 0, 1/4) for A sites, and (0, 0, 0) and (3/8, 0, 1/4) for the octahedrally- and tetrahedrally-coordinated iron sites, respectively. Two latter positions are marked in Fig. 5.7 as Fe1 and Fe2, correspondingly. Contrary to the cations, oxygen anions are significantly displaced from their ideal position having coordinates (0, 0, 1/8). However, neither anion displacement nor free volume shows any correlation with ionic transport. For example, $Y_{2.5}Ca_{0.5}Fe_5O_{12-\delta}$ exhibits maximum ionic conductivity and minimum V_{sf} values with respect to other compositions listed in Table 5.5. This suggests, in particular, that the concept of free volume [293,294], developed for perovskite-type phases, cannot be applied for the garnet structure.

Table 5.5. Crystallographic parameters of selected $A_3Fe_5O_{12}$ -based phases.

Composition	V, Å^3	V_{sf}, Å^3	x (O)	y (O)	z (O)
$Gd_3Fe_5O_{12}$	1941.0(1)	0.4683	-0.029(0)	0.055(8)	0.152(2)
$Gd_{2.2}Pr_{0.8}Fe_5O_{12}$	1954.8(1)	0.4673	-0.028(8)	0.057(4)	0.146(6)
$Gd_{2.5}Ca_{0.5}Fe_5O_{12}$	1934.1(1)	0.4638	-0.029(7)	0.057(2)	0.147(8)
$Y_{2.5}Ca_{0.5}Fe_5O_{12}$	1896.1(3)	0.4587	-0.027(1)	0.058(2)	0.148(4)

In the garnet lattice (Fig. 5.7), transport of an oxygen ion in any definite direction requires subsequent elementary jumps via the Fe-O octahedra and tetrahedra edges. The complexity of garnet structure leads to a variety of possible jump combinations; the total number of angles formed by edges of neighboring octahedra and tetrahedra is larger than 80. However, if the driving force vector is parallel to the direction of a first jump, the most probable second jump should have a direction as close as possible to the first; the angle between two subsequent elementary jumps of oxygen ions (β) should be minimum. In other words, the ion migration channel size (so-called "bottleneck") should be compared for chains of consecutive oxygen sites, where the angle between each two O-O bonds is as close as possible to 180^0. Table 5.6 compares geometrical parameters of the oxygen site chains forming minimum β angles, in the lattice of $Y_{2.5}Ca_{0.5}Fe_5O_{12-\delta}$ and $Gd_{2.5}Ca_{0.5}Fe_5O_{12-\delta}$. Four combinations of the

octahedron and tetrahedron edges, where the (180^0-β) angle is larger than 140^0, are selected for comparison. Note that the ideal perovskite structure presents a 3-dimensional network of linear diffusion pathways where $\beta = 0^0$. Linear diffusion pathways might also be assumed in the case of cubic fluorite-type ionic conductors. In the garnet lattice, the maximum angles formed by O-O bonds in the oxygen site chains are considerably lower than 180^0. The nonlinear diffusion pathway is probably an important reason for the relatively low ionic conductivity of garnet-type phases (Fig. 5.6).

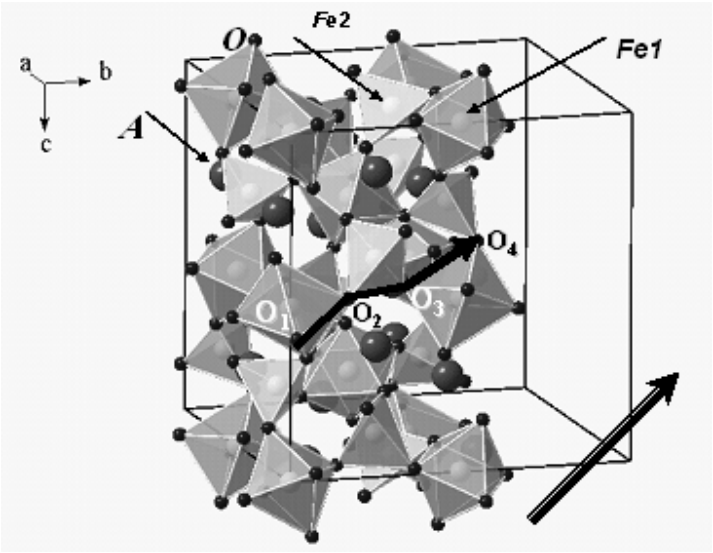

Fig. 5.7. The garnet structure. The labels O_1, O_2, O_3 and O_4 correspond to oxygen sites providing the most probable diffusion pathway along the driving force (right arrow).

In addition to the angle between directions of an elementary jump and driving force, the height of the energetic barrier between two sites and, therefore, the jump probability is influenced by the bottleneck size [294,295]. The size of selected jump channels (S), equal to the area of the largest circle that may be placed between three surrounding cations in the jump direction, is given in Table 5.7. This size should be understood as a parameter resulting from the saddle point critical radius, suggested as the conduction-determining factor in perovskites [294,295]. The channels considered in Table 5.7 were selected as most probable for ionic motion if the driving force is parallel to the first jump along one octahedron edge, as illustrated by Fig. 5.7, and if this probability is proportional to S×cos(β). Comparison of the values of S and S×cos(β) for $Y_{2.5}Ca_{0.5}Fe_5O_{12-\delta}$ and $Gd_{2.5}Ca_{0.5}Fe_5O_{12-\delta}$ phases shows that the former has larger channels for ionic motion and smaller jump distances. These factors may

explain the higher oxygen ionic conductivity of $Y_{2.5}Ca_{0.5}Fe_5O_{12-\delta}$ compared to $Gd_{2.5}Ca_{0.5}Fe_5O_{12-\delta}$ (Fig. 5.6).

Table 5.6. Comparison of the geometrical parameters of selected O-O chains, having maximum angles, in the lattices of $Gd_{2.5}Ca_{0.5}Fe_5O_{12}$ and $Y_{2.5}Ca_{0.5}Fe_5O_{12}$.

$Gd_{2.5}Ca_{0.5}Fe_5O_{12}$			$Y_{2.5}Ca_{0.5}Fe_5O_{12}$		
O_1-O_2 distance, Å	O_2-O_3 distance, Å	O_1-O_2-O_3 angle, (180-β)	O_1-O_2 distance, Å	O_2-O_3 distance, Å	O_1-O_2-O_3 angle, (180-β)
2.874	2.968	147.5	2.794	2.991	148.2
2.874	2.968	148.8	2.794	2.991	150.0
2.710	2.917	156.3	2.660	2.898	156.5
2.710	3.145	161.9	2.660	3.174	162.2

Note: the oxygen anions are located in crystallographically equivalent positions and labeled O_1, O_2, and O_3 for convenience. The bonds O_1-O_2 and O_2-O_3 correspond to the edges of the iron-oxygen octahedron and tetrahedron, respectively.

One necessary comment is that the ionic motion channels in perovskite-like oxides are often smaller than those along edges of Fe-O octahedra in garnets. For example, the value of S for the cubic perovskite phase $La_{0.3}Sr_{0.7}FeO_{3-\delta}$ is as low as 1.09 $Å^2$. This is smaller than for octahedron edges and comparable with tetrahedron edges in garnet solid solutions (Table 5.7). However, for cubic perovskite lattice $\beta = 0^0$; the elementary jump probablity in $La_{0.3}Sr_{0.7}FeO_{3-\delta}$, expressed via the quantity $S\times\cos(\beta)$, is higher than that for the tetrahedra edges. Ionic conduction in garnets may be limited by the ion transfer between oxygen sites at the tetrahedra corners.

Table 5.7. Comparison of the geometrical parameters of ion jumps in the direction of one Fe-O octahedron edge of $Gd_{2.5}Ca_{0.5}Fe_5O_{12}$ and $Y_{2.5}Ca_{0.5}Fe_5O_{12}$.

Jump	$Gd_{2.5}Ca_{0.5}Fe_5O_{12}$				$Y_{2.5}Ca_{0.5}Fe_5O_{12}$			
	Distance, Å	β, °	S, $Å^2$	$S\times\cos(\beta)$, $Å^2$	Distance, Å	β, °	S, $Å^2$	$S\times\cos(\beta)$, $Å^2$
O_1-O_2	2.710	0	1.513	1.513	2.660	0	1.561	1.561
O_2-O_3	2.917	23.7	0.975	0.893	2.898	23.5	1.064	0.976
O_3-O_4	2.710	23.7	1.513	1.386	2.660	23.5	1.561	1.432

A final comment is needed on ionic polarizability and ionic relaxation from normal lattice positions during ionic hopping. All these factors influence the ionic conductivity, promoting significant changes in simple geometrical parameters derived as if ions behaved as hard spheres and immobile in their normal lattice positions. Recent modeling on ionic motion in complex structures (e.g., perovskites [18], apatites [94]) suggests the possibility of several cooperative displacements of ions from their normal positions, providing lower energy pathways for ionic motion. None of these aspects has taken into consideration in the previous discussion.

6. Phase interaction and oxygen transport in $(La_{0.9}Sr_{0.1})_{0.98}Ga_{0.8}Mg_{0.2}O_{3-\delta}$-$La_{0.8}Sr_{0.2}Fe_{0.8}Co_{0.2}O_{3-\delta}$ composites

6.1. Phase composition

XRD analysis of all LSGM-LSFC composite ceramics indicated an apparent formation of one single perovskite-type phase with a rhombohedral distortion, typical for LSFC, whilst LSGM has a monoclinically-distorted perovskite lattice [276]. Unit cell parameters of the parent phases and composites are given in Table 6.1. Fig. 6.1A compares XRD patterns of LSGM, LSFC and LLc1320, where the component interaction was a minimum compared to other gas-tight ceramics. The solid-state interaction between these phases occurs considerably faster than in $Ce_{0.8}Gd_{0.2}O_{2-\delta}$-$La_{0.8}Sr_{0.2}Fe_{0.8}Co_{0.2}O_{3-\delta}$ (CGO-LSFC) and $Ce_{0.8}Gd_{0.2}O_{2-\delta}$-$La_{0.7}Sr_{0.3}MnO_{3-\delta}$ (CGO-LSM) composites where the components have different lattices. In the latter cases, sintering at 1698-1828 K resulted in moderate reaction, mainly associated with diffusion of A-site cations of LSFC or LSM into ceria [77].

Table 6.1. Properties of LSGM, LSFC and composite ceramics.

Composition	Space	a, Å	b, Å	c, Å	ρ_{exp}, g/cm^3	ρ_{exp} / ρ_{theor}, %
LSGM	I2/a	7.82(9)	5.54(6)	5.52(8)	6.24	95.2
LSFC	$R\bar{3}c$	5.52(1)	-	13.37(6)	6.14	94.0
LL1320	$R\bar{3}c$	5.52(5)	-	13.39(4)	6.25	94.6
LLc1320	$R\bar{3}c$	5.52(5)	-	13.38(5)	6.18	93.5
LL1410	$R\bar{3}c$	5.52(6)	-	13.39(2)	6.22	94.2
LLc1410	$R\bar{3}c$	5.52(7)	-	13.38(5)	6.33	95.9

For complete reaction the result would be a single perovskite phase with nominal composition $La_{0.849}Sr_{0.139}Ga_{0.476}Fe_{0.324}Mg_{0.119}Co_{0.081}O_{3-\delta}$. Fig. 6.1B compares the theoretical unit cell volume of this phase, estimated assuming a linear volume dependence on the composition (Vegard's rule), with the experimental values calculated from XRD data. Although a simple Vegard-type relation cannot be observed in this case, as the lattice of LSGM is monoclinically-distorted, data in Fig. 6.1B shows that the average lattice parameters of LSGM-LSFC composites are far from the level expected in the case of complete interdiffusion. In fact, the unit cell volume of all LSGM-LSFC materials is close to that of the LSFC phase. This suggests that the interaction in the course of sintering occurs primarily via diffusion of iron and cobalt cations into LSGM. If the mobility of these ions is higher than that of Ga^{3+},

one might expect co-existence of Ga-enriched regions, surrounded by Fe-rich areas with respect to the equilibrium composition.

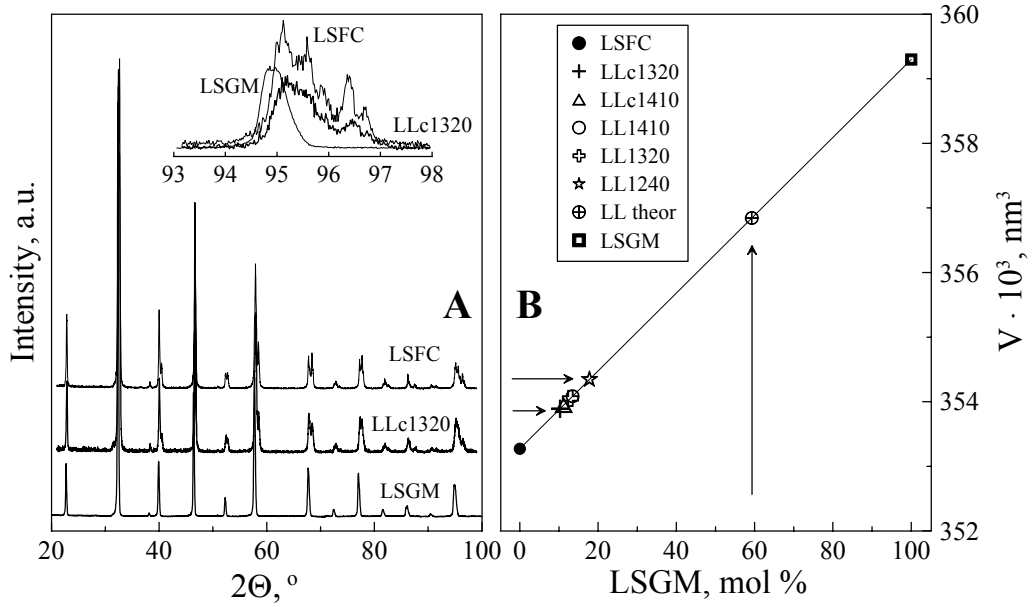

Fig. 6.1. XRD patterns (A) and unit cell volume (B) of LSGM, LSFC and composites.

6.2. Microstructure

The microstructures of polished LSGM-LSFC samples are compared in Fig. 6.2. SEM studies confirmed the synthesis of relatively good quality materials, in particular with low porosity. The sintering temperature and preliminary annealing of LSGM powder have no significant influence on the average grain size, varying for all LSGM-LSFC composites in the narrow range 1-3 μm. SEM back-scattering mode showed local inhomogeneities visible as dark regions of ceramic grains (Fig. 6.2D). The size and content of these domains increased when using coarse LSGM and when the sintering temperature decreases. This is illustrated in Fig. 6.2E and F, comparing back-scattered SEM micrographs of two composites, LL1410 and LLc1410, both sintered at 1683 K. The EDS analysis indicated that the chemical composition in these regions is certainly different from the average composition. As an example, Fig. 6.3 presents the distribution of the Ga/Fe concentration ratio in several positions; the dark domain is enriched with gallium, while the neighbouring grains are Ga-depleted. Hence, as expected, the solid-state reaction of LSGM and LSFC phases in the course of sintering is not complete. The prepared composites are not homogeneous; the level of inhomogeneity

may increase decreasing sintering temperature and preliminary coarsening of LSGM. One should note, however, that for the LL1320 and LLc1320 series the sintering temperature and time were close to the minimum necessary to obtain gas-tight ceramics. Attempts to obtain dense materials with low level of interaction between LSGM and LSFC, particularly by sintering at 1413 K for 1 hour and by de-activation of both components by thermal treatment, failed.

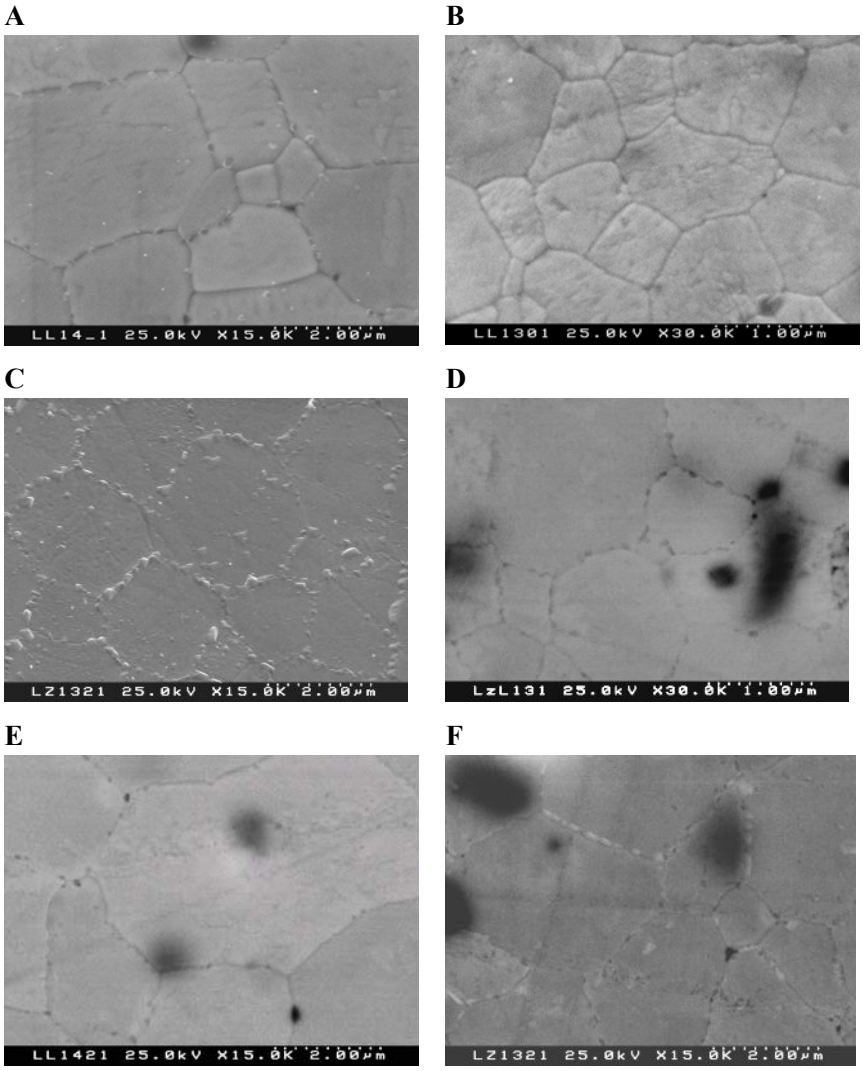

Fig. 6.2. SEM micrographs of composite ceramics: LL1410 (A and E), LLc1410 (B and F), LL1320 (C) and LLc1320 (D). The micrographs D, E and F were obtained in back-scattering mode.

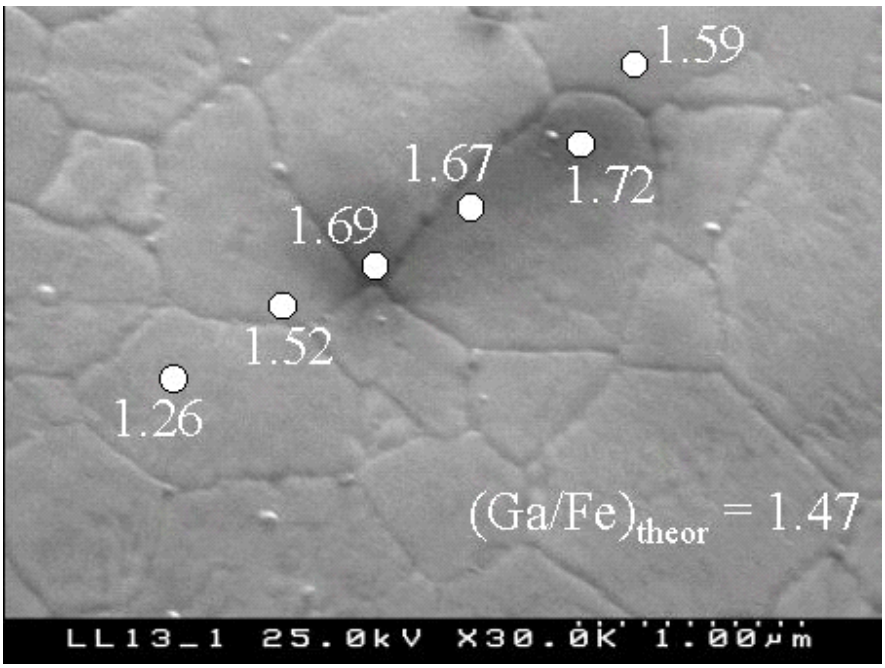

Fig. 6.3. SEM micrograph of LL1320 ceramics. The atomic Ga/Fe ratios in several points were evaluated by EDS analysis.

6.3. Dilatometric studies

As described in Part 2, different powder preparation procedures were used for the LL and LLc series (Methods 1 and 2, respectively). Sintering of ball-milled powders resulted in almost complete solid-state reaction between the phases. The latter procedure including thermal treatment of precursors was employed in order to decrease LSGM reactivity. However, despite of coarsening and shorter sintering periods, phase interaction detected by XRD and SEM/EDS was still significant. Dilatometric tests of green compacts (Fig. 6.4A) confirmed that active shrinkage, probably associated with cation interdiffusion, starts at approximately 1123-1273 K. Although the use of coarsened LSGM powder (Method 2) results in lower shrinkage, has no essential effect on the starting sintering temperature. This suggests, in particular, that interaction between the LSGM electrolyte and perovskite cathodes based on $LaMO_3$ (M = Fe, Co) may occur at cell fabrication temperatures, 1273-1423 K.

The dilatometric curves of dense LSGM-LSFC materials show a break at 873–973 K (Fig. 6.4B). At 373-923 K, the average thermal expansion coefficients (TECs) vary in the range (12.4 - 13.5)$\times 10^{-6}$ K^{-1}, quite similar to the TEC of single-phase LSFC ceramics (Table 6.2). Further heating leads to increasing TEC values up to (17.8-19.8)$\times 10^{-6}$ K^{-1}. Such behaviour is typical for Fe-containing

ceramic materials and results from oxygen losses on heating, providing an additional chemical contribution to the lattice thermal expansion [198,263].

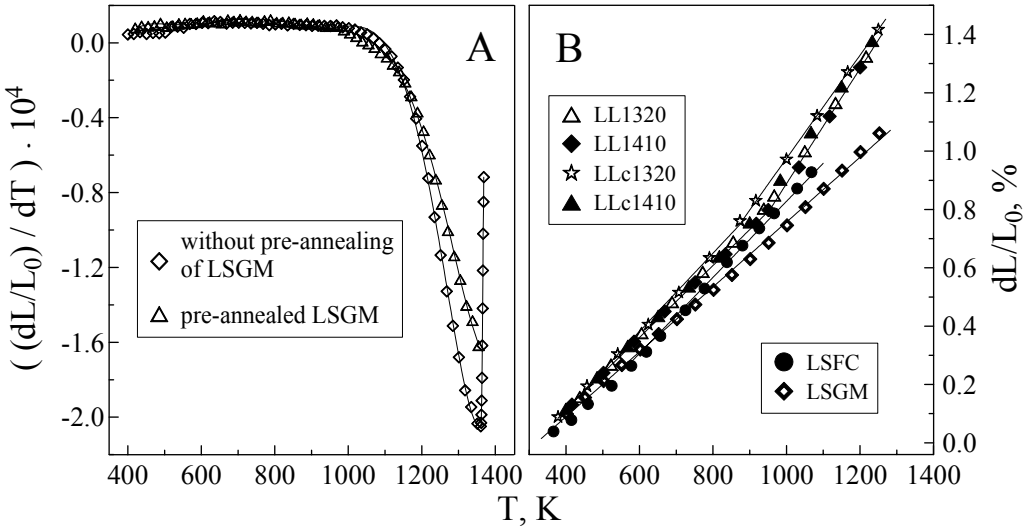

Fig. 6.4. Shrinkage curves for LL and LLc green compacts (A) and dilatometric curves of LSGM, LSFC and LSGM-LSFC ceramics (B) in air.

It should be mentioned that the TEC values of LSGM-LSFC ceramics are considerably higher than for the $LaGaO_3$-based solid electrolyte, although the starting content of LSGM in the composites is 60 wt.% (approximately 59 mol.%). This enhances the role of inhomogeneous cation distribution on the overall materials performance. Most probably, the high TECs of these composite ceramics are determined by the Fe-enriched volume, while isolated Ga-rich domains with lower expansion remain under stress. As a result, lower sintering temperatures and use of coarsened LSGM powder, which provides larger Ga-enriched domains (Fig. 6.2), lead to decreasing TECs in the high-temperature range (Table 6.2).

6.4. Total conductivity

Fig. 6.5A presents the temperature dependencies of total conductivity (σ) of LSGM-LSFC ceramics in air. Data on oxygen permeability, discussed below, suggests that the oxygen ion transference numbers are lower than 0.03; the total conductivity is predominantly p-type electronic. As expected, the performance of LSGM-LSFC ceramics is similar in trend to LSFC, whilst the values of σ are 10-30 times lower (Fig. 6.5B).

Table 6.2. TECs and parameters of Arrhenius model for the total conductivity of LSGM, LSFC and LSGM-LSFC ceramics.

Composition	T, K	$\alpha \times 10^6$ K^{-1}	T, K	E_A, kJ/mol	$\ln(A_0)$, (S K)/cm
LSGM	373-1273	11.1 ± 0.1	643-1223	96 ± 7	15 ± 1
LSFC	373-1073	12.9 ± 0.2	423-893	12.3 ± 0.5	13.5 ± 0.1
LL1320	373-923	12.81 ± 0.01	298-848	26.2 ± 0.5	12.1 ± 0.1
	923-1273	18.96 ± 0.01			
LLc1320	373-923	13.48 ± 0.01	298-848	24.0 ± 0.3	12.2 ± 0.1
	923-1273	17.79 ± 0.01			
LL1410	373-923	12.36 ± 0.1	298-848	25.1 ± 0.5	11.9 ± 0.1
	923-1273	19.75 ± 0.02			
LLc1410	373-923	12.63 ± 0.01	298-848	24.9 ± 0.2	12.1 ± 0.1
	923-1273	18.98 ± 0.01			

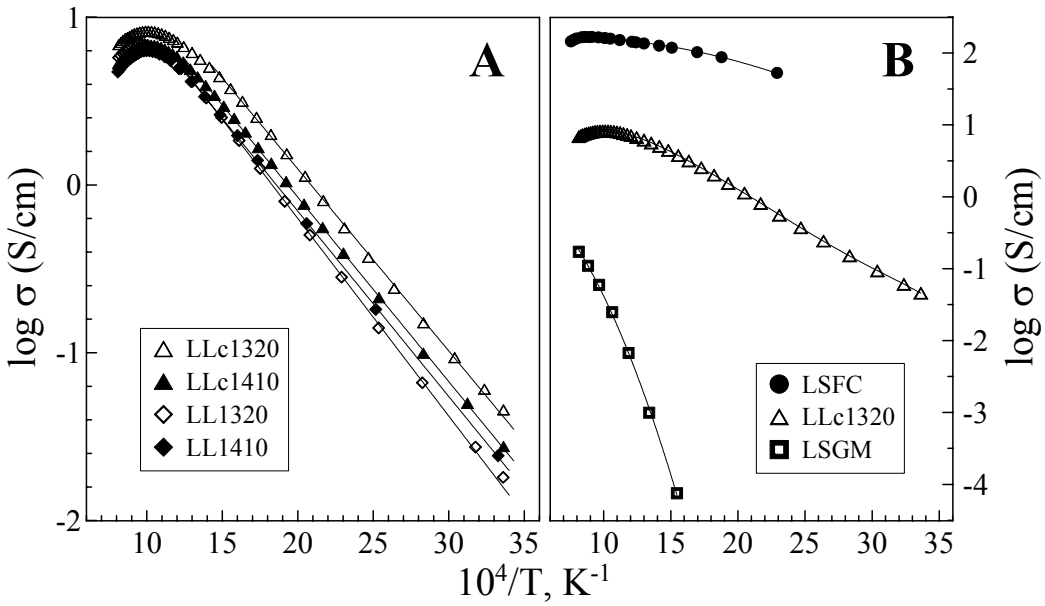

Fig. 6.5. Temperature dependencies of the total conductivity of LSGM, LSFC and LSGM-LSFC ceramics in air.

At 298-873 K, the conductivity of composites follows an Arrhenius dependence; further heating leads to oxygen losses, decreasing electron-hole concentration and, thus, decreasing σ. These

tendencies are in excellent agreement with literature on $LaFeO_3$- and $SrFeO_3$-based systems [31,198,263], where dominant p-type electronic transport via a small-polaron mechanism and increasing oxygen nonstoichiometry on heating results in apparent pseudometallic behaviour.

The values of activation energy (E_a) for the total conductivity in the low-temperature range are listed in Table 6.2. For LSGM-LSFC ceramics, the activation energy varies from 24.0 to 26.2 kJ/mol, which is higher than the corresponding value for LSFC (12.3 kJ/mol), but 4 times lower than the activation energy for the ionically-conductive LSGM (96 kJ/mol). Increasing interaction between LSGM and LSFC leads to a moderate decrease of the total conductivity. With respect to other composite materials, the highest total conductivity values were observed for LLc1320, where the inhomogeneity of ceramics is maximal. It is well known for $LaGaO_3$-$LaMO_3$ (M= Fe, Co, Ni) systems [43,153,275] that incorporation of insulating Ga^{3+} cations, having stable oxidation state, blocks the electronic transport in transition metal-containing perovskites. Therefore, as for thermal expansion, the total conductivity of LSGM-LSFC composites is determined by the iron-rich fraction.

6.5. Oxygen permeability

The oxygen permeation fluxes and oxygen permeability of dense LL1320 membranes are plotted in Fig. 6.6 as a function of the oxygen pressure gradient and membrane thickness (d). At 1173-1223 K, the values of $J(O_2)$ increase and the oxygen fluxes decrease with increasing membrane thickness. This indicates that the overall oxygen transport is affected by both bulk ambipolar conductivity and surface exchange rate. When the temperature decreases, the role of exchange kinetics as permeation-limiting factor increases; the oxygen fluxes tend to be thickness-independent. A similar behaviour, typical for single-phase $La(Sr)Ga(M,Mg)O_{3-\delta}$ (M= Fe, Co, Ni) heavily doped with acceptor-type cations [162,296], was observed for all LSGM-LSFC composites studied in this work.

Fig. 6.6C compares the oxygen permeation fluxes through LSGM-LSFC membranes under a fixed oxygen pressure gradient. As for the total conductivity, maximum oxygen permeability is observed for LLc1320 ceramics, where the interaction degree between LSGM and LSFC phases is minimum compared to other composite materials. The permeability of LLc1320 is quite high; for example, an oxygen flux of 1.1×10^{-7} $mol\times cm^{-2}\times s^{-1}$ was measured through a 1.0 mm thick membrane placed under a $p(O_2)$ gradient of 21/2.1 kPa at 1223 K. This level of oxygen permeability is similar to that of single-phase materials having similar cationic composition (Fig. 6.6D), such as $La_{0.8}Sr_{0.2}Ga_{0.6}Mg_{0.2}M_{0.2}O_{3-\delta}$ (M = Fe, Co) [162] or $LaGa_{0.65}Ni_{0.2}Mg_{0.15}O_{3-\delta}$ [296].

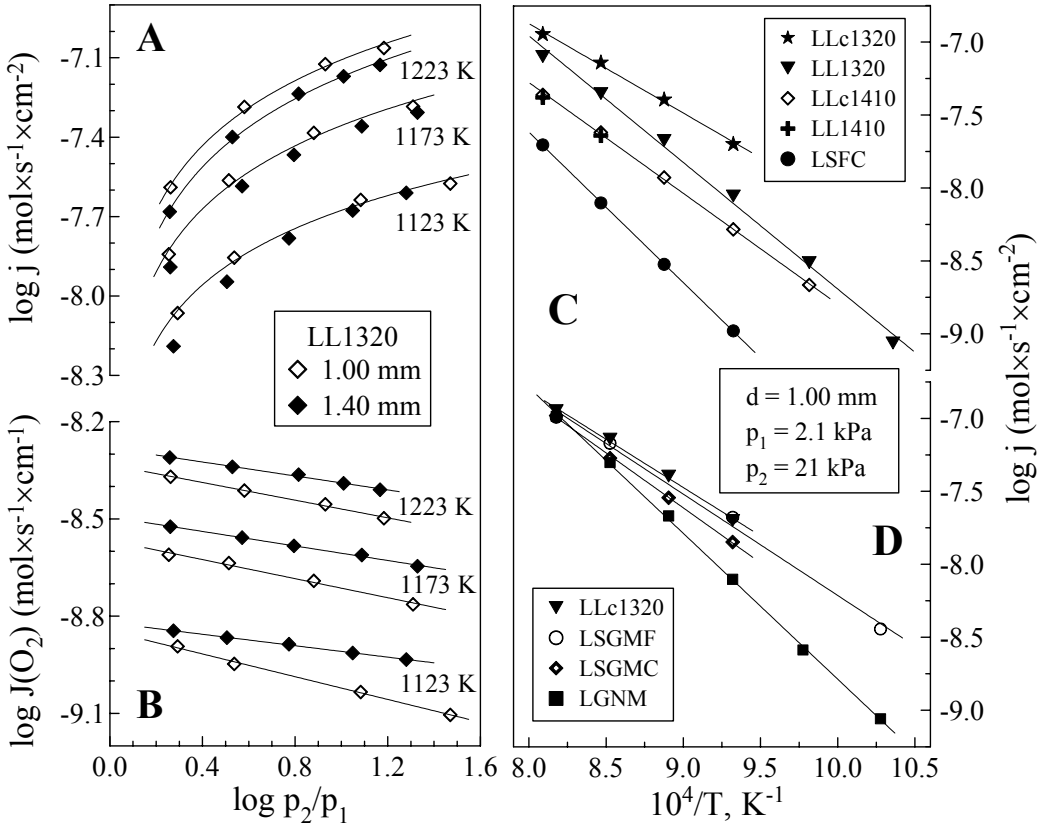

Fig. 6.6. Oxygen pressure gradient dependencies of the permeation flux (A) and permeability (B) of LL1320 membranes, and temperature dependencies of the permeation flux through LSGM-LSFC ceramics at fixed oxygen pressure gradient (C and D). Data on single-phase $La_{0.8}Sr_{0.2}Ga_{0.6}Mg_{0.2}Co_{0.2}O_{3-\delta}$ (LSGMC) [22], $La_{0.8}Sr_{0.2}Ga_{0.6}Mg_{0.2}Fe_{0.2}O_{3-\delta}$ (LSGMF) [22] and $LaGa_{0.65}Ni_{0.2}Mg_{0.15}O_{3-\delta}$ (LGNM) [23] are shown for comparison.

The estimates of oxygen ionic conductivity which can be obtained using Eq. (2.10) are lower than the true values due to significant surface exchange limitations to oxygen permeation (Fig. 6.6B). Nonetheless, such estimation might be of interest in order to reveal factors affecting the level of bulk ambipolar conduction. Fig. 6.7 presents the temperature dependencies of apparent ionic conductivity in LSGM-LSFC composites, calculated from the oxygen permeation fluxes through 1.0 mm thick membranes. Data on LSGM and LSFC, shown for comparison, correspond to the true ionic conductivity of these compositions. In the latter case, the ionic conductivity was directly measured by impedance spectroscopy as the oxygen ion transference numbers measured by the faradaic efficiency

technique are higher than 0.99. For LSFC membranes, no surface effect on the oxygen permeation fluxes was observed. The apparent ionic conductivity of LLc1320 ceramics, exhibiting maximum oxygen transport with respect to other LSGM-LSFC composites, is 4-50 times lower than the conductivity of LSGM. The level of ionic conduction in LSGM-LSFC ceramics is, therefore, presumably the result of the contribution of percolating Ga-rich domains decreasing in relevance due to phase interaction.

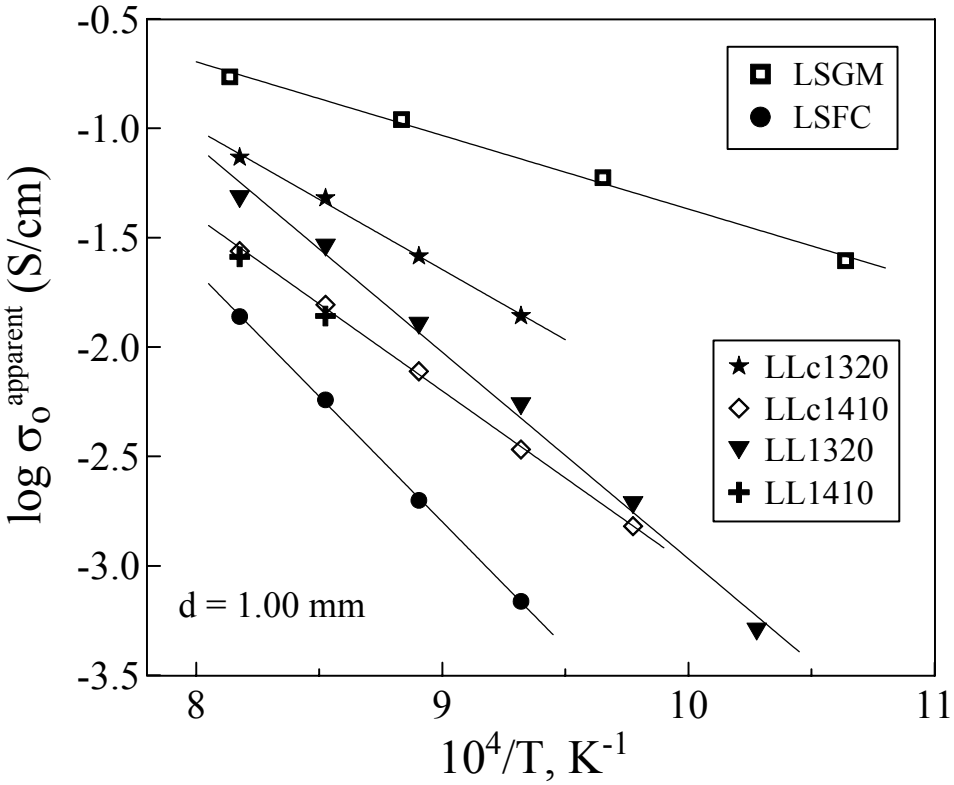

Fig. 6.7. Comparison of the oxygen ionic conductivity in LSGM, LSFC and LSGM-LSFC.

6.6. Critical role of phase interaction

The cation interdiffusion between LSGM and LSFC clearly has a deteriorating influence on the transport properties. In the case of electronic conduction, this effect is rather small (Fig. 6.5A); the influence of phase interaction on the oxygen ionic transport is much larger (Fig. 6.7). The processing conditions of solid oxide fuel cells, made of $LaGaO_3$-based solid electrolytes and perovskite cathodes based on $La(Fe,Co)O_3$, should hence be optimised in order to prevent extensive interdiffusion between

electrolyte and electrode materials. For oxygen separation membranes, direct combination of LSGM and LSFC in dual-phase composite ceramics seems rather inappropriate as the resultant properties are strongly dependent on phase interaction. Even for optimised membrane microstructures with maximum oxygen transport, this may lead to degradation processes in the course of long-term operation at elevated temperatures.

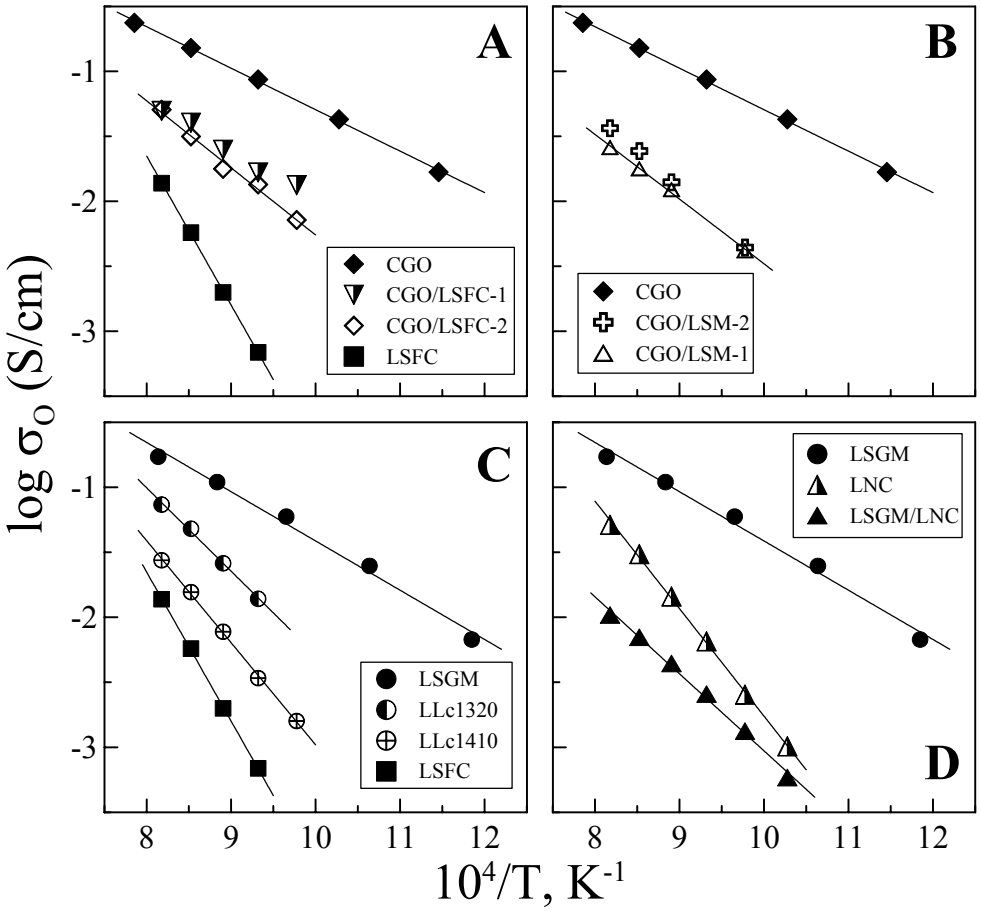

Fig. 6.8. Temperature dependencies of the oxygen ionic conductivity in various systems. Abbreviations are given in Tables 2.2 and 6.3.

Although in a less pronounced manner, phase interaction was found to suppress oxygen transport in ceria-based composites [77] where LSFC (Fig. 6.8A) or $La_{0.7}Sr_{0.3}MnO_{3-\delta}$ (Fig. 6.8C) act as electronically-conductive component. These materials, contrary to LSGM-LSFC, are dual-phase after sintering (consist of fluorite- and perovskite-type phases). Nonetheless, XRD and SEM/EDS studies

revealed a certain diffusion of Ce and, possibly, Gd cations into LSFC or LSM, and La into ceria. This interaction increases with sintering temperature and time, being responsible for the observed decline of oxygen ionic conductivity.

Table 6.3. Abbreviations and processing conditions.

Composition	Abbreviation	$T_{sintering}$, K	$t_{sintering}$, h
$Ce_{0.8}Gd_{0.2}O_{2-\delta}$	CGO	1873	4
$La_{0.7}Sr_{0.3}MnO_{3-\delta}$	LSM	1743	5
$La_2Ni_{0.7}Co_{0.3}O_{4\pm\delta}$	LNC	1503	2
50 wt% CGO - 50 wt% LSFC	CGO/LSFC-1	1773	2
	CGO/LSFC-2	1698-1828*	12
50 wt% CGO - 50 wt% LSM	CGO/LSM-1	1793	4
	CGO/LSM-2	1793	2
60 wt% LSGM - 40 wt% LNC	LSGM/LNC	1503	2

*Samples were sintered while temperature was increased from 1698 to 1828 K by steps of 10-20 K. Duration of each step was 1 hour.

The fast reaction in the LSGM-LSFC system is partly associated with the structural similarity of the phase components, namely perovskites with comparable lattice parameters, forming a continuous solid solution. Therefore, for dual-phase membranes, LSGM should be preferably combined with an electronically- or mixed-conduction phase having a non-perovskite structure. In order to evaluate the suitability of K_2NiF_4-type nickelates for this goal, $La_2Ni_{0.8}Cu_{0.2}O_{4\pm\delta}$ was tested. No continuous solid solution may be formed due to interaction between this compound and LSGM, though formation of intermediate Ruddlesden-Popper phases cannot be excluded. One might thus expect an improved performance of LSGM/LNC composite membranes in the case of no phase interaction.

However, XRD analysis of LSGM/LNC composites showed formation of a secondary phase based on $La_3Ni_2O_7$, which belongs to the Ruddlesden-Popper series. The inhomogeneous microstructure of LSGM/LNC comprises large grains of the parent components and small grains of the segregated phase; the EDS analysis indicated that the latter grains are enriched with Mg and Ni with respect to the regular bulk, thus suggesting formation of $La_3(Ni,Mg)_2O_7$ solid solution [297]. As a result, the level of ionic transport in LSGM/LNC is lower with respect to both parent compounds (Fig. 6.8D). This fact, due to Mg depletion in LSGM and, possibly, from a low ionic conductivity of $La_3(Ni,Mg)_2O_7$, again stresses the critical role of component interaction in the oxide composites.

7. Ionic and electronic conduction in $La_{10}(Si,Al)_6O_{26\pm\delta}$-based apatites

7.1. The system $La_{10-x}Si_{1-y}Al_yO_{26\pm\delta}$ ($0 \le x \le 0.33$, $0.5 \le y \le 1.5$)

7.1.1. Structure, microstructure and thermal expansion

XRD analysis confirmed that all $La_{10-x}Si_{1-y}Al_yO_{26\pm\delta}$ ($0 \le x \le 0.33$, $0.5 \le y \le 1.5$) ceramic materials are single-phase; the lattice parameters and space groups are listed in Table 7.1. Incorporation of Al^{3+} having larger radius with respect to Si^{4+} increases the unit cell volume, analogously to doping with Ga^{3+} and Ge^{4+} [87,93]. At fixed B-site composition, increasing A-site deficiency has an opposite effect, in agreement with data on $La_{10-x}Si_6O_{27-3x/2}$ [298].

Table 7.1. Properties of $La_{10-x}Si_{1-y}Al_yO_{26\pm\delta}$ ceramics.

Composition	S.G.	a, Å	c, Å	ρ_{exp} / ρ_{theor}, %	T, K	$\alpha \times 10^6$ K^{-1}
$La_{9.67}Si_{4.5}Al_{1.5}O_{25.75}$	$P\bar{3}$	9.733(3)	7.235(6)	96.7	373-1173	9.99 ± 0.01
$La_{9.67}Si_5AlO_{26}$	$P6_3$	9.732(1)	7.223(6)	97.4	373-1173	9.92 ± 0.01
$La_{9.67}Si_{5.5}Al_{0.5}O_{26.25}$	$P6_3/m$	9.712(2)	7.207(6)	93.8	373-1273	9.39 ± 0.02
$La_{9.83}Si_{4.5}Al_{1.5}O_{26}$	$P\bar{3}$	9.734(3)	7.236(6)	96.7	373-1173	8.86 ± 0.02
$La_{9.83}Si_{5.5}Al_{0.5}O_{26.5}$	$P6_3/m$	9.709(4)	7.207(9)	91.3	373-1273	10.80 ± 0.02
$La_{10}Si_5AlO_{26.5}$	$P6_3/m$	9.729(5)	7.235(9)	91.6	473-1173	9.08 ± 0.02
$La_{10}Si_{5.5}Al_{0.5}O_{26.75}$	$P6_3/m$	9.716(5)	7.212(7)	90.5	373-1273	8.68 ± 0.01

The SEM/EDS studies showed the high quality of the silicate ceramics, in particular low porosity and an absence of compositional inhomogeneities at the grain boundaries, within the limits of experimental uncertainty of the EDS technique. Typical SEM micrographs are presented in Fig. 7.1. The average grain size is quite similar for all ceramics and varies from 1 to 4 μm. The results of SEM/EDS inspections agree well with the impedance spectra of $La_{10-x}Si_{6-y}Al_yO_{27-3x/2-y/2}$ apatites (Fig. 7.2), which suggest no considerable grain-boundary contribution to the total resistivity at temperatures above 873-923 K. The impedance spectra consisted of one or two arcs. In the first case, the high- and low-frequency intercepts to the real axis correspond to the total resistance of a sample and the DC resistance of the cell, respectively. The latter quantity comprises electrodes polarization resistance and the total resistance of a sample. In the second case, the high-frequency arc can be approximated by a resistance-capacitance (RC) element; the deviation of the high-frequency intercept from origin was found negligible, within the limits of experimental error. For such spectra, the total resistivity can be calculated from the intermediate-frequency intercept. Due to the limited range of available frequencies

(20 Hz – 1 MHz), only part of these arcs is often visible in the impedance spectra; nonetheless, these are sufficient to separate the total resistivity of the samples and to ensure the absence of grain-boundary contributions.

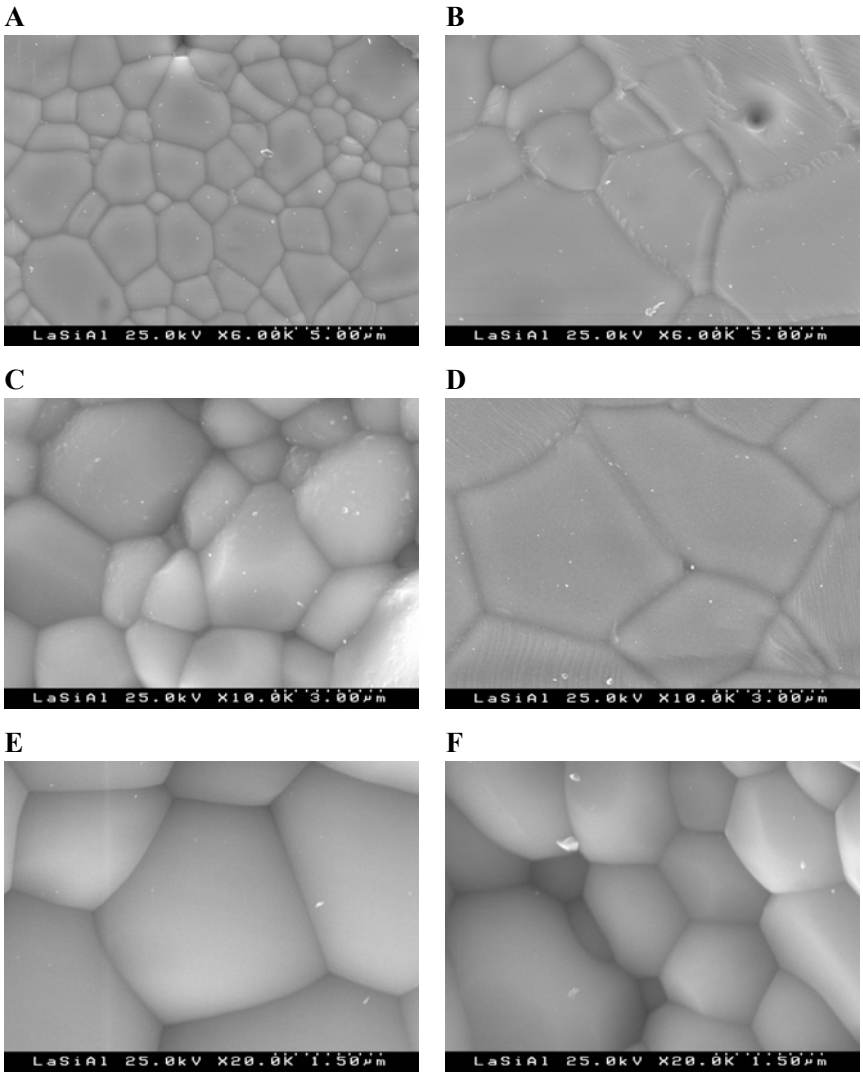

Fig. 7.1. SEM micrographs of apatite ceramics: $La_{9.67}Si_{5.5}Al_{0.5}O_{26.25}$ (A), $La_{10}Si_{5.5}Al_{0.5}O_{26.75}$ (B), $La_{9.83}Si_{4.5}Al_{1.5}O_{26}$ (C), $La_{9.83}Si_{5.5}Al_{0.5}O_{26.5}$ (D), $La_{9.67}Si_{4.5}Al_{1.5}O_{25.75}$ (E) and $La_{9.67}Si_5AlO_{26}$ (F).

The dilatometric curves of $La_{10-x}Si_{6-y}Al_yO_{27-3x/2-y/2}$ in air are approximately linear within the studied temperature range (Fig. 7.3). The average thermal expansion coefficients (TECs) calculated

from the dilatometric data are relatively low, 8.7×10^{-6} to 10.8×10^{-6} K^{-1} (Table 7.1). These values are close to those of commonly used solid electrolytes and electrode materials, such as stabilised zirconia [55] and lanthanum-strontium manganites [153].

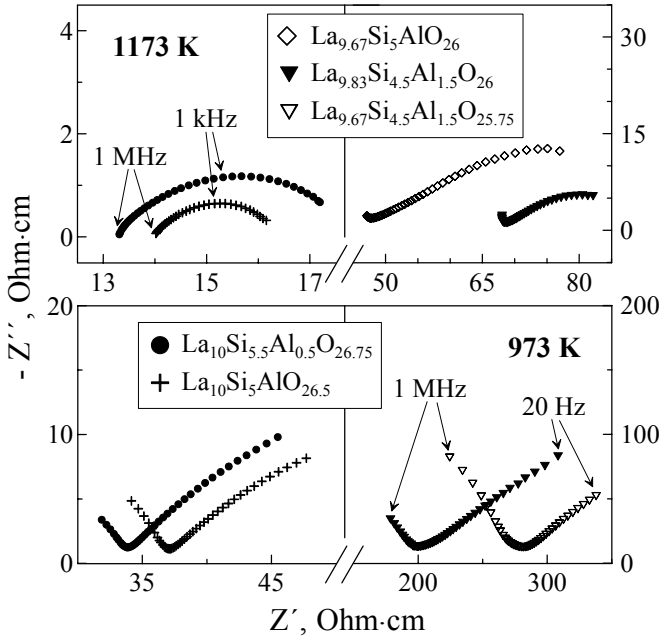

Fig. 7.2. Examples of the impedance spectra of $La_{10-x}Si_{1-y}Al_yO_{26\pm\delta}$ ceramics with porous Pt electrodes in air.

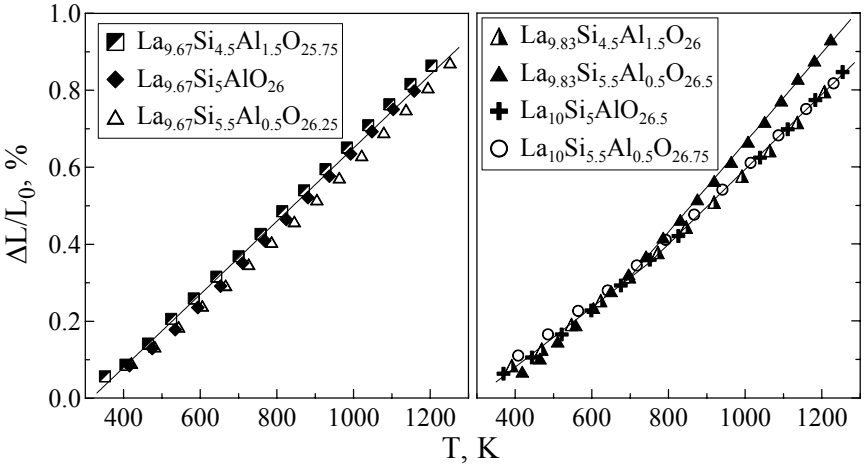

Fig. 7.3. Dilatometric curves of $La_{10-x}Si_{1-y}Al_yO_{26\pm\delta}$ ceramics in air.

7.1.2. Ionic conduction

The Arrhenius plots of the electrical transport of $La_{10-x}Si_{1-y}Al_yO_{26\pm\delta}$ ceramics are shown in Fig. 7.4. The FE measurements clearly demonstrated predominant ionic conductivity. At 973-1223 K in air, the electronic contribution to the total conduction is about 0.5% or lower (Table 7.2). The activation energy for ionic transport is relatively low and varies in the range 56-67 kJ/mol (Table 7.2).

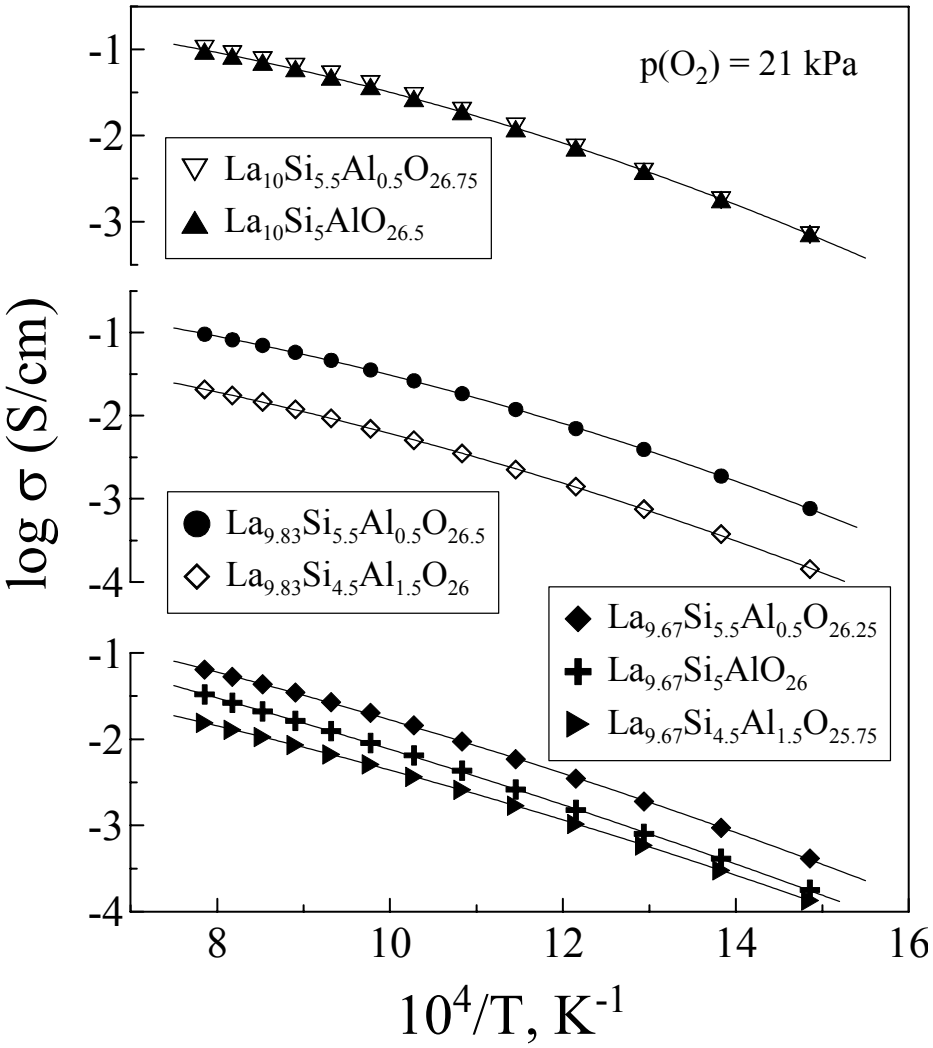

Fig. 7.4. Total conductivity of $La_{10-x}Si_{1-y}Al_yO_{26\pm\delta}$ ceramics in air.

The fact that the oxygen ionic conduction dominates, was confirmed by data on oxygen pressure dependencies of total conductivity and Seebeck coefficient. One representative example is

given in Fig. 7.5. The conductivity is almost $p(O_2)$ independent, while the thermopower under oxidizing conditions is positive; the slope of α *vs. ln* $p(O_2)$ is close to -R/4F, the theoretical value for a pure oxygen ionic conductor where the partial molar entropy and the transported heat of oxygen ions are both $p(O_2)$-independent [299,300]. This type of behavior is typical for solid electrolytes such as stabilized zirconia [299]. Note that, in Fig. 7.5, the range of moderately low oxygen pressures is excluded from consideration due to errors in the oxygen sensor readings, associated with stagnated diffusion processes in the gas phase.

Table 7.2. Oxygen ion transference numbers (t_O) and activation energies (E_A) of the partial oxygen ionic (σ_O) and electronic (σ_e) conductivities of $La_{10-x}Si_{1-y}Al_yO_{26\pm\delta}$ ceramics in air.

Composition	t_O				E_A	
	1223 K	1123 K	1073 K	973 K	σ_O	σ_e
$La_{9.67}Si_{4.5}Al_{1.5}O_{25.75}$	-	-	-	-	60 ± 1	-
$La_{9.67}Si_5AlO_{26}$	0.9959	0.9959	0.9964	0.9965	67 ± 1	72 ± 3
$La_{9.67}Si_{5.5}Al_{0.5}O_{26.25}$	0.9956	0.9962	0.9966	0.9979	63 ± 2	89 ± 8
$La_{9.83}Si_{4.5}Al_{1.5}O_{26}$	0.9949	0.9951	0.9951	0.9948	60 ± 2	57 ± 2
$La_{9.83}Si_{5.5}Al_{0.5}O_{26.5}$	0.9967	0.9975	0.9982	0.9989	57 ± 3	100 ± 6
$La_{10}Si_5AlO_{26.5}$	0.9959	0.9968	0.9975	0.9985	56 ± 3	96 ± 6
$La_{10}Si_{5.5}Al_{0.5}O_{26.75}$	0.9995	0.9996	0.9996	0.9997	56 ± 3	68 ± 3

The activation energies for ionic and electronic conductivities correspond to the temperature ranges 873-1273 and 973-1223 K, respectively.

The oxygen ionic transport was found to increase with increasing oxygen content in the apatite lattice (Fig. 7.4); the highest conductivity is found for silicate compositions containing 26.25-26.75 oxygen atoms per formula unit. These results corroborate that migration of interstitial O^{2-} is the major mechanism for ionic conductivity in apatites with relatively high oxygen concentration, in agreement with literature [94,95,298]. Note also that the diffusion of interstitial oxygen is expected to be significantly faster than that of the oxygen vacancies [94]. At the same time, the vacancy formation due to Frenkel-type disorder in the oxygen sublattice may still play an important role, enabling ion jumps between interstitial and regular sites. Such disorder, and also SiO_4 tetrahedra relaxation are both promoted by A-site deficiency [85,91,94]. This explains moderate differences in the ionic conductivity of compositions where the nominal oxygen content is similar, but the concentrations of A-site cation vacancies are different (Fig. 7.4).

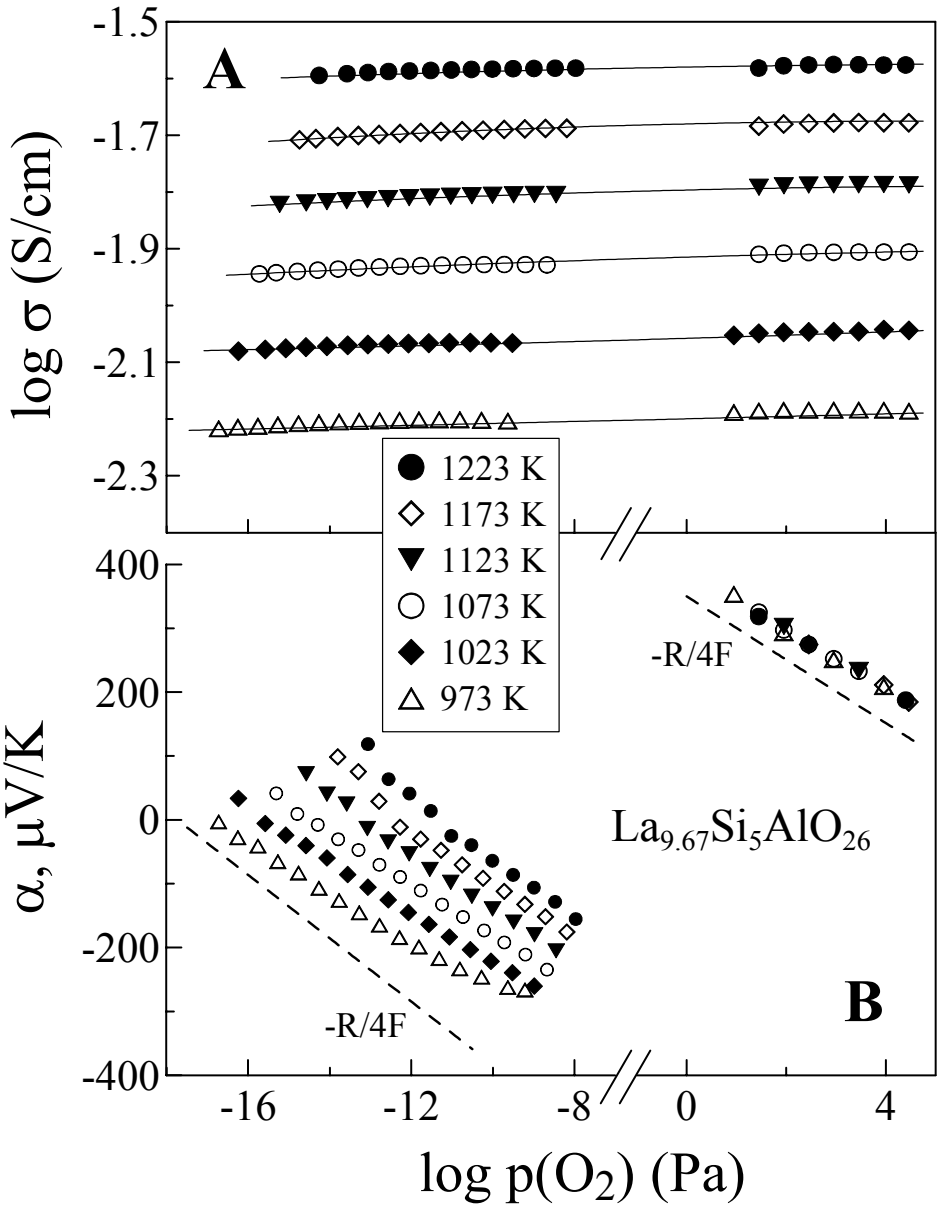

Fig. 7.5. Oxygen pressure dependencies of the total conductivity (A) and Seebeck coefficient (B) of $La_{9.67}Si_5AlO_{26}$ ceramics.

7.1.3. Electronic conductivity

Fig. 7.6 presents the temperature dependence of the partial electronic conductivity, calculated from results of impedance spectroscopy and FE measurements in air. The activation energy varies from 57 to 100 kJ/mol (Table 7.2). The relation between the E_a values for ionic and electronic conductivities

determines the variations of transference numbers with temperature. As for doped $LaGaO_3$ and CGO [111], the oxygen ion transference numbers of most silicates increase when temperature decreases, while the composition with maximum aluminum concentration, $La_{9.83}Si_{4.5}Al_{1.5}O_{26}$, exhibits the opposite behavior (Table 7.2). The latter trend is similar to $LaAlO_3$-based solid electrolytes [301].

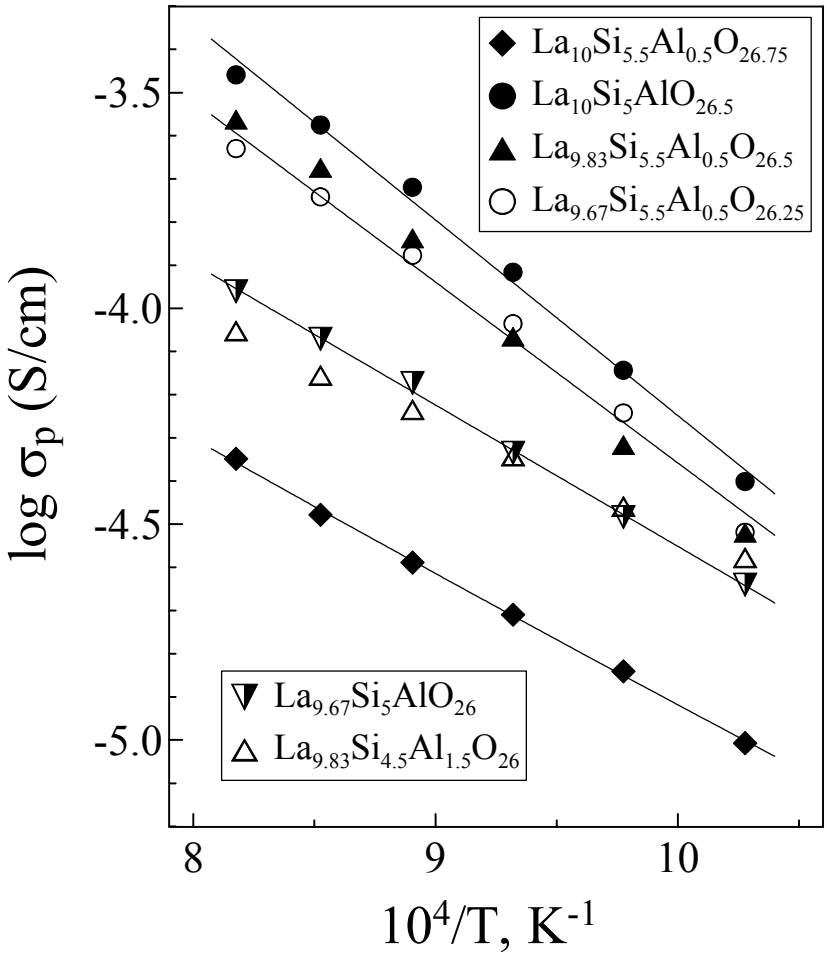

Fig. 7.6. Temperature dependencies of the partial p-type electronic conductivity of $La_{10-x}Si_{1-y}Al_yO_{26\pm\delta}$ ceramics.

When the concentration of mobile oxygen interstitials is high and essentially $p(O_2)$-independent, the transference numbers under equilibrium conditions can be described assuming a power dependence of the p-type electronic conductivity on the oxygen partial pressure:

$$t_O = \frac{\sigma_O}{\sigma_O + \sigma_p^0 p(O_2)^{1/m}} \tag{7.1}$$

where σ_O is the oxygen ionic conductivity, σ_p^0 is the p-type electronic conductivity at unit oxygen pressure, and m is a positive exponent. The theoretical value of m for solid electrolytes with $p(O_2)$-independent chemical potential of oxygen ions is 4. If the localization of holes on lattice point defects is significant, the exponent may achieve lower values [2]. Under non-zero gradient of oxygen chemical potential (μ), the average transference numbers are

$$\overline{t_O} = \frac{1}{\mu_2 - \mu_1}\int_{\mu_1}^{\mu_2} t_O d\mu \tag{7.2}$$

where μ_1 and μ_2 are the chemical potentials corresponding to $p(O_2)$ values at the electrodes, p_1 and p_2. Substitution of Eq. (7.1) into Eq. (7.2) and consequent integration yield

$$\overline{t_O}(p_1, p_2) = -m \cdot \ln\frac{k_1 p_2^{-1/m} + 1}{k_1 p_1^{-1/m} + 1} \cdot \left(\ln\frac{p_2}{p1}\right)^{-1} \tag{7.3}$$

where $k_1 = \sigma_o/\sigma_p^0$. The fitting results using Eq. (7.3), below referred to as Model 1, are shown in Fig. 7.7A by solid lines. This formula describes adequately the observed $p(O_2)$ dependence of the oxygen ion transference numbers.

For $La_{9.67}Si_{5.5}Al_{0.5}O_{26.25}$ and $La_{9.83}Si_{4.5}Al_{1.5}O_{26}$, however, the variations of $\overline{t_o}$ are very small, less than 0.0005, although the average transference numbers still increase on reducing $p(O_2)$. Such a behavior may indicate either a significant concentration of n-type charge carriers, comparable to the hole concentration, or a substantial change in the mobile interstitials content according to:

$$1/2O_2 = O_i'' + 2h^{\bullet} \tag{7.4}$$

The total conductivity, predominantly ionic, indeed exhibits a slight decrease on reducing $p(O_2)$, Fig. 7.5. An oxygen pressure-dependent component was therefore added to the term of Eq. (7.1), describing the oxygen ionic conductivity:

$$t_O = \frac{\sigma_O^c + \sigma_O^0 p(O_2)^{1/m}}{\sigma_O^c + \sigma_O^0 p(O_2)^{1/m} + \sigma_p^0 p(O_2)^{1/m}} \tag{7.5}$$

where σ_o^0 is the $p(O_2)$-dependent contribution to σ_0 at unit oxygen pressure, σ_o^c is the $p(O_2)$-independent contribution determined by the charge of cations in the apatite lattice. Notice that the reaction expressed by Eq. (7.4) implies equal exponents for the power dependencies of point defect concentrations on the oxygen pressure; in the case of interstitial oxygen-ion conductivity theoretical

value of m is 6. Substitution of Eq. (7.5) into Eq. (7.2) and consequent integration give another model for the ion transference numbers (Model 2):

$$\overline{t_O}(p_1, p_2) = 1 - m \cdot k_2 \cdot \ln\frac{k_3 p_2^{1/m} + 1}{k_3 p_1^{1/m} + 1} \cdot \left(\ln\frac{p_2}{p1}\right)^{-1} \qquad (7.6)$$

where $k_2 = \sigma_p^0/(\sigma_o^0 + \sigma_p^0)$ and $k_3 = (\sigma_o^0 + \sigma_p^0)/\sigma_o^c$. Fig. 7.7B and C compares the fitting results obtained using Models 1 and 2. For better visualization, the regression analysis was performed with both variable and fixed m. Model 2 provides a slightly better description of the experimental data (Fig. 7.7C), thus suggesting the presence of a small $p(O_2)$-dependent contribution to the ionic conductivity. The results are clearly more adequate when m is lower than 6. This may be associated to partial localization of holes in the vicinity of $O_i^{//}$ and $Al_{Si}^{/}$ (Chapter 7.1.4).

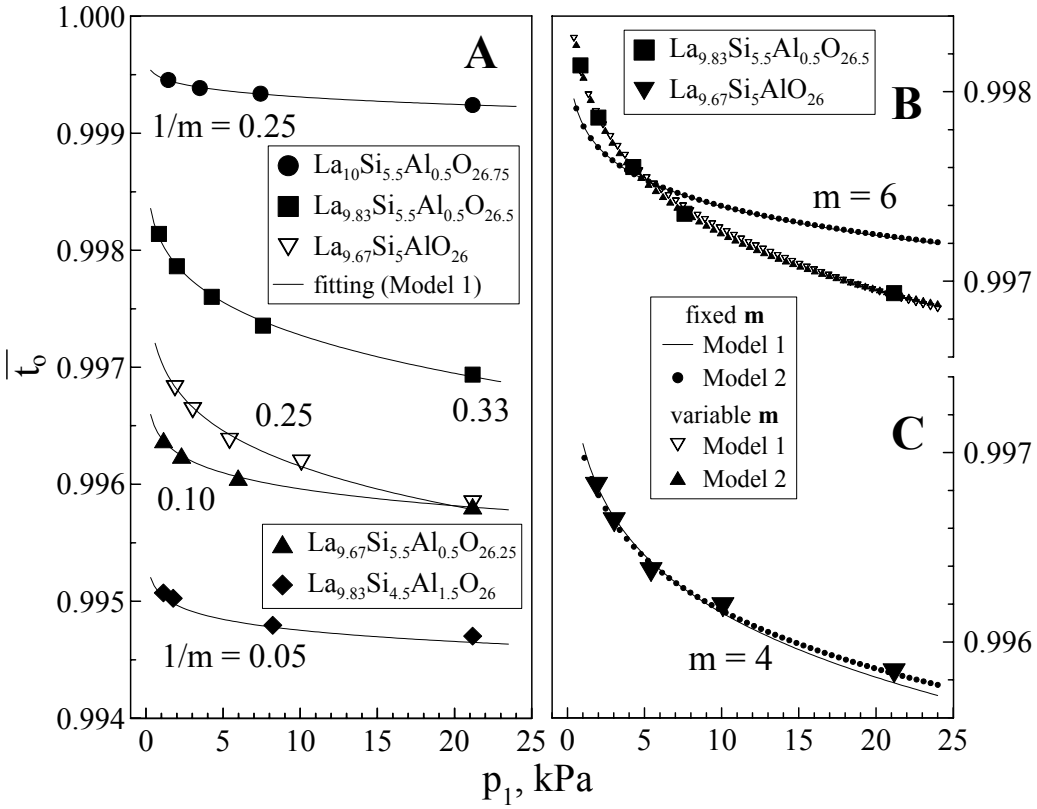

Fig. 7.7. Dependencies of the average oxygen ion transference numbers of apatite ceramics, determined by FE measurements, on the oxygen pressure.

7.1.4. Correlations between ionic and electron-hole transport

One important tendency, also observed for Fe-substituted apatites (Part 7.3), relates to the general correlation between total oxygen content, ionic transport and electronic conductivity (Fig. 7.8). The anomalous behavior of $La_{10}Si_{5.5}Al_{0.5}O_{26.75}$ may be caused either by local deviations from the nominal composition or by a change in the interstitials location due to high oxygen content, close to a possible maximum. For instance, contrary to A-site deficient $La_{9.83}Si_{4.5}Al_{1.5-y}Fe_yO_{26+\delta}$ where the interstitials are located in the vicinity of oxygen channels running through the lattice, $La_{10}Si_5FeO_{26.5}$ exhibits oxygen incorporation into the closest neighborhood of Si-site cations (Part 7.3). This assumption is in agreement with the plateau-like tendency in the ionic conductivity vs. oxygen content curves (Fig. 7.8A).

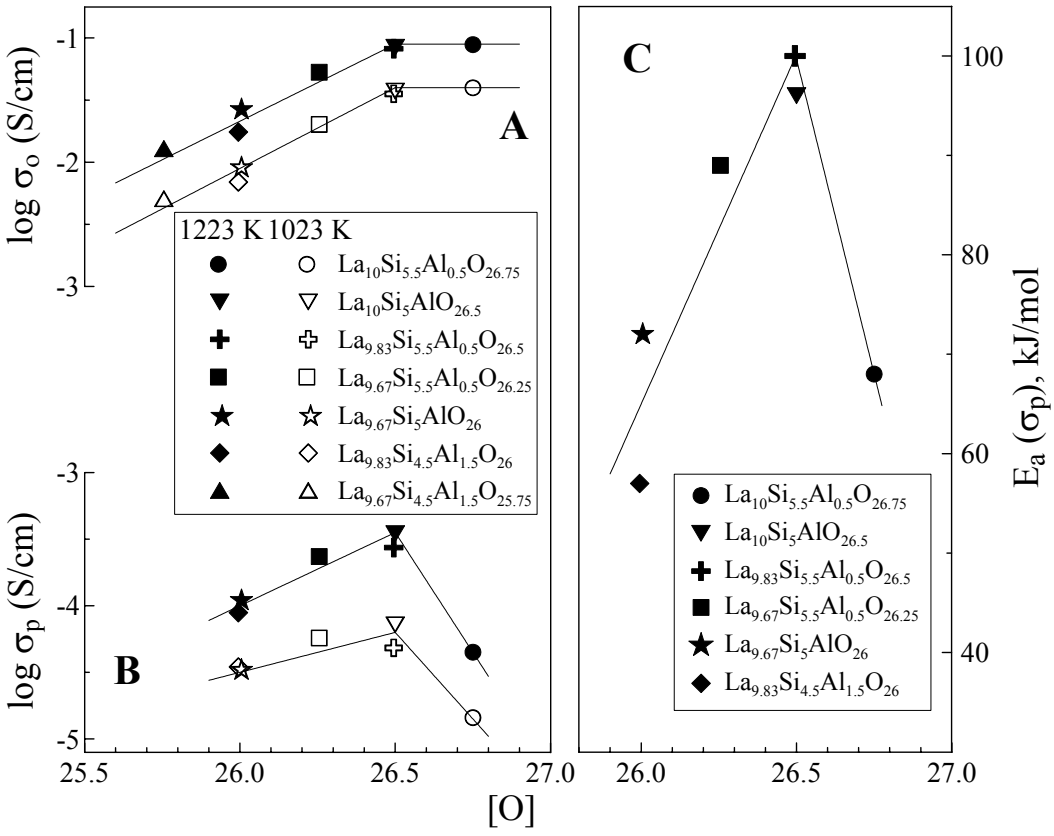

Fig. 7.8. Relationships between nominal oxygen content and partial ionic (A), p-type electronic (B) conductivities and activation energy (C) for the p-type electronic conductivity.

In the case of iron doping, the correlation between ionic and electronic conductivities results from the oxygen intercalation process (see Eq. (7.4)) which increases the concentrations of oxygen interstitials and holes, both the mobile charge carriers. A similar mechanism may also be expected for $La_{10-x}Si_{6-y}Al_yO_{27-3x/2-y/2}$. In the latter case, however, the lattice contains no variable-valence cations; the amount of hyperstoichiometric oxygen, which can be incorporated into the apatite structure in addition to the oxygen concentration determined by the cations charge, should be very small. One can expect, therefore, the presence of additional electronic charge carriers when the total oxygen content increases. As a hypothesis, one may suggest the localization of the electronic charge carriers on lattice defects having opposite charge, similar to other solid electrolytes with perovskite- and fluorite-type structure [302]. In particular, the location of holes formed due to intrinsic electronic disorder ($0 = e' + h^{\bullet}$) is expected in the vicinity of O_i'' and Al_{Si}'; the electrons may be localized on oxygen vacancies having effective positive charge. In this case, increasing concentration of interstitial oxygen should shift the electron-hole equilibrium towards formation of holes. Although one could also expect an increase in the mobility of holes and lower activation energy due to decreasing jump distance and, thus, lower energetic barrier for electron-hole transport when the oxygen content increases, this is not observed experimentally. In fact, the corresponding E_a values show a tendency similar to the electron-hole conductivity (σ_p) variation, Fig. 7.8B and C. Such tendency indicates that the migration energy becomes higher with increasing holes concentration, probably due to strong coulombic interaction between p-type electronic charge carriers. Note that the decrease of the ion transference numbers on increasing $p(O_2)$, Fig. 7.7, confirms that the electronic conduction in $La_{10-x}Si_{6-y}Al_yO_{27-3x/2-y/2}$ under oxidizing conditions is dominantly p-type.

7.1.5. Stability in reducing atmospheres

The measurements of the total conductivity of $La_{10-x}Si_{6-y}Al_yO_{27-3x/2-y/2}$ ceramics in flowing air, argon and 10%H_2-90%N_2 mixture showed that only a minor decrease in conduction is observed at low oxygen chemical potentials (Fig. 7.9). A similar conclusion was drawn analyzing the results of isothermal measurements of total conductivity vs. oxygen pressure (Fig. 7.10). The conductivity drop is more pronounced for apatites with higher oxygen content, suggesting that increasing oxygen interstitial concentration leads to decreasing metal-oxygen bond strength and, hence, increases oxygen losses from the lattice. The maximum decrease of the conductivity is observed for $La_{10}Si_{5.5}Al_{0.5}O_{26.75}$. At $p(O_2) = 10^{-14}$-10^{-8} Pa, this composition exhibits a level of ionic transport lower than that of $La_{9.83}Si_{5.5}Al_{0.5}O_{26.5}$, although the nominal oxygen content in the former is higher. On cooling the

conductivity changes become negligible; no changes in the σ values of $La_{10-x}Si_{6-y}Al_yO_{27-3x/2-y/2}$ on reducing oxygen pressure are observed below 1123 K. For the phases with relatively low oxygen content, such as $La_{9.83}Si_{4.5}Al_{1.5}O_{26}$, the conductivity is entirely $p(O_2)$-independent within all the studied temperature range.

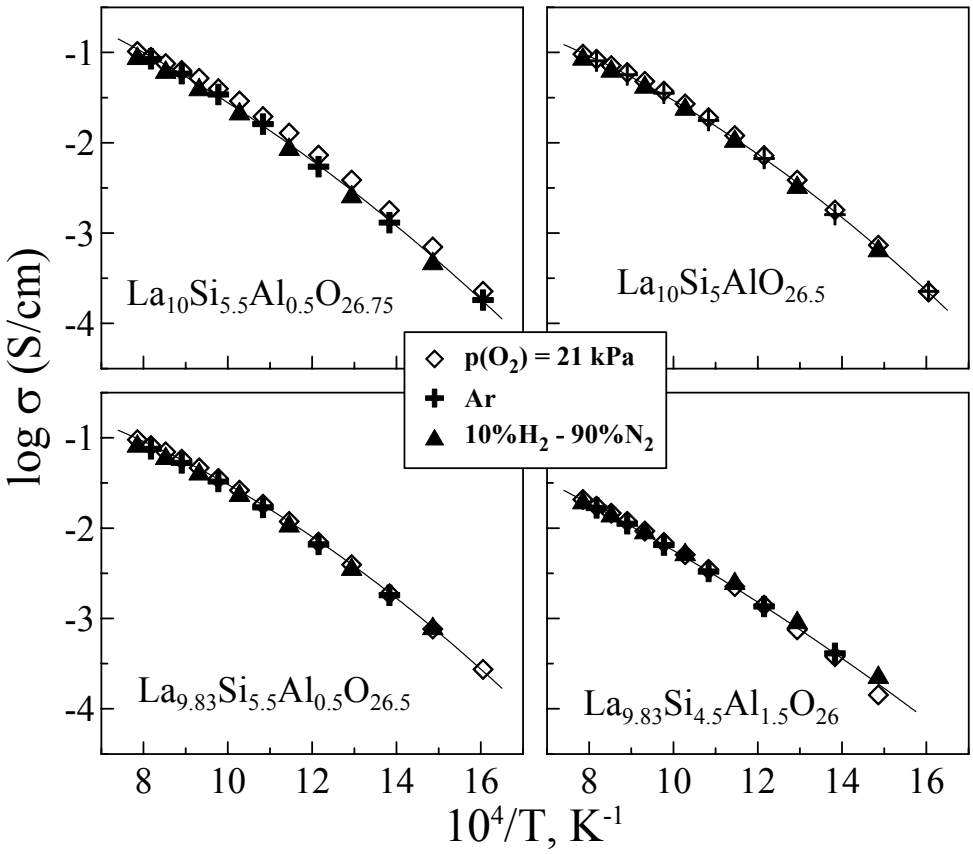

Fig. 7.9. Temperature dependencies of the total conductivity of $La_{10-x}Si_{6-y}Al_yO_{27-3x/2-y/2}$ ceramics in air, argon and dry 10%H_2-90%N_2.

Neither segregation of secondary phases nor obvious microstructural changes were detected by XRD and SEM/EDS after treatment in reducing atmospheres for 50-70 h. The thermopower at low oxygen partial pressures becomes negative (Fig. 7.5B), but the slope of *α vs. ln p(O_2)* is still close to the theoretical value for a pure oxygen-ionic conductor, -R/4F [299]. The measurements of average ion transference numbers confirmed the absence of considerable n-type electronic contribution to the total

conductivity at relatively low oxygen pressures. For example, the $\overline{t_O}$ value of $La_{9.67}Si_5AlO_{26}$ under air/10%H_2-90%N_2 gradient is about 0.999 at 1273 K.

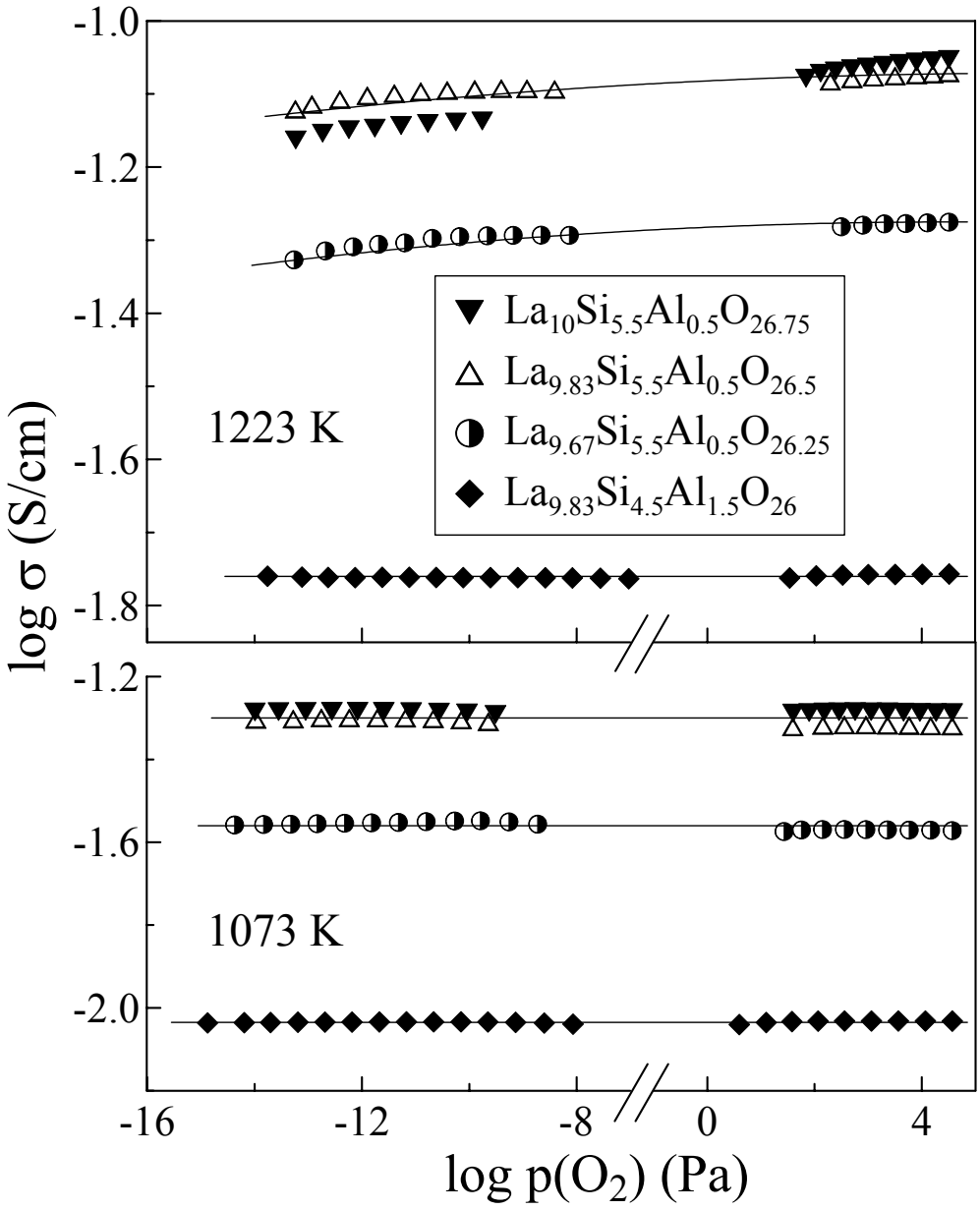

Fig. 7.10. Oxygen pressure dependencies of the total conductivity of $La_{10-x}Si_{6-y}Al_yO_{27-3x/2-y/2}$ ceramics.

However, the long-term stability tests in reducing gases demonstrated a slow irreversible degradation of samples at temperatures above 1100 K, associated to minor volatilization of SiO from the surface layers of the apatite ceramics. For example, after approximately 600 h of oxygen partial pressure cycling in CO-CO_2 atmosphere, the conductivity of $La_{9.83}Si_{5.5}Al_{0.5}O_{26.5}$ ceramics at 1223 K decreased by 18%. The maximum degradation was observed after the first 120-150 h; subsequent annealing results in very small changes. Similar data were obtained in the course of long-term treatment in flowing H_2-N_2 gas mixture (Fig. 7.11). In this case, the conductivity drop for $La_{10}Si_5AlO_{26.5}$ ceramics at 1173 K is about 21%.

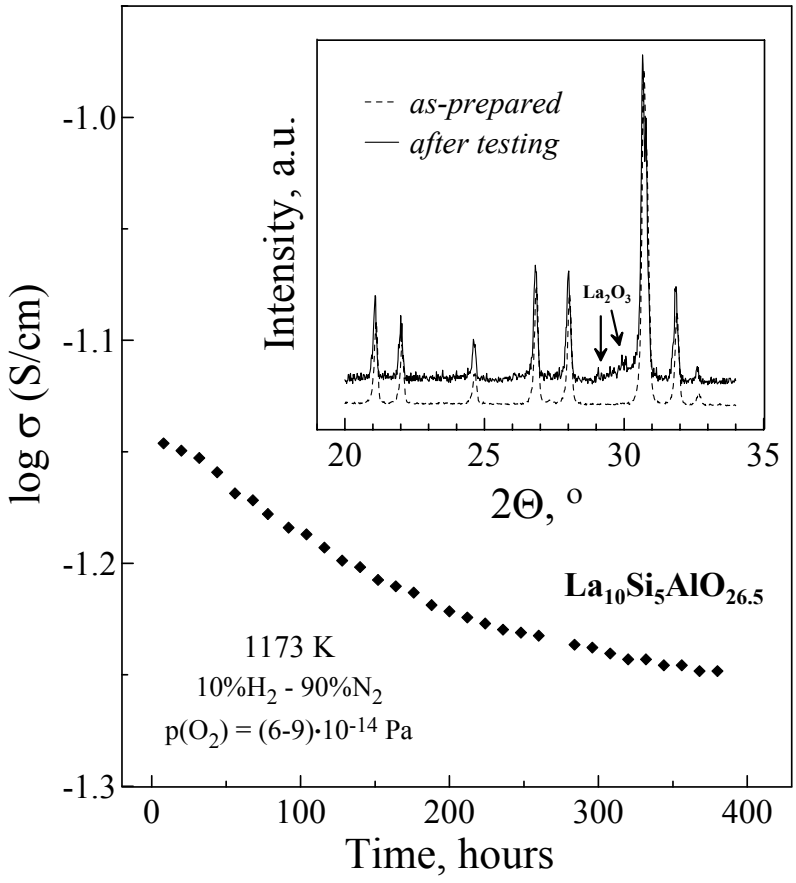

Fig. 7.11. Time dependence of the total conductivity of $La_{10}Si_5AlO_{26.5}$ in flowing 10%H_2-90%N_2 at 1173 K. The inset shows representative fragments of XRD patterns of $La_{10}Si_5AlO_{26.5}$ ceramics before and after treatment. The strongest reflections of segregated La_2O_3 are marked by arrows.

The XRD analysis of the ceramics surface exposed to hydrogen-containing atmosphere during approximately 400 h, confirmed the presence of lanthanum oxide traces (inset of Fig. 7.11). The secondary phase segregation at the surface is also visible in the SEM micrographs; one example is given in Fig. 7.12A. The XRD and SEM/EDS inspection of the ceramics bulk revealed no changes after long-term treatment in reducing environments (Fig. 7.12B), indicating that the conductivity variations with time are mainly related to surface layers.

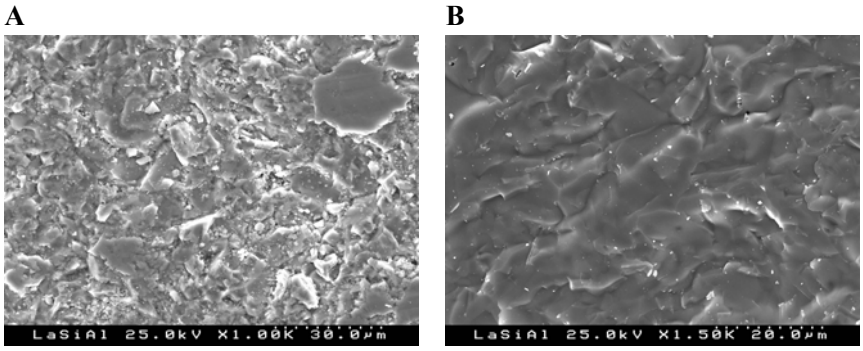

Fig. 7.12. SEM micrographs of surface (A) and fractured bulk (B) of $La_{10}Si_5AlO_{26.5}$ ceramics after long-term annealing in 10%H_2-90%N_2 mixture at 1173 K.

7.2. The $La_{7-x}Sr_3Si_6O_{26-\delta}$ ceramics: assessment of vacancy contribution to the ionic conductivity

The $La_{7-x}Sr_3Si_6O_{26-\delta}$ system was considered appropriate for studying the behavior of oxygen-deficient apatites, where the oxygen vacancy concentration is close to the maximum that may be tolerated by the apatite structure. The cell parameters and TECs are given in Table 7.3, typical SEM micrographs are presented in Fig. 7.13. In the case of Sr-substituted phases, the grains have a specific elongated shape with a length of 5-15 μm.

Table 7.3. Properties of $La_{7-x}Sr_3Si_6O_{26-\delta}$ ceramics.

Composition	S.G.	a, Å	c, Å	ρ_{exp} / ρ_{theor}, %	T, K	$\alpha \times 10^6$ K^{-1}
$La_7Sr_3Si_6O_{25.5}$	$P6_3/m$	9.720(5)	7.251(6)	97.8	373-1273	8.92 ± 0.01
$La_6Sr_3Si_6O_{24}$	$P6_3/m$	9.709(9)	7.240(9)	84.0	373-1273	9.14± 0.02

SEM analysis of $La_7Sr_3Si_6O_{25.5}$ ceramics confirmed a low porosity and an apparent absence of liquid phase formation at the grain boundaries, whereas the formation of a glassy phase at the

boundaries was revealed for $La_6Sr_3Si_6O_{24}$. This observation is in agreement with the Rietveld refinement results showing that this material is La-rich with respect to the nominal composition, thus suggesting a segregation of a SiO_2-rich phase, probably amorphous. A similar conclusion was drawn from the picnometric measurements. The apparent density of $La_6Sr_3Si_6O_{24}$ ceramics was only 84.0% of the theoretical density, calculated assuming single formation of the apatite phase. This confirms the presence of a silica-rich glass having low density. Nonetheless, the impedance spectroscopy indicated no significant grain-boundary contribution to the total resistivity for $La_6Sr_3Si_6O_{24}$ at T > 823-873 K, as well as no impurity peaks were observed in the XRD patterns of $La_6Sr_3Si_6O_{24}$.

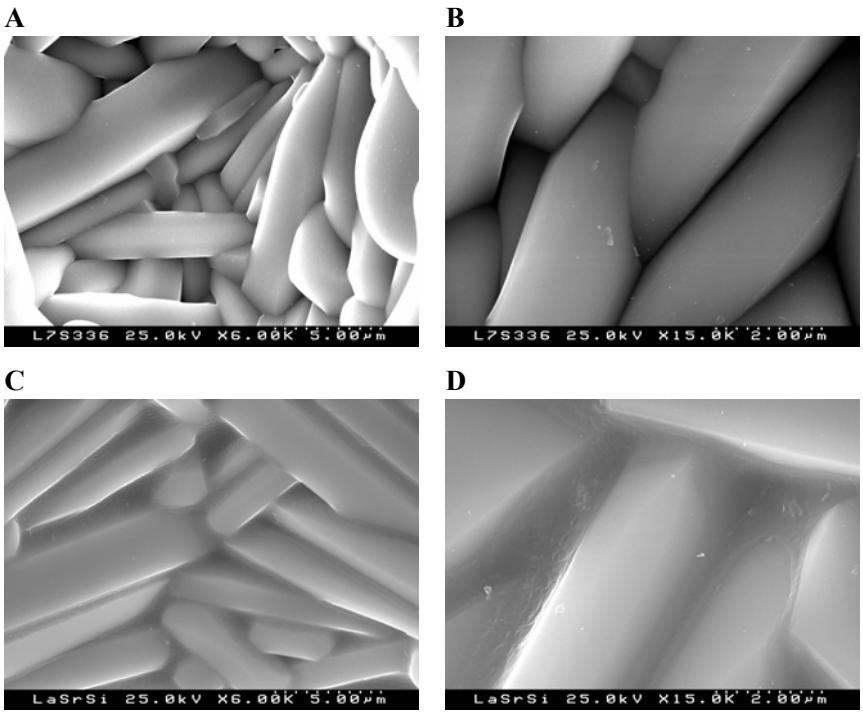

Fig. 7.13. SEM micrographs of $La_7Sr_3Si_6O_{25.5}$ (A and B) and $La_6Sr_3Si_6O_{24}$ (C and D).

Oxygen-deficient $La_7Sr_3Si_6O_{25.5}$ and $La_6Sr_3Si_6O_{24}$ show a similar level of total conductivity (Fig. 7.14) indicating that a silica-rich phase segregated in the latter material seems to have no blocking effect. The electrical transport of $La_{7-x}Sr_3Si_6O_{26-\delta}$ is 10^3-10^6 times lower than that of $La_{9.83}Si_{4.5}Al_{1.5}O_{26}$, whilst the activation energy is about 3 times higher. No detailed transport studies of $La_6Sr_3Si_6O_{24}$ were performed, as the true composition of $La_6Sr_3Si_6O_{24}$ ceramics differs significantly from the nominal one. The EMF measurements clearly demonstrated that $La_7Sr_3Si_6O_{25.5}$ is an oxygen ion-conducting solid

electrolyte. At 973-1223 K in O_2/air gradient, the electron transference numbers (t_e) of this material vary within 0.02-0.04. The atomistic simulation results [94] indicate that the preferential ionic transport mechanism for $La_7Sr_3Si_6O_{25.5}$ is via linear vacancy jumps between O5 sites. Such mechanism does not exclude, however, oxygen incorporation into the vacant O5 positions, generating electron holes and affecting the vacancy concentration. Very low level of ionic conduction in oxygen-deficient $La_7Sr_3Si_6O_{25.5}$ suggests a negative effect of decreasing oxygen interstitial concentration and simultaneous increasing oxygen vacancy content on the ionic transport properties. A similar effect can be expected for Fe-doped apatites at low oxygen pressure.

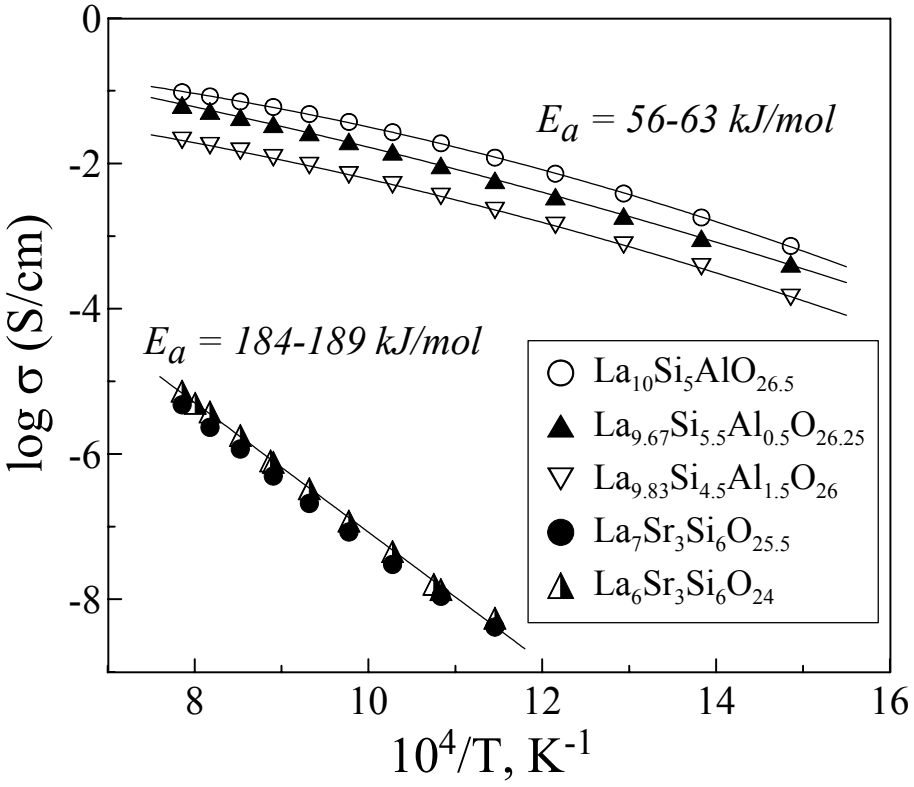

Fig. 7.14. Comparison of the total conductivity of $La_{7-x}Sr_3Si_6O_{26-\delta}$ and $La_{10-x}Si_{1-y}Al_yO_{26\pm\delta}$ ceramics.

7.3. Transport properties of $La_{10-x}Si_{6-y}Fe_yO_{26\pm\delta}$ ($0 \le x \le 0.67$, $1 \le y \le 2$) apatites

7.3.1. Crystal structure

According to XRD data, single apatite-type phases were formed in all cases, except for $La_{9.33}Si_5FeO_{25.5}$. The space groups and lattice parameters, determined by Rietveld refinement (see Appendix 1D), are listed in Table 7.4. Doping with iron leads to increasing unit cell volume due to a larger radius of Fe^{3+} cations when compared to Si^{4+}; the creation of A-site vacancies has an opposite effect.

Table 7.4. Properties of $La_{10-x}Si_{6-y}Fe_yO_{26\pm\delta}$ ceramics.

Composition	S.G.	a, Å	c, Å	ρ_{exp} / ρ_{theor}, %	T, K	$\alpha \times 10^6$ K^{-1}
$La_{10}Si_5FeO_{26.5}$	$P6_3/m$	9.757(3)	7.255(1)	98.8	373-1273	8.22 ± 0.03
$La_{10}Si_{4.5}Fe_{1.5}O_{26.25}$	$P6_3/m$	9.765(8)	7.255(7)	98.3	373-1273	8.61 ± 0.03
$La_{10}Si_4Fe_2O_{26}$	$P6_3$	9.788(7)	7.268(7)	99.0	373-1273	9.90 ± 0.01
$La_{9.33}Si_5FeO_{25.5}$	$P6_3/m$	9.749(8)	7.230(7)	-	373-1273	9.02 ± 0.01

Inspection of the XRD patterns of $La_{9.33}Si_5FeO_{25.5}$ revealed minor extra peaks corresponding to the perovskite-type lanthanum ferrite (PDF card 74-2203). $LaFeO_3$ was thus included in the refinement as the second phase. The weight fraction of $LaFeO_3$ in $La_{9.33}Si_5FeO_{25.5}$ was estimated as 3.2%, which corresponds to a molar ratio between the perovskite and apatite phases of approximately 0.26. Within the limits of experimental uncertainty, this estimation is in agreement with the Mössbauer spectroscopy data indicating about 34% of $LaFeO_3$ phase (Appendix 4, Table 3). Such a large amount of segregated lanthanum ferrite suggests a decrease in the solubility of iron in the silicate lattice when the A-site deficiency increases.

7.3.2. Ceramic microstructure and thermal expansion

SEM/EDS studies confirmed the high quality of $La_{10-x}Si_{6-y}Fe_yO_{26\pm\delta}$ materials, in particular a low porosity and an apparent absence of liquid phase formation at the grain boundaries. These observations agree well with the impedance spectra of $La_{10-x}Si_{6-y}Fe_yO_{26\pm\delta}$ apatites, which suggest no considerable grain-boundary contribution to the total resistivity at temperatures above 873-923 K. Typical SEM micrographs are presented in Fig. 7.15. Surprisingly, the average grain size for $La_{10}Si_5FeO_{26.5}$ and $La_{9.33}Si_5FeO_{25.5}$ both sintered at 1773 K, in the range 3-5 μm, is considerably larger than that of $La_{10}Si_{4.5}Fe_{1.5}O_{26.25}$ and $La_{10}Si_4Fe_2O_{26}$, sintered at 1823 and 1873 K, respectively.

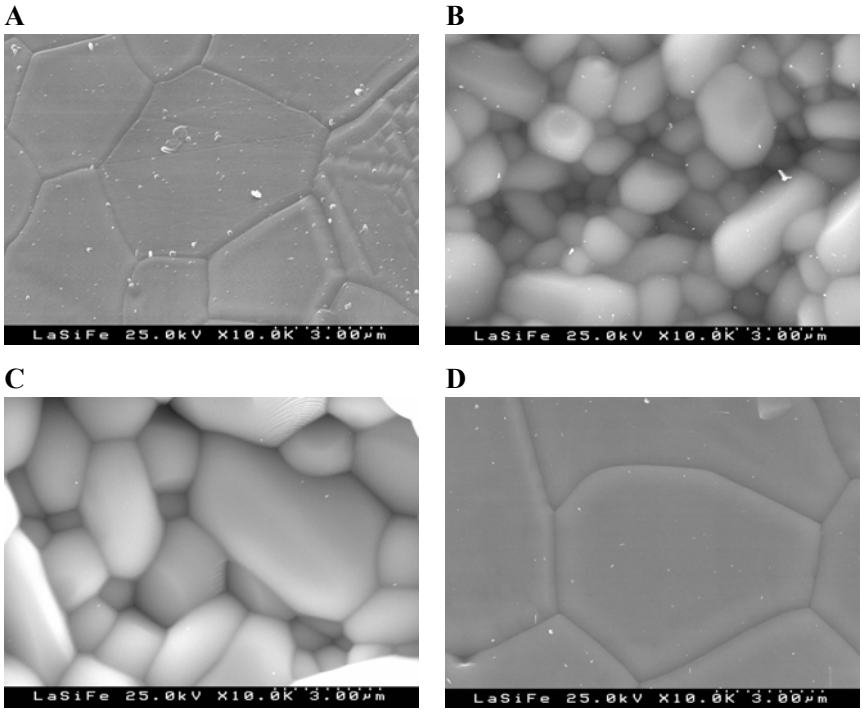

Fig. 7.15. SEM micrographs of $La_{10}Si_5FeO_{26.5}$ (A), $La_{10}Si_{4.5}Fe_{1.5}O_{26.25}$ (B), $La_{10}Si_4Fe_2O_{26}$ (C) and $La_{9.33}Si_5FeO_{25.5}$ (D).

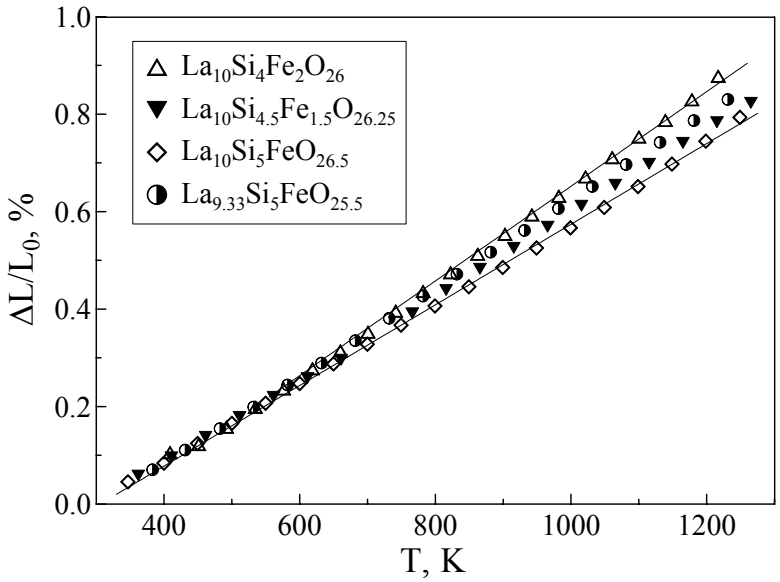

Fig. 7.16. Dilatometric curves of $La_{10-x}Si_{6-y}Fe_yO_{26\pm\delta}$ materials in air.

Dilatometric curves of $La_{10-x}Si_{6-y}Fe_yO_{26\pm\delta}$ ceramics were found approximately linear within the studied temperature range, 373-1273 K (Fig. 7.16). TECs vary from 8.22×10^{-6} to 9.90×10^{-6} K^{-1} (Table 7.4) and compare well with those of $La_{10-x}Si_{1-y}Al_yO_{26\pm\delta}$ electrolytes (Table 7.1). A correlation between TEC values and iron content in the $La_{10}Si_{6-x}Fe_xO_{27-x/2}$ series can be related, most probably, to minor oxygen losses on heating, which is expected to increase with increasing iron concentration.

7.3.3. Ion transference numbers and partial conductivities

Fig. 7.17 presents the temperature dependencies of the total conductivity of $La_{10-x}Si_{6-y}Fe_yO_{26\pm\delta}$ phases in air. In the single-phase $La_{10}Si_{6-x}Fe_xO_{27-x/2}$ series, the substitution of Si with Fe leads to decreasing electrical transport and increasing activation energy (Table 7.5) due to lower oxygen concentration in the crystal lattice. High ionic transport observed for $La_{10}Si_5FeO_{26.5}$ and $La_{10}Si_{4.5}Fe_{1.5}O_{26.25}$ is obviously due to O7 interstitials, predicted by atomistic modeling [94] and confirmed by Mössbauer spectroscopy (Appendix 4). The higher conductivity of $La_{9.33}Si_5FeO_{25.5}$ when compared to $La_{10}Si_4Fe_2O_{26}$ might be related to the segregation of secondary highly-conductive perovskite-type phase in $La_{9.33}Si_5FeO_{25.5}$ ceramics.

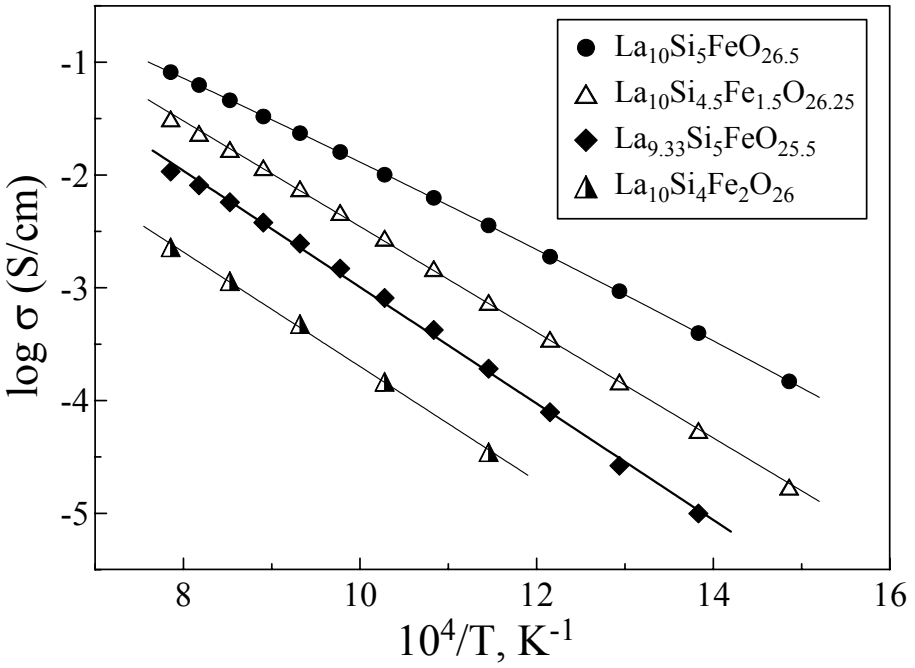

Fig. 7.17. Temperature dependencies of the total conductivity of $La_{10-x}Si_{6-y}Fe_yO_{26\pm\delta}$ materials in air.

In the case of $La_{9.33}Si_5FeO_{25.5}$, the low activation energy for electronic transport and the increase of ion transference numbers with temperature are partly explained by the segregation of $LaFeO_3$ having a relatively high p-type conductivity in air [186].

Table 7.5. Oxygen ion transference numbers (t_O) and activation energies (E_A) of the partial oxygen ionic (σ_O) and electronic (σ_e) conductivities of $La_{10-x}Si_{6-y}Fe_yO_{26\pm\delta}$ ceramics in air.

Composition	t_O				E_A	
	1223 K	1123 K	1073 K	973 K	σ_O	σ_e
$La_{10}Si_5FeO_{26.5}$	0.9945	0.9953	0.9959	0.9961	81 ± 1	94 ± 5
$La_{10}Si_{4.5}Fe_{1.5}O_{26.25}$	0.9932	0.9926	0.9921	0.9913	95 ± 2	84 ± 2
$La_{10}Si_4Fe_2O_{26}$	0.9700	0.9710	0.9710	0.9709	107 ± 4	104 ± 3
$La_{9.33}Si_5FeO_{25.5}$	0.9915	0.9862	0.9818	0.9640	102 ± 3	44 ± 4

The activation energies for ionic and electronic conductivities correspond to the temperature ranges 873-1273 and 973-1223 K, respectively.

Although the electronic transport might be expected to increase when the concentration of variable-valence iron cations increases, the partial electronic conductivity (σ_e) exhibits an opposite trend (Fig. 7.18) and correlates with oxygen content.

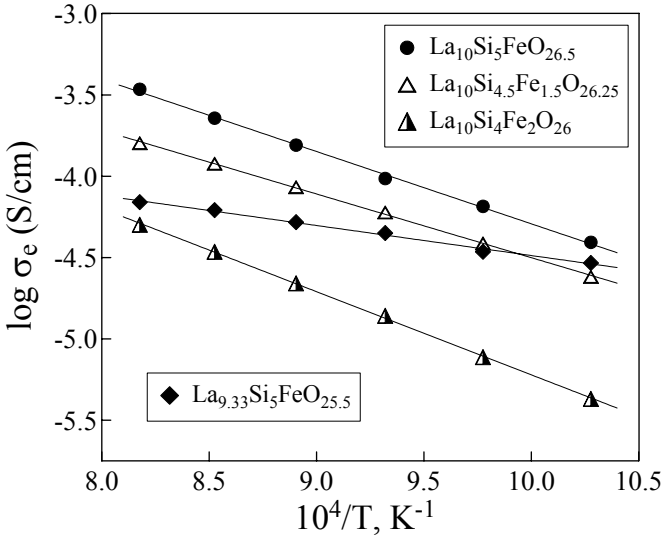

Fig. 7.18. Temperature dependencies of the partial electronic conductivity of $La_{10-x}Si_{6-y}Fe_yO_{26\pm\delta}$ ceramics in air.

Such behavior can be explained assuming that bonding of hyperstoichiometric oxygen in the apatite lattice is weaker than that of anions forming regular $(Si,Fe)O_4$ tetrahedra. In this situation, heating may lead to minor oxygen losses compensated by the generation of n-type electronic charge carriers. In the case of oxygen-stoichiometric $La_{10}Si_4Fe_2O_{26}$, electronic conduction is believed to occur via migration of holes formed due to charge disproportionation of Fe^{3+}; although the concentrations of holes and electrons should be similar, the p-type carriers typically possess a significantly higher mobility [186]. Decreasing x in $La_{10}Si_{6-x}Fe_xO_{27-x/2}$ apatites should hence increase the role of n-type electronic conduction. This hypothesis is supported by data on ion transference numbers as a function of the oxygen pressure (Fig. 7.19). For $La_{10}Si_4Fe_2O_{26}$, the t_o values increase when $p(O_2)$ decreases, unambiguously indicating that the electronic conduction under oxidizing conditions is predominantly p-type. These variations can be described by Eqs. (7.3) or (7.6).

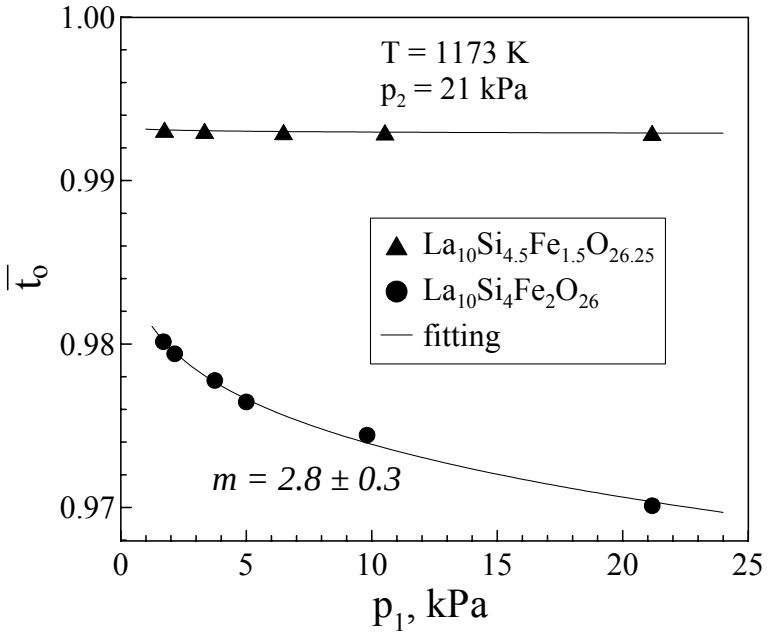

Fig. 7.19. Dependencies of the average oxygen ion transference numbers of apatite ceramics, determined by FE measurements, on the oxygen pressure.

Both $La_{10}Si_4Fe_2O_{26}$ and $La_{10}Si_{4.5}Fe_{1.5}O_{26.25}$ exhibit positive m values; for the latter composition, however, 1/m is close to 0, thus suggesting that within this narrow $p(O_2)$ range the concentrations of n- and p-type charge carriers are comparable.

7.3.4. Behavior at reduced oxygen chemical potentials

The $p(O_2)$ dependencies of total conductivity and Seebeck coefficient confirm that, under oxidizing conditions, $La_{10}Si_{6-x}Fe_xO_{27-x/2}$ are solid electrolytes (Fig. 7.20). At $p(O_2) > 10^{-5}$ Pa, the conductivity remains essentially independent of the oxygen pressure. The Seebeck coefficient in oxidizing atmospheres is positive; the slope of α *vs. ln* $p(O_2)$ is close to (-R/4F), the theoretical value for a pure solid electrolyte. Under reducing conditions, however, the conductivity of $La_{10}Si_5FeO_{26.5}$ starts to decrease, while the thermopower variations suggest that the ionic transport is still dominant. Such a tendency is due to decreasing oxygen ionic charge carrier concentration.

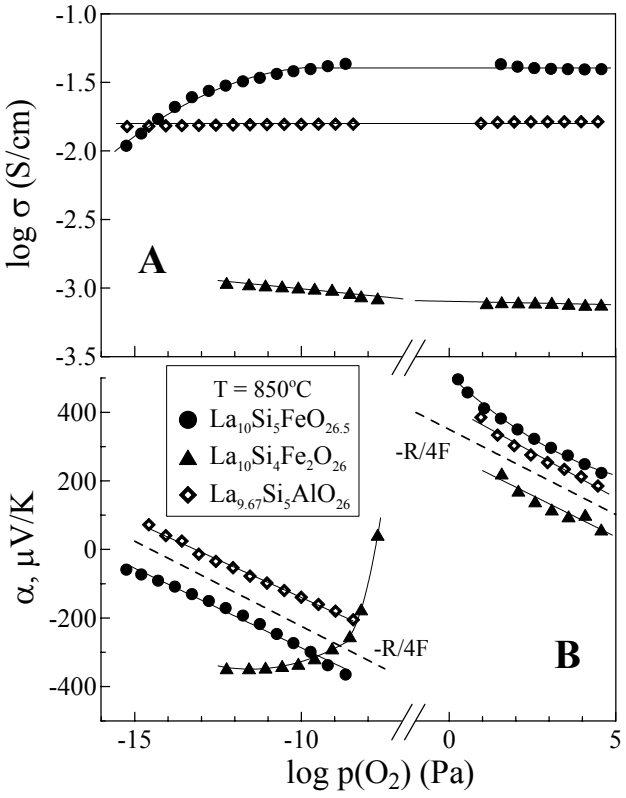

Fig. 7.20. Oxygen pressure dependencies of the total conductivity (A) and Seebeck coefficient (B) of $La_{10}Si_5FeO_{26.5}$ and $La_{10}Si_4Fe_2O_{26}$ apatite ceramics. Data on $La_{9.67}Si_5AlO_{26}$ are given for comparison.

The conductivity of $La_{10}Si_4Fe_2O_{26}$ slightly increases on reduction, whereas the Seebeck coefficient shows a behavior indicative of increasing n-type electronic transport [186]. Most likely, the

latter trend masks a drop in ionic conduction, expected when the oxygen content is lower than stoichiometric [89,298]. If compared to the $La_{9.67}Si_5AlO_{26}$ apatite where no variable-valence cations are incorporated into the lattice, the conduction stability of $La_{10}Si_{6-x}Fe_xO_{27-x/2}$ phases in reducing environments is rather poor. This is also illustrated in Fig. 7.21 showing the temperature dependencies of the total conductivity in various gas mixtures.

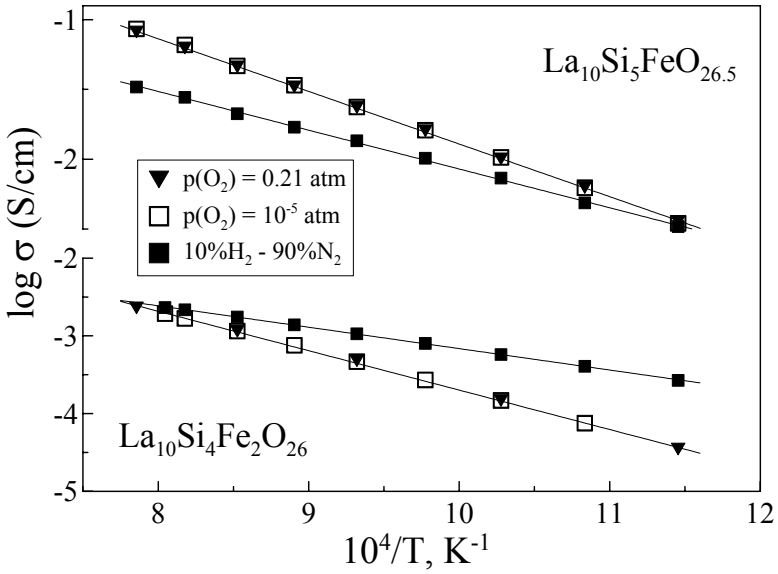

Fig. 7.21. Temperature dependencies of the total conductivity of $La_{10}Si_5FeO_{26.5}$ and $La_{10}Si_4Fe_2O_{26}$ apatites in various atmospheres.

No phase decomposition or secondary phases in reducing environments were detected by XRD. Analogously, the Mössbauer spectra showed no traces of metallic iron in reduced apatites; even the concentration of Fe^{2+} was found lower than the detection limit (Appendix 4, Table 4).

The results show that, due to Fe^{3+} stabilization in the apatite lattice, Fe-doped $La_{10-x}(Si,Al)O_{26\pm\delta}$ materials keep the ionic conductivity dominant down to relatively low oxygen chemical potentials. Since the materials with prevailing vacancy-based oxygen diffusion mechanisms possess drastically lower ionic transport (Chapter 7.2), even minor changes in the oxygen stoichiometry have a strong effect on the ionic conduction (Fig. 7.21). The transition from interstitial-migration to the vacancy mechanism, accompanied with ionic conductivity drop, is likely to occur for apatites with low iron content; iron doping seems to suppress this transition, simultaneously increasing the n-type electronic conductivity under reducing conditions.

7.4. Transport properties of apatite-type $La_{9.83}Si_{4.5}Al_{1.5-x}Fe_xO_{26\pm\delta}$ ($0 \le x \le 1.5$) oxides

7.4.1. Crystal structure

XRD analysis of $La_{9.83}Si_{4.5}Al_{1.5-x}Fe_xO_{26\pm\delta}$ ceramics showed formation of single apatite-type phases. The space groups and lattice parameters, determined by Rietveld refinement, are listed in Table 7.6. Doping with iron leads to increasing unit cell volume due to a large radius of Fe^{3+} cations if compared to Al^{3+} [8]. Data on relative changes of the material density in the course of sintering ($\Delta\rho/\rho_{gr}$) are in agreement with the observation [86] that iron additions increase the sinterability of the apatite ceramics. In fact, sintering of solid-electrolyte materials is usually promoted by additions of transition metal oxides [257]. This feature may be very important taking into account the poor sinterability of doped apatite-type silicates [86,89,298].

Table 7.6. Properties of $La_{9.83}Si_{4.5}Al_{1.5-x}Fe_xO_{26\pm\delta}$ ceramics.

Composition	S.G.	a, Å	c, Å	ρ_{exp} / ρ_{theor}, %	$\Delta\rho$ / ρ_{gr}, %	T, K	$\alpha \times 10^6$, K^{-1}
$La_{9.83}Si_{4.5}Al_{1.5}O_{26}$	$P\bar{3}$	9.734(3)	7.236(6)	96.7	56.7	373-1273	8.86 ± 0.02
$La_{9.83}Si_{4.5}AlFe_{0.5}O_{26}$	$P\bar{3}$	9.746(3)	7.246(4)	95.8	70.5	373-1273	8.91 ± 0.03
$La_{9.83}Si_{4.5}Al_{0.5}FeO_{26}$	$P\bar{3}$	9.757(1)	7.250(9)	96.3	72.8	373-1273	9.50 ± 0.02
$La_{9.83}Si_{4.5}Fe_{1.5}O_{26}$	$P6_3$	9.772(6)	7.262(0)	97.5	74.9	373-1273	9.04 ± 0.01

The Mössbauer spectra of $La_{9.83}Si_{4.5}Al_{1.5-y}Fe_yO_{26}$ consist of asymmetric doublets (Appendix 4, Fig. 3). The IS values estimated for these doublets (Appendix 4, Table 5) are typical of Fe^{3+} and Fe^{4+} [265]. Note that to compensate Fe^{4+} formation, $La_{9.83}Si_{4.5}Al_{0.5}FeO_{26}$ and $La_{9.83}Si_{4.5}Fe_{1.5}O_{26}$ should contain hyperstoichiometric oxygen. In the case of the $La_{9.83}Si_{4.5}AlFe_{0.5}O_{26}$ spectrum, no Fe^{4+} was detected. However, since the quality of the latter spectrum is relatively poor due to the low total iron content in this sample, the accuracy of the corresponding data is worse than for other apatite phases.

The absence of tetravalent iron was also observed for the lanthanum-stoichiometric apatite $La_{10}Si_4Fe_2O_{26}$ (Appendix 4, Table 4). The A-site deficiency leads, however, to formation of Fe^{4+}, the fraction of which increases with increasing total iron content. Most probably, this tendency is associated with Frenkel-type disordering in O5 sites, induced by lanthanum vacancies [89,94]. The resultant local lattice distortions may cause displacement of a part of the O5 anions into nearby O6 interstitial positions [89,94]. As O6 sites are located midway between the channel O5 positions [89], this type of disorder should not increase the coordination number of iron cations. The structure refinement results of $La_{9.83}Si_{4.5}Al_{1.5-y}Fe_yO_{26}$ show that the La distribution between different sites is

dependent on iron concentration (Table 7.7). Namely, most lanthanum vacancies are located in La1 and La2 positions for y = 0 and 0.5, and in La3 sites for y = 1.0 and 1.5. As La3 cations are the nearest neighbors of O5 anions, these vacancies may promote incorporation of extra oxygen into O5 vacancies formed due to Frenkel disorder, thus favoring Fe^{4+} formation.

Table 7.7. Selected results of the structural refinement of $La_{9.83}Si_{4.5}Al_{1.5-x}Fe_xO_{26\pm\delta}$ phases.

Composition	Lanthanum site occupancy			Agreement factors	
	Site	Wyckoff position	Occupancy	R_p, %	χ^2
$La_{9.83}Si_{4.5}Al_{1.5}O_{26}$	La1	2d	0.9(1)	9.71	1.96
	La2	2d	0.9(8)		
	La3	6g	1.0(0)		
$La_{9.83}Si_{4.5}AlFe_{0.5}O_{26}$	La1	2d	0.96(3)	9.63	4.10
	La2	2d	0.94(1)		
	La3	6g	1.0(0)		
$La_{9.83}Si_{4.5}Al_{0.5}FeO_{26}$	La1	2d	1.0(0)	9.22	3.33
	La2	2d	1.0(0)		
	La3	6g	0.97(4)		
$La_{9.83}Si_{4.5}Fe_{1.5}O_{26}$	La1	2b	1.0(0)	9.53	3.54
	La2	2b	1.0(0)		
	La3	6c	0.97(8)		

7.4.2. Ceramic microstructure and thermal expansion

SEM/EDS studies confirmed that $La_{9.83}Si_{4.5}Al_{1.5-x}Fe_xO_{26\pm\delta}$ ceramics had low porosity and an apparent absence of phase impurities or liquid phase formation at the grain boundaries. Impedance spectra of $La_{9.83}Si_{4.5}Al_{1.5-x}Fe_xO_{26\pm\delta}$ apatites also show no considerable grain-boundary contribution to the total resistivity at temperatures above 823-873 K (Fig. 7.22). Typical SEM micrographs are presented in Fig. 7.23. The average grain size, 1-3 μm, is similar for $La_{9.83}Si_{4.5}Al_{1.5}O_{26}$, sintered at 1923 K, and for $La_{9.83}Si_{4.5}AlFe_{0.5}O_{26}$, $La_{9.83}Si_{4.5}Al_{0.5}FeO_{26}$ and $La_{9.83}Si_{4.5}Fe_{1.5}O_{26}$, sintered at 1873 K. Dilatometric curves of $La_{9.83}Si_{4.5}Al_{1.5-x}Fe_xO_{26\pm\delta}$ ceramics were found approximately linear within the studied temperature range, 373-1273 K (Fig. 7.24). TECs vary from 8.86×10^{-6} to 9.50×10^{-6} K^{-1} (Table 7.6) and compare well with those of $La_{10-x}Si_{1-y}Al_yO_{26\pm\delta}$ and $La_{10}Si_{6-x}Fe_xO_{27-x/2}$ electrolytes (Tables 7.1 and 7.4).

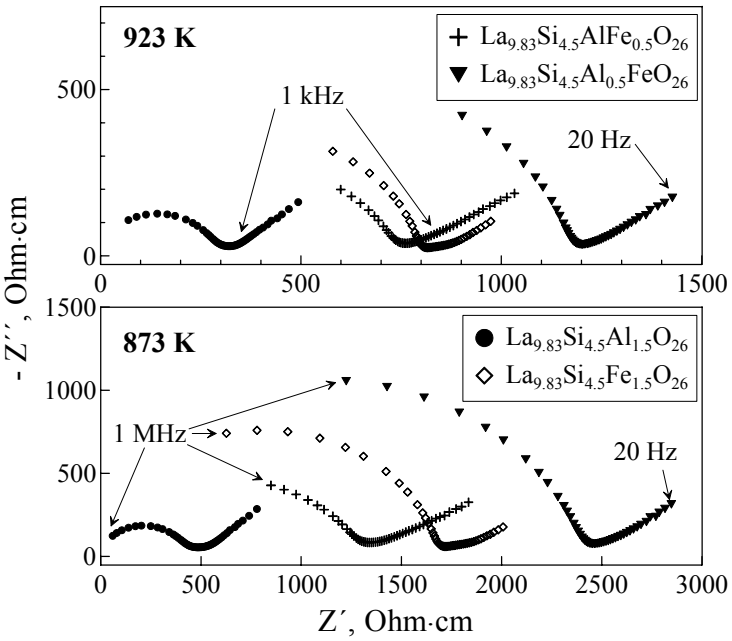

Fig. 7.22. Examples of the impedance spectra of $La_{9.83}Si_{4.5}Al_{1.5-x}Fe_xO_{26\pm\delta}$ ceramics with porous Pt electrodes in air.

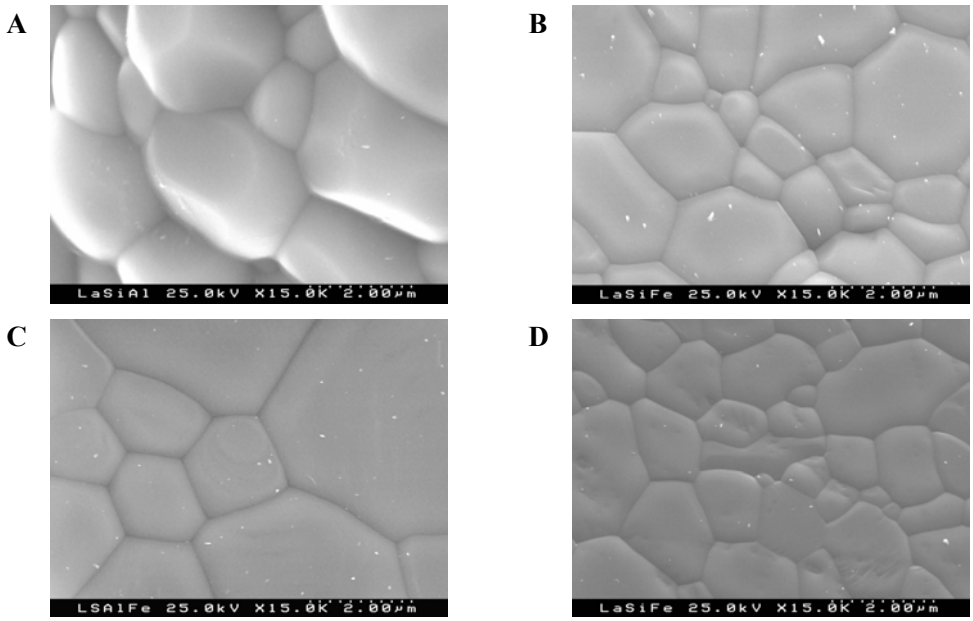

Fig. 7.23. SEM micrographs of $La_{9.83}Si_{4.5}Al_{1.5}O_{26}$ (A), $La_{9.83}Si_{4.5}AlFe_{0.5}O_{26}$ (B), $La_{9.83}Si_{4.5}Al_{0.5}FeO_{26}$ (C) and $La_{9.83}Si_{4.5}Fe_{1.5}O_{26}$ (D).

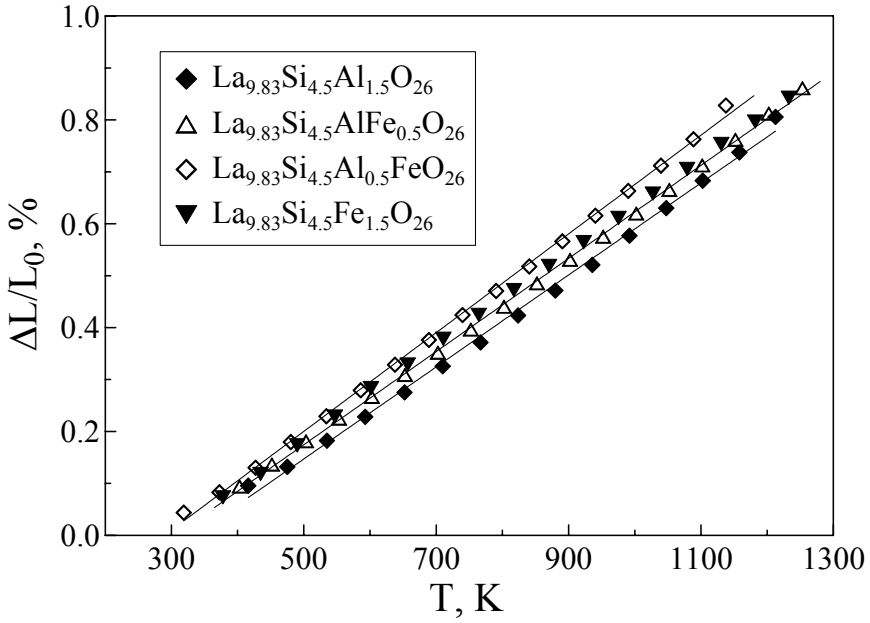

Fig. 7.24. Dilatometric curves of $La_{9.83}Si_{4.5}Al_{1.5-x}Fe_xO_{26\pm\delta}$ materials in air.

7.4.3. Ion transference numbers and partial conductivities

Fig. 7.25 presents the temperature dependencies of the total conductivity of $La_{9.83}Si_{4.5}Al_{1.5-x}Fe_xO_{26\pm\delta}$ apatite phases. The substitution of Al with Fe leads to increasing activation energy (Table 7.8). Therefore, Fe doping results in decreasing electrical transport in the low-temperature range, whilst at temperatures above 900 K this tendency is reversed. Compared to $La_{9.83}Si_{4.5}Al_{1.5-x}Fe_xO_{26\pm\delta}$, the conductivity of A-site stoichiometric $La_{10}Si_4Fe_2O_{26\pm\delta}$ (Fig. 7.25) is 6-10 times lower.

Table 7.8. Oxygen ion transference numbers (t_O) and activation energies (E_A) of the partial oxygen ionic (σ_O) and electronic (σ_e) conductivities of $La_{9.83}Si_{4.5}Al_{1.5-x}Fe_xO_{26\pm\delta}$ ceramics in air.

Composition	t_O				E_A	
	1223 K	1123 K	1073 K	973 K	σ_O	σ_e
$La_{9.83}Si_{4.5}Al_{1.5}O_{26}$	0.9949	0.9951	0.9951	0.9948	60 ± 2	57 ± 2
$La_{9.83}Si_{4.5}AlFe_{0.5}O_{26}$	0.9913	0.9906	0.9894	0.9864	77 ± 3	56 ± 3
$La_{9.83}Si_{4.5}Al_{0.5}FeO_{26}$	0.9906	0.9922	0.9924	0.9931	93 ± 4	104 ± 2
$La_{9.83}Si_{4.5}Fe_{1.5}O_{26}$	0.9888	0.9915	0.9927	0.9940	99 ± 4	123 ± 4

The activation energies for ionic and electronic conductivities correspond to the temperature ranges 873-1273 and 973-1223 K, respectively.

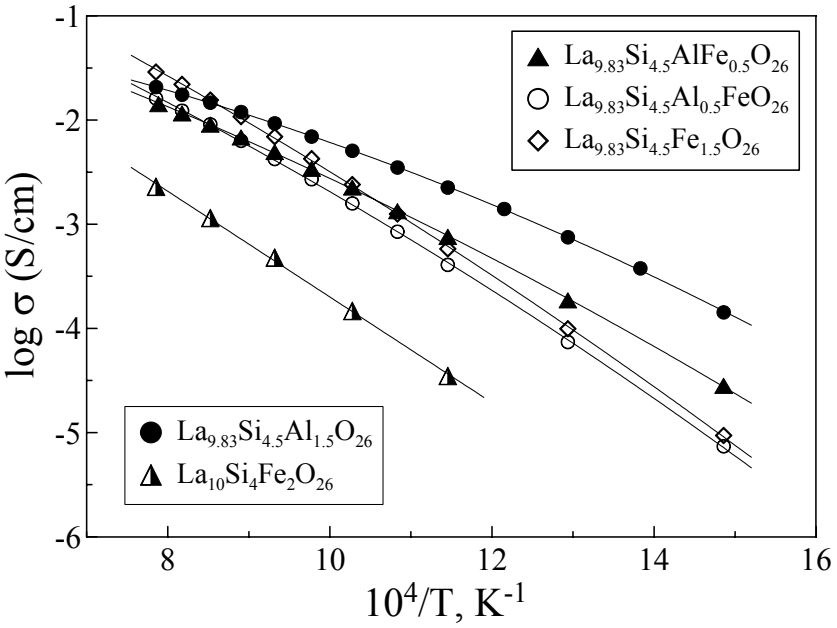

Fig. 7.25. Temperature dependencies of the total conductivity of $La_{9.83}Si_{4.5}Al_{1.5-x}Fe_xO_{26\pm\delta}$ materials in air. Data on $La_{10}Si_4Fe_2O_{26\pm\delta}$ are given for comparison.

The FE (Table 7.8) and EMF (Fig. 7.26) measurements clearly showed that $La_{9.83}Si_{4.5}Al_{1.5-x}Fe_xO_{26\pm\delta}$ apatites are oxygen ion-conducting solid electrolytes under oxidizing conditions. At 973-1223 K, the oxygen ion transference numbers determined by the FE method in air are close to 0.99 (Table 7.8). As for doped $LaGaO_3$ and CGO [111], the oxygen ion transference numbers of $La_{9.83}Si_{4.5}Al_{0.5}FeO_{26}$ and $La_{9.83}Si_{4.5}Fe_{1.5}O_{26}$ increase when temperature decreases, while the compositions with maximum Al concentration, $La_{9.83}Si_{4.5}AlFe_{0.5}O_{26}$ and $La_{9.83}Si_{4.5}Al_{1.5}O_{26}$, exhibit the opposite behavior. The latter trend is similar to $LaAlO_3$-based solid electrolytes [301].

The temperature dependencies of the partial electronic conductivity of $La_{9.83}Si_{4.5}Al_{1.5-x}Fe_xO_{26\pm\delta}$ apatites in air, calculated from total conductivity and FE data, are presented in Fig.7.27. As suggested by Mössbauer spectroscopy (Appendix 4, Table 5), the electronic conductivity under oxidizing conditions is predominantly p-type.

At temperatures above 1173 K, the electron-hole transport in $La_{9.83}Si_{4.5}Al_{1.5-x}Fe_xO_{26\pm\delta}$ increases with iron additions when the concentration of Fe^{4+} increases, in agreement with the Mössbauer spectroscopy results (Appendix 4, Table 5). Due to the stabilization of Fe^{3+} in the A-site stoichiometric lattice, the p-type conductivity of $La_{10}Si_4Fe_2O_{26}$ is lower compared to Fe-containing $La_{9.83}Si_{4.5}Al_{1.5-x}Fe_xO_{26\pm\delta}$, despite the higher iron content in the former. For $La_{10}Si_4Fe_2O_{26}$, the Mössbauer spectroscopy

indicates the absence or a very low concentration of Fe^{4+}, below the detection limit (Appendix 4, Table 4); the holes participating in the transport processes are formed, most likely, due to intrinsic electronic disorder or iron disproportionation at high temperatures.

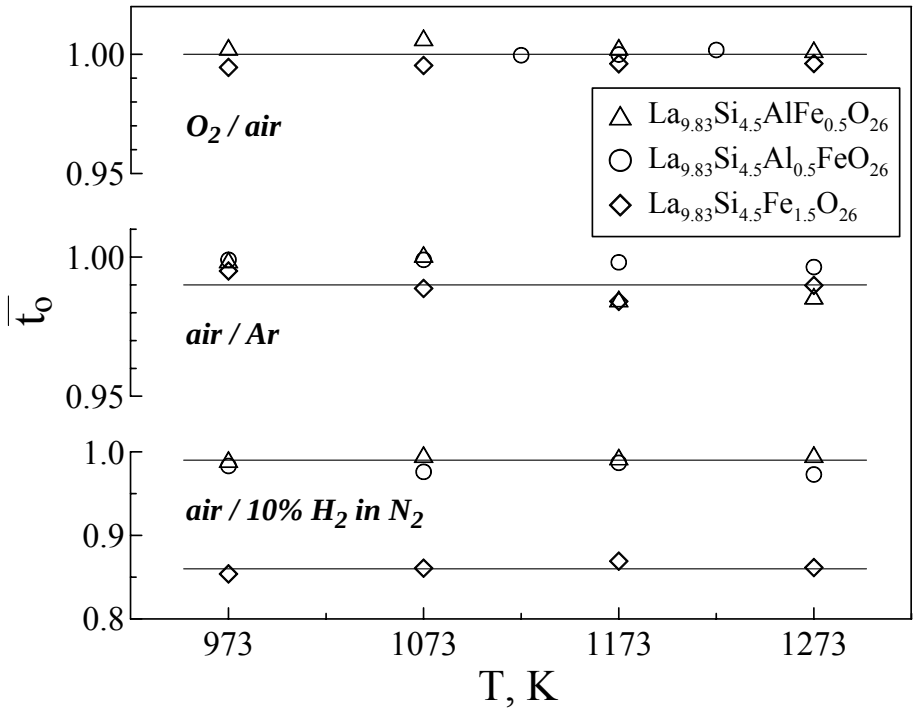

Fig. 7.26. Oxygen ionic transference numbers of $La_{9.83}Si_{4.5}Al_{1.5-x}Fe_xO_{26\pm\delta}$ in various oxygen pressure gradients.

The mechanism of Fe^{4+} charge compensation via incorporation of extra oxygen into vacant O5 sites, formed due to Frenkel-type disorder, suggests a correlation between partial ionic and p-type electronic conductivities in the apatite phases. Such correlation is indeed observed, as illustrated by the inset in Fig. 7.27. Therefore, the results on $La_{9.83}Si_{4.5}Al_{1.5-x}Fe_xO_{26\pm\delta}$ support the hypothesis [89,94,298] that the oxygen interstitial migration mechanism provides dominant or, at least, significant contribution to ionic transport in apatite silicates. Another necessary comment is that increasing iron content leads to an increasing activation energy for the electronic transport (Table 7.8), as for the $La_{10-x}Si_{6-y}Al_yO_{27-3x/2-y/2}$ system (Chapter 7.1.4). This may be associated with an increasing contribution of the formation enthalpy of ionic charge carriers, namely oxygen interstitials or vacancies in the O5 sites, to the total E_a values.

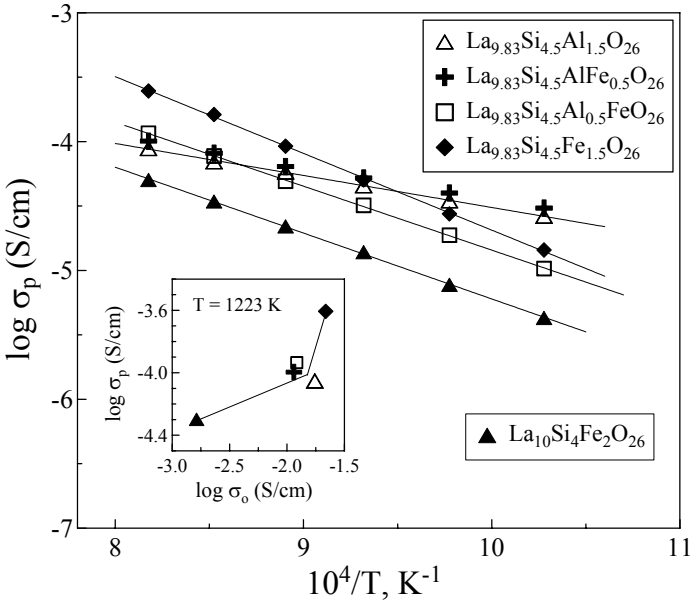

Fig. 7.27. Temperature dependencies of the p-type electronic conductivity of $La_{9.83}Si_{4.5}Al_{1.5-x}Fe_xO_{26\pm\delta}$ in air. The inset shows a correlation between partial oxygen ionic and p-type electronic conductivities. Data on $La_{10}Si_4Fe_2O_{26\pm\delta}$ are given for comparison.

7.4.4. Behavior at reduced oxygen pressures

Reducing oxygen pressures below 10^{-10}-10^{-5} Pa leads to decreasing conductivity of Fe-containing $La_{9.83}Si_{4.5}Al_{1.5-x}Fe_xO_{26}$, whereas the electrical transport of $La_{9.83}Si_{4.5}Al_{1.5}O_{26}$ is $p(O_2)$ independent. However, when the iron content increases, the tendency to the conductivity drop can be even reversed, as illustrated by Fig. 7.28, showing the temperature dependencies of the total conductivity in various gas mixtures. A similar trend, even more pronounced, was also revealed for Fe-rich $La_{10}Si_4Fe_2O_{26}$ (Fig. 7.21), indicative of significant contribution of the n-type electronic transport.

Analogously to $La_{10-x}Si_{6-y}Fe_yO_{26\pm\delta}$ ceramics (Chapter 7.3.4), no phase decomposition of $La_{9.83}Si_{4.5}Al_{1.5-x}Fe_xO_{26}$ in reducing environments was detected by XRD and Mössbauer spectroscopy (Appendix 4, Table 5), though low oxygen pressures reduce all iron to the trivalent state.

The $p(O_2)$ dependencies of the total conductivity and Seebeck coefficient (Fig. 7.29) suggest predominant oxygen ionic transport within the studied oxygen pressure range. Data on average ion transference numbers under large oxygen chemical potential gradients (Fig. 7.26) confirmed that Fe-doped $La_{9.83}Si_{4.5}Al_{1.5-x}Fe_xO_{26}$ remain solid electrolytes in these conditions. As expected, the electronic contribution is maximal for $La_{9.83}Si_{4.5}Fe_{1.5}O_{26}$ oxide.

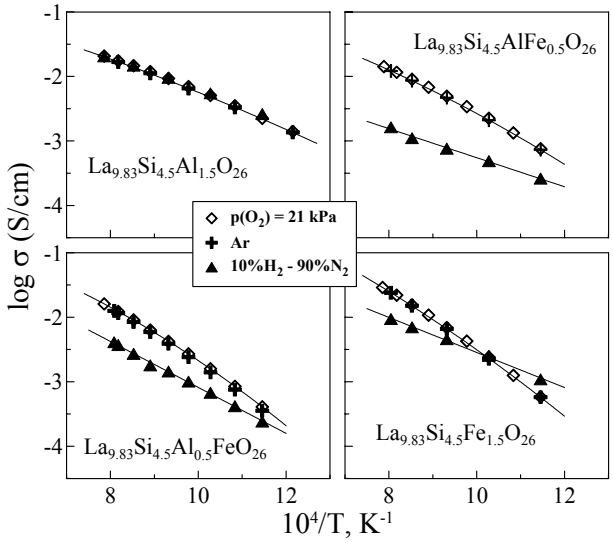

Fig. 7.28. Temperature dependencies of the total conductivity of $La_{9.83}Si_{4.5}Al_{1.5-x}Fe_xO_{26\pm\delta}$ apatites in various atmospheres.

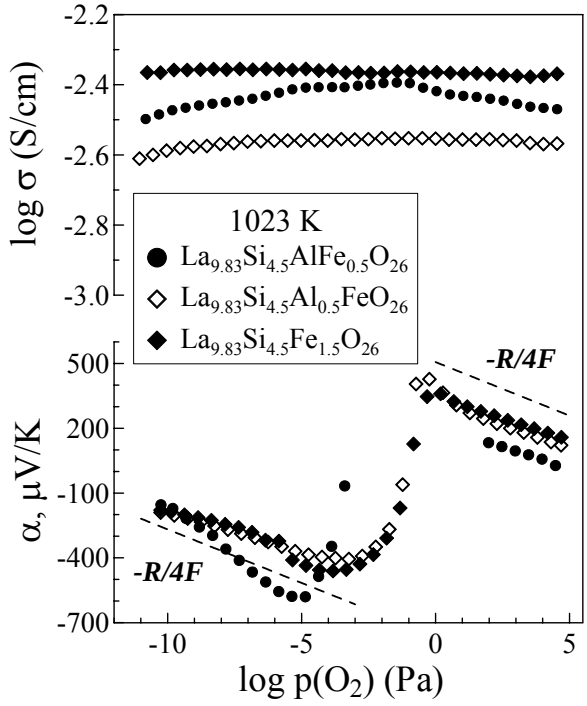

Fig. 7.29. Oxygen pressure dependencies of the total conductivity and Seebeck coefficient of $La_{9.83}Si_{4.5}Al_{1.5-x}Fe_xO_{26\pm\delta}$ apatite ceramics.

7.5. The system $La_{9.83-x}Pr_xSi_{4.5}Fe_{1.5}O_{26\pm\delta}$ ($0 \le x \le 6$)

7.5.1. Crystal structure

The XRD analysis showed that all $La_{9.83-x}Pr_xSi_{4.5}Fe_{1.5}O_{26\pm\delta}$ ($0 \le x \le 6$) are single-phase; the space groups and lattice parameters determined by the Rietveld refinement are summarized in Table 7.9. Doping with praseodymium leads to decreasing unit cell volume due to a smaller radius of Pr^{3+} and Pr^{4+} cations when compared to La^{3+} [8]. The transition of $(La,Pr)_{9.83}Si_{4.5}Fe_{1.5}O_{26}$ lattice space group from $P6_3$ to $P\bar{3}$ occurs with increasing praseodymium concentration and is also associated, most likely, with decreasing average size of the A-site cations.

Table 7.9. Properties of $La_{9.83-x}Pr_xSi_{4.5}Fe_{1.5}O_{26\pm\delta}$ ceramics.

Composition	S.G.	a, Å	c, Å	ρ_{exp} / ρ_{theor}, %	T, K	$\alpha \times 10^6$, K^{-1}
$La_{9.83}Si_{4.5}Fe_{1.5}O_{26}$	$P6_3$	9.772(6)	7.262(0)	97.5	373-1273	9.04 ± 0.01
$La_{6.83}Pr_3Si_{4.5}Fe_{1.5}O_{26}$	$P6_3$	9.739(8)	7.214(9)	99.3	373-1173	9.34 ± 0.03
$La_{3.83}Pr_6Si_{4.5}Fe_{1.5}O_{26}$	$P\bar{3}$	9.708(1)	7.175(7)	99.1	373-1173	9.20 ± 0.01

While the Mössbauer spectrum of reduced $La_{9.83}Si_{4.5}Fe_{1.5}O_{26}$ (Appendix 5, Fig. 4) suggests tetrahedrally-coordinated Fe^{3+} only (Appendix 5, Table 6), the spectrum of $La_{9.83}Si_{4.5}Fe_{1.5}O_{26}$ annealed in air indicates the presence of tetravalent iron as well. According to the lattice electroneutrality condition, the presence of Fe^{4+} in oxidized $La_{9.83}Si_{4.5}Fe_{1.5}O_{26+\delta}$ requires incorporation of extra oxygen for charge compensation; the estimated oxygen hyperstoichiometry (δ) is about 0.2. Since the IS values of trivalent iron are characteristic of tetrahedral coordination [265], Mössbauer data suggests that the extra oxygen anions are not incorporated in the nearest neighborhood of Fe^{3+}. Such behavior seems in agreement with neutron diffraction data [89], showing the presence of an interstitial position (O6) in the channel surrounded by Ln3 sites. As expected, the extra oxygen leaves the lattice on reduction, and all iron cations in the reduced apatite exist as Fe^{3+} (Appendix 5, Table 6).

On the contrary to the oxidized $La_{9.83}Si_{4.5}Fe_{1.5}O_{26+\delta}$, the Mössbauer spectra of Pr-containing apatites annealed in air (Appendix 5, Fig. 4) indicate that all iron is tetrahedrally-coordinated Fe^{3+}. The formation of Fe^{4+} ions, which appears mostly in perovskite-related structures, was only found for $La_{9.83}Si_{4.5}Al_{1.5-x}Fe_xO_{26\pm\delta}$ – lanthanum-deficient apatites doped with iron (Appendix 4). Most probably, the latter phenomenon is associated with Frenkel-type disorder in O5 sites, induced by A-site vacancies; namely, the resultant local distortions of the lattice may cause incorporation of extra oxygen into O5 vacancies formed due to displacement of part of the O5 anions to nearby O6 sites, thus

favoring Fe^{4+} formation [89]. The praseodymia additions to $La_{9.83-x}Pr_xSi_{4.5}Fe_{1.5}O_{26}$ have an opposite effect, decreasing Fe^{4+} concentration down to an undetectable level. On the other hand, the values of oxygen ionic conductivity discussed below are similar for all $(La,Pr)_{9.83}Si_{4.5}Fe_{1.5}O_{26}$ compositions. In combination with literature data [94,298], showing a critical interstitial contribution to the ionic transport, these trends suggest that doping with praseodymium reduces the average oxidation state of iron cations ($Pr^{3+} + Fe^{4+} \rightarrow Pr^{4+} + Fe^{3+}$), whilst the interstitial oxygen anions are still present. The mixed valence of praseodymium cations, $Pr^{3+/4+}$, is also in agreement with enhanced p-type electronic conductivity observed in Pr-doped apatites.

7.5.2. Ceramics characterization

SEM/EDS studies confirmed that $La_{9.83-x}Pr_xSi_{4.5}Fe_{1.5}O_{26\pm\delta}$ materials had low porosity and a minor difference in the cation composition of the ceramic grain bulk and boundary region, suggesting that segregation of dopant cations along the boundaries can be neglected. Also, apparently no traces of liquid phase formation were found at the grain boundaries. These observations are in agreement with impedance spectroscopy data, which indicated no significant grain-boundary contribution to the total resistivity at temperatures above 873-923 K. Typical SEM micrographs of $La_{6.83}Pr_3Si_{4.5}Fe_{1.5}O_{26}$ and $La_{3.83}Pr_6Si_{4.5}Fe_{1.5}O_{26}$ oxides are presented in Fig. 7.30. Their average grain size is similar to that of $La_{9.83}Si_{4.5}Fe_{1.5}O_{26}$ (Fig. 7.23D), as expected for oxides sintered at the same temperature (1873 K), and varies within a narrow range, 1-4 μm. Dilatometric curves of the studied materials are approximately linear at temperatures from 373-1173 K (Fig. 7.31); TECs are very close and vary from 9.04×10^{-6} to 9.34×10^{-6} K^{-1} (Table 7.9).

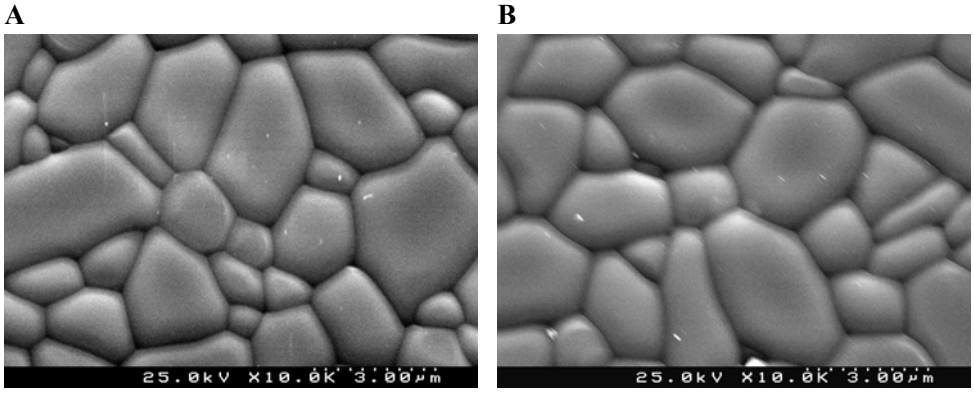

Fig. 7.30. SEM micrographs of $La_{6.83}Pr_3Si_{4.5}Fe_{1.5}O_{26}$ (A) and $La_{3.83}Pr_6Si_{4.5}Fe_{1.5}O_{26}$ (B).

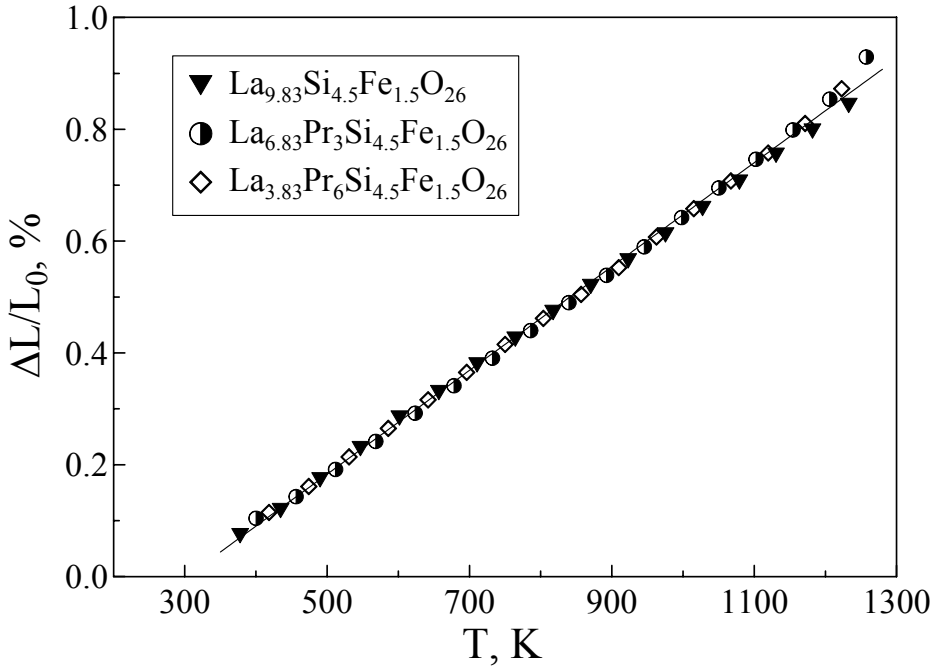

Fig. 7.31. Dilatometric curves of $La_{9.83-x}Pr_xSi_{4.5}Fe_{1.5}O_{26}$ apatites in air.

7.5.3. Ionic and electronic conduction under oxidizing conditions

Fig. 7.32 presents the temperature dependencies of the total conductivity of $La_{9.83-x}Pr_xSi_{4.5}Fe_{1.5}O_{26}$ apatites, which is predominantly oxygen ionic in air, as shown by FE (Table 7.10) and EMF (Fig. 7.33A) measurements. For $La_{3.83}Pr_6Si_{4.5}Fe_{1.5}O_{26}$, the electronic contribution to the total conductivity is 1-2% at 973-1223 K. The ion transference numbers of $La_{3.83}Pr_6Si_{4.5}Fe_{1.5}O_{26+\delta}$ increase with increasing temperature. In the intermediate temperature range (<1000 K), the conductivity of Pr-substituted apatites is slightly lower with respect to the parent compound, $La_{9.83}Si_{4.5}Fe_{1.5}O_{26+\delta}$. At higher temperatures, the values of σ become similar for all $La_{9.83-x}Pr_xSi_{4.5}Fe_{1.5}O_{26}$ compositions.

Although doping with praseodymium slightly increases the activation energy for the ionic transport (Table 7.10), the concentration of ionic charge carriers seems essentially unaffected. In other words, increasing x in $La_{9.83-x}Pr_xSi_{4.5}Fe_{1.5}O_{26}$ results in decreasing Fe^{4+} content, but the Pr-containing apatites are still oxygen-hyperstoichiometric due to the presence of Pr^{4+}. The increase in the activation energy for ionic transport may be partly related to the incorporation of Pr^{4+}, statistically distributed in the lattice, into the Ln3 sites. This should lead to increasing coulombic interaction between the mobile

O5/O6 anions and their nearest neighborhood, thus increasing ion migration energy. Also, praseodymia additions induce a lattice contraction (Table 7.9) and decreasing size of ion migration channels.

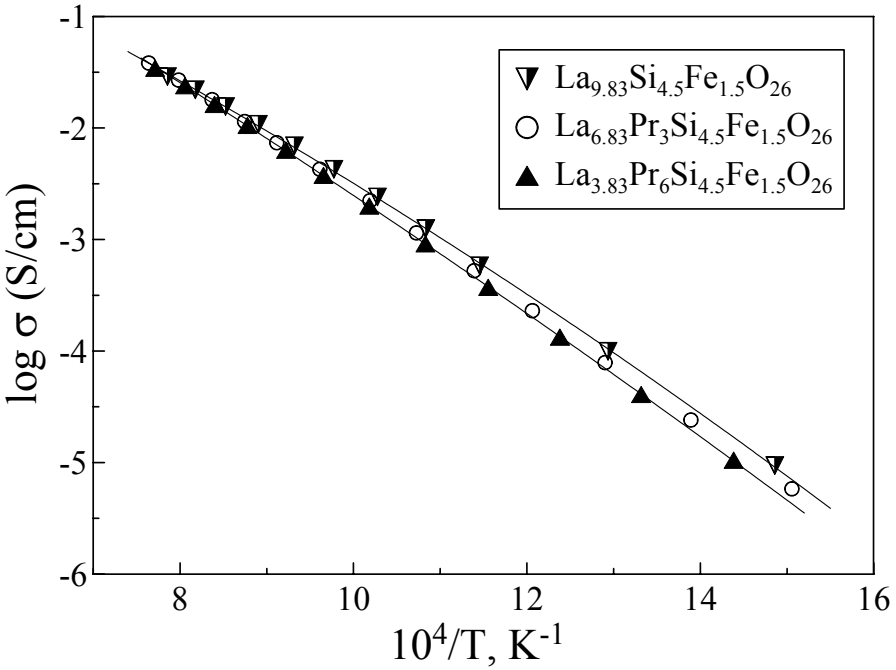

Fig. 7.32. Temperature dependencies of the total conductivity of $La_{9.83-x}Pr_xSi_{4.5}Fe_{1.5}O_{26}$ ceramics in air.

Table 7.10. Oxygen ion transference numbers (t_O) and activation energies (E_A) of the partial oxygen ionic (σ_O) and electronic (σ_e) conductivities of $La_{9.83-x}Pr_xSi_{4.5}Fe_{1.5}O_{26}$ ceramics in air.

Composition	t_O				E_A	
	1223 K	1123 K	1073 K	973 K	σ_O	σ_e
$La_{9.83}Si_{4.5}Fe_{1.5}O_{26}$	0.9888	0.9915	0.9927	0.9940	99 ± 4	123 ± 4
$La_{6.83}Pr_3Si_{4.5}Fe_{1.5}O_{26}$	-	-	-	-	107 ± 1	-
$La_{3.83}Pr_6Si_{4.5}Fe_{1.5}O_{26}$	0.9868	0.9854	0.9840	0.9793	109 ± 1	88 ± 2

The activation energies for ionic and electronic conductivities correspond to the temperature ranges 873-1273 and 973-1223 K, respectively.

The oxygen ionic transference numbers of $La_{3.83}Pr_6Si_{4.5}Fe_{1.5}O_{26}$ increase with decreasing oxygen pressure, following Eqs. (7.3) and (7.6). This indicates that the electronic transport is

predominantly p-type. Fig. 3.33B gives the temperature dependencies of the partial p-type electronic conductivity, calculated from the total conductivity and FE data in air.

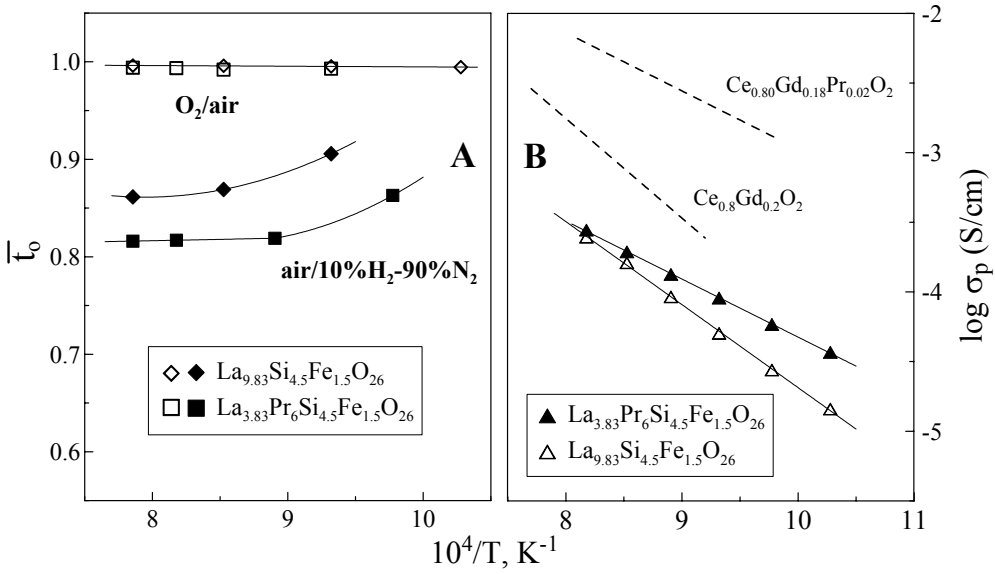

Fig. 7.33. Temperature dependencies of the oxygen ionic transference number in various $p(O_2)$ gradients (A) and partial p-type electronic conductivity (B) of $La_{9.83-x}Pr_xSi_{4.5}Fe_{1.5}O_{26}$ ceramics in air.

As for CGO [305], doping of apatite-type $La_{9.83}Si_{4.5}Fe_{1.5}O_{26+\delta}$ with praseodymium substantially increases the electron-hole conduction, whereas the activation energy for p-type conductivity decreases from 123 down to 88 kJ/mol (Table 7.10). The most likely reason is an increasing concentration of sites participating in the electron-hole transport. While $Fe^{3+/4+}$ cations in the lattice of $La_{9.83}Si_{4.5}Fe_{1.5}O_{26+\delta}$ are isolated, the hole jump distance becomes substantially shorter when more than 50% A sites are occupied with $Pr^{3+/4+}$ cations, thus decreasing the energetic barrier for hole migration. Nevertheless, the p-type conductivity of $La_{3.83}Pr_6Si_{4.5}Fe_{1.5}O_{26+\delta}$ remains much lower than that of $Ce_{0.80}Gd_{0.18}Pr_{0.02}O_{2-\delta}$, where the electron-hole conduction is due to the presence of praseodymium oxide segregated at the grain boundaries [305].

7.5.4. Transport properties in reducing atmospheres

The dominant oxygen ionic conductivity of $(La,Pr)_{9.83}Si_{4.5}Fe_{1.5}O_{26}$ in oxidizing atmospheres is confirmed by the oxygen partial pressure dependencies of total conductivity and Seebeck coefficient,

as illustrated by Fig. 7.34. When the oxygen pressure is higher than 1-10 Pa, the total conductivity is essentially $p(O_2)$ independent. In these conditions the Seebeck coefficient of apatite phases is positive; the slope of α *vs. ln* $p(O_2)$ curves is close to the theoretical value for a pure oxygen ionic conductor, -R/4F [300].

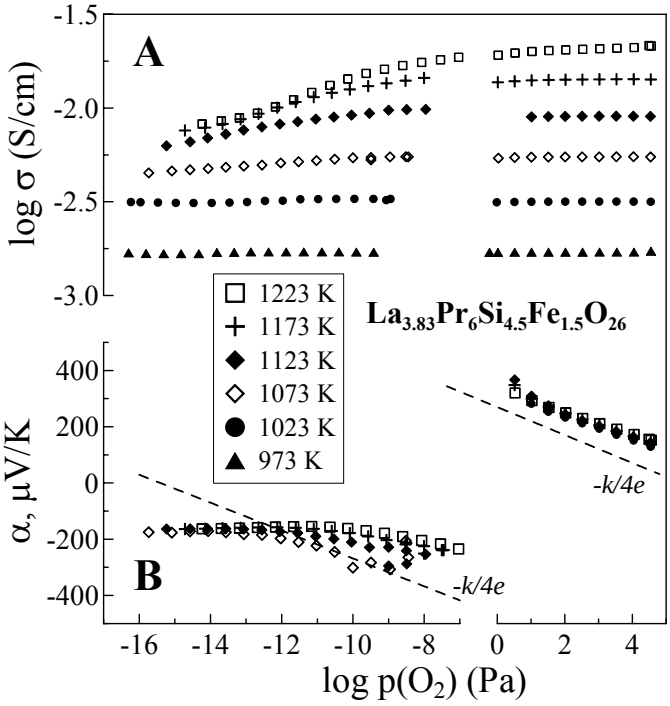

Fig. 7.34. Oxygen pressure dependencies of the total conductivity (A) and Seebeck coefficient (B) of $La_{3.83}Pr_6Si_{4.5}Fe_{1.5}O_{26}$.

Reducing $p(O_2)$ below 10^{-10}-10^{-5} Pa leads to a gradual decrease of the total conductivity of $La_{3.83}Pr_6Si_{4.5}Fe_{1.5}O_{26}$. No phase decomposition in reducing environments was detected by XRD and Mössbauer spectroscopy. Therefore, the conductivity behavior at low $p(O_2)$ indicates a decrease in ionic transport, caused by reducing concentration of oxygen interstitials and, possibly, significant contribution of a vacancy mechanism for oxygen ion diffusion [94,298].

The Seebeck coefficient of $La_{9.83-x}Pr_xSi_{4.5}Fe_{1.5}O_{26}$ in reducing atmospheres becomes negative (Fig. 7.34B), but different from the theoretical trend for a pure ionic conductor, for which a linear α *vs. ln* $p(O_2)$ dependence with slope (-R/4F) could be expected [300]. Data on average ion transference numbers under large oxygen chemical potential gradients (Fig. 7.33A) confirm a significant increase of

the electronic conductivity in these conditions. Contrary to the oxidizing atmospheres, the electronic contribution to total conductivity under air/H_2 gradient increases up to 15% for $La_{9.83}Si_{4.5}Fe_{1.5}O_{26}$ and about 20% for $La_{3.83}Pr_6Si_{4.5}Fe_{1.5}O_{26}$, suggesting that the decrease in ionic conduction is accompanied with increasing n-type electronic transport. This tendency becomes more pronounced at temperatures below 900-1000 K when $La_{9.83}Si_{4.5}Fe_{1.5}O_{26}$ and $La_{3.83}Pr_6Si_{4.5}Fe_{1.5}O_{26}$ exhibit an increase in the total conductivity at low oxygen chemical potentials (Fig. 7.35), indicative of non-negligible n-type electronic contribution.

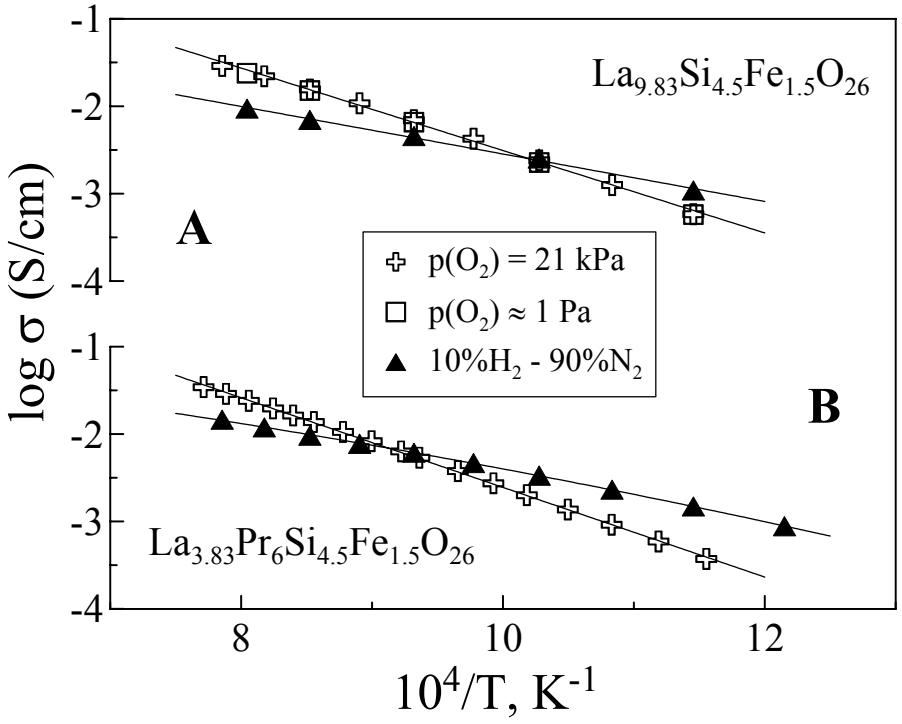

Fig. 7.35. Temperature dependencies of the total conductivity of $La_{9.83}Si_{4.5}Fe_{1.5}O_{26}$ (A) and $La_{3.83}Pr_6Si_{4.5}Fe_{1.5}O_{26}$ (B) in various atmospheres.

Summary

This thesis is focused on the analysis of transport properties, defect chemistry, thermal expansion and stability of a wide range of oxygen ion-conducting ceramic materials, namely perovskite-type (Parts 3 and 4) and garnet-type (Part 5), composite (Part 6) mixed conductors, and also apatite-type solid electrolytes (Part 7). Particular emphasis is given to the identification of promising compositions for SOFCs and natural gas conversion membranes, including assessment of oxygen ion transport mechanisms, and studies of relationships between microstructure and partial ionic and electronic conductivities. Finally, tubular membranes for the partial oxidation of methane were successfully fabricated from one developed material, $SrFe_{0.7}Al_{0.3}O_{3-\delta}$ with alumina additions (Part 3).

In Part 3, the phase relationships and oxygen permeability in the $SrFe_{1-x}Al_xO_{3-\delta}$ system are analyzed. The maximum solubility of Al^{3+} cations corresponds to $x \approx 0.35$. The substitution of iron with aluminum increases the perovskite unit cell volume and stability, and decreases the thermal expansion and electronic conductivity. The temperature-activated character and the level of hole mobility, 0.009-0.016 $cm^2V^{-1}s^{-1}$ at 1073-1223 K, suggest a small-polaron mechanism. Reducing oxygen partial pressure results in increasing ionic conduction and ion transference numbers, followed by a progressive increase of the n-type electronic contribution to the total conductivity. Single-phase $SrFe_{1-x}Al_xO_{3-\delta}$ ($x = 0.1$-0.3) shows high levels of oxygen permeability, limited by both bulk ambipolar conductivity and surface exchange. Further doping leads to 2-3 times lower oxygen permeation, whereas minor additions of Al_2O_3 increase ionic transport.

Part 4 presents data on phase relationships and oxygen ionic conduction in perovskite-type $La_{1-x}Sr_xFe_{1-y}Ga_yO_{3-\delta}$. The maximum oxygen permeability, increasing with gallium additions, was found for the $La_{0.3}Sr_{0.7}Fe_{1-y}Ga_yO_{3-\delta}$ series where the solubility range of Ga^{3+} corresponds to $y = 0$-0.30. The thermal expansion decreases on Ga doping and increases with Sr content. Oxygen transport through $La_{0.3}Sr_{0.7}FeO_{3-\delta}$ is limited by both surface exchange and bulk ambipolar conduction, whereas $La_{0.3}Sr_{0.7}Fe_{1-x}Ga_xO_{3-\delta}$ ($x = 0.2$-0.4) membranes showed a negligible effect of interfacial kinetics, suggesting that the B-site substitution enhances the exchange rate. If compared to $SrFe_{1-x}Al_xO_{3-\delta}$ ($x = 0.1$-0.3), Ga-doped $La_{0.3}Sr_{0.7}FeO_{3-\delta}$ membranes exhibit a slightly higher permeation, but their practical use for oxygen separation and oxidation of hydrocarbons is hampered, particularly due to high cost.

In Part 5, the crystal structure and transport properties of extensively doped garnet-type $Gd_3Fe_5O_{12}$ and $Y_3Fe_5O_{12}$ oxides are discussed. Contrary to Fe-containing perovskites, the thermal expansion of garnets at 373-1273 K is linear and relatively low, with average TECs of $(9.4\text{-}10.9)\times10^{-6}$ K^{-1}. The total conductivity, predominantly p-type electronic in air, increases when acceptor-type

cations are incorporated in the lattice. This type of doping leads also to increasing oxygen permeability and ionic conductivity. Nevertheless, due to nonlinear diffusion pathway and hampered oxygen transfer at the edges of Fe-O tetrahedra, the oxygen ionic conductivity is low and characterized by high activation energy values, 176-224 kJ/mol.

Part 6 is centered on the processing and characterization of microheterogeneous $(La_{0.9}Sr_{0.1})_{0.98}Ga_{0.8}Mg_{0.2}O_{3-\delta}$-$La_{0.8}Sr_{0.2}Fe_{0.8}Co_{0.2}O_{3-\delta}$ (LSGM-LSFC) ceramics selected as a model composite system, in comparison with single-phase $La(Sr)Ga(Fe,Mg,Co)O_{3-\delta}$ perovskites. Sintering in conditions necessary to obtain gas-tight LSGM-LSFC membranes results in almost complete reaction between the parent compounds owing to similarity of crystal structures and fast cation interdiffusion. The level of inhomogeneity increases with decreasing sintering temperature and/or preliminary coarsening of LSGM powder. The hole conductivity values vary between those of LSFC and LSGM and decrease moderately on increasing the interaction level. The maximum oxygen permeation fluxes were found for the membranes with minimum interaction degree. Similar trends were also observed for $Ce_{0.8}Gd_{0.2}O_{2-\delta}$ (CGO) - LSFC, CGO - $La_{0.7}Sr_{0.3}MnO_{3-\delta}$, LSGM - $La_2Ni_{0.8}Cu_{0.2}O_{4+\delta}$ and $SrCoO_{3-\delta}$ - $Sr_2Fe_3O_{6.5\pm\delta}$, emphasizing a critical influence of phase interaction on the ionic transport in oxide composite materials.

Part 7 summarizes data on apatite-type silicates, including $La_{10-x}Si_{1-y}Al_yO_{26\pm\delta}$, $La_{10-x}Si_{6-y}Fe_yO_{26\pm\delta}$, $La_{9.83}Si_{4.5}Al_{1.5-x}Fe_xO_{26\pm\delta}$ and $La_{9.83-x}Pr_xSi_{4.5}Fe_{1.5}O_{26\pm\delta}$. The conductivity of these materials is predominantly oxygen ionic, with the electronic contribution lower than 5% for Fe- and Pr-containing phases, and lower than 0.5% for Al-substituted silicates. The latter group exhibits low activation energy for ionic transport, and high ionic conductivity at 873-1073 K, comparable to that of ceria- and LSGM-based solid electrolytes. For Fe-containing apatites, tetravalent iron was found only for A-site deficient oxides under oxidizing conditions, while the presence of Pr stabilizes Fe^{3+}. The ionic transport increases with oxygen concentration in the lattice, indicating that interstitial diffusion is much faster than the vacancy migration. No phase decomposition in reducing atmospheres was detected by XRD and Mössbauer spectroscopy. However, the long-term stability tests in reducing conditions demonstrated a slow irreversible degradation at temperatures above 1100 K, associated with minor volatilization of SiO from the surface layers of apatite ceramics.

Conclusions and research perspectives

Data on ferrite-based membrane materials, presented in this thesis, show a maximum performance for $La_{0.3}Sr_{0.7}Fe(Ga)O_{3-\delta}$ perovskites and $SrFe(Al)O_3$-based composite ceramics. Practical use of the former group is, however, less likely due to relatively high cost of Ga-containing compounds and volatilization of gallium oxides under operation conditions. Although the oxygen permeability of $SrFe(Al)O_3$-based materials is slightly lower, these exhibit two clear advantages, namely the cost and stability of all components. Further developments in this field should therefore be focused on the Sr-Fe-Al-O system, with primary emphasis on dual-phase composite ceramics. The key issues include microstructural optimization, decreasing membrane thickness, and development of methods for surface modification of the composite ceramics in order to enhance the surface exchange kinetics which will become the performance-limiting factor for thin membranes.

The results of this thesis suggest also that the critical aspect, determining ion transport properties and long-term stability of oxide composite materials, is the interaction of constituent phases. The development of composite materials should, hence, be centered on systems where no phase interaction is thermodynamically possible including solid solutions of the components. In particular, subsequent optimization of $SrFe(Al)O_3$-based composite ceramics should be centred on compositions close to the solid solution formation limits, such as A-site deficient $Sr_{1-x}Fe_{0.7}Al_{0.3}O_{3-\delta}$ and $SrAl_2O_4$.

The kinetic demixing in $SrFe(Al)O_{3-\delta}$ ceramics, caused by non-negligible mobility of the constituent cations at operation temperatures, influences the long-term membrane stability. The information on kinetic demixing mechanisms, available in the literature, is still scarce, although this may lead to degradation of the membrane performance, due to ceramics desintegration and interaction of migrating cations with gas species. The basic approaches of further optimization of composition and processing conditions of $SrFe(Al)O_3$-based membranes, aimed to suppress these microstructural changes, include: (i) incorporation of small amounts of secondary phases preventing grain-boundary diffusion; (ii) use of sintering aids to provide nearly zero porosity to avoid surface diffusion in the pores; (iii) doping with low-mobility cations to hamper cation migration in the lattice; and (iv) creation of a compositional gradient compensating the driving force for cation transport under $p(O_2)$ gradients.

In the case of dual-phase oxide composites comprising a phase with predominant oxygen ionic transport and an electronically-conducting component, the solid-electrolyte volume fraction should be increased to a maximum, limited by the percolation boundary of the second phase. Special care should be given, however, to suppressing grain growth of the electronic conductor and homogeneous distribution. One composite system which may deserve further attention is $Ce(Gd)O_2$-based ceramics

with minimum content of a mixed-conducting perovskite phase distributed mainly along grain boundaries.

Also, the thesis demonstrated that silicate-based apatites are promising solid electrolytes for intermediate-temperature SOFCs. At the same time, although no essential volatilization of silicon oxide in reducing atmospheres was found at temperatures below 1073-1123 K, this process may still lead to slow degradation hardly noticed for short periods of time. Possible approaches to suppress such degradation may include: (i) extensive substitution of silicon by cations which form no volatile phases, (ii) protection of the silicate surface exposed to reducing atmosphere with a thin layer of other ion-conducting materials, and (iii) design of composition-gradient structures. For the protective layers, of special interest might be ceria-based electrolytes known for their catalytic activity towards total oxidation. The n-type electronic conductivity of ceria-based materials, significant under reducing conditions, cannot decrease the SOFC performance as electronic transport in the apatite-type electrolytes is quite low.

References

1. Jost W., Diffusion in solids, liquids and gases, Academic Press, New York, 1952.
2. Kofstad P., Nonstoichiometry, diffusion and electrical conductivity in binary metal oxides. Wiley-Interscience, New York, 1972.
3. C. Wagner, Beitrag zur Theorie des Anlaufvorgangs. Z. Phys. Chem., **21** (1933) 25-41.
4. F.A. Kröger, H.J. Vink, Relations between the concentrations of imperfections in crystalline solids. Solid State Physics, **3** (1956) 307-435.
5. Bouwmeester, H. J. M. and Burggraaf, A. J., Dense ceramic membranes for oxygen separation. In *Fundamentals of Inorganic Membrane Science and Technology*, eds. A. J. Burggraaf and L. Cot. Elsevier, Amsterdam, 1996, pp. 435-528.
6. H. J. M. Bouwmeester, H. Kruidhof and A. J. Burggraaf, Importance of the surface exchange kinetics as rate limiting step in oxygen permeation through mixed-conducting oxides. Solid State Ionics, **72** (1994) 185-194.
7. H.-H. Moebius, Oxygen current density coefficient of oxide materials as a parameter for selection in development of electrodes with solid electrolytes. Extended Abstract 37th Meeting of the Int. Society of Electrochemistry, **1** (1986) 136-139.
8. R. D. Shannon, Revised effective ionic radii and systematic studies of interatomic distances in halides and chalcogenides. Acta Crystallogr., **A32** (1976) 751-767.
9. V.M. Goldschmidt, Skrifter Norske Viedenskaps - Akad. Oslo. I. Mathemat. Naturwiss. Klasse No 8, 1926.
10. S. Hashimoto and H. Iwahara, Structural, thermal and electrical properties of Ce-doped $SrMnO_3$. J. Electroceram., **4** (2000) 225-231.
11. K.W. Kirby, B.A. Wechsler, Phase relations in the barium titanate – titanium oxide system. J. Am. Ceram. Soc., **74** (1991) 1841-1847.
12. N. Ramadas, ABO_3-type oxides – their structure and properties – a bird's eye view. Mater. Sci. and Eng., **36** (1978) 231-239.
13. D. Lybye, F.W. Poulsen, M. Mogensen, Conductivity of A- and B-site doped $LaAlO_3$, $LaGaO_3$, $LaScO_3$ and $LaInO_3$ perovskites. Solid State Ionics, **128** (2000) 91-103.
14. M. A. Pena and J.L.G. Fierro, Chemical structures and performance of perovskite oxides. Chem. Rev., **101** (2001) 1981-2017.
15. A.M. Yankin and V.F. Balakirev, Phase relations in the reduction of solid solutions in the Co-Mn-Ti-O system. Inorg. Mater., **37** (2001) 58-64.

16. T. Ishigaki, S. Yamauchi, K. Kishio, J. Mizusaki and K. Fueki, Diffusion of oxide ion vacancies in perovskite-type oxides. J. Solid State Chem., **73** (1988) 179-187.
17. M. Cherry, M.S. Islam and C.R.A. Catlow, Oxygen ion migration in perovskite-type oxides. J. Solid State Chem., **118** (1995) 125-132.
18. M.S. Islam, Computer modelling of defects and transport in perovskite oxides. Solid State Ionics, **154-155** (2002) 75-85.
19. T.L. Nguen, M. Dokiya, S. Wang, H. Tagawa, T. Hashimoto, The effect of oxygen vacancy on the oxide ion mobility in $LaAlO_3$-based oxides. Solid State Ionics, **130** (2000) 229-241.
20. M. Feng, J.B. Goodenough, A superior oxide-ion electrolyte. Eur. J. Solid State Inorg. Chem., **31** (1994) 663-672.
21. T. Ishihara, H. Matsuda and Y. Takita, Doped $LaGaO_3$ perovskite type oxide as a new oxide ionic conductor. J. Am. Chem. Soc., **116** (1994) 3801-3803.
22. T. Ishihara, H. Matsuda, Y. Takita, Effects of rare earth cations doped for La site on the oxide ionic conductivity of $LaGaO_3$-based perovskite type oxide. Solid State Ionics, **79** (1995) 147-151.
23. J.A.M. van Roosmalen, J.P.P. Hujismans and L. Plomp, Electrical conductivity in $La_{1-x}Sr_xMnO_{3+\delta}$. Solid State Ionics, **66** (1993) 279-284.
24. H.-I. Yoo and C.-S. Kim, Electrical properties and defect structure of $Y_{1-x}Ca_xFeO_3$ orthoferrites. Solid State Ionics, **53-56** (1992) 583-591.
25. A.N. Petrov, O.F. Kononchuk, A.V. Andreev, V.A. Cherepanov, P. Kofstad, Crystal properties, electrical and magnetic properties of $La_{1-x}Sr_xCoO_{3-y}$. Solid State Ionics, **80** (1995) 189-199.
26. Y. Teraoka, H.M. Zhang, K. Okamoto and N. Yamazoe, Mixed ionic-electronic conductivity of $La_{1-x}Sr_xCo_{1-y}Fe_yO_{3-\delta}$ perovskite-like oxides. Mater. Res. Bull., **23** (1988) 51-58.
27. Y. Teraoka, H.M. Zhang, S. Furukawa and N. Yamazoe, Oxygen permeation through perovskite-type oxides. Chem. Lett., (1985) 1743-1746.
28. Y. Teraoka, T. Nobunaga and N. Yamazoe, Effect of cation substitution on the oxygen semipermeability of perovskite-type oxides. Chem. Lett., (1988) 503-506.
29. Y. Teraoka, T. Nobunaga, K. Okamoto, N. Miura, N. Yamazoe, Influence of constituent metal cations in substituted $LaCoO_3$ on mixed conductivity and oxygen permeability. Solid State Ionics, **48** (1991) 207-212.
30. T. Nakamura, G. Petzow and L.J. Gauckler, Stability of the perovskite phase $LaBO_3$ (B = V, Cr, Mn, Fe, Co, Ni) in reducing atmosphere. I. Experimental results. Mater. Res. Bull., **14** (1979) 649-659.

31. J.W. Stevenson, T.R. Armstrong, R.D. Carneim, L.R. Pederson and W.J. Weber, Electrochemical properties of mixed conducting perovskites $La_{1-x}M_xCo_{1-y}Fe_yO_{3-\delta}$ (M = Sr, Ba, Ca). J. Electrochem. Soc., **143** (1996) 2722-2729.
32. S. Steinsvik, T. Norby and P. Kofstad, Electrical conductivity and defect structure in the system $SrTi_{1-x}Fe_xO_{3-y}$ (x = 0.1-0.8). In *Electroceramics IV*, eds. R. Waser, S. Hoffmann, D. Bonnenberg, Ch. Hoffmann. Verlag der Augustinus Buchhandlung, Aachen, Germany, **PV II** (1994) 691-696.
33. S. Xie, W. Liu, K. Wu, P.H. Yang, G.Y. Meng, C.S. Chen, Mixed oxygen ionic and electronic conduction in $CaFe_{0.2}Ti_{0.8}O_{3-\delta}$: a combined oxygen permeation and electrical conductivity study. Solid State Ionics, **118** (1999) 23-28.
34. S. Hashimoto, H. Kishimoto, H. Iwahara, Conduction properties of $CaTi_{1-x}M_xO_{3-\alpha}$ (M = Ga, Sc) at elevated temperatures. Solid State Ionics, **139** (2001) 179-187.
35. D.-K. Lee and H.-I. Yoo, Electrochemical determination of the oxygen permeability of $La_{1-x}Ca_xCrO_{3-\delta}$ (x = 0.27). J. Electrochem. Soc., **147** (2000) 2835-2843.
36. L. Siwen, C. You, F. Lianqing, Y. Weishen, L. Liwu, M. Jian and R. Yufang, Oxygen permeating properties of the mixed conducting membranes without cobalt. Mater. Res. Bull., **33** (1998) 183-188.
37. Z. Shao, G. Xiong, Y. Cong, W. Yang, Synthesis and oxygen permeation study of novel perovskite-type $BaBi_xCo_{0.2}Fe_{0.8-x}O_{3-\delta}$ ceramic membranes. J. Membr. Sci., **164** (2000) 167-176.
38. J. Tong, W. Yang, R. Cai, B. Zhu, G. Xiong, L. Lin, Investigation on the structure stability and oxygen permeability of titanium-doped perovskite-type oxides of $BaTi_{0.2}Co_xFe_{0.8-x}O_{3-\delta}$ (x = 0.2-0.6). Separ. Purif. Technol., **32** (2003) 289-299.
39. T. Ramos, A. Atkinson, Oxygen diffusion and surface exchange in $La_{1-x}Sr_xFe_{0.8}Cr_{0.2}O_{3-\delta}$ (x = 0.2, 0.4 and 0.6). Solid State Ionics, **170** (2004) 275-286.
40. L. Mikkelsen, I.G. Krogh Andersen, E.M. Skou, Oxygen transport in $La_{1-x}Sr_xFe_{1-y}Mn_yO_{3-\delta}$ perovskites. Solid State Ionics, **152-153** (2002) 703-707.
41. K. Huang, H.Y. Lee and J.B. Goodenough, Sr- and Ni-doped $LaCoO_3$ and $LaFeO_3$ perovskites. New cathode materials for solid-oxide fuel cells. J. Electrochem. Soc., **145** (1998) 3220-3227.
42. H.W. Brinkman, H. Kruidhof, A.J. Burgraaf, Mixed conducting yttrium-barium-cobalt-oxide for high oxygen permeation. Solid State ionics, **68** (1994) 173-176.
43. R.T. Baker, B. Gharbage and F.M.B. Marques, Ionic and electronic conduction in Fe and Cr doped (La,Sr)GaO_3. J. Electrochem. Soc., **144** (1997) 3130-3135.
44. F. Chen, M. Liu, Study of transition metal oxide doped $LaGaO_3$ as electrode materials for LSGM-based solid oxide fuel cells. J. Solid State Electrochem., **3** (1998) 7-14.

45. H. Ullmann, N. Trofimenko, A. Naoumidis and D. Stöver, Ionic/electronic mixed conduction relations in perovskite-type oxides by defect structure. J. Eur. Ceram. Soc., **19** (1999) 791-796.
46. T. Ishihara, T. Shibayama, H. Nishiguchi, Y. Takita, Oxide ion conductivity in $La_{0.8}Sr_{0.2}Ga_{0.8}Mg_{0.2-x}Ni_xO_3$ perovskite oxide and application for the electrolyte of solid oxide fuel cells. J. Mater. Sci., **36** (2001) 1125-1131.
47. J.Y. Yi, G.M. Choi, Phase characterization and electrical conductivity of $LaSr(GaMg)_{1-x}Mn_xO_3$ system. Solid State Ionics, **148** (2002) 557-565.
48. S. Lee, K.S. Lee, S.K. Woo, J.W. Kim, T. Ishihara, D.K. Kim, Oxygen-permeating property of $LaSrBFeO_3$ (B = Co, Ga) perovskite membrane surface-modified by $LaSrCoO_3$. Solid State Ionics, **158** (2003) 287-296.
49. T. Ishihara, H. Matsuda, Y. Mizuhara and Y. Takita, Improved oxygen ion conductivity of $NdAlO_3$ perovskite-type oxide by doping with Ga. Solid State Ionics, **70/71** (1994) 234-238.
50. T. Ishihara, H. Matsuda and Y. Takita, Oxide ion conductivity in doped $NdAlO_3$ perovskite-type oxides. J. Electrochem. Soc., **141** (1994) 3444-3449.
51. K. Yamaji, T. Horita, N. Sakai, H. Yokokawa, Comparison between $La_{0.9}Ba_{0.1}Ga_{0.8}Mg_{0.2}O_{2.85}$ and $La_{0.9}Sr_{0.1}Ga_{0.8}Mg_{0.2}O_{2.85}$ as SOFC electrolytes, Solid State Ionics, **152-153** (2002) 517-523.
52. H. Kato, T. Kudo, H. Naito, H. Yugami, Electrical conductivity of Al-doped $La_{1-x}Sr_xScO_{3-\delta}$ perovskite-type oxides as electrolyte materials for low-temperature SOFC. Solid State Ionics, **159** (2003) 217-222.
53. A. Manthiram, J.F. Kuo and J.B. Goodenough, Characterization of oxygen-deficient perovskites as oxide-ion electrolytes. Solid State Ionics, **62** (1993) 225-234.
54. H. He, X. Huang, L. Chen, Sr-doped $LaInO_3$ and its possible application in a single layer SOFC. Solid State Ionics, **130** (2000) 183-193.
55. V.V. Kharton, E.N. Naumovich, A.A. Vecher, Research on the electrochemistry of oxygen ion conductors in the former Soviet Union. I. ZrO_2-based ceramic materials. J. Solid State Electrochem., **3** (1999) 61-81.
56. V.V. Kharton, A.A. Yaremchenko, E.N. Naumovich, F.M.B. Marques, Research on the electrochemistry of oxygen ion conductors in the former Soviet Union. III. HfO_2-, CeO_2- and ThO_2-based oxides. J. Solid State Electrochem., **4** (2000) 243-266.
57. V.V. Kharton, A.A. Yaremchenko, E.N. Naumovich, F.M.B. Marques, Research on the electrochemistry of oxygen ion conductors in the former Soviet Union. IV. Bismuth oxide-based ceramics. J. Solid State Electrochem., **5** (2001) 160-187.

58. S.P.S. Badwal, Zirconia-based solid electrolytes: microstructure, stability and ionic conductivity. Solid State Ionics, **52** (1992) 23-32.
59. N.M. Sammes, G.A. Tompsett, H. Näfe and F. Aldinger, Bismuth based oxide electrolytes – structure and ionic conductivity. J. Eur. Ceram. Soc., **19** (1999) 1801-1826.
60. P. Shuk, H.-D. Wiemhöfer, U. Guth, W. Göpel, M. Greenblatt, Oxide ion conducting solid electrolytes based on Bi_2O_3. Solid State Ionics, **89** (1996) 179-196.
61. J. Kimpton, T.H. Randle, J. Drennan, Investigation of electrical conductivity as a function of dopant-ion radius in the systems $Zr_{0.75}Ce_{0.08}M_{0.17}O_{1.92}$ (M = Nd, Sm, Gd, Dy, Ho, Y, Er, Yb, Sc). Solid State Ionics, **149** (2002) 89-98.
62. M. Mogensen, N.M. Sammes, G. A. Tompsett, Physical, chemical and electrochemical properties of pure and doped ceria. Solid State Ionics, **129** (2000) 63-94.
63. H. Inaba, H. Tagawa, Ceria-based solid electrolytes. Solid State Ionics, **83** (1996) 1-16.
64. K. Eguchi, T. Setoguchi, T. Inoue and H. Arai, Electrical properties of ceria-based oxides and their application to solid oxide fuel cells. Solid State Ionics, **52** (1992) 165-172.
65. T.J. Mazanec, T.L. Cable and J.G. Frye, Jr., Electrocatalytic cells for chemical reaction. Solid State Ionics, **53-56** (1992) 111-118.
66. Y. Shen, A. Joshi, M. Liu and K. Krist, Structure, microstructure and transport properties of mixed ionic-electronic conductors based on bismuth oxide. Part I. Bi-Y-Cu-O system. Solid State Ionics, **72** (1994) 209-217.
67. J.E. ten Elshof, N.Q. Nguyen, M.W. den Otter, and H.J.M. Bouwmeester, Oxygen permeation properties of dense $Bi_{1.5}Er_{0.5}O_3$-Ag cermet membranes. J. Electrochem. Soc., **144** (1997) 4361-4366.
68. D.S. McLachlan, M. Blaszkiewicz, and R.E. Newnham, Electrical resistivity of composites. J. Am. Ceram. Soc., **73** (1990) 2187-2203.
69. Z. Wu, M. Liu, Modelling of ambipolar transport properties of composite mixed ionic-electronic conductors. Solid State Ionics, **93** (1997) 65-84.
70. F.M. Figueiredo, F.M.B. Marques, J.R. Frade, Electrical properties and thermal expansion of $LaCoO_3/La_2(Zr,Y)_2O_7$ composites. Solid State Ionics, **138** (2001) 173-182.
71. U. Nigge, H.-D. Wiemhöfer, E.W.J. Römer, H.J.M. Bouwmeester, T.R. Schulte, Composites of $Ce_{0.8}Gd_{0.2}O_{1.9}$ and $Gd_{0.7}Ca_{0.3}CoO_{3-\delta}$ as oxygen permeable membranes for exhaust gas sensors. Solid State Ionics, **146** (2002) 163-174.
72. R. A. Cutler, D.L. Meixner, Ceria – lanthanum strontium manganite composites for use in oxygen generation systems. Solid State Ionics, **159** (2003) 9-19.

73. C.S. Chen, B.A. Boukamp, H.J.M. Bouwmeester, G.Z. Cao, H. Kruidhof, A.J.A. Winnubst, A.J. Burgraaf, Microstructural development, electrical properties and oxygen permeation of zirconia-palladium composites. Solid State Ionics, **76** (1995) 23-28.
74. Y.M. Park and G.M. Choi, Mixed ionic and electronic conduction in YSZ-NiO composite. J. Electrochem. Soc., **146** (1999) 883-889.
75. J. Kim, Y.S. Lin, Synthesis and oxygen permeation properties of ceramic-metal dual-phase membranes. J. Membr. Sci., **167** (2000) 123-133.
76. C.S. Chen, A.J. Burgraaf, Stabilized bismuth oxide – noble metal mixed conducting composites as high temperature oxygen separation membranes. J. Appl. Electrochem., **29** (1999) 355-360.
77. V.V. Kharton, A.V. Kovalevsky, A.P. Viskup, A.L. Shaula, F.M. Figueiredo, E.N. Naumovich and F.M.B. Marques, Oxygen transport in $Ce_{0.8}Gd_{0.2}O_{2-\delta}$ - based composite membranes. Solid State Ionics, **160** (2003) 247-258.
78. K. Wu, S. Xie, G.S. Jiang, W. Liu, C.S. Chen, Oxygen permeation through $(Bi_2O_3)_{0.74}(SrO)_{0.26}$-Ag (40% v/o) composite. J. Membr. Sci., **188** (2001) 189-193.
79. C.S. Chen, H. Kruidhof, H.J.M. Bouwmeester, H. Verweij, A.J. Burgraaf, Thickness dependence of oxygen permeation through erbia-stabilized bismuth oxide-silver composites. Solid State Ionics, **99** (1997) 215-219.
80. H. Wang, W.S. Yang, Y. Cong, X. Zhu, Y.S. Lin, Structure and oxygen permeability of a dual-phase membrane. J. Membr. Sci., **224** (2003) 107-115.
81. C.S. Chen, H. Kruidhof, H.J.M. Bouwmeester, H. Verweij, A.J. Burgraaf, Oxygen permeation through oxygen ion oxide-noble metal dual phase composites. Solid State Ionics, **86-88** (1996) 569-572.
82. S. Nakayama, T. Kageyama, H. Aono and Y. Sadaoka, Ionic conductivity of lanthanoid silicates, $Ln_{10}(SiO_4)_6O_3$ (Ln = La, Nd, Sm, Gd, Dy, Y, Ho, Er and Yb). J. Mater. Chem., **5** (1995) 1801-1805.
83. H. Benmoussa, M. Mikou, A. Bensaoud, A. Bouhaouss, R. Morineaux, Electrical properties of lanthanum containing vanadocalcic oxyapatite. Mater. Res. Bull., **35** (2000) 369-375.
84. H. Arikawa, H. Nishiguchi, T. Ishihara, Y. Takita, Oxide ion conductivity in Sr-doped $La_{10}Ge_6O_{27}$ apatite oxide. Solid State Ionics, **136-137** (2000) 31-37.
85. E.J. Abram, D.C. Sinclair and A.R. West, A novel enhancement of ionic conductivity in the cation-deficient apatite $La_{9.33}(SiO_4)_6O_2$. J. Mater. Chem., **11** (2001) 1978-1979.

86. J. McFarlane, S. Barth, M. Swaffer, J.E.H. Sansom and P.R. Slater, Synthesis and conductivities of the apatite-type systems, $La_{9.33+x}Si_{6-y}M_yO_{26+z}$ (M = Co, Fe, Mn) and $La_8Mn_2Si_6O_{26}$. Ionics, **8** (2002) 149-154.
87. J.E.H. Sansom, J.R. Tolchard, P.R. Slater, M.S. Islam, Synthesis and structural characterization of the apatite-type phases $La_{10-x}Si_6O_{26+z}$ doped with Ga. Solid State Ionics, **167** (2004) 17-22.
88. S. Nakayama, M. Higuchi, Electrical properties of apatite-type oxide ionic conductors $RE_{9.33}(SiO_4)_6O_2$ (RE = Pr, Nd and Sm) single crystals. J. Mater. Sci. Lett., **20** (2001) 913-915.
89. J.E.H. Sansom, D. Richings, P.R. Slater, A powder neutron diffraction study of the oxide-ion-conducting apatite-type phases, $La_{9.33}Si_6O_{26}$ and $La_8Sr_2Si_6O_{26}$. Solid State Ionics, **139** (2001) 205-210.
90. L. Leon-Reina, M.C. Martin-Sedeno, E.R. Losilla, A. Cabeza, M. Martinez-Lara, S. Bruque, F.M.B. Marques, D.V. Sheptyakov and M.A.G. Aranda, Crystalchemistry and oxide ion conductivity in the lanthanum oxygermanate apatite series. Chem. Mater., **15** (2003) 2099-2108.
91. J.R. Tolchard, J.E.H. Sansom, P.R. Slater, M.S. Islam, Effect of Ba and Bi doping on the synthesis and sintering of Ge-based apatite phases. J. Solid State Electrochem., **8** (2004) 668-673.
92. L. Leon-Reina, E.R. Losilla, M. Martinez-Lara, S. Bruque and M.A.G. Aranda, Interstitial oxygen conduction in lanthanum oxy-apatite electrolytes. J. Mater. Chem., **14** (2004) 1142-1149.
93. J.E.H. Sansom, P.R. Slater, Oxide ion conductivity in the mixed Si/Ge apatite-type phases $La_{9.33}Si_{6-x}Ge_xO_{26}$. Solid State Ionics, **167** (2004) 23-27.
94. J.R. Tolchard, M.S. Islam and P.R. Slater, Defect chemistry and oxygen ion migration in the apatite-type materials $La_{9.33}Si_6O_{26}$ and $La_8Sr_2Si_6O_{26}$. J. Mater. Chem., **13** (2003) 1956-1961.
95. P.R. Slater and J.E.H. Sansom, The synthesis and characterisation of new apatite-type oxide ion conductors. Solid State Phenom., **90-91** (2003) 195-200.
96. O. Yamamoto, Solid oxide fuel cells: fundamental aspects and prospects. Electrochim. Acta, **45** (2000) 2423-2435.
97. Hirschenhofer J.H., Stauffer D.B., Engleman R.R. and Klett M.G., Fuel cell handbook, 4th ed., U.S. Department of Energy, Morgantown, WV, 1998.
98. M. Dokiya, SOFC system and technology, Solid State Ionics, **152-153** (2002) 383-392.
99. J.P.P. Huijsmans, Ceramics in solid oxide fuel cells. Curr. Opin. Solid State Mater. Sci., **5** (2001) 317-323.
100. S.P.S. Badwal, Stability of solid oxide fuel cell components. Solid State Ionics, **143** (2001) 39-46.

101. H.-H. Möbius, On the history of solid electrolyte fuel cells. J. Solid State Electrochem., **1** (1997) 2-16.

102. M. Mori, T. Abe, H. Itoh, O. Yamamoto, Y. Takeda, T. Kawahara, Cubic-stabilized zirconia and alumina composites as electrolytes in planar type solid oxide fuel cells. Solid State Ionics, **74** (1994) 157-164.

103. O. Yamamoto, Y. Arati, Y. Takeda, N. Imanishi, Y. Mizutani, M. Kawai, Y. Nakamura, Electrical conductivity of stabilized zirconia with ytterbia and scandia. Solid State Ionics, **79** (1995) 137-142.

104. M. Hirano, S. Watanabe, E. Kato, Y. Mizutani, M. Kawai, Y. Nakamura, High electrical conductivity and high fracture strength of Sc_2O_3-doped zirconia ceramics with submicrometer grains. J. Am. Ceram. Soc., **82** (1999) 2861-2925.

105. Y. Ji, J. Liu, Z. Lu, X. Zhao, T. He, W. Su, Study on the properties of Al_2O_3-doped $(ZrO_2)_{0.92}(Y_2O_3)_{0.08}$ electrolyte. Solid State Ionics, **126** (1999) 277-283.

106. P. Huang and A. Petric, Superior oxygen ion conductivity of lanthanum gallate doped with strontium and magnesium. J. Electrochem. Soc., **143** (1996) 1644-1648.

107. J. Van Herle, R. Ihringer, N.M. Sammes, G. Tompsett, K. Kendall, K. Yamada, C. Wen, T. Kawada, M. Ihara, J. Mizusaki, Concept and technology of SOFC for electric vehicles. Solid State Ionics, **132** (2000) 333-342.

108. E.F. Sverdrup, A.D. Glasser, D.H. Archer, Fuel cell comprising a stabilized zirconium oxide electrolyte and a doped indium or tin oxide cathode. US Patent 3,558,360, 1971 (filed 8.1.1968).

109. C.S. Tedmon, H.S. Spacil, S.P. Mitoff, Cathode material and performance in high-temperature zirconia electrolyte fuel cells. J. Electrochem. Soc., **116** (1969) 1170-1175.

110. Y. Takeda, R. Kanno, M. Noda, Y. Tomida, O. Yamamoto, Cathodic polarization phenomena of perovskite oxide electrodes with stabilized zirconia. J. Electrochem. Soc., **134** (1987) 2656-2661.

111. V.V. Kharton, F.M.B. Marques, A. Atkinson, Transport properties of solid oxide electrolyte ceramics: a brief review. Solid State Ionics, **174** (2004) 135-149.

112. P. Shuk, L. Tichonova, U. Guth, Materials for electrodes based on rare earth manganites. Solid State Ionics, **68** (1994) 177-184.

113. L.-W. Tai, M.M. Nasrallah, H.U. Anderson, D.M. Sparlin, S.R. Sehlin, Structure and electrical properties of $La_{1-x}Sr_xCo_{1-y}Fe_yO_3$. Part 1. The system $La_{0.8}Sr_{0.2}Co_{1-y}Fe_yO_3$. Solid State Ionics, **76** (1995) 259-271.

114. X. Liu, J. Gao, Y. Liu, R. Peng, D. Peng, G. Meng, Microstructure and electrical properties of porous $Y_{1-x}Ca_xFeO_3$ cathode materials by gelcasting process. Solid State Ionics, **152-153** (2002) 531-536.

115. H. Ullmann, N. Trofimenko, F. Tietz, D. Stöver, A. Ahmad-Khanlou, Correlation between thermal expansion and oxide ion transport in mixed conducting perovskite-type oxides for SOFC cathodes. Solid State Ionics, **138** (2000) 79-90.

116. R. Chiba, F. Yoshimura, Y. Sakurai, Properties of $La_{1-y}Sr_yNi_{1-x}Fe_xO_3$ as a cathode material for a low-temperature operating SOFC. Solid State Ionics, **152-153** (2002) 575-582.

117. I. Kaus, H.U. Anderson, Electrical and thermal properties of $La_{0.2}Sr_{0.8}Cu_{0.1}Fe_{0.9}O_{3-\delta}$ and $La_{0.2}Sr_{0.8}Cu_{0.2}Fe_{0.8}O_{3-\delta}$. Solid State Ionics, **129** (2000) 189-200.

118. D. Kuščer, J. Holc, M. Hrovat, D. Kolar, Correlation between the defect structure, conductivity and chemical stability of $La_{1-y}Sr_yFe_{1-x}Al_xO_{3-\delta}$ cathodes for SOFC. J. Eur. Ceram. Soc., **21** (2001) 1817-1820.

119. G.C. Kostogloudis, G. Tsiniarakis, C. Ftikos, Chemical reactivity of perovskite oxide SOFC cathodes and yttria stabilized zirconia. Solid State Ionics, **135** (2000) 529-535.

120. H.-C. Yu, K.-Z. Fung, $La_{1-x}Sr_xCuO_{2.5-\delta}$ as new cathode materials for intermediate temperature solid oxide fuel cells. Mater. Res. Bull., **38** (2003) 231-239.

121. T. Takeda, R. Kanno, Y. Kawamoto, Y. Takeda and O. Yamamoto, New cathode materials for solid oxide fuel cells. J. Electrochem. Soc., **147** (2000) 1730-1733.

122. M.S.D. Read, M.S. Islam, F. King, F.E. Hancock, Defect chemistry of $La_2Ni_{1-x}M_xO_4$ (M = Mn, Fe, Co, Cu): relevance to catalytic behavior. J. Phys. Chem. B, **103** (1999) 1558-1562.

123. V.V. Vashook, N.E. Trofimenko, H. Ullmann, L.V. Makhnach, Oxygen nonstoichiometry and some transport properties of $LaSrNiO_{4-\delta}$ nickelate. Solid State Ionics, **131** (2000) 329-336.

124. T.M. Gür, R.A. Huggins, High temperature oxygen transport and electrochemical behavior of $YBa_2Cu_3O_x$. J. Electrochem. Soc., **140** (1993) 1990-2000.

125. H.S. Spacil, Electrical device including nickel-containing stabilized zirconia electrode. US Patent 3,503,809, 1970 (filed 30.10.1964).

126. J. Liu, S.A. Barnett, Operation of anode-supported solid oxide fuel cells on methane and natural gas. Solid State Ionics, **158** (2003) 11-16.

127. D. Skarmoutsos, A. Tsoga, A. Naoumidis, P. Nikolopoulos, 5 mol% TiO_2-doped Ni-YSZ anode cermets for solid oxide fuel cells. Solid State Ionics, **135** (2000) 439-444.

128. H. Kim, C. Lu, W.L. Worrell, J.M. Vohs, and R.J. Gorte, Cu-Ni cermet anodes for direct oxidation of methane in solid-oxide fuel cells. J. Electrochem. Soc., **149** (2002) A247-A250.

129. O.A. Marina, C. Bagger, S. Primdahl, M. Mogensen, A solid oxide fuel cell with a gadolinia-doped ceria anode: preparation and performance. Solid State Ionics, **123** (1999) 199-208.

130. J. Liu, B.D. Madsen, Z.Q. Li and S.A. Barnett, A fuel-flexible ceramic-based anode for solid oxide fuel cells. Electrochem. and Solid State Lett., **5** (2002) A122-A124.

131. S. Hamakawa, R. Shiozaki, T. Hayakawa, K. Suzuki, K. Murata, K. Takehira, M. Koizumi, J. Nakamura, and T. Uchijima, Partial oxidation of methane to synthesis gas using $Ni/Ca_{0.8}Sr_{0.2}TiO_3$ anode catalyst. J. Electrochem. Soc., **147** (2000) 839-844.

132. G. Pudmich, B.A. Boukamp, M. Gonzalez-Cuenca, W. Jungen, W. Zipprich, F. Tietz, Chromite/titanate based perovskites for application as anodes in solid oxide fuel cells. Solid State Ionics, **135** (2000) 433-438.

133. M. Stojanović, C.A. Mims, H. Moudallal, Y.L. Yang, and A.J. Jacobson, Reaction kinetics of methane oxidation over $LaCr_{1-x}Ni_xO_3$ perovskite catalysts. J. Catalysis, **166** (1997) 324-332.

134. N. Gunasekaran, S. Rajadurai, J.J. Carberry, N. Bakshi, C.B. Alcock, Surface characterization and catalytic properties of $La_{1-x}A_xMO_3$ perovskite oxides. Part II. Studies on $La_{1-x}Ba_xMnO_3$ ($0 \leq x \leq 0.2$) oxides. Solid State Ionics, **81** (1995) 243-249.

135. M. Weston, I.S. Metcalfe, $La_{0.6}Sr_{0.4}Co_{0.2}Fe_{0.8}O_3$ as an anode for direct methane activation in SOFCs. Solid State Ionics, **113-115** (1998) 247-251.

136. D. Kek, N. Bonanos, M. Mogensen, S. Pejovnik, Effect of electrode material on the oxidation of H_2 at the metal-$Sr_{0.995}Ce_{0.95}Y_{0.05}O_{2.970}$ interface. Solid State Ionics, **131** (2000) 249-259.

137. P.R. Slater, J.T.S. Irvine, Synthesis and electrical characterization of the tetragonal tungsten bronze type phases, $(Ba/Sr/Ca/La)_{0.6}M_xNb_{1-x}O_{3-\delta}$ (M = Mg, Ni, Mn, Cr, Fe, Ni, In, Sn): evaluation as potential anode materials for solid oxide fuel cells. Solid State Ionics, **124** (1999) 61-72.

138. P. Holtappels, F.W. Poulsen, M. Mogensen, Electrical conductivities and chemical stabilities of mixed conducting pyrochlores for SOFC applications. Solid State Ionics, **135** (2000) 675-679.

139. J. Canales-Vázquez, S.W. Tao, J.T.S. Irvine, Electrical properties in $La_2Sr_4Ti_6O_{19-\delta}$: a potential anode for high temperature fuel cells. Solid State Ionics, **159** (2003) 159-165.

140. B.C.H. Steele, Materilas for IT-SOFC stacks. 35 years R&D: the inevitability of gradualness? Solid State Ionics, **134** (2000) 3-20.

141. Hilpert, K., Quadakkers, W.J., and Singheiser, L., Interconnects. In *Handbook of fuel cells – fundamentals, technology and applications*, eds. W. Vielstich, A. Lamm, H. A. Gasteiger. John Wiley & Sons, Ltd, Chichester, 2003, pp. 1037-1054.

142. Z. Zeng, K. Natesan, Corrosion of metallic interconnects for SOFC in fuel gases. Solid State Ionics, **167** (2004) 9-16.

143. J.-H. Kim, R.-H. Song, S.-H. Hyun, Effect of slurry-coated $LaSrMnO_3$ on the electrical property of Fe-Cr alloy for metallic interconnect of SOFC. Solid State Ionics, **174** (2004) 185-191.

144. X. Chen, P.Y. Hou, C.P. Jacobson, S.J. Visco, L.C. De Jonghe, Protective coating on stainless steel interconnect for SOFCs: oxidation kinetics and electrical properties. Solid State Ionics, **176** (2005) 425-433.

145. B.C.H. Steele, Material science and engineering: the enabling technology for the commercialization of fuel cell systems. J. Mater. Sci., **36** (2001) 1053-1068.

146. J. Kilner, S. Benson, J. Lane and D. Waller, Ceramic ion conducting membranes for oxygen separation. Chemistry and Industry, (1997) 907-911.

147. R.M. Thorogood, Developments in air separation, Gas Separ. and Purif., **5** (1991) 83-94.

148. P.N. Dyer, R.E. Richards, S.L. Russek, D.M. Taylor, Ion transport membrane technology for oxygen separation and syngas production. Solid State Ionics, **134** (2000) 21-33.

149. P.V. Hendriksen, P.H. Larsen, M. Mogensen, F.W. Poulsen, K. Wiik, Prospects and problems of dense oxygen permeable membranes. Catalysis Today, **56** (2000) 283-295.

150. Z. Shao, H. Dong, G. Xiong, Y. Cong, W. Yang, Performance of a mixed-conducting ceramic membrane reactor with high oxygen permeability for methane conversion. J. Membr. Sci., **183** (2001) 181-192.

151. V.V. Kharton, E.N. Naumovich, A.V. Nikolaev, Materials of high-temperature electrochemical oxygen membranes. J. Membr. Sci., **111** (1996) 149-157.

152. V.V. Kharton, A.A. Yaremchenko, A.V. Kovalevsky, A.P. Viskup, E.N. Naumovich, P.F. Kerko, Perovskite-type oxides for high-temperature oxygen separation membranes. J. Membr. Sci., **163** (1999) 307-317.

153. V.V. Kharton, A.A. Yaremchenko, E.N. Naumovich, Research on the electrochemistry of oxygen ion conductors in the former Soviet Union. II. Perovskite-related oxides. J. Solid State Electrochem., **3** (1999) 303-326.

154. H.J.M. Bouwmeester, Dense ceramic membranes for methane conversion. Catal. Today, **82** (2003) 141-150.

155. U. Balachandran, J.T. Dusek, S.M. Sweeney, R.B. Poeppel, R.L. Mieville, P.S. Maiya, M.S. Kleefisch, S.Pei, T.P. Kobylinski, C.A. Udovich, A.C. Bose, Methane to syngas via ceramic membranes. Amer. Ceram. Soc. Bull., **74** (1995) 71-75.

156. S.Pei, M.S. Kleefisch, T.P. Kobylinski, J. Faber, C.A. Udovich, V. Zhang-McCoy, B. Dabrowski, U. Balachandran, R.L. Mieville and R.B. Poeppel, Failure mechanisms of ceramic

membrane reactors in partial oxidation of methane to synthesis gas. Catal. Lett., **30** (1995) 201-212.

157. J.R. Frade, V.V. Kharton, A. Yaremchenko, E. Naumovich, Methane to syngas conversion. Part I. Equilibrium conditions and stability requirements of membrane materials. J. Power Sources, **130** (2004) 77-84.

158. C.-Y. Tsai, A.G. Dixon, Y.H. Ma, W.R. Moser and M.R. Pascucci, Dense perovskite, $La_{1-x}A_xFe_{1-y}Co_yO_{3-\delta}$ (A = Ba, Sr, Ca), membrane synthesis, applications, and characterization. J. Am. Ceram. Soc., **81** (1998) 1437-1444.

159. W.S. Wang, Z.P.Shao, Y. Cong, G.X. Xiong, Mixed conducting membranes with high oxygen vacancies, Chinese Patent, Application No. 99 1 13004.9.

160. Y. Lu, A.G. Dixon, W.R. Moser, Y.H. Ma, U. Balachandran, Oxygen-permeable dense membrane reactor for the oxidative coupling of methane. J. Membr. Sci., **170** (2000) 27-34.

161. T. Ishihara and Y. Takita, Partial oxidation of methane into syngas with oxygen permeating ceramic membrane reactors. Catal. Surv. Japan, **4** (2000) 125-133.

162. A.L. Shaula, A.A. Yaremchenko, V.V. Kharton, D.I. Logvinovich, E.N. Naumovich, A.V. Kovalevsky, J.R. Frade, F.M.B. Marques, Oxygen permeability of $LaGaO_3$-based ceramic membranes. J. Membr. Sci., **221** (2003) 69-77.

163. V.V. Kharton, E.V. Tsipis, I.P. Marozau, A.A. Yaremchenko, A.A. Valente, A.P. Viskup, J.R. Frade, E.N. Naumovich, J. Rocha, Transport and electrocatalytic properties of $La_{0.3}Sr_{0.7}Co_{0.8}Ga_{0.2}O_{3-\delta}$ membranes. J. Solid State Electrochem., **9** (2005) 10-20.

164. J. Tong, W. Yang, R. Cai, B. Zhu, and L. Lin, Novel and ideal zirconium-based dense membrane reactors for partial oxidation of methane to syngas. Catal. Lett., **78** (2002) 129-137.

165. A.A. Yaremchenko, A.A. Valente, V.V. Kharton, E.V. Tsipis, J.R. Frade, E.N. Naumovich, J. Rocha, and F.M.B. Marques, Oxidation of dry methane on the surface of oxygen ion-conducting membranes. Catal. Lett., **91** (2003) 169-174.

166. U. Balachandran, J.T. Dusek, P.S. Maiya, B. Ma, R.L. Mieville, M.S. Kleefisch, C.A. Udovich, Ceramic membrane reactor for converting methane to syngas. Catal. Today, **36** (1997) 265-272.

167. B. Ma, J.P. Hodges, J.D. Jorgensen, D.J. Miller, J.W. Richardson, Jr., and U. Balachandran, Structure and property relationships in mixed-conducting $Sr_4(Fe_{1-x}Co_x)_6O_{13\pm\delta}$ materials. J. Solid State Chem., **141** (1998) 576-586.

168. M. Schwartz, J.H. White, A.F. Sammels, Solid state oxygen anion and electron mediating membrane and catalytic membrane reactors containing them. US Patent 6,033,632, 2000 (filed 29.4.1996).

169. V.V. Kharton, A.A. Yaremchenko, A.L. Shaula, M.V. Patrakeev, E.N. Naumovich, D.I. Logvinovich, J.R. Frade, and F.M.B. Marques, Transport properties and stability of Ni-containing mixed conductors with perovskite- and K_2NiF_4-type structure. J. Solid State Chem., **177** (2004) 26-37.

170. Suitor, J.W., Clark, D.J. and Losey, R.W., Development of alternative oxygen production source using a zirconia solid electrolyte membrane. In *Technical progress report for fiscal years 1987, 1988 and 1990*. Jet Propulsion Laboratory Internal Document D7790, 1990.

171. F.T. Ciacchi, S.P.S. Badwal, V. Zelizko, Tubular zirconia-yttria electrolyte membrane technology for oxygen separation. Solid State Ionics, **152-153** (2002) 763-768.

172. W.N. Lawless, Solid-state generation of oxygen using ceramic honeycombs. Solid State Ionics, **52** (1992) 219-224.

173. J. Guan, R. Doshi, G. Lear, K. Montgomery, E. Ong, and N. Minh, Ceramic oxygen generators with thin-film zirconia electrolytes. J. Am. Ceram. Soc., **85** (2002) 2651-2654.

174. S.P.S. Badwal and F.T. Ciacchi, Ceramic membrane technologies for oxygen separation. Adv. Mater., **13** (2001) 993-996.

175. R. Doshi, Y. Shen and C.B. Alcock, Oxygen pumping characteristics of oxide ion electrolytes at low temperatures. Solid State Ionics, **68** (1994) 133-137.

176. Fabry, P. and Siebert, E., Electrochemical sesors. In *Handbook of Solid State Electrochemistry*, eds. P. J. Gellings and H.J.M. Bouwmeester. Elsevier, CRC press, Florida, 1997, pp. 329-369.

177. N. Docquier, S. Candel, Combustion control and sensors: a review. Prog. Energy Combust. Sci., **28** (2002) 107-150.

178. G. Reinhardt, R. Mayer, M. Rösch, Sensing small molecules with amperometric sensors. Solid State Ionics, **150** (2002) 79-92.

179. P. Schmidt-Zhang, K.-P. Sandow, F. Adolf, W. Göpel, U. Guth, A novel thick film sensor for simultaneous O_2 and NO monitoring in exhaust gases. Sens. Actuators B, **70** (2000) 25-29.

180. T. Hibino, A. Hashimoto, S. Kakimoto, and M. Sano, Zirconia-based potentiometric sensors using metal oxide electrodes for detection of hydrocarbons. J. Electrochem. Soc., **148** (2001) H1-5.

181. West A.R., Solid state chemistry and its applications. John Wiley & Sons, East Kilbride, 1984.

182. J.B. Goodenough and J.-S. Zhou, Localized to itinerant electronic transitions in transition-metal oxides with the perovskite structure. Chem. Mater., **10** (1998) 2980-2993.

183. M. Rajendran, A.K. Bhattacharya, Production of rare-earth orthoferrite ceramic fibres by aqueous sol-gel blow spinning process. J. Eur. Ceram. Soc., **24** (2004) 111-117.

184. H.W. Brinks, H. Fjellvag, A. Kjekshus, and B.C. Hauback, Structure and magnetism of $Pr_{1-x}Sr_xFeO_{3-\delta}$. J. Solid State Chem., **150** (2000) 233-249.

185. N. Dasgupta, R. Krishnamoorthy, K.T. Jacob, Crystal structure and thermal and electrical properties of the perovskite solid solution $Nd_{1-x}Sr_xFeO_{3-\delta}$ ($0 \leq x \leq 0.4$). Solid State Ionics, **149** (2002) 227-236.

186. J. Mizusaki, T. Sasamoto, W.R. Cannon, and H.K. Bowen, Electronic conductivity, Seebeck coefficient, and defect structure of $LaFeO_3$. J. Am. Ceram. Soc., **65** (1982) 363-368.

187. C. H. Yo, I.Y. Jung, K.H. Ryu, K.S. Ryu, and J.H. Choy, A study of the nonstoichiometry and physical properties of the perovskite $Nd_{1-x}Ca_xFeO_{3-y}$ system. J. Solid State Chem., **114** (1995) 265-270.

188. B. Fu, W. Huebner, M.f. Trubelja and V.S. Stubican, $(Y_{1-x}Ca_x)FeO_3$: A potential cathode material for solid oxide fuel cells. In *SOFC III*, eds. S.C. Singhal, H. Iwahara. The Electrochem. Soc., **PV 93-4** (1993) 276-287.

189. J. Mizusaki, T. Sasamoto, W.R. Cannon, and H.K. Bowen, Electronic conductivity, Seebeck coefficient, and defect structure of $La_{1-x}Sr_xFeO_3$ (x = 0.1, 0.25). J. Am. Ceram. Soc., **66** (1983) 247-252.

190. V.V. Kharton, A.P. Viskup, E.N. Naumovich, A.A. Tonoyan, and O.P. Reut, Oxygen ionic transport in A-site-deficient perovskites $La(Pb)FeO_3$. Mater. Res. Bull., **33** (1998) 1087-1093.

191. F.W. Poulsen, G. Lauvstad and R. Tunold, Conductivity and Seebeck measurements on strontium ferrates. Solid State Ionics, **72** (1994) 47-53.

192. V.L. Kozhevnikov, I.A. Leonidov, M.V. Patrakeev, and E.B. Mitberg, Electrical properties of the ferrite $SrFeO_y$ at high temperatures. J. Solid State Chem., **158** (2000) 320-326.

193. M.V. Patrakeev, J.A. Bahteeva, E.B. Mitberg, I.A. Leonidov, V.L. Kozhevnikov, and K.R. Poeppelmeier, Electron/hole and ion transport in $La_{1-x}Sr_xFeO_{3-\delta}$. J. Solid State Chem., **172** (2003) 219-231.

194. J.E. ten Elshof, H.J.M. Bouwmeester, H. Verweij, Oxygen transport through $La_{1-x}Sr_xFeO_{3-\delta}$ membranes. I. Permeation in air/He gradients. Solid State Ionics, **81** (1995) 97-109.

195. J.E. ten Elshof, H.J.M. Bouwmeester, H. Verweij, Oxygen transport through $La_{1-x}Sr_xFeO_{3-\delta}$ membranes. II. Permeation in air/CO, CO_2 gradients. Solid State Ionics, **89** (1996) 81-92.

196. K.S. Roh, K.H. Ryu, and C.H. Yo, Nonstoichiometry and physical properties of the $SrSn_{1-x}Fe_xO_{3-y}$ system. J. Solid State Chem., **142** (1999) 288-293.

197. D.P. Fagg, V.V. Kharton, J.R. Frade, A.A.L. Ferreira, Stability and mixed ionic-electronic conductivity of (Sr,La)(Ti,Fe)$O_{3-\delta}$ perovskites. Solid State Ionics, **156** (2003) 45-57.

198. V.V. Kharton, A.V. Kovalevsky, E.V. Tsipis, A.P. Viskup, E.N. Naumovich, J.R. Jurado, J.R. Frade, Mixed conductivity and stability of A-site-deficient Sr(Fe,Ti)$O_{3-\delta}$ perovskites. J. Solid State Electrochem., **7** (2002) 30-36.

199. P. Adler and S. Eriksson, Structural properties, Mössbauer spectra, and magnetism of perovskite-type oxides $SrFe_{1-x}Ti_xO_{3-y}$. Z. Anorg. Allg. Chem., **626** (2000) 118-124.

200. L. Kindermann, D. Das, H. Nickel, K. Hilpert, Chemical compatibility of the $LaFeO_3$ base perovskites $(La_{0.6}Sr_{0.4})_zFe_{0.8}M_{0.2}O_{3-\delta}$ (z = 1, 0.9; M = Cr, Mn, Co, Ni) with yttria stabilized zirconia. Solid State Ionics, **89** (1996) 215-220.

201. W.T. Stephens, T.J. Mazanec, H.U. Anderson, Influence of gas flow rate on oxygen flux measurements for dense oxygen conducting ceramic membranes. Solid State Ionics, **129** (2000) 271-284.

202. M.K. Kuznetsov, Q.A. Pankhurst, I.P. Parkin and Y.G. Morozov, Self-propagating high-temperature synthesis of chromium substituted lanthanum orthoferrites $LaFe_{1-x}Cr_xO_3$ ($0 \leq x \leq 1$). J. Mater. Chem., **11** (2001) 854-858.

203. H. Taguchi, Relationships between crystal structure and electrical properties of $Nd(Cr_{1-x}Fe_x)O_3$. J. Solid State Chem., **131** (1997) 108-114.

204. C. George, G. Majkic, W. Lo, K. Salama, Processing of dense $La_{0.2}Sr_{0.8}Fe_{0.8}Cr_{0.2}O_{3-\delta}$ oxygen membranes. Mater. Sci. Eng., **B83** (2001) 198-203.

205. J. Yoo, A. Verma, and A.J. Jacobson, The temperature and oxygen partial pressure dependence of the electrical conductivity of $La_{0.2}Sr_{0.8}Cr_{0.2}Fe_{0.8}O_{3-\delta}$. In *Ionic and Mixed Conducting Ceramics IV*, eds. T.A. Ramanarayanan, W.L. Worrell, M. Mogensen. The Electrochem. Soc., Pennington, USA, **PV 28** (2001) 27-35.

206. I.D. Fawcett, G.M. Veith, M. Greenblatt, M. Croft, I. Nowik, Properties of the perovskites, $SrMn_{1-x}Fe_xO_{3-\delta}$ (x = 1/3, 1/2, 2/3). Solid State Sci., **2** (2000) 821-831.

207. G. Caboche, L.-C. Dufour, F. Morin, An X-ray powder diffraction study of lanthanum-strontium ferromanganites. Solid State Ionics, **144** (2001) 211-222.

208. S.S. Bashkirov, V.V. Parfenov, I.A. Abdel-Latif, L.D. Zaripova, Mössbauer effect and electrical properties studies of $SmFe_xMn_{1-x}O_3$ (x = 0.7, 0.8 and 0.9). J. Alloys. Comp., **387** (2005) 70-73.

209. S. Diethelm, J. Van Herle, P.H. Middleton, D. Favrat, Oxygen permeation and stability of $La_{0.4}Ca_{0.6}Fe_{1-x}Co_xO_{3-\delta}$ (x = 0, 0.25, 0.5) membranes. J. Power Sources, **118** (2003) 270-275.

210. H. Ullmann, N. Trofimenko, Composition, structure and transport properties of perovskite-type oxides. Solid State Ionics, **119** (1999) 1-8.

211. K. Wiik, S. Aasland, H.L. Hansen, I.L. Tangen, R. Ødegård, Oxygen permeation in the system $SrFeO_{3-x}$-$SrCoO_{3-y}$. Solid State Ionics, **152-153** (2002) 675-680.

212. L.-W. Tai, M.M. Nasrallah, H.U. Anderson, D.M. Sparlin, S.R. Sehlin, Structure and electrical properties of $La_{1-x}Sr_xCo_{1-y}Fe_yO_3$. Part 2. The system $La_{1-x}Sr_xCo_{0.2}Fe_{0.8}O_3$. Solid State Ionics, **76** (1995) 273-283.

213. G.C. Kostogloudis, C. Ftikos, Crystal structure, thermal expansion and electrical conductivity of $Pr_{1-x}Sr_xCo_{0.2}Fe_{0.8}O_{3-\delta}$ ($0 \leq x \leq 0.5$). Solid State Ionics, **135** (2000) 537-541.

214. N.E. Trofimenko, H. Ullmann, Oxygen stoichiometry and mixed ionic-electronic conductivity of $Sr_{1-a}Ce_aFe_{1-b}Co_bO_{3-x}$ perovskite-type oxides. J. Eur. Ceram. Soc., **20** (2000) 1241-1250.

215. A. Petric, P. Huang, F. Tietz, Evaluation of La-Sr-Co-Fe-O perovskites for solid oxide fuel cells and gas separation membranes. Solid State Ionics, **135** (2000) 719-725.

216. L.-W. Tai, M.M. Nasrallah, and H.U. Anderson, Thermochemical stability, electrical conductivity, and Seebeck coefficient of Sr-doped $LaCo_{0.2}Fe_{0.8}O_{3-\delta}$. J. Solid State Chem., **118** (1995) 117-124.

217. H. Falcón, A.E. Goeta, G. Punte, and R.E. Carbonio, Crystal structure refinement and stability of $LaFe_xNi_{1-x}O_3$ solid solutions. J. Solid State Chem., **133** (1997) 379-385.

218. R. Chiba, F. Yoshimura, Y. Sakurai, An investigation of $LaNi_{1-x}Fe_xO_3$ as a cathode material for solid oxide fuel cells. Solid State Ionics, **124** (1999) 281-288.

219. V.V. Kharton, A.P. Viskup, E.N. Naumovich, and V.N. Tikhonovich, Oxygen permeability of $LaFe_{1-x}Ni_xO_{3-\delta}$ solid solutions. Mater. Res. Bull., **34** (1999) 1311-1317.

220. R. Genouel, C. Michel, N. Nguyen, F. Studer, M. Hervieu, and B. Raveau, On the cubic perovskites $La_{0.2}Sr_{0.8}Cu_{0.4}M_{0.6}O_{3-y}$ (M = Co, Fe). J. Solid State Chem., **119** (1995) 260-270.

221. J. Tong, W. Yang, B. Zhu, R. Cai, Investigation of ideal zirconium-doped perovskite-type ceramic membrane materials for oxygen separation. J. Membr. Sci., **203** (2002) 175-189.

222. M. Wyss, A. Reller, H.R. Oswald, Preparation and thermochemical reactivity of strontium iron zirconium oxides $SrFe_{1-x}Zr_xO_{3-\delta}$. Solid State Ionics, **101-103** (1997) 547-554.

223. V. Thangadurai, P.S. Beurmann, W. Weppner, Mixed oxide ion and electronic conductivity in perovskite-type $SrSnO_3$ by Fe substitution. Mater. Sci. Eng., **B100** (2003) 18-22.

224. D. Kuščer, D. Hanžel, J. Holc, M. Hrovat, and D. Kolar, Defect structure and electrical properties of $La_{1-y}Sr_yFe_{1-x}Al_xO_{3-\delta}$. J. Am. Ceram. Soc., **84** (2001) 1148-1154.

225. K. Mori, T. Fukunaga, K. Shibata, K. Iwase, S. Harjo, A. Hoshikawa, K. Itoh, T. Kamiyama, T. Ishigaki, Structural properties of Fe-doped lanthanum gallate. Physica B, **352** (2004) 147-155.

226. T. Ishihara, T. Yamada, H. Arikawa, H. Nishiguchi, Y. Takita, Mixed electronic-oxide ionic conductivity and oxygen permeating property of Fe-, Co- or Ni-doped $LaGaO_3$ perovskite oxide. Solid State Ionics, **135** (2000) 631-636.

227. A.A. Yaremchenko, M.V. Patrakeev, V.V. Kharton, F.M.B. Marques, I.A. Leonidov, V.L. Kozhevnikov, Oxygen ionic and electronic conductivity of $La_{0.3}Sr_{0.7}Fe(Al)O_{3-\delta}$ perovskites. Solid State Sci., **6** (2004) 357-366.

228. Q. Ming, M.D. Nersesyan, A. Wagner, J. Ritchie, J.T. Richardson, D. Luss, A.J. Jacobson, Y.L. Yang, Combustion synthesis and characterization of Sr and Ga doped $LaFeO_3$. Solid State Ionics, **122** (1999) 113-121.

229. J. Holc, D. Kuščer, M. Hrovat, S. Bernik, D. Kolar, Electrical and microstructural characterization of $(La_{0.8}Sr_{0.2})(Fe_{1-x}Al_x)O_3$ and $(La_{0.8}Sr_{0.2})(Mn_{1-x}Al_x)O_3$ as possible SOFC cathode materials. Solid State Ionics, **95** (1997) 259-268.

230. G.W. Coffey, J. Hardy, L.R. Pedersen, P.C. Rieke, E.C. Thomsen, M. Walpole, Electrochemical properties of lanthanum strontium aluminium ferrites for the oxygen reduction reaction. Solid State Ionics, **158** (2003) 1-9.

231. Y. Tsuruta, T. Todaka, H. Nisiguchi, T. Ishihara, and Y. Takita, Mixed electronic-oxide ionic conductor of Fe-doped $La(Sr)GaO_3$ perovskite oxide for oxygen permeating membrane. Electrochem. Solid-State Lett., **4** (2001) E13-E15.

232. J.T. Ritchie, J.T. Richardson, and D. Luss, Ceramic membrane reactor for synthesis gas production. AIChE, **47** (2001) 2092-2101.

233. J.P. Hodges, S. Short, J.D. Jorgensen, X. Xiong, B. Dabrowski, S.M. Mini, and C.W. Kimball, Evolution of oxygen-vacancy ordered crystal structures in the perovskite series $Sr_nFe_nO_{3n-1}$ (n = 2, 4, 8 and ∞), and the relationship to electronic and magnetic properties. J. Solid State Chem., **151** (2000) 190-209.

234. M.V. Patrakeev, I.A. Leonidov, V.L. Kozhevnikov, V.V. Kharton, Ion-electron transport in strontium ferrites: relationships with structural features and stability. Solid State Sci., **6** (2004) 907-913.

235. V.V. Kharton, I.P. Marozau, N.P. Vyshatko, A.L. Shaula, A.P. Viskup, E.N. Naumovich, F.M.B. Marques, Oxygen ionic conduction in brownmillerite $CaAl_{0.5}Fe_{0.5}O_{2.5+\delta}$. Mater. Res. Bull., **38** (2003) 773-782.

236. S.N. Ruddlesden and P. Popper, New compounds of the K_2NiF_4 type. Acta Cryst., **10** (1957) 538-540.

237. A. Fossdal, M.-A. Einarsrud, and T. Grande, Phase equilibria in the pseudo-binary system SrO-Fe_2O_3. J. Solid State Chem., **177** (2004) 2933-2942.

238. F. Prado, T. Armstrong, A. Caneiro, and A. Manthiram, Structural stability and oxygen permeation properties of $Sr_{3-x}La_xFe_{2-y}Co_yO_{7-\delta}$ ($0 \leq x \leq 0.3$ and $0 \leq y \leq 1.0$). J. Electrochem. Soc., **148** (2001) J7-J14.

239. T. Armstrong, F. Prado, A. Manthiram, Synthesis, crystal chemistry, and oxygen permeation properties of $LaSr_3Fe_{3-x}Co_xO_{10}$ ($0 \leq x \leq 1.5$). Solid State Ionics, **140** (2001) 89-96.

240. A.J. Jennings, S.J. Skinner, and O. Helgason, Structural properties of $La_xSr_{2-x}FeO_{4\pm\delta}$ at high temperature and under reducing conditions. J. Solid State Chem., **175** (2003) 207-217.

241. Y.A. Shilova, M.V. Patrakeev, E.B. Mitberg, I.A. Leonidov, V.L. Kozhevnikov, and K.R. Poeppelmeier, Order-disorder enhanced oxygen conductivity and electron transport in Ruddlesden-Popper ferrite-titanate $Sr_3Fe_{2-x}Ti_xO_{6+\delta}$. J. Solid State Chem., **168** (2002) 275-283.

242. M.A. Darroukh, V.V. Vashook, H. Ullmann, F. Tietz, I.A. Raj, Oxides of the AMO_3 and A_2MO_4-type: structural stability, electrical conductivity and thermal expansion. Solid State Ionics, **158** (2003) 141-150.

243. A. Manthiram, F. Prado, T. Armstrong, Oxygen separation membranes based on intergrowth structures. Solid State Ionics, **152-153** (2002) 647-655.

244. S. Guggilla, T. Armstrong, and A. Manthiram, Synthesis, crystal chemistry, and electrical properties of the intergrowth oxides $Sr_{4-x}Ca_xFe_{6-y}Co_yO_{13+\delta}$. J. Solid State Chem., **145** (1999) 260-266.

245. T. Armstrong, F. Prado, Y. Xia, and A. Manthiram, Role of perovskite phase on the oxygen permeation properties of the $Sr_4Fe_{6-x}Co_xO_{13+\delta}$ system J. Electrochem. Soc., **147** (2000) 435-438.

246. S. Guggilla and A. Manthiram, Crystal chemical characterization of the mixed conductor $Sr(Fe,Co)_{1.5}O_y$ exhibiting unusually high oxygen permeability. J. Electrochem. Soc., **144** (1997) L120-L122.

247. A. Fossdal, L.T. Sagdahl, M.-A. Einarsrud, K. Wiik, T. Grande, P.H. Larsen, F.W. Poulsen, Phase equilibria and microstructure in $Sr_4Fe_{6-x}Co_xO_{13}$ ($0 \leq x \leq 4$) mixed conductors. Solid State Ionics, **143** (2001) 367-377.

248. R. Bredesen, T. Norby, A. Bardal, V. Lynum, Phase relatios, chemical diffusion and electrical conductivity in pure and doped $Sr_4Fe_6O_{13}$ mixed conductor materials. Solid State Ionics, **135** (2000) 687-697.

249. J.C. Waerenborgh, M. Avdeev, M.V. Patrakeev, V.V. Kharton, J.R. Frade, Redox behaviour of $Sr_4Fe_6O_{13\pm\delta}$ by Mössbauer spectroscopy and neutron diffraction. Mater. Lett., **57** (2003) 3245-3250.

250. Y.B. Lee, K.P. Chae, S.H. Lee, Mössbauer study of substituted YIG, Y-Gd-Fe-In-O system. J. Phys. Chem. Solids, **62** (2001) 1335-1340.

251. A.N. Petrov, G.V. Denisov, V.M. Zhukovskii, Nature of electrotransport in yttrium iron garnet. Inorg. Mater. (Transl. of Neorg. Mater.), **22** (1986) 579-584.

252. A.M. Abo El Ata, N.A. Sharaf, M.A. Ahmed, B.M. Shalaby, Conduction mechanism in $Y_{3-2x}Ca_{2x}Fe_{5-x}V_xO_{12}$ garnet ferrites. Solid State Sci., **6** (2004) 639-646.

253. S. Wissmann, V. Wurmb, F.J. Litterst, R. Dieckmann and K.D. Becker, The temperature-dependent cation distribution in magnetite. J. Phys. Chem. Solids, **59** (1998) 321-330.

254. A.K. Nikumbh, A.V. Nagawade, V.B. Tadke, P.P. Bakare, Electrical, magnetic and Mössbauer properties of cadmium-cobalt ferrites prepared by the tartarate precursor method. J. Mater. Sci., **36** (2001) 653-662.

255. Y. Purushotham, J.S. Chandel, S.P. Sud, V.K. Babbar, K.V. Reddy, P.V. Reddy, Electrical transport properties of some substituted nickel ferrites. Mater. Sci. and Eng., **B34** (1995) 67-73.

256. Y.-I. Jang, H.-I. Yoo, Phase stability and ionic transference number of a ferrite spinel, $Mn_{0.54}Zn_{0.35}Fe_{2.11}O_4$. Solid State Ionics, **84** (1996) 77-88.

257. D.P. Fagg, V.V. Kharton, J.R. Frade, p-Type electronic transport in $Ce_{0.8}Gd_{0.2}O_{2-\delta}$: the effect of transition metal oxide sintering aids. J. Electroceram., **9** (2002) 199-207.

258. N. Trofimenko, H. Ullmann, Transition metal doped lanthanum gallates. Solid State Ionics, **118** (1999) 215-227.

259. L.A. Chick, L.R. Pederson, G.D. Maupin, J.L. Bates, L.E. Thomas, G.L. Exarhos, Glycine-nitrate combustion synthesis of oxide ceramic powders. Mater. Lett., **10** (1990) 6-12.

260. J. Rodriguez-Carvajal, Recent advances in magnetic-structure determination by neutron powder diffraction. Physica B, **192** (1993) 55-69.

261. J. Hesse, A. Rübartsch, Model independent evaluation of overlapped Mössbauer spectra. J. Phys. E, **7** (1974) 526-532.

262. V.V. Kharton, F.M.B. Marques, Interfacial effects in electrochemical cells for oxygen ionic conduction measurements. I. The e.m.f. method. Solid State Ionics, **140** (2001) 381-394.

263. V.V. Kharton, A.A. Yaremchenko, M.V. Patrakeev, E.N.Naumovich and F.M.B. Marques, Thermal and chemical induced expansion of $La_{0.3}Sr_{0.7}(Fe,Ga)O_{3-\delta}$ ceramics, J. Europ. Ceram. Soc., **23** (2003) 1417-1426.

264. M.V. Patrakeev, E.B. Mitberg, A.A. Lakhtin, I.A. Leonidov, V.L. Kozhevnikov, V.V. Kharton, M. Avdeev, F.M.B. Marques, Oxygen nonstoichiometry, conductivity, and Seebeck coefficient of $La_{0.3}Sr_{0.7}Fe_{1-x}Ga_xO_{2.65+\delta}$ perovskites. J. Solid State Chem., **167** (2002) 203-213.

265. J.C. Waerenborgh, F.M. Figueiredo, J.R. Frade, M.T. Colomer, J.R. Jurado, Fe^{4+} content and ordering of anion vacancies in partially reduced $AFe_xTi_{1-x}O_{3-y}$ (A = Ca, Sr; $x \leq 0.6$) perovskites. An ^{57}Fe Mössbauer spectroscopy study. J. Phys. Cond. Matt., **13** (2001) 8171-8187.

266. P.D. Battle, T.C. Gibb, S. Nixon, A study of the ordering of oxygen vacancies in the rare-earth perovskites $Sr_2MFe_3O_{8+y}$ by Mössbauer spectroscopy. J. Solid State Chem., **79** (1989) 86-98.

267. S. Wissmann and K.D. Becker, Localization of electrons in nonstoichiometric $SrFeO_{3-\delta}$. Solid State Ionics, **85** (1996) 279-283.

268. F.M.B. Marques and G.P. Wirtz, Oxygen fugacity control in nonflowing atmospheres. I. Experimental observations in CO/CO_2 and O_2/N_2 mixtures. J. Am. Ceram. Soc., **75** (1992) 369-374.

269. T. Katsura, K. Kitayama, T. Sugihara, N. Kimizuka, Thermochemical properties of lanthanoid-iron-perovskite at high temperatures. Bull. Chem. Soc. Japan, **48** (1975) 1809-1811.

270. H. Peters, G. Mann, Elektrochemische untersuchung des gleichgewichtes $FeO+CO_2$–reversible–FeO+CO. *Z. Elektrochem.*, **63** (1959) 244-248.

271. K.Q. Huang, R.S. Tichy, J.B. Goodenough, Superior perovskite oxide-ion conductor; strontium- and magnesium-doped $LaGaO_3$: I, phase relationships and electrical properties. J. Am. Ceram. Soc., **81** (1998) 2565-2575.

272. N.M. Sammes, G.A. Tompsett, R.J. Phillips, A.M. Cartner, Characterization of doped lanthanum gallates by X-ray diffraction and Raman spectroscopy. Solid State Ionics, **111** (1998) 1-7.

273. G. Ch. Kostogloudis, Ch. Ftikos, A. Ahmad-Khanlou, A. Naoumidis, D. Stöver, Chemical compatibility of alternative perovskite oxide SOFC cathodes with doped lanthanum gallate solid electrolyte. Solid State Ionics, **134** (2000) 127-138.

274. S.E. Dann, D.B. Curie, M.T. Weller, M.F. Thomas, A.D. Al-Rawwas, The effect of oxygen stoichiometry on phase relations and structure in the system $La_{1-x}Sr_xFeO_{3-\delta}$ ($0 \leq x \leq 1$, $0 \leq y \leq 0.5$). J. Solid State Chem., **109** (1994) 134-144.

275. V.V. Kharton, A.P. Viskup, E.N. Naumovich, N.M. Lapchuk, Mixed electronic and ionic conductivity of $LaCo(M)O_3$ (M = Ga, Cr, Fe or Ni). I. Oxygen transport in perovskites $LaCoO_3$-$LaGaO_3$. Solid State Ionics, **104** (1997) 67-78.

276. P.R. Slater, J.T.S. Irvine, T. Ishihara, Y. Takita, High-temperature powder neutron diffraction study of the oxide ion conductor $La_{0.9}Sr_{0.1}Ga_{0.8}Mg_{0.2}O_{2.85}$. J. Solid State Chem., **139** (1998) 135-143.

277. Y. Takeda, K. Kanno, T. Takada, O. Yamamoto, M. Takano, N. Nakayama, Y. Bando, Phase relation in the oxygen nonstoichiometric system, $SrFeO_x$ ($2.5 \leq x \leq 3.0$). J. Solid State Chem., **63** (1986) 237-249.

278. J.-C. Grenier, N. Ea, M. Pouchard, P. Hagenmuller, Structural transitions at high temperature in $Sr_2Fe_2O_5$. J. Solid State Chem., **58** (1985) 243-252.

279. A. Atkinson and T. Ramos, Chemically-induced stresses in ceramic oxygen ion-conducting membranes. Solid State Ionics, **129** (2000) 259-269.

280. A. Atkinson, Chemically-induced stresses in gadolinium-doped ceria solid oxide fuel cell electrolytes. Solid State Ionics, **95** (1997) 249-258.

281. H. Hayashi, M. Suzuki and H. Inaba, Thermal expansion of Sr- and Mg-doped $LaGaO_3$. Solid State Ionics, **128** (2000) 131-139.

282. S. Kim, S. Wang, X. Chen, Y.L. Yang, N. Wu, A. Ignatiev, A.J. Jacobson, B. Abeles, Oxygen surface exchange in mixed ionic electronic conductors: Application $La_{0.5}Sr_{0.5}Fe_{0.8}Ga_{0.2}O_{3-\delta}$. J. Electrochem. Soc., **147** (2000) 2398-2406.

283. R.A. Niquist and R.O. Kagel, IR spectra of inorganic compounds. Vol. 4. Academic Press, (1997) San Diego.

284. V.V. Kharton, A.P. Viskup, A.V. Kovalevsky, F.M. Figueiredo, J.R. Jurado, A.A. Yaremchenko, E.N. Naumovich and J.R. Frade, Surface-limited ionic transport in perovskites $Sr_{0.97}(Ti,Fe,Mg)O_{3-\delta}$. J. Mater. Chem., **10** (2000) 1161-1169.

285. B.E. Levin, Yu.D. Tretiakov and L.M. Letyuk, Physicochemical basis for synthesis, properties and application of ferrites, Metallurgiya (1979) Moscow.

286. D. Vandormael, F. Grandjean, D. Hautot, G.J. Long, Mössbauer spectral evidence for rhombohedral symmetry in $R_3Fe_5O_{12}$ garnets with R = Y, Eu and Dy. J. Phys. Cond. Mater., **13** (2001) 1759-1772.

287. J. Tsagaroyannis, K. Haralambous, Z. Loizos, N. Spyrellis, Gadolinium iron ferrites – composition and structure. Mater. Lett., **14** (1992) 214-221.

288. V.V. Kharton, F.M. Figueiredo, L. Navarro, E.N. Naumovich, A.V. Kovalevsky, A.A. Yaremchenko, A.P. Viskup, A. Carneiro, F.M.B. Marques and J.R. Frade, Ceria-based materials for solid oxide fuel cells. J. Mater. Sci., **36** (2001) 1105-1117.

289. V.V. Kharton, A.V. Kovalevsky, A.A. Yaremchenko, F.M. Figueiredo, E.N. Naumovich, A.L. Shaulo and F.M.B. Marques, Surface modification of $La_{0.3}Sr_{0.7}CoO_{3-\delta}$ ceramic membranes. J. Membr. Sci., **195** (2002) 277-287.

290. S.R. Rotman, H.L. Tuller, Defect-property correlations in garnet crystals. VII: The electrical conductivity and defect structure of yttrium aluminum and yttrium iron garnet solid solutions. J. Electroceram., **2** (1998) 95-104.

291. Runge H., Brosda S., Guth U., Investigation of the conductivity in mixed oxides based on Ga_2O_3. In *Ionic and Mixed Conducting Ceramics III*, ed. T.A. Ramanaraynan. The Electrochemical Society Proceedings Series, Pennington, NJ, 1998, PV 97-24, pp. 363-369.

292. V.V. Kharton, A.P. Viskup, A.V. Kovalevsky, E.N. Naumovich, and F.M.B. Marques, Ionic transport in oxygen-hyperstoichiometric phases with K_2NiF_4-type structure. Solid State Ionics, **143** (2001) 337-353.

293. H. Hayashi, H. Inaba, M. Matsuyama, N.G. Lan, M. Dokiya and H. Tagawa, Structural consideration on the ionic conductivity of perovskite-type oxides. Solid State Ionics, **122** (1999) 1-15.

294. A.F. Sammels, R.L. Cook, J.H. White, J.J. Osborne and R.C. MacDuff, Rational selection of advanced solid electrolytes for intermediate temperature fuel cells. Solid State Ionics, **52** (1992) 111-123.

295. J.A. Kilner and R.J. Brook, A study of oxygen ion conductivity in doped non-stoichiometric oxides. Solid State Ionics, **6** (1982) 237-252.

296. A.L. Shaula, A.P. Viskup, V.V. Kharton, D.I. Logvinovich, E.N. Naumovich, J.R. Frade and F.M.B. Marques, Oxygen permeability of $LaGa_{0.65}Ni_{0.2}Mg_{0.15}O_{3-\delta}$ ceramics: effect of synthesis method. Mater. Res. Bull., **38** (2003) 353-362.

297. A.L. Shaula, V.V. Kharton, F.M.B. Marques, A.V. Kovalevsky and E.N. Naumovich, Phase interaction and oxygen transport in oxide composite materials. Brit. Ceram. Trans., **103** (2004) 211-218.

298. S. Tao and J.T.S. Irvine, Preparation and characterization of apatite-type lanthanum silicates by a sol-gel process. Mater. Res. Bull., **36** (2001) 1245-1258.

299. E. Ahlgren and F.W. Poulsen, Thermoelectric power of YSZ. Solid State Ionics, **70-71** (1994) 528-532.

300. S. Yamaguchi, K. Kobayashi, K. Abe, S. Yamazaki, Y. Iguchi, Electrical conductivity and thermoelectric power measurements of $Y_2Ti_2O_7$. Solid State Ionics, **113-115** (1998) 393-402.

301. P.S. Anderson, F.M.B. Marques, D.C. Sinclair, A.R. West, Ionic and electronic conduction in $La_{0.95}Sr_{0.05}GaO_{3-\delta}$, $La_{0.95}Sr_{0.05}AlO_{3-\delta}$ and $Y_{0.95}Sr_{0.05}AlO_{3-\delta}$. Solid State Ionics, **118** (1999) 229-239.

302. I. Kosacki, V. Petrovsky, H.U. Anderson, Modelling and characterization of electrical transport in oxygen conducting solid electrolytes. J. Electroceram., **4** (2000) 243-249.

303. Goldanski V.I. and Herber R.H., Chemical applications of Mössbauer spectroscopy. Academic Press, New York, 1968.

304. R.G. Burns, T.C. Solberg, ^{57}Fe-bearing oxide, silicate and aluminosilicate minerals – crystal structure trends in Mössbauer spectra. ACS Symp. Ser., **415** (1989) 262-283.

305. V.V. Kharton, A.P. Viskup, F.M. Figueiredo, E.N. Naumovich, A.A. Yaremchenko and F.M.B. Marques, Electron-hole conduction in Pr-doped $Ce(Gd)O_{2-\delta}$ by faradaic efficiency and emf measurements. Electrochim. Acta, **46** (2001) 2879-2889.

Appendix 1

Examples of structural refinement results of oxide materials studied in this work

A. $SrFe_{0.7}Al_{0.3}O_{3-\delta}$ perovskite

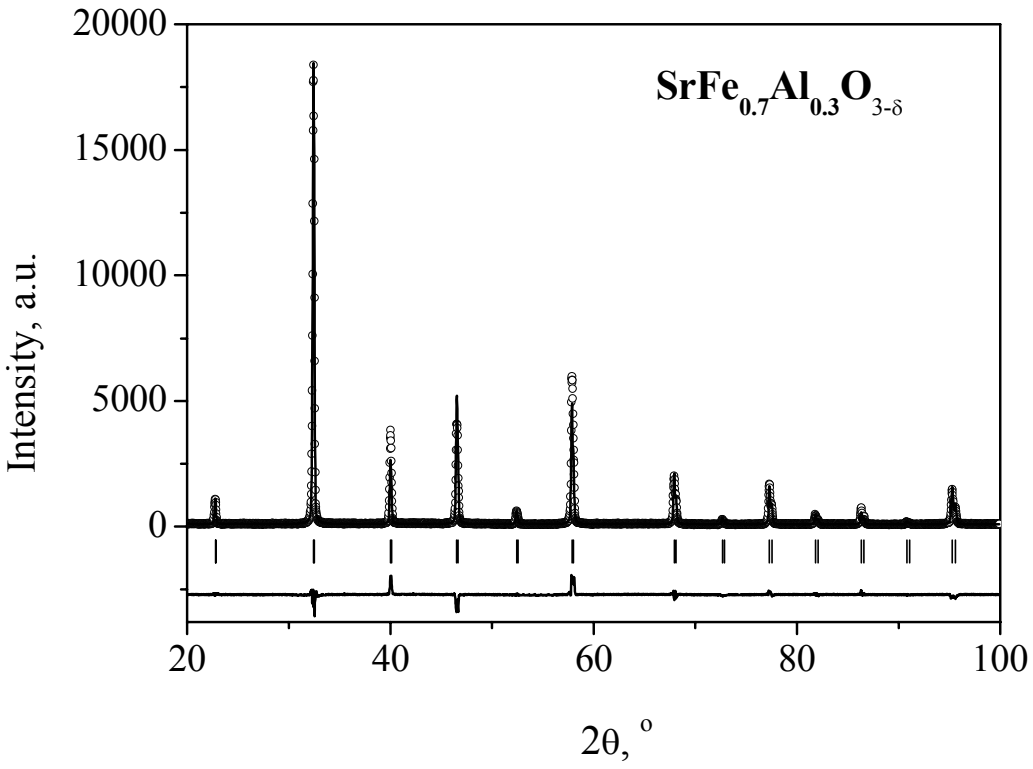

Fig. 1. Observed, calculated and difference XRD patterns of $SrFe_{0.7}Al_{0.3}O_{3-\delta}$ equilibrated in air at RT.

Table 1. Crystal structure data of $SrFe_{0.7}Al_{0.3}O_{3-\delta}$.

Crystal system	Space group	Unit cell parameters, Å	Cell volume, $Å^3$	R_p %	R_{wp} %	χ^2
cubic	$Pm\bar{3}m$ (no. 221)	a = 3.900(4)	59.34(3)	10.6	13.9	4.5

Atom	Wyck.	x	y	z	Occ.	B_{iso}, $Å^2$
Sr	1b	1/2	1/2	1/2	1.00(8)	0.54(0)
Fe	1a	0	0	0	0.67(2)	0.54(1)
Al	1a	0	0	0	0.32(8)	0.54(1)
O	3d	1/2	0	0	0.92(8)	1.32(7)

B. $La_{0.3}Sr_{0.7}Fe_{0.8}Ga_{0.2}O_{3-\delta}$ perovskite

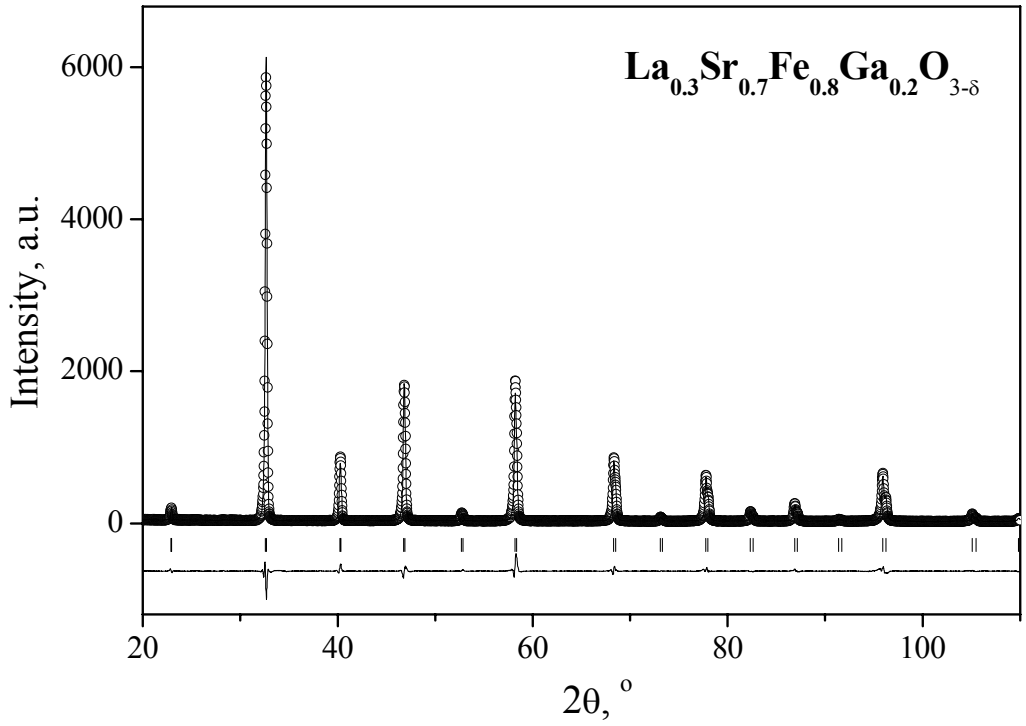

Fig. 2. Observed, calculated and difference XRD patterns of $La_{0.3}Sr_{0.7}Fe_{0.8}Ga_{0.2}O_{3-\delta}$ equilibrated in air at RT.

Table 2. Crystal structure data of $La_{0.3}Sr_{0.7}Fe_{0.8}Ga_{0.2}O_{3-\delta}$.

Crystal system	Space group	Unit cell parameters, Å	Cell volume, $Å^3$	R_p %	R_{wp} %	χ^2
cubic	$Pm\bar{3}m$ (no. 221)	a = 3.881(7)	58.49(3)	5.7	7.2	0.4

Atom	Wyck.	x	y	z	Occ.	B_{iso}, $Å^2$
La	1b	1/2	1/2	1/2	0.24(7)	0.41(5)
Sr	1b	1/2	1/2	1/2	0.75(3)	0.41(5)
Fe	1a	0	0	0	0.81(2)	0.54(5)
Ga	1a	0	0	0	0.18(8)	0.54(5)
O	3d	1/2	0	0	0.99(2)	1.50(1)

C. $Gd_3Fe_5O_{12}$ garnet

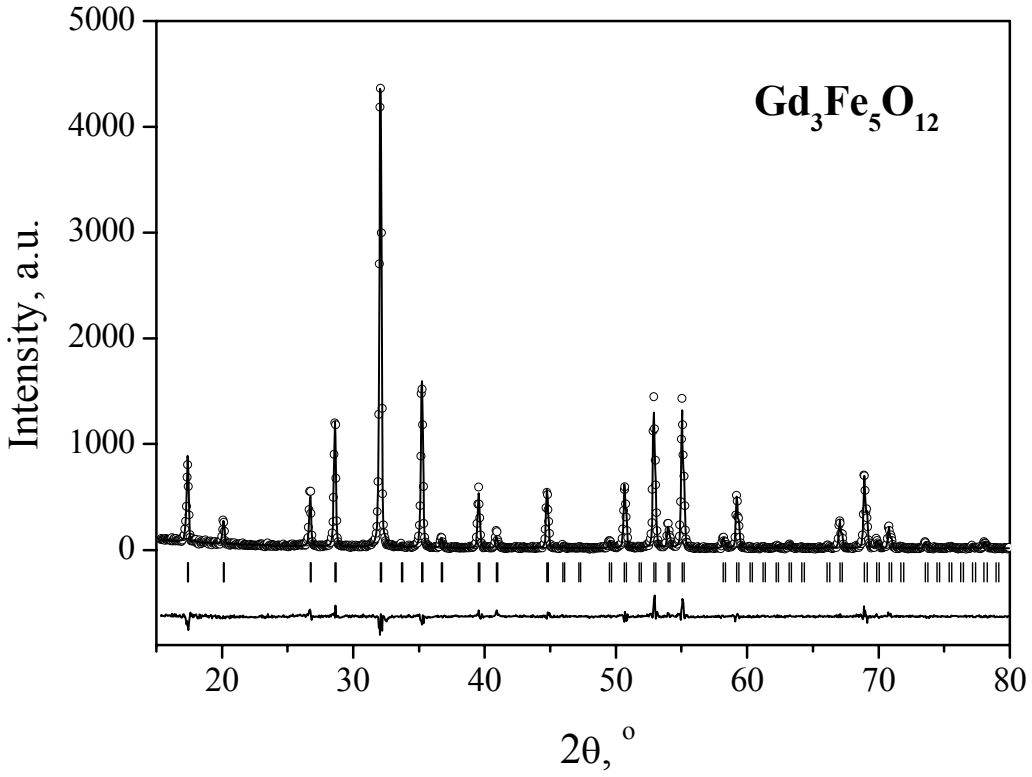

Fig. 3. Observed, calculated and difference XRD patterns of $Gd_3Fe_5O_{12}$ equilibrated in air at RT.

Table 3. Crystal structure data of $Gd_3Fe_5O_{12}$.

Crystal system	Space group	Unit cell parameters, Å	Cell volume, $Å^3$	R_p %	R_{wp} %	χ^2
cubic	$Ia\bar{3}d$ (no. 230)	a = 12.474(1)	1941.0(1)	9.7	14.0	1.7

Atom	Wyck.	x	y	z	Occ.	B_{iso}, $Å^2$
Gd	24c	1/8	0	1/4	0.99(3)	0.39(7)
Fe1	16a	0	0	0	1.00(5)	0.49(8)
Fe2	24d	3/8	0	1/4	0.99(8)	0.62(3)
O	96h	-0.029(0)	0.055(8)	0.152(2)	1.06(4)	0.92(5)

D. $La_{10}Si_5FeO_{26.5}$ apatite

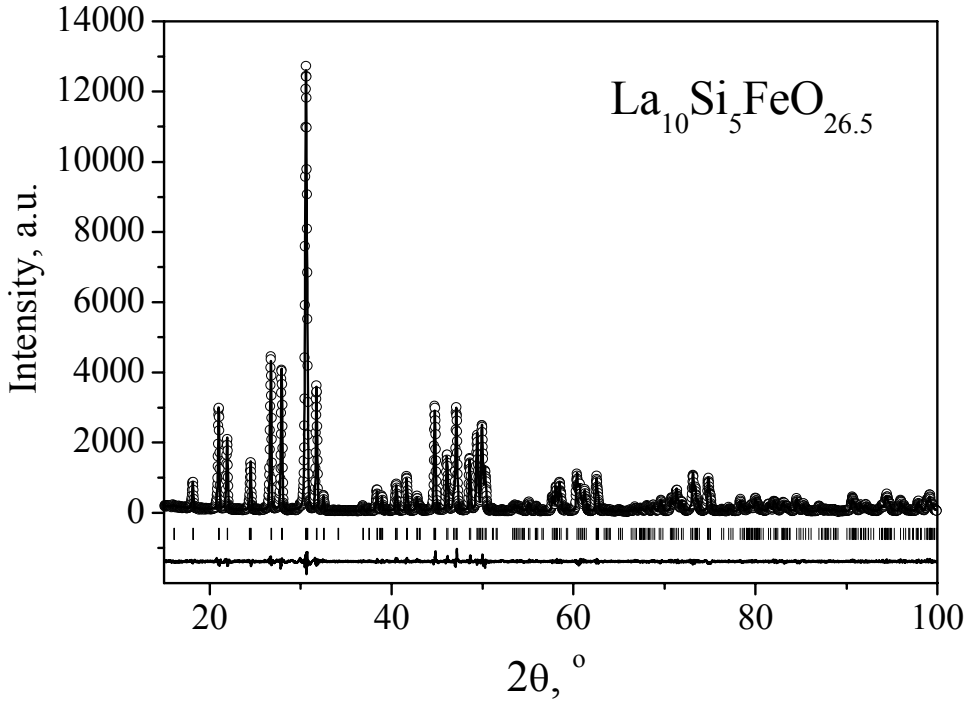

Fig. 4. Observed, calculated and difference XRD patterns of $La_{10}Si_5FeO_{26.5}$ equilibrated in air at RT.

Table 4. Crystal structure data of $La_{10}Si_5FeO_{26.5}$.

Crystal system	Space group	Unit cell parameters, Å	Cell volume, Å^3	R_p %	R_{wp} %	χ^2
hexagonal	$P6_3/m$ (no. 176)	a = 9.757(3) c = 7.255(1)	598.1(8)	5.8	8.2	1.9

Atom	Wyck.	x	y	z	Occ.	B_{iso}, Å^2
La1	6h	0.231(2)	-0.010(9)	1/4	1.02(1)	1.01(7)
La2	4f	1/3	2/3	-0.000(4)	0.99(5)	1.19(2)
Si	6h	0.402(9)	0.376(4)	1/4	0.83(1)	1.12(7)
Fe	6h	0.402(9)	0.376(4)	1/4	0.16(9)	1.12(7)
O1	6h	0.323(2)	0.487(3)	1/4	1.01(8)	1.20(7)
O2	6h	0.596(8)	0.469(3)	1/4	1.01(3)	0.55(6)
O3	12i	0.347(7)	0.260(1)	0.067(4)	1.01(9)	1.60(8)
O4	2a	0	0	1/4	1.03(5)	1.26(5)

Appendix 2

Mössbauer spectroscopy of $SrFe_{1-x}Al_xO_{3-\delta}$ perovskites

The Mössbauer spectra of $SrFe_{1-x}Al_xO_{3-\delta}$ equilibrated with atmospheric oxygen and then slowly cooled down to room temperature (Fig. 1) are similar to those reported for $SrFeO_{3-\delta}$ [233] and $SrFe_{1-x}Ti_xO_{3-\delta}$ perovskites [199]. These spectra can be analyzed using two quadrupole doublets attributed to Fe^{3+} and Fe^{4+}. Considerable broadening of the Lorentzian peaks of the Fe^{3+} doublet suggests contributions from both penta- and hexa-coordinated species with different near-neighbor configurations of oxygen vacancies, Fe^{4+} and Al^{3+}.

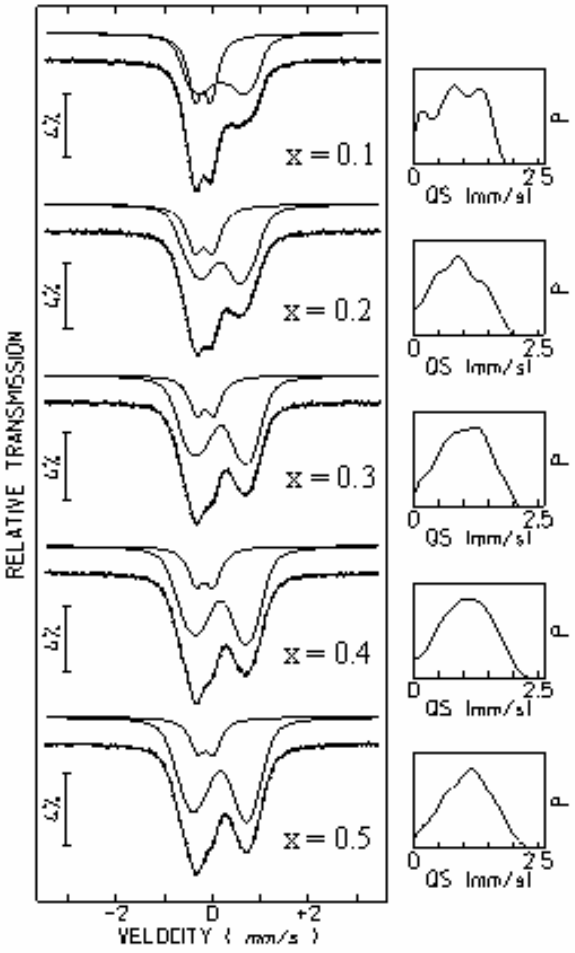

Fig. 1. Room-temperature Mössbauer spectra of $SrFe_{1-x}Al_xO_{3-\delta}$ equilibrated in air (see text). The probability distributions (P) of the Fe^{3+} quadrupole splittings (QS) are given on the right-hand side of the corresponding spectra.

A distribution of Fe^{3+} quadrupole doublets was, therefore, refined employing a correlation between quadrupole splitting (QS) and isomer shift (IS). Estimated parameters for the spectra and relative intensities (I) of Fe^{3+} and Fe^{4+} for the series are given in Table 1. Clearly, Al addition increases the proportion of trivalent Fe, as observed for Ga-, Ti- and Sn-doped $SrFeO_{3-\delta}$ based phases [196,199,264]. For all spectra, the average Fe^{3+} IS values lie in the expected range, 0.25-0.31 mm/s, for penta- and hexa-coordinated ions [265]. Higher IS corresponds to lower QS suggesting, as expected, that local distortion of the coordinating polyhedra increases on lowering the coordination number.

Table 1. Parameters estimated from the Mössbauer spectra of $SrFe_{1-x}Al_xO_{3-\delta}$ at 295 K.

Composition	Fe^{3+}			Fe^{4+}		
	<IS> , mm/s	<QS> , mm/s	I, %	IS, mm/s	QS, mm/s	I, %
$SrFe_{0.9}Al_{0.1}O_{3-\delta}$	0.30	0.89	64%	-0.06	0.34	36%
$SrFe_{0.8}Al_{0.2}O_{3-\delta}$	0.29	0.89	72%	-0.06	0.38	28%
$SrFe_{0.7}Al_{0.3}O_{3-\delta}$	0.29	1.02	79%	-0.04	0.36	21%
$SrFe_{0.6}Al_{0.4}O_{3-\delta}$	0.29	1.06	81%	-0.04	0.36	19%
$SrFe_{0.5}Al_{0.5}O_{3-\delta}$	0.28	1.08	83%	-0.03	0.34	17%

Notes:
IS is the isomer shift relative to metallic α-Fe at 295 K;
<IS> and <QS> are the average IS and QS values estimated from the Fe^{3+} QS distribution;
Estimated standard deviations are < 2% for I and < 0.02 mm/s for the other parameters.

For $SrFe_{0.9}Al_{0.1}O_{3-\delta}$, three local minima are observed in the QS distribution, whereas, for x > 0.1, the distribution is smoother; this shows that the number of different types of Fe environments increases. The average QS value increases with Al content, indicating greater disorder around Fe^{3+}. Concomitantly, the average IS may be observed to decrease, due to a greater number of pentacoordinated sites in Al-rich phases; however, the values are equivalent within experimental error.

Tetrahedrally-coordinated Fe^{3+} is associated with IS < 0.20 mm/s at room temperature [265] and QS > 1.5 mm/s, as exhibited in $Sr_2LaFe_3O_8$ [266], in the related perovskite series $CaFe_{1-x}Ti_xO_{3-\delta}$ [265] or in brownmillerite-type $SrFeO_{2.5}$ [267]. For $SrFe_{1-x}Al_xO_{3-\delta}$ equilibrated with atmospheric oxygen, a significant fraction of large QS values is only found for samples with x > 0.3. Moreover, for

QS > 1.5 mm/s, the corresponding value of IS, 0.25 mm/s, suggests distorted penta-coordinated iron sites. Therefore, although formation of a small fraction of four-fold Fe^{3+} with quadrupole doublets of QS ≥ 1.5 mm/s cannot be ruled out due to the large number of strongly overlapping contributions to the spectra, this effect seems negligible, in agreement with the disordered oxygen sublattice observed by XRD.

In contrast to the case of Fe^{3+}, no significant improvement in the refinement of the Fe^{4+} quadrupole doublet was achieved on employing a QS distribution. The IS values are lower than those obtained both for $SrFeO_3$ (0.05-0.07 mm/s) [151] and $SrFe_{0.9}Ti_{0.1}O_{2.95}$ (0.07 mm/s) [199,265], indicating that the Fe^{4+} species are predominantly isolated.

Appendix 3

Mössbauer spectra of $Gd_{3-x}A_xFe_5O_{12}$ (A = Pr, Ca; x = 0-0.8) garnets

The Mössbauer spectrum of $Gd_3Fe_5O_{12}$ (Fig. 2A) is similar to those reported for rare-earth iron garnet ferrites [286]. It was successively fitted with either two or three sextets. The first model implied that Fe^{3+} on each site, tetrahedral and octahedral, contributes with one sextet to the spectrum. According to the literature [286], the different orientations of the main axis V_{zz} of the electric field gradient and the magnetic hyperfine field B_{hf} on the octahedral sites should give rise to two sextets with the same IS and quadrupole splittings QS, slightly different B_{hf}, and with a relative area ratio of 3:1. For $Ia\bar{3}d$ symmetry, the angle between V_{zz} and B_{hf} on the tetrahedral sites is always the same and therefore only one sextet is expected for this site.

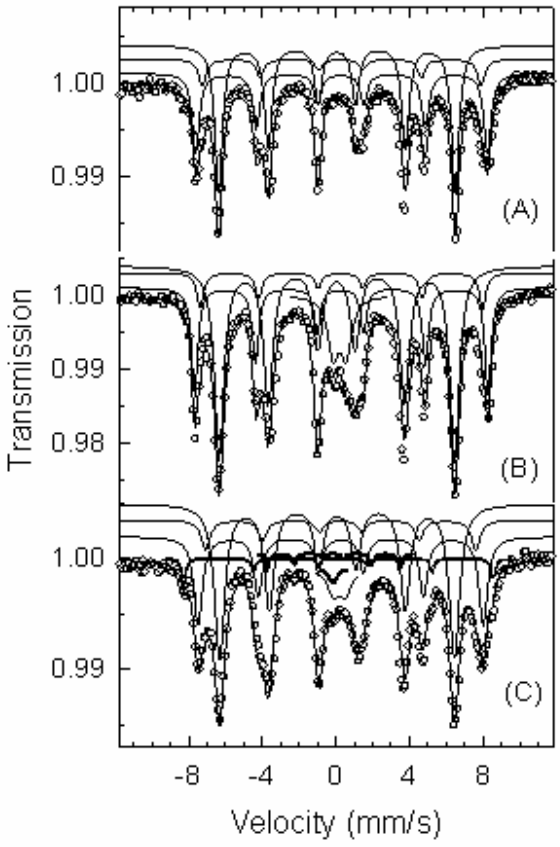

Fig. 2. Mössbauer spectra of $Gd_3Fe_5O_{12}$ (A), $Gd_{2.2}Pr_{0.8}Fe_5O_{12}$ (B) and $Gd_{2.5}Ca_{0.5}Fe_5O_{12}$ (C) at 295 K. The Fe^{4+} sextet and doublet are drawn with the thickest lines.

The three-sextet refinement resulted in a better fitting of the experimental data than the two-sextet fit. A more complex refinement with a total of six sextets resulting from a rhombohedral distortion of the $Ia\bar{3}d$ symmetry, as described for $R_3Fe_5O_{12}$ (R = Y, Eu, Dy) [286], was also attempted but no further improvement of the refinement quality was achieved. The values obtained by the three-sextet fit are summarized in Table 2. Since the relative concentration of tetrahedral to octahedral sites in the garnet structure is 3:2, the estimated relative areas (I) agree with the expected full-site occupation by Fe^{3+}.

Table 2. Parameters estimated from the Mössbauer spectra at 295 K.

Composition	Iron state	IS, mm/s	QS, mm/s	Γ, mm/s	I, %
$Gd_3Fe_5O_{12}$	Fe^{3+} (CN=6)	0.40	0.05	0.46	31
	Fe^{3+} (CN=6)*	0.40	0.05	0.46	10
	Fe^{3+} (CN=4)	0.17	0.01	0.47	59
$Gd_{2.2}Pr_{0.8}Fe_5O_{12}$	Fe^{3+} (CN=6)	0.39	0.05	0.40	23
	Fe^{3+} (CN=6)*	0.39	0.05	0.60	8
	Fe^{3+} (CN=4)	0.16	0.02	0.60	60
	Fe^{3+} (CN=5)	0.30	0.70	0.70	9
$Gd_{2.5}Ca_{0.5}Fe_5O_{12}$	Fe^{3+} (CN=6)	0.38	-0.01	0.52	26
	Fe^{3+} (CN=6)*	0.38	-0.01	0.52	9
	Fe^{3+} (CN=4)	0.18	-0.01	0.62	54
	Fe^{3+} (CN=5)	0.30	0.64	0.70	4.5
	Fe^{4+} (doublet)	-0.05	0.25	0.27	0.7
	Fe^{4+} (sextet)	-0.04	0.03	0.26	2.3
	$GdFeO_3$ and α-Fe_2O_3	0.37	-0.24	0.26	2.9

The $Gd_{2.2}Pr_{0.8}Fe_5O_{12}$ spectrum is shown in Fig. 2B. As expected, the dominant contribution to the spectrum of $Gd_{2.2}Pr_{0.8}Fe_5O_{12}$ is typical for trivalent iron in garnets and was fitted with the same model as for undoped ferrite. The main difference between the shapes of these spectra relates to the strong absorption observed close to zero velocity in the first case, which can be analyzed considering a quadrupole doublet. The estimated IS for this doublet, 0.30 mm/s (Table 2), is low for octahedrally coordinated Fe^{3+}. In oxide materials similar values are usually found for penta-coordinated Fe^{3+} [265]. The estimated I (Table 2) shows that the penta-coordinated Fe^{3+} in $Gd_{2.2}Pr_{0.8}Fe_5O_{12}$ is primarily formed

at the expense of the octahedral Fe^{3+}. Disorder resulting from the loss of the O^{2-} coordinating this octahedral Fe^{3+} may disturb the Fe-O-Fe super-exchange interactions and explain the rapid fluctuations of the magnetic moments of the resulting penta-coordinated Fe^{3+} which appear as paramagnetic in the Mössbauer spectrum.

The Mössbauer spectrum of $Gd_{2.5}Ca_{0.5}Fe_5O_{12}$ also shows a significant absorption around zero velocity (Fig. 2C). Furthermore, a small resolved peak around -8.5 mm/s and a shoulder of the highest velocity peak are clearly observed. The additional sextet necessary to fit these peaks has a B_{hf} similar to those of α-Fe_2O_3 or $GdFeO_3$ (Table 2); the estimated quadrupole shift, ε, is also similar to that of α-Fe_2O_3. Although both $GdFeO_3$ and α-Fe_2O_3 may easily form during the synthesis of $Gd_3Fe_5O_{12}$ [287], these phases are not detected in the cases of Ca-free gadolinium ferrite and $Gd_{2.2}Pr_{0.8}Fe_5O_{12}$. Hence, one may conclude that calcium content in $Gd_{2.5}Ca_{0.5}Fe_5O_{12}$ is slightly higher than the solid solution formation limit, resulting in the segregation of $Gd(Ca)FeO_3$ perovskite and iron oxide. The amount of these phases is however very low, less than 3% (Table 2). This fact together with the high degree of overlap with the strong garnet peaks prevents XRD identification of secondary phases and any reliable fit of the Mössbauer spectra where one sextet for each of the impurity phases should be considered.

Some differences between the Mössbauer spectrum of $Gd_{2.5}Ca_{0.5}Fe_5O_{12}$ and those of other garnets seem to indicate the presence of Fe^{4+}. In contrast to the $Gd_{2.2}Pr_{0.8}Fe_5O_{12}$ spectrum, for Ca-containing material the central absorption around zero velocity could not be properly fitted by a symmetrical quadrupole doublet, as extra absorption around -0.05 mm/s would not be accounted for by such a doublet. The most reasonable origin for this difference relates to the presence of a second additional doublet. In the refinement with two doublets, the main one has the same parameters as the doublet assigned to penta-coordinated Fe^{3+} in $Gd_{2.2}Pr_{0.8}Fe_5O_{12}$; the less intense has a low IS typical of Fe^{4+} [265]. Oh the other hand, a very small peak around -2.5 mm/s is only observed in the $Gd_{2.5}Ca_{0.5}Fe_5O_{12}$ spectrum (Fig. 2C), although barely seen within the background noise. This peak cannot be accounted for the contributions of $Gd(Ca)FeO_3$ and α-Fe_2O_3 impurities. If a sextet with parameters consistent with those of Fe^{4+} [199] is considered in the refinement (Table 2), a small peak around -2.5 mm/s should indeed be observed. Moreover, a significantly better refinement is also achieved. In order to check if such an improvement is not a mathematical artifact of the refinement method, attempts to fit a sextet with similarly low IS and B_{hf} in the spectra of the other samples were made. In both $Gd_3Fe_5O_{12}$ and $Gd_{2.2}Pr_{0.8}Fe_5O_{12}$ cases, the area of this sextet always converged to negligible values, in contrast to $Gd_{2.5}Ca_{0.5}Fe_5O_{12}$. A part of Fe^{4+} seems to be magnetically ordered, while another part appears paramagnetic as the penta-coordinated Fe^{3+}.

Appendix 4

Mössbauer spectroscopy of $La_{10-x}Si_{6-y}Fe_yO_{26\pm\delta}$ ($0 \le x \le 0.67$, $1 \le y \le 2$) and $La_{9.83}Si_{4.5}Al_{1.5-x}Fe_xO_{26\pm\delta}$ ($0 \le x \le 1.5$) apatites

The Mössbauer spectrum of $La_{10}Si_4Fe_2O_{26}$, fitted with one quadrupole doublet, consists of two symmetric peaks with almost equal area and width (Fig. 3). The IS estimate (Table 3) is typical for tetrahedrally-coordinated Fe^{3+}. Oxygen excess in $La_{10}Si_4Fe_2O_{26}$, if any, is lower than the detection limit. On the contrary, the doublet peaks of $La_{10}Si_{6-x}Fe_xO_{27-x/2}$ (x = 1.0 and 1.5) are substantially asymmetric (Fig. 3). This cannot be attributed to a Goldanskii-Karyagin effect or slow paramagnetic relaxation as decreasing the temperature from 297 down to 10 K resulted in no considerable changes in the ratios of the peak areas and widths [303]. The asymmetry cannot be explained also by texture effects since the areas and widths ratios are independent of the angle between the γ-ray beam and the Mössbauer absorber surface, i.e. the packing direction of apatite particles in the absorber.

Table 3. Parameters estimated from the RT Mössbauer spectra of $La_{10-x}Si_{6-y}Fe_yO_{26\pm\delta}$.

Composition	Iron state	IS, mm/s	QS, mm/s	Γ, mm/s	I, %
$La_{10}Si_5FeO_{26.5}$	Fe^{3+} (CN=4)	0.11	0.76	0.46	63
	Fe^{3+} (CN=5)	0.29	0.89	0.29	37
$La_{10}Si_{4.5}Fe_{1.5}O_{26.25}$	Fe^{3+} (CN=4)	0.11	0.73	0.39	81
	Fe^{3+} (CN=5)	0.29	0.87	0.31	19
$La_{10}Si_4Fe_2O_{26}$	Fe^{3+} (CN=4)	0.12	0.69	0.34	100
$La_{9.33}Si_5FeO_{25.5}$	Fe^{4+}	0.00	0.27	0.30	4
	Fe^{3+} (CN=4)	0.14	0.73	0.43	62
	Fe^{3+} ($LaFeO_3$)	0.40	-0.07	0.27	34

Since no alternative justification can be found for the asymmetry of these spectra, a second symmetric doublet, with most of the corresponding area contributing to the largest absorption peak in each spectrum, was considered. The parameters of the first doublet, with IS = 0.11 mm/s, are typical of tetrahedral Fe^{3+} in other apatites; the second doublet has IS = 0.29 mm/s, characteristic of Fe^{3+} with higher coordination, and can be ascribed to penta-coordinated trivalent iron cations [265]. This strongly suggests the existence of interstitial O^{2-} anions in the nearest neighborhood of Fe^{3+}. Such conclusion is in excellent agreement with the results of atomistic modeling [94], which revealed two energy-preferential interstitial positions (O7) close to SiO_4 tetrahedra in the apatite unit cell. The occupation of O7 sites should increase the coordination of iron cations. Considering the third doublet

with parameters typical of Fe^{4+} showed no significant improvement for the final fit. Due to the strong overlap of the three doublets, it is impossible to assure whether any Fe^{4+} is formed.

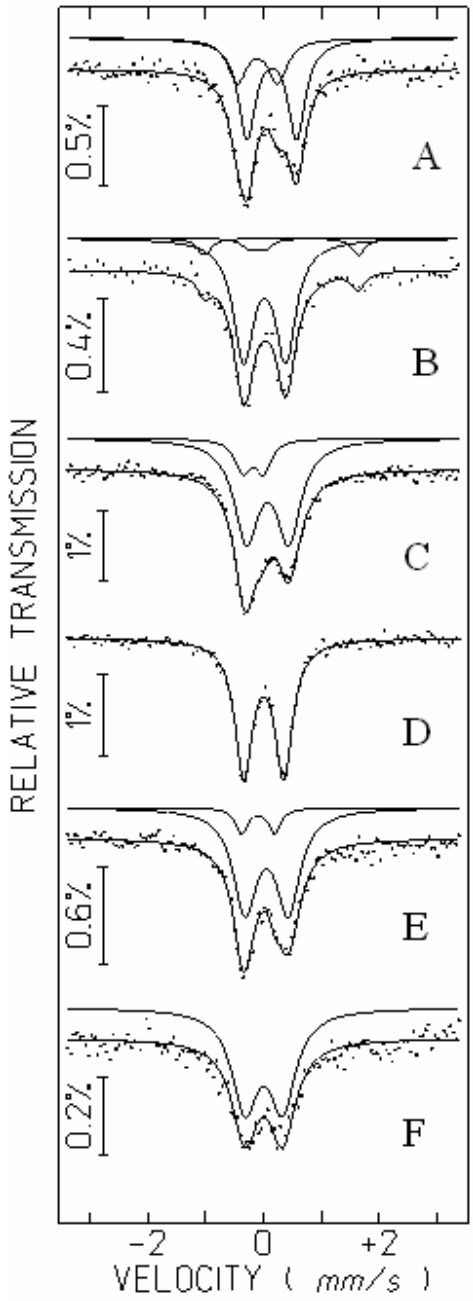

Fig. 3. RT Mössbauer spectra of $La_{10}Si_5FeO_{26.5}$ (A), $La_{9.33}Si_5FeO_{25.5}$ (B), $La_{9.83}Si_{4.5}Fe_{1.5}O_{26}$ (C), $La_{10}Si_4Fe_2O_{26}$ (D), $La_{9.83}Si_{4.5}Al_{0.5}FeO_{26}$ (E), and $La_{9.83}Si_{4.5}AlFe_{0.5}O_{26}$ (F).

The Mössbauer spectrum of $La_{9.33}Si_5FeO_{25.5}$ exhibits a sextet with parameters (Table 3) typical of $LaFeO_3$ [274]. An asymmetry of the central doublet might be caused by the fact that the distance between the low-velocity peaks of tetrahedrally- and octahedrally-coordinated Fe^{3+} is shorter if compared to the corresponding high-velocity peaks (Fig. 3). However, a second doublet characteristic of Fe^{4+} slightly improves the final fit, thus indicating the presence of a small amount of tetravalent iron in the apatite phase. Mössbauer spectra showed no traces of metallic iron in reduced apatites; even the concentration of Fe^{2+} was found lower than the detection limit (Table 4).

Table 4. Parameters estimated from the RT Mössbauer spectra of $La_{10}Si_4Fe_2O_{26}$.

Pretreatment	Iron state	IS, mm/s	QS, mm/s	Γ, mm/s	I, %
Oxidation	Fe^{3+} (CN=4)	0.12	0.69	0.34	100
Reduction	Fe^{3+} (CN=4)	0.14	0.69	0.42	100

The oxidation and reduction procedures included annealing (1173-1273 K, 5-10 h) in air or flowing H_2-H_2O-N2 mixture with $p(O_2) \approx 3\times10^{-14}$ Pa, respectively.

The Mössbauer spectra of $La_{9.83}Si_{4.5}Al_{1.5-y}Fe_yO_{26}$ consist of asymmetric doublets (Fig. 3). Due to reasons discussed above each spectrum was fitted considering two symmetric doublets. The IS values estimated for these doublets (Table 5) are typical of Fe^{3+} and Fe^{4+} [265]. In the case of the $La_{9.83}Si_{4.5}AlFe_{0.5}O_{26}$ spectrum, no Fe^{4+} was detected. However, since the quality of the latter spectrum is relatively poor due to the low total iron content in this sample, the accuracy of the corresponding data is worse compared than for other apatite phases.

Table 5. Parameters estimated from the RT Mössbauer spectra of $La_{9.83}Si_{4.5}Al_{1.5-x}Fe_xO_{26\pm\delta}$.

Composition	Pretreatment	Iron state	IS, mm/s	QS, mm/s	Γ, mm/s	I, %
$La_{9.83}Si_{4.5}AlFe_{0.5}O_{26}$	oxidation	Fe^{3+} (CN=4)	0.14	0.66	0.55	100
$La_{9.83}Si_{4.5}Al_{0.5}FeO_{26}$	oxidation	Fe^{4+}	0.02	0.57	0.25	11
		Fe^{3+} (CN=4)	0.17	0.75	0.50	89
	reduction	Fe^{3+} (CN=4)	0.12	0.70	0.33	100
$La_{9.83}Si_{4.5}Fe_{1.5}O_{26}$	oxidation	Fe^{4+}	0.01	0.33	0.44	26
		Fe^{3+} (CN=4)	0.18	0.77	0.48	74
	reduction	Fe^{3+} (CN=4)	0.14	0.76	0.40	100

The oxidation and reduction procedures included annealing (1173-1273 K, 5-10 h) in air or flowing H_2-H_2O-N2 mixture with $p(O_2) \approx 3\times10^{-14}$ Pa, respectively.

When discussing the Mössbauer spectroscopy data, one should note that the Fe^{4+} oxidation state is rather uncommon and appears mostly in ABO_3 perovskite-related structures. In natural silicates such as annites, pyroxenes or smectites [304], tetra-coordinated Si can be substituted by iron but always in the form of Fe^{3+}. A similar situation is observed for the La-stoichiometric $La_{10}Si_4Fe_2O_{26}$. In the case of $La_{10}Si_{4.5}Fe_{1.5}O_{26.25}$ and $La_{10}Si_5FeO_{26.5}$, incorporation of extra oxygen occurs in the interstitial sites neighboring $(Si,Fe)O_4$ units. The A-site deficiency leads to formation of Fe^{4+}.

Appendix 5

Mössbauer spectra of $La_{9.83-x}Pr_xSi_{4.5}Fe_{1.5}O_{26\pm\delta}$ ($0 \leq x \leq 6$) apatites

Mössbauer spectrum of reduced $La_{9.83}Si_{4.5}Fe_{1.5}O_{26}$ shows a symmetric doublet (Fig. 4) with IS and quadrupole splitting (Table 6) typical of tetrahedrally-coordinated Fe^{3+} [265], whereas the spectrum of $La_{9.83}Si_{4.5}Fe_{1.5}O_{26}$ annealed in air is substantially asymmetric, indicating that besides the main doublet due to tetrahedrally-coordinated Fe^{3+} an additional doublet may be present. The asymmetry of this spectrum cannot be related to a Goldanskii-Karyagin effect, slow paramagnetic relaxation or texture effects due to reasons already discussed in Appendix 3. Therefore, a second symmetric doublet with most of the corresponding area contributing to the largest absorption peak of the spectrum envelope was considered.

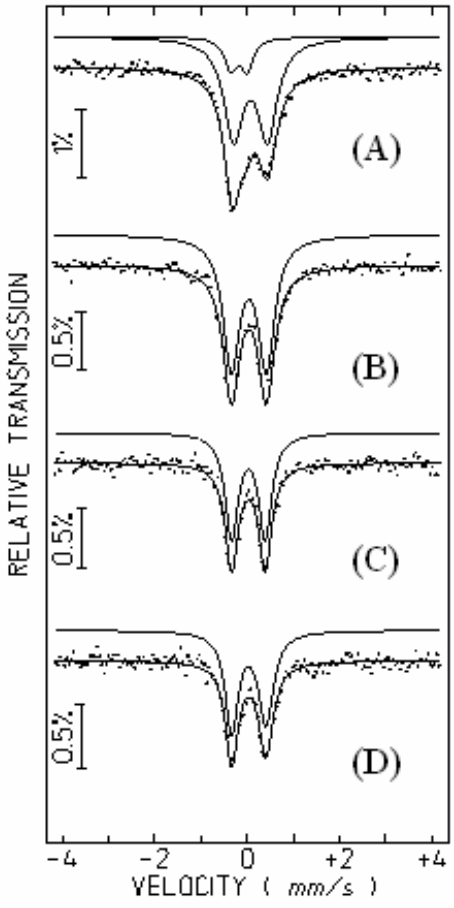

Fig. 4. RT Mössbauer spectra of $La_{9.83}Si_{4.5}Fe_{1.5}O_{26}$ after annealing in air (A) and reduction (B), $La_{6.83}Pr_3Si_{4.5}Fe_{1.5}O_{26}$ (C) and $La_{3.83}Pr_6Si_{4.5}Fe_{1.5}O_{26}$ (D) after oxidation in air.

The IS values estimated for this additional doublet (Table 6) are typical of tetravalent iron [265]. Within the limits of experimental error, the estimated quadrupole splittings of Fe^{3+} and Fe^{4+} are temperature-independent in the range 10-297 K. This fact, and also the similar variation of the corresponding IS values with temperature, explain why the asymmetry of the spectra does not depend on temperature.

On the contrary, the Mössbauer spectra of Pr-containing apatites annealed in air consist of single quadrupole doublets (Fig. 4), indicating that all iron is tetrahedrally-coordinated Fe^{3+} (Table 6).

Table 6. Parameters estimated from the RT Mössbauer spectra of $La_{9.83-x}Pr_xSi_{4.5}Fe_{1.5}O_{26\pm\delta}$.

Composition	Pretreatment	Iron state	IS, mm/s	QS, mm/s	Γ, mm/s	I, %
$La_{9.83}Si_{4.5}Fe_{1.5}O_{26}$	oxidation	Fe^{4+}	0.01	0.33	0.44	26
		Fe^{3+} (CN=4)	0.18	0.77	0.48	74
	reduction	Fe^{3+} (CN=4)	0.12	0.76	0.40	100
$La_{6.83}Pr_3Si_{4.5}Fe_{1.5}O_{26}$	oxidation	Fe^{3+} (CN=4)	0.14	0.73	0.34	100
$La_{3.83}Pr_6Si_{4.5}Fe_{1.5}O_{26}$	oxidation	Fe^{3+} (CN=4)	0.15	0.74	0.36	100

The oxidation and reduction procedures included annealing (1173-1273 K, 5-10 h) in air or flowing H_2-H_2O-N_2 mixture with $p(O_2) \approx 3\times10^{-14}$ Pa, respectively.

List of Symbols

c_k - concentration of k-type particles

D_k - diffusion coefficient of k-type particles

D_s - oxygen self-diffusion coefficient

d - membrane thickness

d_c - critical thickness

d_j - jump distance

E - voltage

E_a - activation energy

E_{cell} - cell voltage

E_o - open-circuit voltage

E_{sensor} - sensor electromotive force

E_{sample} - sample electromotive force

e - elementary charge (1.60219×10^{-19} C)

F - Faraday constant (96484.56 C mol^{-1})

ΔG_i - free energy change of process i

ΔH_i – enthalpy change of process i

I_k - current density of k-type particles

I_{pump} - current through the pump

I_{sample} - current through the sample

j_k - flux density of k-type particles

$J(O_2)$ - specific oxygen permeability

k_s - surface exchange coefficient

N_A - Avogadro constant (6.02205×10^{23} mol^{-1})

n - concentration of electrons

p - concentration of holes

q - transported heat of a polaron

R - molar gas constant (8.31441 J mol^{-1} K^{-1})

R_{AC} - sample resistance under alternating current

R_{DC} - sample resistance under direct current

R_e - electronic resistance of sample

R_M - external variable resistance

R_o - oxygen-ionic resistance of sample

R_η - polarization resistance of electrodes

R_{Ohm} - ohmic resistance of electrodes and electrolyte

r - radius

S - membrane surface area

S_A - sample cross area

ΔS_i - entropy change of process i

s - transported entropy of a polaron

T - absolute temperature

t_k - transference number of k-type particles

U_{sample} - voltage applied to a sample

u_k - mobility of k-type particles

V - elementary cell volume

z_k - charge number of k-type particles

α - Seebeck coefficient; thermal expansion coefficient

δ - oxygen nonstoichiometry

η_k - electrochemical potential of k-type particles

μ_k - chemical potential of k-type particles

ν - jump frequency

ν_o - vibration (jump attempt) frequency

ρ - density

σ - total conductivity

σ_{amb} - ambipolar conductivity

σ_k - partial conductivity of k-type particles

υ_k - velocity of k-type particles

φ - electrical potential

ω - volume fraction

List of Abbreviations

AC	alternating current
AEE	alkaline-earth element
CGO	gadolinia-doped ceria
DC	direct current
DTA	differential thermal analysis
EDS	energy dispersive spectroscopy
EMF	electromotive force
FE	faradaic efficiency
GNP	glycine-nitrate processing
LBFC	$(La,Ba)(Fe,Co)O_{3-\delta}$
LSFC	$(La,Sr)(Fe,Co)O_{3-\delta}$
LSGM	$(La,Sr)(Ga,Mg)O_{3-\delta}$
LSM	$(La,Sr)MnO_{3-\delta}$
MIEC	mixed ionic and electronic conductor
OP	oxygen permeability
REE	rare-earth element
SEM	scanning electron microscopy
S.G.	space group
SOFC	solid oxide fuel cell
SSR	solid-state route
TEC	thermal expansion coefficient
TGA	thermogravimetric analysis
TPB	three phase boundary
XRD	X-ray diffraction
YSZ	yttria-stabilized zirconia